

**OVERHEATING OF LOW-ALLOY FORGING STEELS  
FOR NUCLEAR POWER PLANT ROTORS AND VESSELS**

by

John T. Murphy

B.S., Mechanical Engineering  
University of Notre Dame (1982)

and

M.S., Civil Engineering  
University of Notre Dame (1985)

Submitted to the Department of Nuclear Engineering  
in partial fulfillment of the requirements for the degree of

DOCTOR OF PHILOSOPHY

at the

MASSACHUSETTS INSTITUTE OF TECHNOLOGY

January 1995

ology

Signature of Author . . .



.....  
Department of Nuclear Engineering  
January 25, 1995

Certified by .

.....  
Dr. Ronald G. Ballinger  
Thesis Supervisor

Accepted by . . . . .

.....  
Dr. Allan F. Henry  
Chairman, Departmental Committee on Graduate Studies

1995

1995

# OVERHEATING OF LOW-ALLOY FORGING STEELS FOR NUCLEAR POWER PLANT ROTORS AND VESSELS

by

John T. Murphy

Submitted to the Department of Nuclear Engineering  
on January 25, 1995, in partial fulfillment of the  
requirements for the degree of Doctor of Philosophy  
in Nuclear Engineering

## ABSTRACT

An experimental investigation was made of the precipitation behavior of manganese sulfide (MnS) in low-alloy forging steels when cooled slowly from high temperatures. 3.5NiCrMoV low-pressure turbine steel and A 508 Cl 4 nuclear reactor pressure vessel material was studied. Material samples were subjected to heat treatments simulating forging heats, over a range of preheating temperatures and cooling rates. Charpy V-Notch tests were employed to examine the influence of temperature and cooling rate on impact energy. SEM and TEM examination of fractured material and extracted precipitates was used to establish the variation of precipitate morphology over the temperature-cooling rate domain. A trace analysis of chemically etched material was performed to determine the orientation relationship between observed rod-shaped manganese sulfides and the parent austenite matrix. The analysis required developing a new solution method for calculating austenite orientation from the traces on two surfaces of annealing twins occurring on {111} planes. The new method also provided information on the uniqueness and uncertainty of the calculated solutions. A coherent interface between the austenite and MnS was proposed to explain the orientation relationship which was determined. The implications of the observed MnS distributions and morphologies for material performance in nuclear power applications were discussed.

Thesis Supervisor: Ronald G. Ballinger

Title: Associate Professor of Nuclear Engineering and Materials Science and Engineering



## **Dedication**

To my wife Sarah  
with love and gratitude

## Acknowledgments

I would like first to acknowledge the support of my advisor, Prof. Ron Ballinger. From day one my experience at MIT has been shaped by Ron's enthusiasm for research and teaching, willingness to take on any new challenge, and estimable work ethic. I hope I take with me a fraction of the drive and intensity he exhibits. I am also grateful for the encouragement and advice of Profs. Regis Pelloux and Sam Allen, who were essential in dispelling all the doubts and confusion.

It has been my great privilege to be associated with the Alcator C-Mod project at the MIT Plasma Fusion Center. The excellent work of everyone I have known on C-Mod is a mark I will strive for throughout my life. The support and advice of Herb Becker, Steve Fairfax, Jim Rosati, Bill Beck, Bill Burke, Frank Silva and many others transformed the flywheel from a Gordian knot into a rewarding challenge. In particular I am grateful for the supervision of Dave Gwinn. More than anyone, Dave pushed the limits of what I believed I could achieve. I will consider myself indeed fortunate if I work for one like him again.

It has been an honor to be part of the Department of Nuclear Engineering. The outstanding tradition of teaching and research established by Benedict, Kaplan and others is exemplified by members of the present faculty from whom I had the pleasure of learning, including Profs. Ken Russell, Ian Hutchinson, Elias Gyftopoulos, Larry Lidsky and Jeff Freidberg.

Throughout my program I have had the friendship, assistance and example of numerous students and staff, including Martin Morra, Chang-Heui Jang, Jeff O'Donnell, Ilsoon Hwang, Frank Wong, Glenn Romanowski, Pete Stahle, and Dan Riesner. Without them the past years would have been significantly more difficult and less enjoyable. In particular I am thankful for the deep friendships of Dan Wang, Hiu Au, John Chun, and Jun Matsumoto.

I must express my gratitude to many "on the outside." None of this would have been contemplated if not for the love, security and comfort furnished to our son Christopher by his day-care providers, the Bellanger-Rakauskas, Ryan-Vallely

and Buck households. Many old friends refused to allow me to drop off the screen, even though they received no assistance from me in that effort. Similarly my family and my wife's have patiently tolerated my half-participation in family life without complaint. I recognize the great debt I owe them all, and look forward to attempting to repay it.

Finally, I note the two fundamental truths concerning my time at MIT: 1) I learned and achieved only a tiny fraction of what Christopher has in his first two years, and 2) the most enjoyable, rewarding and essential aspect of the whole experience was living through it with my wife Sarah.

## Table of Contents

Abstract.....	2
Dedication .....	3
Acknowledgments .....	4
Table of Contents.....	6
List of Figures .....	9
List of Tables .....	15
1.0 Introduction .....	16
1.1. Alcator C-Mod Flywheel.....	17
1.2. Thesis Organization .....	21
2.0 Literature Review .....	22
2.1. Low-Alloy Forging Steels.....	22
2.2. Manganese Sulfide Inclusions in Steel .....	31
2.2.1. Influence and Control of Sulfur in Steel .....	31
2.2.2. Basic Thermodynamics and Crystallography of MnS .....	32
2.2.3. MnS Influence on Material Performance in Low-Alloy Steels .....	41
2.2.4. Overheating.....	45
2.3. Precipitation Orientation Relationships.....	55
3.0 Research Objectives .....	59
4.0 Experimental Procedure.....	62
4.1. Overheating Tests .....	62
4.1.1. Material.....	62
4.1.2. Heat Treatment.....	63
4.1.2.1. Austenitization Temperature Tests .....	66
4.1.2.2. Martensitic Material Tests.....	68
4.1.2.3. Cooling Rate Tests.....	69
4.1.3. Test Matrix .....	73
4.1.4. Fracture Tests.....	73
4.1.5. Microscopy .....	76
4.1.5.1. Optical Fractography .....	76
4.1.5.2. SEM Fractography.....	79
4.1.5.3. Optical Metallography .....	80
4.1.5.4. Auger Spectroscopy .....	83

4.2. Sulfide-Rod Orientation Relationship .....	84
4.2.1. TEM of MnS Rod Extractions .....	84
4.2.2. Trace Analysis.....	86
4.2.2.1. Geometry and Analysis .....	86
4.2.2.2. Experimental Procedure.....	97
5.0 Results .....	99
5.1. Overheating Tests .....	99
5.1.1. Impact Energy.....	99
5.1.2. Microscopy and Metallography .....	101
5.1.2.1. Optical and SEM Fractography .....	101
3.5NiCrMoV Cooling Rate Tests .....	101
3.5NiCrMoV Austenitization Temperature Tests .....	118
3.5NiCrMoV Martensitic Tests .....	130
A 508 Cl 4 Tests .....	135
5.1.2.2. Optical Metallography .....	140
Final Microstructural Characterization.....	140
Prior Austenite Grain Structure .....	149
Inclusion Characteristics .....	152
5.2. Sulfide-Rod Orientation Relationship .....	160
5.2.1. Extraction Replicas.....	160
5.2.2. Trace Analysis.....	167
5.2.2.1. Metallography for Input Data .....	167
5.2.2.2. Computer Model Results .....	167
6.0 Discussion .....	182
6.1 Overheating Tests .....	182
6.1.1 Initial Material Condition .....	182
6.1.2 Precipitation Phenomena Variation with Temperature and Cooling Rate.....	183
6.1.2.1 Phenomena Versus Cooling Rate.....	183
6.1.2.2 Phenomena Versus Austenitizing Temperature .....	190
6.1.3 A 508 Cl 4 Material Tests.....	191
6.1.4 Implications for Forging Procedure .....	193
6.1.5 Implications for Material Performance .....	194
6.1.5.1 Rod Morphology Transition.....	194
6.1.5.2 Necessity for Superclean Specification .....	196

6.1.5.3	Susceptibility of Overheated Material to Environmental Cracking.....	197
6.2	Manganese Sulfide Inclusion Characteristics .....	198
6.2.1	Rod-Matrix Orientation Relationship .....	198
6.2.2	Implications for Other MnS Morphologies .....	202
7.0	Summary, Conclusions and Future Work.....	203
7.1	Summary and Conclusions.....	203
7.2	Future Work.....	206
References.....		208
A	Trace Analysis FORTRAN Programs and Output.....	219
A.1.	TRACE Code for Determining Austenite Orientation.....	220
A.2.	TRACE Output for Trace Analyses .....	226
A.3.	RODS Code for Determining Rod Crystallographic Orientation .....	243
A.4.	RODS Output for Trace Analyses.....	249
B	Remarks on Heat Treatment of Specimens in Air .....	252

## List of Figures

Figure 1.1	Diagram of Alcatraz C-Mod Flywheel.....	17
Figure 1.2	Diagram of Flywheel Fabrication Procedure .....	19
Figure 2.1	Free Energy of Formation of Pure Sulfides [from 46] .....	33
Figure 2.2	Free Energy of Formation of Sulfides in Solutions With Compositions of Typical Steels [from 46] .....	34
Figure 2.3	Crystal Structure of MnS.....	35
Figure 2.4	Appearance of Type I Manganese Sulfide on a Polished and Etched Surface [from 55] .....	36
Figure 2.5	Appearance of Type I Manganese Sulfide on a Fracture Surface [from 69] .....	36
Figure 2.6	Appearance of Type II Manganese Sulfide on a Polished and Etched Surface [from 55] .....	37
Figure 2.7	Appearance of Type II Manganese Sulfide on a Deep-Etched Surface [from 69] .....	37
Figure 2.8	Appearance of Type III Manganese Sulfide on a Polished and Etched Surface [from 55] .....	38
Figure 2.9	Appearance of Type III Manganese Sulfide on a Fracture Surface [from 69] .....	38
Figure 2.10	Type IV Ribbon Morphology Manganese Sulfide, Discovered by Kiessling and Lange [from 55] .....	40
Figure 2.11	So-Called "Widmanstätten Platelets" of Manganese Sulfide [from 55] .....	40
Figure 2.12	Equiaxed Type I/III MnS Flattened out into High-Aspect Ratio "Stringers" by Rolling [from 69].....	42
Figure 2.13	Extremely High Aspect Ratio Stringers [from 100].....	43
Figure 2.14	Partially Spheroidized Stringer [from 69].....	44
Figure 2.15	Impact Energy vs. Austenitizing Temperature for Steels of Various Sulfur Contents [from 15].....	48
Figure 2.16	Microfacets Due to Transgranular Precipitation of Sulfides on Crystallographic Planes [from 2].....	49
Figure 2.17	Rod-Shaped Sulfides Observed by Hale, Preston and Nutting in Overheated 3.5NiCrMoV [from 11] .....	52

Figure 2.18	Structural Ledges Which Maximize Atomic Matching in Austenite-Ferrite Interface [from 58] .....	56
Figure 2.19	Annealing Twins Formed in Annealed Stainless Steel [from 108] .....	58
Figure 4.1	Flywheel 2 Preliminary Heat Treatment Schematic [after 45] .....	63
Figure 4.2	Test Ring Location on Piece and Within As-Forged Profile .....	65
Figure 4.3	Furnace Apparatus for Cooling Rate Tests .....	70
Figure 4.4	Configuration of Ceramic Bath Cooling Rate Test .....	72
Figure 4.5	Parallel Fence Structure of Type II MnS, Revealed by Warm 50% Nitric Acid [from 67] .....	82
Figure 4.6	Apparatus for Removing Extraction Replica Film Via the Acetone Float Method .....	85
Figure 4.7	Specimen Appropriate for Two-One Trace Analysis (Specimen 5-1-S1) .....	87
Figure 4.8	Geometry of Two-One Trace Analysis.....	89
Figure 4.9	Austenite Crystal Orientation Represented by "Pyramid" Defined by the Upper Octahedral Planes .....	90
Figure 4.10	Austenite Crystal Orientation Rotation Geometry .....	91
Figure 4.11	Directions of Normal Vectors of the Other Three Octahedral Planes .....	93
Figure 4.12	Geometry of Local/Specimen Coordinate Transformation.....	95
Figure 5.1	Flat Facet on As-Received Control Material.....	104
Figure 5.2	Higher Magnification of Dimples and Sulfides on Facet in Figure 5.1 .....	104
Figure 5.3	Optical Micrograph of Distorted Facets on As-Received Control Material .....	105
Figure 5.4	SEM Micrograph of Distorted Facets in Figure 5.3 .....	105
Figure 5.5	Higher Magnification Micrograph of Distorted Facets in Figure 5.3 .....	106
Figure 5.6	Large PAGB Facet on Fracture Surface of Alumina-Quenched Material.....	106
Figure 5.7	Inclusion-Free Dimples on Facet in Figure 5.6.....	107
Figure 5.8	Fracture Surface Surrounding Facet of Figure 5.6, Typical of Tough, Ductile, Intragranular Failure .....	107
Figure 5.9	Elevated Facet Containing a Prior Austenite Grain Boundary Edge in a 10°C/min Control-Cooled Material.....	108



Figure 5.10	Higher Magnification Micrograph of Inclusions and Dimples on Facet of Figure 5.9 .....	108
Figure 5.11	Microfacets Adjacent to Edge Facet of Figure 5.9.....	109
Figure 5.12	Opened Grain Boundary Triple Point on Surface of 5°C/min Control-Cooled Material .....	109
Figure 5.13	Higher Magnification Micrograph of Inclusions and Dimples on Facet of Figure 5.12 .....	110
Figure 5.14	Higher Magnification Micrograph of Split Rod Precipitate in Figure 5.13 .....	110
Figure 5.15	EDS Spectrum of Rod Precipitate in Figure 5.21 .....	111
Figure 5.16	Sulfide "Rafts" Developed on 5°C/min Control-Cooled Material.....	112
Figure 5.17	Fine Dendritic Structure of Sulfide Rafts in Figure 5.16.....	112
Figure 5.18	Large Low-Ductility Facet on Surface of 1°C/min Control-Cooled Material .....	113
Figure 5.19	Higher Magnification View Showing Low-Ductility Nature of Surface of Large Facet in Figure 5.18 .....	113
Figure 5.20	Elongated Dimples and High-Aspect Ratio Sulfide Rods Surrounding Large Facet in Figure 5.18.....	114
Figure 5.21	Typical High-Aspect Ratio Sulfide Rod From Region About Large Facet in Figure 5.18 .....	114
Figure 5.22	Large Facet on Surface of 1°C/min Control-Cooled Material.....	115
Figure 5.23	Higher Magnification Micrograph Of Low-Ductility Nature of Large Facet in Figure 5.22.....	115
Figure 5.24	Long Sulfide Rods and Dimples in "Basket-Weave" Distribution About Large Facet in Figure 5.18 .....	116
Figure 5.25	"Basket-Weave" Pattern of Sulfide Rods on Fracture Surface of Material Cooled at Slowest Rate of 0.5°C/min .....	116
Figure 5.26	High-Magnification Micrograph of Clean Cleavage Fracture in Sulfide Rod .....	117
Figure 5.27	Shiny and Dull Fracture Surfaces of As-Received and Quenched and Tempered Material, Respectively .....	121
Figure 5.28	Large Facet With Fine Dimples and Sulfides on Austenitization Temperature Test As-Received Material.....	121
Figure 5.29	Typical Fracture Surrounding Large Facets on Austenitization Temperature Test As-Received Material.....	122

Figure 5.30	Typical Fracture Surface of Austenitization Temperature Test Quenched and Tempered Material .....	122
Figure 5.31	Large PAGB Facet on 1200°C Control-Cooled Material.....	123
Figure 5.32	Higher Magnification Micrograph of Aligned Embryonic Rod Sulfides on PAGB Facet in Figure 5.31 .....	123
Figure 5.33	Dense Region of High-Aspect Ratio Dimples and Rods, Aligned Within Subregions, on 1250°C- Control-Cooled Material.....	124
Figure 5.34	More Aligned High-Aspect Ratio Dimples and Rods on Additional 1250°C Material .....	124
Figure 5.35	Aligned High-Aspect Ratio Dimples and Rods on 1300°C Material.....	125
Figure 5.36	Sulfide Rod "Turning the Corner" on 1300°C Control-Cooled Material.....	125
Figure 5.37	Microfacet on 1300°C Control-Cooled Material .....	126
Figure 5.38	Large Low-Ductility PAGB Facet Surrounded by Microfacets and Aligned Rods on 1350°C Control-Cooled Material .....	126
Figure 55.	High-Magnification Micrograph of Microfacet, Indicating Fractal-Like Structure .....	127
Figure 56.	High-Magnification View of Sponge-Like Morphology of 1400°C Slow-Cooled Material .....	127
Figure 5.41	Large PAGB Facet With Ductile Dimples Nucleated at Fine Sulfides on 1200°C Air-Quenched Material .....	128
Figure 5.42	Large PAGB Facet With Ductile Dimples But Without Sulfide Nucleators.....	128
Figure 5.43	Inclusion-Free Ductile Dimples on Facet of Figure 5.42.....	129
Figure 5.44	Tough, Fibrous Fracture Outside of PAGB Facets on 1350°C Air-Quenched Material .....	129
Figure 5.45	Large PAGB Facet on Fracture Surface of Control-Cooled Martensitic Material.....	131
Figure 5.46	Impression of Martensite Lathes or Plates Formed at the Austenite Boundary on Facet of Figure 5.45 .....	131
Figure 5.47	Aligned Troughs Amid Cleavage Fracture Field in Martensitic Material of Figure 5.45.....	132
Figure 5.48	High-Magnification Micrograph of Rod Trough in Figure 5.47.....	132

Figure 5.49	Large PAGB Facet on Fracture Surface of Air-Quenched Martensitic Material.....	133
Figure 5.50	Detailed Structure of Air-Quenched Martensitic Material PAGB Facet in Figure 5.49 .....	133
Figure 5.51	Finer Cleavage Morphology in Air-Quenched Martensitic Material.....	134
Figure 5.91	Dark-Field Image of Extracted Rod Exhibiting Contrast Boundary Possibly Due to Crystal Grain Boundary .....	171
Figure 5.92	Surface of Figure 5.91 (Surface A) After Sawcut to Intersect Twin 1 is Made, Re-Etched With Villela's Reagent .....	171
Figure 5.93	New Surface Produced by Sawcut to Intersect Twin (Surface B), Etched With Villela's Reagent.....	172
Figure 5.94	Micrograph of Etched Surface of Figure 5.91 (Surface A), Etched With Villela's Reagent, Showing Rod Adjacent to Twin Trace.....	172
Figure 5.95	Composite Micrograph of Etched Surface of Figure 5.91 (Surface B), Etched With Villela's Reagent, Showing Common Edge at Top and Rod Trace at Lower Center .....	173
Figure 5.96	Dot Product Solution Curves for Remaining Octahedral Planes Versus Analysis Rotation Angle for Specimen 5-1-S1.....	175
Figure 5.97	Dot Product Solution Curves for Remaining Octahedral Planes Versus Analysis Rotation Angle for Specimen 5-1-S2.....	176
Figure 5.98	Dot Product Solution Curves for Remaining Octahedral Planes Versus Analysis Rotation Angle for Specimen 5-1-1.....	177
Figure 5.99	Dot Product Solution Curves for Remaining Octahedral Planes Versus Analysis Rotation Angle for Specimen 5-1-2.....	178
Figure 5.100	Face-Centered Cubic (FCC) System Stereographic Triangle With Widely Scattered Results of Trace Analysis .....	181
Figure 5.101	Face-Centered Cubic (FCC) System Stereographic Triangle With Closely Agreeing Results of Trace Analysis.....	181
Figure 6.1	Summary Diagram of Precipitation Phenomena Observed in 3.5NiCrMoV .....	184
Figure 6.2	Rapidly-Formed Precipitate Straining Austenite Lattice Planes .....	186
Figure 6.3	Subsequent Precipitates Forming in Elastically Accommodating Zone Adjacent to Initial Precipitate .....	187

Figure 6.4	Generalized Diagram of Precipitation Phenomena Possible in 3.5NiCrMoV With 40 PPM Sulfur.....	192
Figure 6.5	Affect on Fracture Propagation of Rod Bands and Low- Ductility PAGB .....	197
Figure 6.6	Included Angles Between Cubic Crystal [110] Directions .....	199
Figure 6.7	Atomic Matching Between [100] MnS Direction and [110] Austenite Direction .....	201

## List of Tables

Table 2.1	Minimum and Maximum Composition Limits Specified by the ASTM for Various Grades of Rotor and Vessel Forging Steels.....	23
Table 4.1	Chemical Composition of Subject Materials, As Determined by the Manufacturers.....	64
Table 4.2	Sulfur Solubility vs. Temperature for Flywheel Steel, Determined Using Equations From Reference 33 For Manganese Content of 0.38% (Weight %) .....	67
Table 4.3	Heat Treatment Parameters For All Specimens, Grouped By Test Series. ....	74
Table 4.4	Mechanical Tests and Microscopic and Metallurgical Examinations For All Specimens, Grouped By Test Series .....	77
Table 4.5	Metallographic Etchants.....	80
Table 5.1	Impact Energies for All Valid Charpy V-Notch Tests .....	100
Table 5.2	Included Angles Between MnS Rods, Measured From Chrome Trioxide Etch Micrographs, With Estimated Angle of Inclination to Etch Planes .....	156
Table 5.3	Summary of Indexing of TEM Diffraction Patterns From Extraction Replicas.....	166
Table 5.4	Trace Analysis Input Data for All Specimens .....	174
Table 5.5	Cubic System Unit Vectors and Rationalized Miller Indices for the Rod Traces, As Determined by the RODS Code .....	179
Table B.1	Decarburization Levels Determined by Chemical Check .....	252

## 1.0 Introduction

The research described in this thesis was an outgrowth of work related to procuring a forged steel flywheel for the MIT Plasma Fusion Center (PFC). This flywheel is used to increase the energy available for input to an experimental fusion reactor, the Alcator C-Mod tokamak. Difficulties encountered during fabrication of this piece pointed to the need for further investigation of mechanical properties degradation due to high-temperature treatment of the 3.5NiCrMoV grade of forging steel used for the flywheel. This introduction will first describe the flywheel and the problems encountered during production, and then outline the research program which resulted.

### 1.1. Alcator C-Mod Flywheel

The Alcator C-Mod project is a tokamak, a type of magnetic confinement fusion reactor which uses pulsed high-field electromagnets to confine an extremely high-temperature plasma. Like previous tokamaks at the PFC, Alcator C-Mod is powered by an industrial alternator donated to the center by a utility. During operation, the alternator rotor is brought up to speed without the field coils on using a 2000 HP electric motor. The coils are then briefly energized to provide a short-duration high-power pulse for the tokamak's magnets. The total available energy, and thus magnet field strength, is limited by the amount of rotational energy which can be stored in the rotor. In order to increase this energy for the C-Mod experiment, a large steel flywheel was attached to one end of the rotor. A simplified diagram of the flywheel is shown in Figure 1.1. With a rotational inertia of over  $80,000 \text{ kg}\cdot\text{m}^2$ , the flywheel stores 1500 MJ when spinning at 1800 rpm, three times the energy stored in the rotor alone [44].

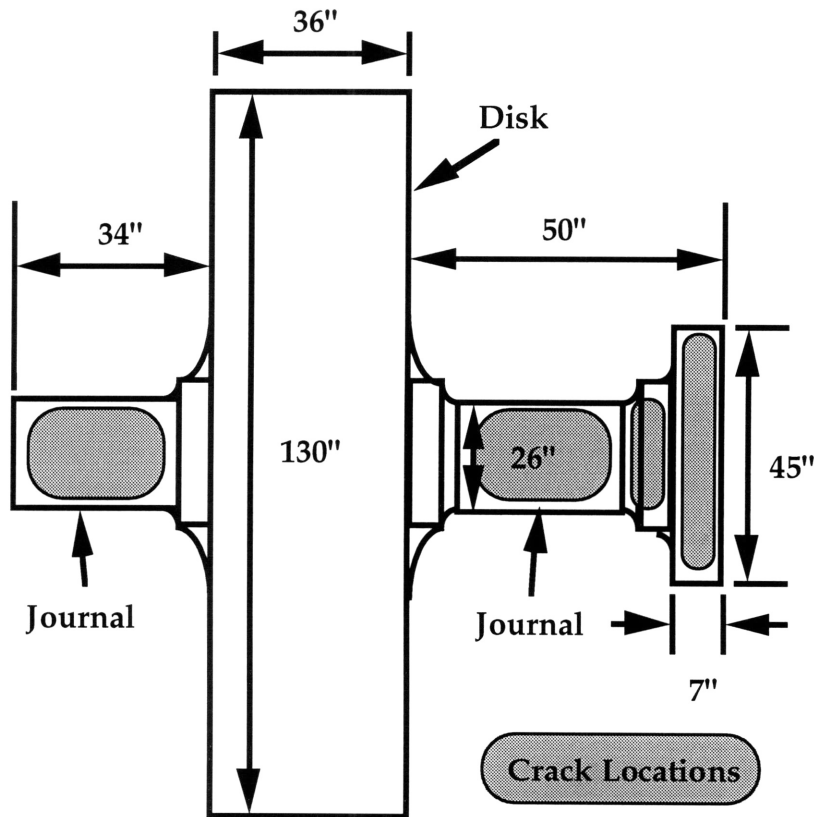


Figure 1.1 Diagram of Alcator C-Mod Flywheel

The flywheel was open-die forged by a major forgings producer using a 3.5NiCrMoV grade low-alloy steel which is typically specified for low-pressure turbine rotors<sup>1</sup>. The fabrication procedure, depicted in Figure 1.2, consisted of a 210 ton ingot pour (A), forging (B), preliminary heat treatment (C), rough machining (D), inspection (E), quality heat treatment (quench and temper, F), final machining (G), and acceptance inspection and testing (H) [45]. The forging process itself was essentially several stretching, or cogging operations, an intermediate upset, further stretching, forging down of the journals, and final upset of the disk. The upsets were demanding, and in order to have adequate formability the starting temperature for most of the process steps was 1280°C. This was 30°C higher than the maximum heat temperature commonly employed for this material.

In the first attempt at manufacture of the flywheel, numerous cracks were detected in both journals during inspections between the preliminary and quality heat treatments, and the piece was internally rejected. A second attempt appeared to be sound up until the inspection after the quality heat treatment, at which point many crack indications, both ultrasonic and magnetic particle, were found in both journals. Once more the piece was internally rejected. In both cases cracks were found only in the journal regions, while the rest of the piece was free of flaws.

A lengthy failure analysis resulted in several conclusions: 1) since flaws were present in the first attempt prior to the quality heat treatment, quench cracking was eliminated as a cause, 2) hydrogen content was acceptably low, thus the cracks were not hydrogen flakes, 3) cracks occurred only in the portions of the piece which were not forged after the final 1280°C heat, 4) material from locations of the second flywheel which contained cracks also exhibited faceted fracture surfaces in impact tests, 5) the sizes and orientations of cracks and facets were similarly distributed, and 6) examination of opened internal flaws by scanning electron microscope often revealed them to be macroscopically-flat planes of dense ductile dimples nucleated on fine manganese sulfide (MnS) inclusions, a common nonmetallic phase found in steel.

---

<sup>1</sup> Table 2.1 in the next section provides chemical compositions of this and other rotor steel grades.



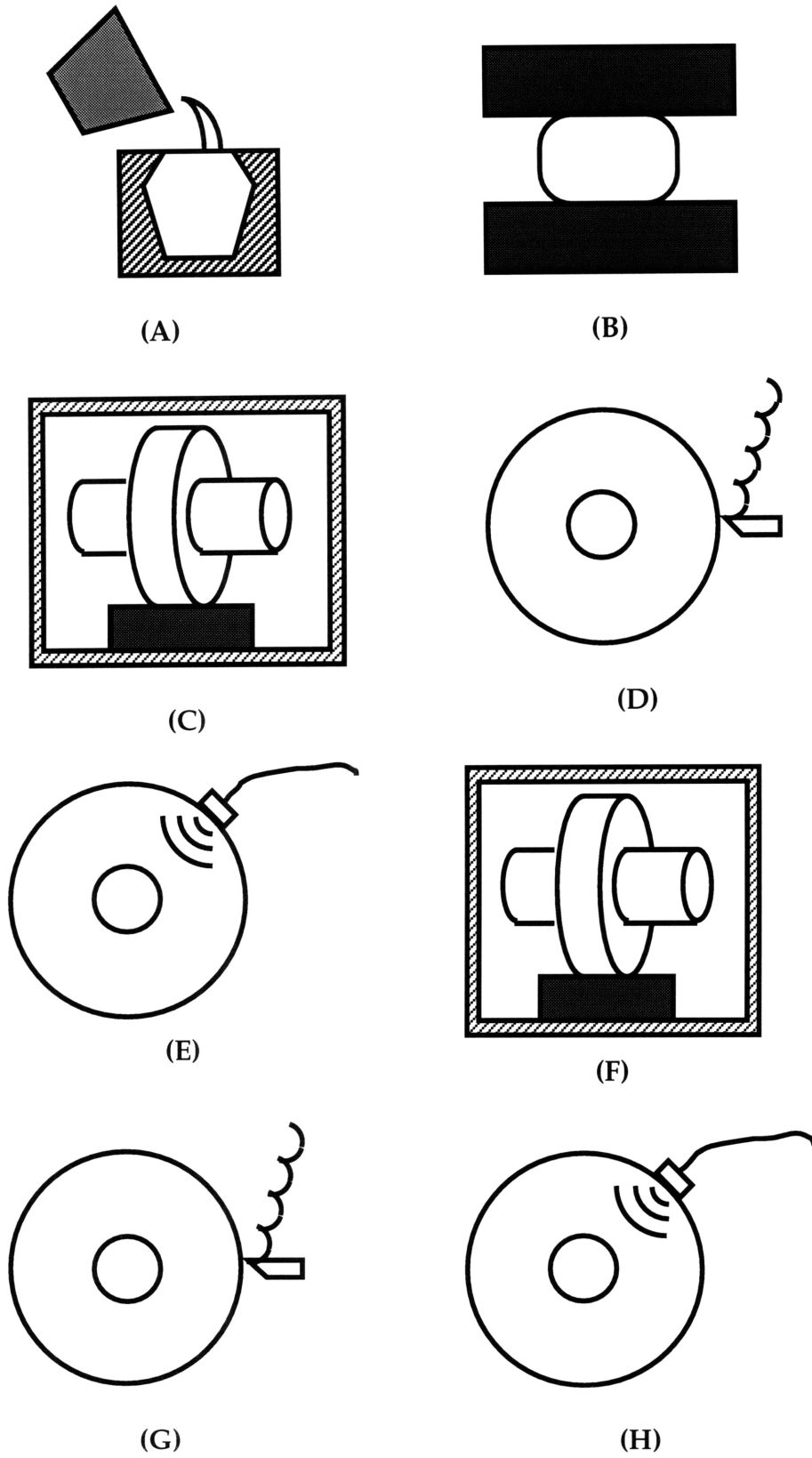


Figure 1.2 Diagram of Flywheel Fabrication Procedure

After a search of the literature, the probable root cause of the cracking was determined to be a forging condition termed "overheating". In this phenomenon, during forging heats a temperature is reached which is high enough for the entire sulfur content of the steel to be taken into solid solution. During subsequent cooling, depending on the cooling rate, dense arrays of fine MnS particles can precipitate at the boundaries of what are, at that temperature, grains of austenite. At room temperature the decorated prior austenite grain boundaries serve as low-energy fracture paths, often resulting in dramatically lowered fracture energy as measured in a Charpy V-Notch (CVN) impact test.

It was obvious from the faceted fracture surfaces covered with dense, fine dimples that the regions of the first two flywheels which contained cracks were overheated. It also seemed clear that the cracks occurred at prior austenite grain boundaries, which must have been overheated. Thus the strategy for crack prevention which was developed by the manufacturer relied upon preventing overheating of the journals. This was achieved by insulating them with magnesium oxide-lined sheet steel caps during the final heat. A full-scale mock-up test, whose results were calibrated with thermal transient finite element analysis, established that the insulated journals would remain below the expected overheating temperature. Although this strategy entailed challenging planning and handling, it was successfully employed during forging of a third attempt. Extensive fracture testing of the final forging failed to reveal any faceting, while thorough ultrasonic inspection of the entire volume confirmed it was free of cracks. Thus, although the exact relationship between overheating and later cracking was unknown, the role of overheating as a precursor to cracking was apparently confirmed.

As will be discussed in the literature review section, the 3.5NiCrMoV grade used for the flywheel is a superlative steel which is likely to see even wider application in the nuclear power industry in the future. Further, as will also be discussed, unusual components which will be required for future reactors may well employ forging procedures similar to that used on the flywheel. Thus it was considered that a further investigation of the overheating behavior of the 3.5NiCrMoV grade was warranted, and this thesis is the result.

## **1.2. Thesis Organization**

The thesis is organized as follows: first the relevant literature is reviewed, concerning both low-alloy forging steel in general as well as the subjects of overheating and precipitate orientation relationships specifically. The objectives of the research are then presented, followed by a detailed description of the experimental techniques and procedures employed to accomplish them. Results of the research follow next, then a section discussing them and another summarizing conclusions which can be drawn and suggesting further work. Finally details of supporting work and computer codes and output are included as appendices.

## 2.0 Literature Review

The literature relevant to the work of this thesis is reviewed here. That concerning low-alloy forging steel in general is addressed first, followed by the subjects of overheating and precipitate orientation relationships.

### 2.1. Low-Alloy Forging Steels

Low-alloy steels are carbon steels containing additions of not more than 5% each of the major alloying elements, such as Ni, Cr, Mo, V and Mn [52]. They are used primarily in rolled-plate or forged form, in a wide variety of critical structural applications. Two major uses of low-alloy forgings in the nuclear power industry are as cylindrical rotors for turbines and generators and as hollow vessels for reactors, steam generators and pump cases. Typical grades and compositions are shown in Table 2.1.

Most modern rotors are manufactured from one of three grades of low-alloy steel, depending on the purpose of the rotor. High and intermediate pressure (HP/IP) turbines typically operate in excess of 500°C. Rotors for this application require good creep properties and a low ductile-brittle transition temperature, which is provided by the CrMoV grade usually specified. Low pressure (LP) turbine rotors, meanwhile, operate at lower temperatures but higher stresses. The 3.5NiCrMoV steel which is the material of choice for such components provides high strength and toughness and a low rate of fatigue crack growth to minimize the risk of fracture from flaw growth during operation [40]. Finally, generator rotors, which operate close to room temperature and at lower stresses, are manufactured from the NiMoV grade. All three grades are governed by American Society for Testing and Materials (ASTM) Standard A 470 [41], which specifies composition limits as summarized in Table 2.1.

The history of steel development for rotor applications has been comprehensively reviewed elsewhere [38,39,73]. This history is marked by two major trends: 1) improvement of material performance in order to satisfy efficiency goals of the power generation industry, and 2) metallurgical development in response to failures of existing materials under increasingly demanding service.

Table 2.1 Minimum and Maximum Composition Limits Specified by the ASTM for Various Grades of Rotor and Vessel Forging Steels [41,42,86] (Note: J Factor calculated neglecting Sn for all besides EPRI superclean.)

Grade	Application	ASTM Specification	C	Mn	P	S	Si	Sn	Ni	Cr	Mo	V	J
													Fact.
NiMoV	generator rotors	A 470 Cl 4	0.28	1.00	0.012	0.015	0.015			1.05	1.05	0.20	
									0.75	1.50	1.50	0.30	162
3.5NiCrMoV	LP rotors	A 470 Cl 5,6,7	0.28	0.60	0.012	0.015	0.100		3.25	1.25	0.25	0.05	
				0.20					4.00	2.00	0.60	0.15	84
3.5NiCrMoV	EPRI superclean goal		0.25	0.02	0.002	0.001	0.020	0.002	3.50	1.65	0.45	0.10	1.6
CrMoV	HP/IP rotors	A 470 Cl 8	0.25				0.015			1.05	1.05	0.20	
			0.35	1.00	0.012	0.015	0.350		0.75	1.50	1.50	0.30	162
NiCrMo, lean	RPV	A 508 Cl 2		0.50			0.150		0.50	0.25	0.55		
			0.27	1.00	0.025	0.025	0.400		1.00	0.45	0.70	0.05	350
NiCrMo	RPV (naval)	A 508 Cl 3		1.20			0.150		0.40		0.45		
			0.25	1.50	0.025	0.025	0.400		1.00	0.25	0.60	0.05	475
NiCrMo	RPV (naval)	A 508 Cl 4		0.20			0.150		2.75	1.50	0.40		
			0.23	0.40	0.020	0.020	0.400		3.90	2.00	0.60	0.03	160

A significant portion of these efforts has focused on elimination or control of so-called "residual" elements, i.e., those which are not added intentionally by the steelmaker but which are present as often undesirable but inevitable impurities from the steelmaking process [39].

A good illustration of this is the application of the CrMoV grade to HP/IP turbine rotors [38]. Prior to World War II power plant steam cycles employed much lower temperatures and pressures. However in the 40s more efficient units operating at higher temperatures resulted in operation of materials for high pressure components in the creep regime. The then existing grades, which were unable to meet the more demanding service, were replaced in HP/IP rotor applications by the CrMoV grade, which had been developed as the result of extensive research to produce a material with the proper balance of creep strength and ductility. Key to this effort was the use of the new electric furnace technology for melting, which produced a cleaner material with fewer inclusions than the old open hearth furnaces [38]. This effort continues today in the program to employ the 12% Cr steels, with even better creep properties, in rotors for high efficiency supercritical plants [73].

The development path of the 3.5NiCrMoV grade is similar. The older NiMoV grade, governed by ASTM Standard A 293 [75], was the standard LP turbine rotor material for many years. However it was inadequate for the larger, more efficient units introduced in the 50s. These units incorporated larger diameter final stages and thus higher spin stresses. In the early 50s a number of the larger units failed catastrophically at stresses which were well below the yield stress [74,117]. A special task force of the ASTM was formed to investigate these incidents and make recommendations as to how to prevent such occurrences in the future [38]. Among their recommendations were the need to minimize the presence of initial flaws, such as hydrogen flakes, and the need to develop a tougher material which was less susceptible to embrittlement [76].

As described by Curran [38], the new 3.5NiCrMoV grade was developed for this service. In contrast to the NiMoV steel, in this grade the Mn level was lowered to avoid temper embrittlement (a phenomenon which will be discussed later). Manganese, however, promotes hardenability which is essential in heat treatment of thick sections such as rotors. To compensate for the loss of Mn

manufacturers added nickel, which promotes toughness as well as hardenability. Finally, to achieve the high strength levels necessary for the largest last-stage buckets, about 1.5% chrome was added. Introduction of this alloy in 1959, along with specification of vacuum degassing of molten steel to eliminate hydrogen flaking, did much to reduce the possibility of failure by fracture in LP turbines. Modern users also frequently require the additional steps of employing vacuum carbon deoxidation (VCD) to reduce the number of silicate inclusions which occur in silicon-deoxidized ("killed") steel, along with quenching in water rather than oil after quality heat treatment for higher strength for the largest units, especially nuclear.

A more recent example of in-service failure which is driving current metallurgical development of rotor steel is stress-corrosion cracking (SCC) of shrunk-on turbine disks. A common fabrication route in LP turbines is to forge a rotor and barrel, onto which separately-forged disks are "shrunk-fit", with machined mechanical keyways for position control. These keyways have proven to be initiating sites for SCC, and extensive cracking of disks in service has been reported, including those manufactured from the 3.5NiCrMoV grade [77]. This problem has been the focus of major research concerning, among other issues, the effect on SCC susceptibility of microstructure and alloying element segregation [78,79]. A production-end solution developed by the forging industry has been to fabricate "monoblock" rotors, in which the disks are integral with the rotor barrel, and no keyed interface is necessary. Forging of such extremely large structures from the 3.5NiCrMoV grade has pushed the limits of ingot-making and forging capabilities [80,81].

Probably the most highly investigated subject in low-alloy steels today is the subject of "super-clean" technology, in which several measures, including scrap-control and ladle-refining, are employed to produce steels with extremely low concentrations of residual elements such as P, S, Sn, As, and Sb, as well as elements usually intentionally added, such as Mn and Si [5,11,82]. Much work has been focused on the 3.5NiCrMoV grade, in order to reduce the incidence of "temper embrittlement". In this phenomenon, segregation of the previously mentioned impurities to prior austenite grain boundaries during long term exposure to temperatures in the range 375-575°C lowers the fracture appearance transition temperature (FATT) and, in some cases, the upper shelf (CVN) energy

of the material. Room temperature fracture tests yield intergranular surfaces, producing a "rock candy" appearance [35]. The 3.5NiCrMoV grade is especially susceptible, due to a synergistic effect of nickel and chrome in combination [5,83]. This has been an impediment to higher temperature, and thus higher efficiency, operation of LP turbines, which are conventionally restricted to temperatures of less than 350°C. Much of the work in this area has been sponsored by the Electric Power Research Institute (EPRI), and the EPRI specification for superclean 3.5NiCrMoV is included in Table 2.1. Although other criteria have since been proposed, the approximate susceptibility of a steel to temper embrittlement is usually still measured using the "J-factor", a dimensionless composition-dependent parameter calculated by [40]:

$$J = (Mn + Si) \times (P + Sn) \times 10^4$$

where Mn, Si, P and Sn are weight percent contents of manganese, silicon, phosphorus and tin. The J factor has been strongly correlated by Watanabe, et. al. [84] with the susceptibility of a material to temper embrittlement. It has been shown that for the 3.5NiCrMoV steel, J factors less than 10 are required for immunity to temper embrittlement, a goal which is met by the EPRI specification [5]. In addition to preventing temper embrittlement, superclean steels have been shown to have generally superior properties, including toughness, ductility and fatigue resistance [85]. Although several manufacturers now regularly produce LP rotors to superclean specifications [86-88], a debate continues within the industry as to what level of cleanliness is justified by performance requirements [116].

While work continues on these efforts, additional applications for the 3.5NiCrMoV grade continue to arise, such as high-pressure, high-reliability reaction vessels in the chemical industry [89]. The performance requirements for such vessels are similar to those for LP rotors, namely high strength, fatigue resistance, and toughness under moderate temperature service. Low-alloy steels generally have been prime candidates for vessel materials, in particular for the most critical of applications: reactor vessels in nuclear power plants. A typical commercial pressurized water reactor (PWR) will operate at 315°C and 17.2 MPa (2500 psi), necessitating thick-walled vessels [44]. The history of material selection for reactor vessels is similar in many ways to rotors, frequently marked



by metallurgical development in response to failure of previous materials under demanding service.

Existing reactor vessels were typically fabricated from rolled and welded thick-section low-alloy steel plate, with compositions made to standards such as ASTM A 533 and A 302. However operating experience in commercial light-water reactors has demonstrated the extreme embrittling effects of neutron radiation, especially on welded joints. In order to minimize such problems, as well as for general integrity advantages, vendors have long been interested in using forgings for components such as vessels, pump cases and piping joints [3,8]. Many of the components made to date have been fabricated from low-alloy steel specified to ASTM Standard A 508 Cl 2 [42], with composition as listed in Table 2.1, along with a stainless steel cladding welded to the interior for corrosion resistance. Ironically, however, the class 2 grade has shown a susceptibility to "reheat-cracking" (RHC)<sup>1</sup>, a problem which has traditionally been associated with low-alloy weldments, especially plates for pressure vessels [31].

Reheat cracking occurs in a material which has experienced a high-temperature treatment, such as the portion of a weldment lying in the heat-affected zone (HAZ) of a subsequent pass. In this case some materials have been found to be susceptible to cracking during later intermediate temperature reheating, such as in stress relief treatments [39]. Reheat cracking associated with cladding welds in low-alloy reactor vessels was first observed in the early 70s. A comprehensive survey by the Pressure Vessel Research Committee (PVRC) of the Welding Research Council [34] revealed extensive cracking in A 508 Cl 2 components, in contrast to virtually no cracking in identically treated A 508 Cl 3 components. The primary difference between these two classes is composition, with the the class 3 material having higher manganese and lower chrome than the class 2 material. Further, cracking was found only in the portions of the HAZ which were heated twice, once to 1200-1425°C during the first pass and later to 600-700°C during subsequent passes. Cracks were often extremely "tight" and difficult to detect by normal nondestructive techniques. They were determined to be intergranular along prior austenite grain boundaries, and SEM examination of unoxidized fracture surfaces often showed a smooth morphology, free of

---

<sup>1</sup> Also known as "stress-relief cracking" (SRC).

deformation. In light of these results the PVRC recommended switching to the nonsusceptible class 3 grade, a suggestion which was adopted by many manufacturers [3].

In an attempt to understand the underlying mechanism of RHC, Hipplesley, Edwards and others performed load relaxation tests on 2-1/4 Cr 1 Mo steel welds of commercial purity, as well as material doped with phosphorus and tin [7,13,14]. Again as with rotor steels, the importance of such residuals was underscored by their results. Two distinct cracking regimes, operative in different temperature ranges were observed. One, an intergranular fracture by microvoid coalescence with dimples nucleated at MnS inclusions, dominated at higher temperatures while the other, termed a low-ductility mode, prevailed at lower temperatures and was characterized by the deformation-free morphology. Auger analysis of specimens quenched from cracking and fractured demonstrated that the low-ductility mode was associated with equilibrium segregation of phosphorus to the prior austenite grain boundary (PAGB). In contrast, although the tin-doped alloy exhibited low-ductility intergranular decohesion, no equilibrium segregation of tin was detected at the PAGB. This led Hipplesley, et. al. to speculate that the decohesion might actually result due to stress-driven segregation of tin at the PAGB during the test under loading.

McMahon and others extended these ideas to A 508 Cl 2 and A 533 B plate steel [20,21,28-30,32]. Like A 508 Cl 3, the A 533 grade was known to be resistant to reheat cracking. Using material subjected to an HAZ simulation treatment they conducted notched bend load relaxation tests at various temperatures. They attempted to rationalize the difference in susceptibility to RHC between the two steels. Similar to Hipplesley et. al., they noted two distinct cracking morphologies. The microvoid coalescence mode, also termed intergranular cavitation, dominated at lower stresses and higher temperatures, while the low-ductility decohesion mode characterized by featureless surfaces dominated at higher stresses and lower temperatures. Auger spectroscopy of the crack surfaces revealed sulfur segregation with respect to the crack tip. Fractography of the early stages of cracking showed that fracture initiated as microcracking ahead of the notch root. McMahon et. al. hypothesized a model for sulfur behavior similar to that of Hipplesley for phosphorus. In this model, stress-assisted diffusion of sulfur to a growing crack tip lowered the grain boundary cohesive strength,

producing a dynamic peeling apart of the boundary. They hypothesized that the greater susceptibility of 508 Cl 2 versus A 533 (which has a similar composition to A 508 Cl 3) was due to its higher Cr and lower Mn content. They hypothesized that this resulted in a larger amount of less stable CrS available for dissolution and subsequent grain boundary reprecipitation. Further noting that a lower austenitization temperature promotes a transition from the low ductility to the cavitation mode, McMahan suggested that dense fine sulfides were a requirement for the brittle decohesion.

In addition to fabrication problems, welds in nuclear reactor vessels are required to undergo regular and comprehensive inspection during service, as specified in the ASME Boiler and Pressure Vessel Code, Section XI [43]. This represents a significant operational burden in terms of cost, downtime and personnel exposure [44]. This issue, along with susceptibility to radiation embrittlement, is driving most reactor vendors to plan even larger forged vessel components, with a minimum number of welds, in their designs for next generation commercial plants [44,90,91]. To date designs have specified A 508 Cl 2 for the vessel material, despite the potential for difficulties with reheat cracking. With one exception [90] the commercial reactor designs remain in the planning stage. However the US naval nuclear program has maintained a continuous construction program, employing forgings for reactor vessels exclusively. As related by Bodnar & Cappellini [39]:

"The common material for the Navy nuclear reactor vessels is Mil-S-23194F Comp. A, which is the familiar ASTM A 508 Class 2 lean Ni-Cr-Mo grade. Experience over recent years, coupled with the current development within the Navy nuclear program, signals the increasing popularity of the more heavily alloyed Mil-S-23194F Comp. F, which is the ASTM A 508 Class 4 NiCrMo grade counterpart - a version of the HY80 grade... It should be noted that there is a parallel interest by the commercial nuclear program in the use of the Comp. F material.

Since this statement was written, the Comp. F/A 508 Cl 4 grade has become the material of choice for naval reactor pressure vessels. As seen in Table 2.1, the composition of the Comp. F/A 508 Cl 4 material is essentially identical to the 3.5NiCrMoV rotor steel with the exception of vanadium, which is intentionally added as a strong carbide former in the rotor steel, yet is a mere residual in the

A 508 Cl 4 material. As in the commercial program, there is ongoing debate over the need for employing a superclean version of the A 508 Cl 4 material to preclude various in-service degradation problems related to residual element content [12]. The next section will address one of the primary residual elements targeted by superclean techniques, sulfur, and its influence on the properties of steels.

## 2.2. Manganese Sulfide Inclusions in Steel

As described in the previous section, the development and application of low-alloy steels for the power generation industry has been characterized by metallurgical development in response to failures of existing materials, frequently entailing control or elimination of residual elements. Probably no other residual has been the subject of more concerted effort along these lines than sulfur (S). The influence of sulfur on the properties of steels and the various techniques employed for controlling it are reviewed now.

### 2.2.1. Influence and Control of Sulfur in Steel

The subject of sulfur in steel was summarized succinctly by Luyckx [92]:

1. Can't we keep it out of our steels by using sulfur free raw materials in the first place?
2. How can we take the sulfur out of the metal phase before final solidification of the steel?
3. If, for economic reasons, we prefer not to remove sulfur from the metal phase, how can we "engineer" the sulfide inclusions to make them harmless or even useful to our steel properties?

Original sulfur occurs in steel primarily as a carry-over from the blast-furnace coke employed in ironmaking [47]. Even coke made from metallurgically pure coal contains 0.6-0.8% S. Thus some sulfur content is inevitable. Since ingots for critical components such as rotors are cast from melts composed primarily of melted scrap, the actual sulfur content of the liquid metal input represents the end product of the desulphurisation performed on the scrap products themselves. A large number of techniques exist for removing sulfur from liquid metal. These include ladle injection with soda ash ( $\text{Na}_2\text{CO}_3$ ), adding magnesium pellets, or treatment with a calcium slag [47,92]. Although sulfur is soluble in liquid steel, it has very low solubility in the solid form so that any sulfur which remains after solidification usually exists in the form of metal sulfide compounds [46].

The most important of these compounds is iron sulfide (FeS), which induces the forging effect known as "hot shortness", described by Kiessling and Lange in their comprehensive catalog of non-metallic inclusions in steel [46,93]. Pure FeS has a relatively low melting point (1190°C). However in the presence of iron and oxygen, a eutectic can form which melts at a temperature as low as 940°C. The low solubility of sulfur in solid steel produces a steady enrichment of the concentration in the unsolidified liquid, which then freezes last at the grain boundaries. If the material is subsequently reheated above 900°C, for example for later forging heats, the sulfur-rich grain boundaries can melt and then crack during forming operations. This has been a long-time problem in forging, and successful forming requires overcoming it. Traditionally this has been done by adding manganese, which ties up the sulfur as stable manganese sulfide inclusions. The details of this technique and the characteristics of nonmetallic inclusion which results are discussed in the next section.

### 2.2.2. Basic Thermodynamics and Crystallography of MnS

As shown in Figure 2.1, pure manganese sulfide has a much lower free energy of formation than iron sulfide at all temperatures [46]. However the values plotted in Figure 2.1 are for the pure materials, with component activities equal to unity. Steel is actually a complex dilute solution of many elements, which alters the activities of the various components. Determining the true free energies of the constituents is complex. However Jorgensen has determined diagrams of the form of Figure 2.1 for actual typical steel compositions, as shown in Figure 2.2 [94]. As seen here, the iron and manganese sulfide are equally stable at temperatures above 1600°C, however MnS is increasingly more stable as temperatures approach the forging range. Lowering the oxygen content of the steel further suppresses the formation of FeS, so that in heavily deoxidized steels nearly all the sulfur is in the form of manganese sulfides [95].

Along with virtually all other nonmetallic inclusions occurring in steels, Kiessling and Lange [46] have catalogued the properties and characteristics of manganese sulfide. The compound can occur in three crystal structures:  $\alpha$ ,  $\beta$  and  $\beta'$ , of which usually only  $\alpha$  is observed to occur in steel<sup>2</sup>. The  $\alpha$  variety has a rock

---

<sup>2</sup> The hexagonal  $\beta$  phase is reported to have been once observed in a resulphurized steel [76].

salt, NaCl structure, consisting of two interpenetrating face-centered cubic (FCC) lattices, as shown in Figure 2.3. Following the pioneering work of Sims and Dahle [48], the morphology of MnS precipitates is traditionally categorized in three types, the formation of which are governed by the solidification environment and the chemical composition of the steel.

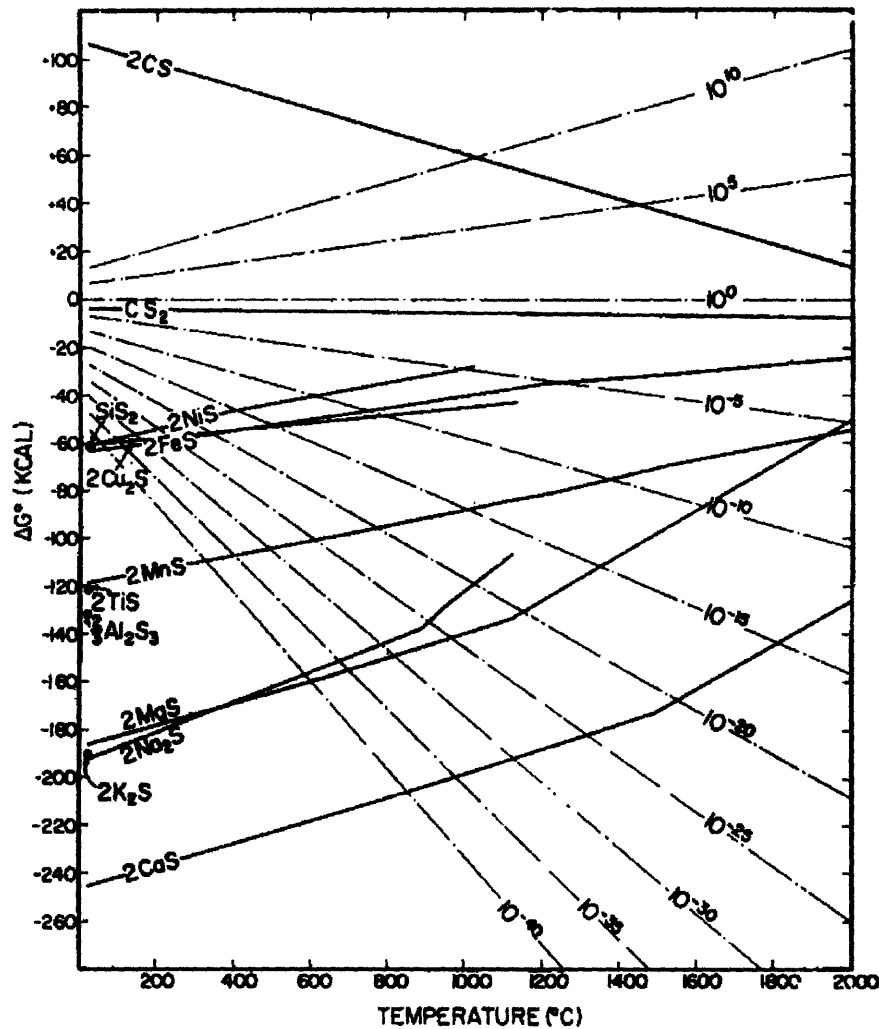


Figure 2.1 Free Energy of Formation of Pure Sulfides [from 46]

Type I MnS forms in steels with a higher oxygen content, so-called "rimmed" or "semi-killed" steels [18], frequently in conjunction with oxide compounds [36], and has a globular appearance when seen on a polished and etched surface as in Figure 2.4 [55]. The three-dimensional appearance is conveyed by Figure 2.5,

which is a scanning electron microscope (SEM) micrograph of a fracture surface whose dimples have nucleated on type I MnS [69]. Type I precipitation has traditionally been held to take place from liquid steel which has become enriched in manganese, sulfur and oxygen due to encountering the miscibility gap in the Fe-MnO-MnS system [36]. Sulfide precipitation thus takes place concurrently with oxide formation [46]. However Ito and coworkers have proposed that this type, along with type III (yet to be described) can precipitate from the solid solution as a result of the peritectic reaction  $\delta \text{Fe} + \text{L} \rightarrow \gamma$  [103]. In this theory, since sulfur has a greater solubility in ferrite than austenite, the sulfur which is supported in solid solution in the  $\delta$  ferrite is precipitated out upon transformation to  $\gamma$  iron [32].

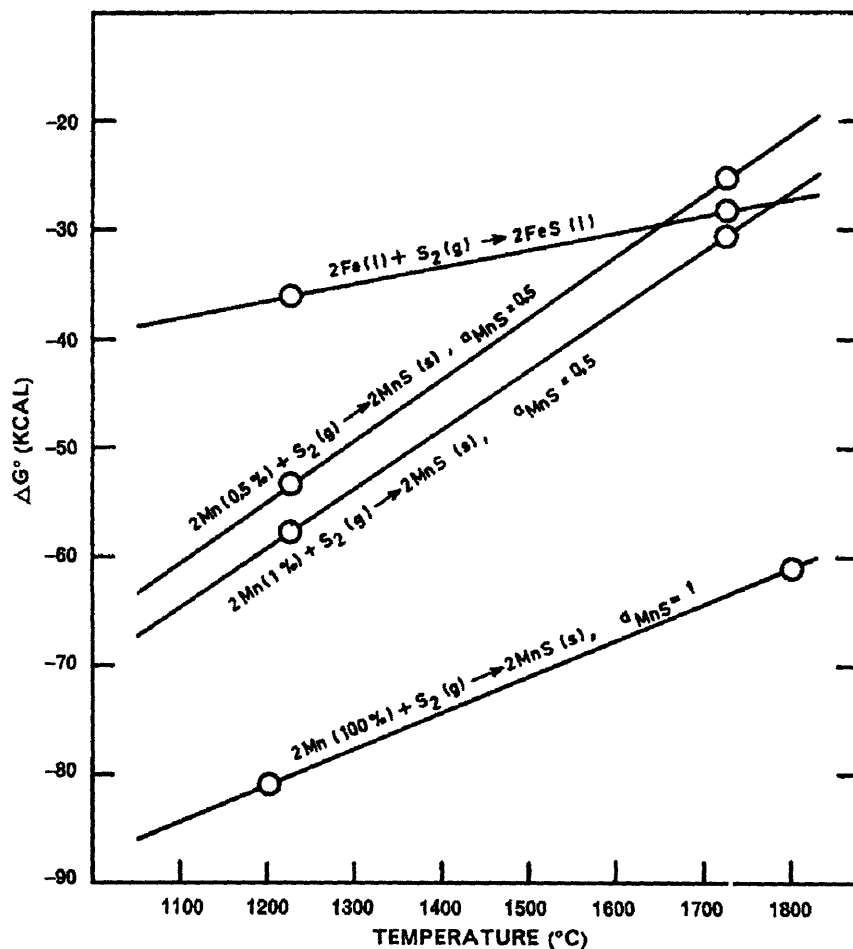


Figure 2.2 Free Energy of Formation of Sulfides in Solutions With Compositions of Typical Steels [from 46]



Type II MnS forms dendritically in steels with lower oxygen concentration, and has a fan or fern-like appearance on polished sections. This is illustrated in Figure 2.6 [55]. However its true three dimensional structure is better examined on a fracture surface under SEM. Figure 2.7 depicts such an image, obtained by deep etching to rapidly and preferentially attack the matrix, leaving the type II sulfides exposed [69]. Type II sulfides are considered to also precipitate from liquid steel as a result of the binary system eutectic reaction  $L \rightarrow Fe + MnS$  [18], thus forming in between the primary grains in thin boundaries or clustered in compact volumes, such as those illustrated in Figure 2.7.

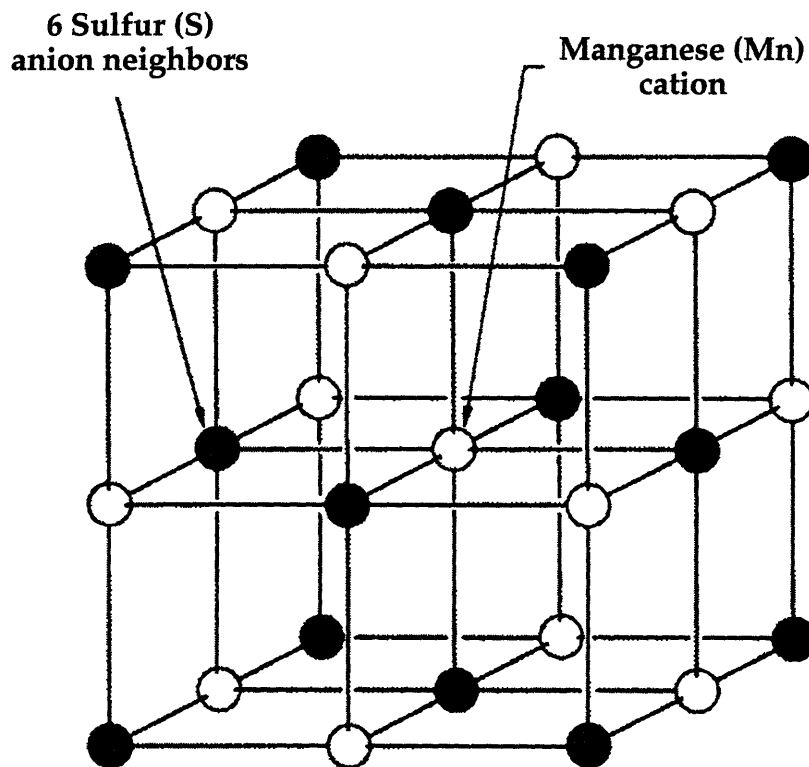


Figure 2.3 Crystal Structure of MnS: Rock Salt (NaCl) Type Consisting of Two Interpenetrating FCC Lattices [after 96]

Type III MnS forms in steels with very low oxygen content, such as those deoxidized with aluminum. Inclusions of this type have an angular or irregular morphology on sectioned surfaces [55]. This morphology is illustrated in

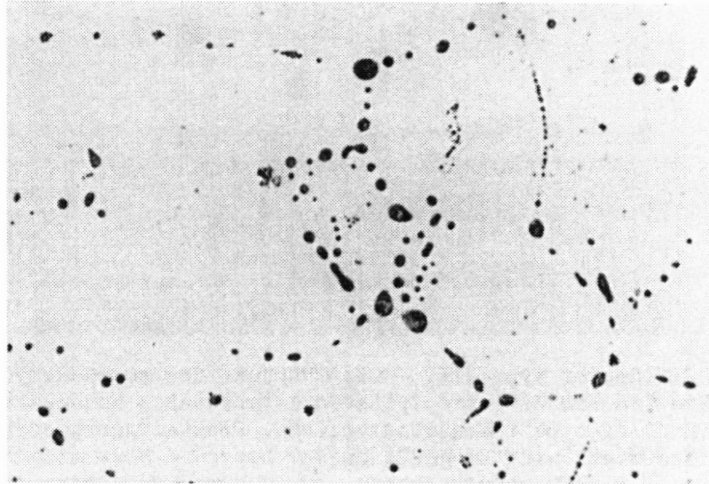


Figure 2.4 Appearance of Type I Manganese Sulfide on a Polished and Etched Surface [from 55]

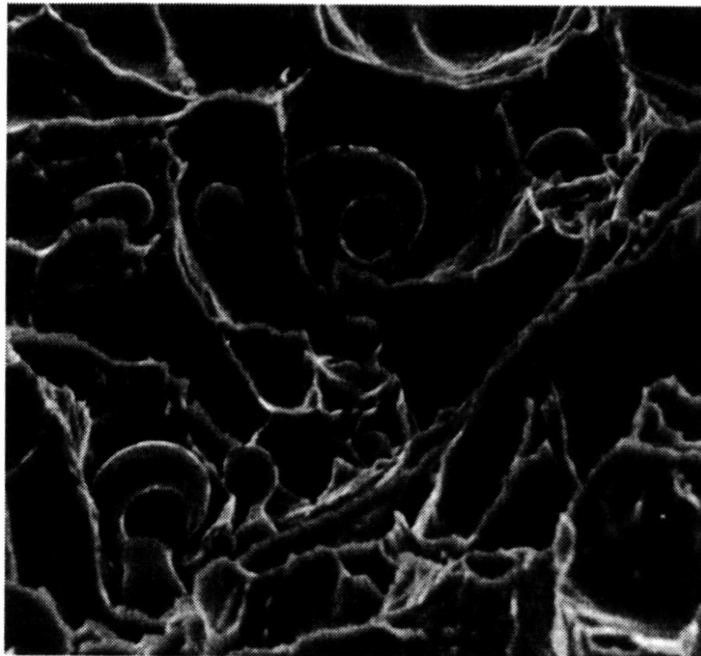


Figure 2.5 Appearance of Type I Manganese Sulfide on a Fracture Surface [from 69]

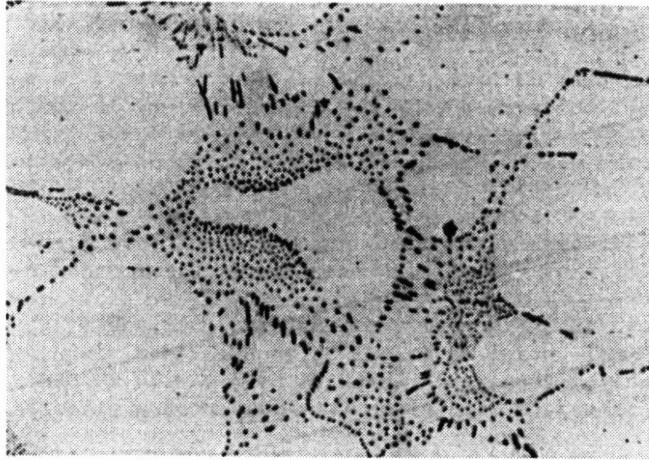


Figure 2.6 Appearance of Type II Manganese Sulfide on a Polished and Etched Surface [from 55]

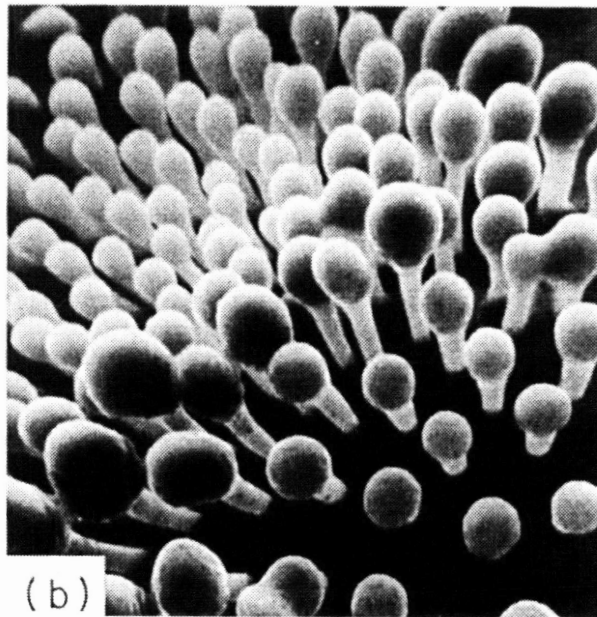


Figure 2.7 Appearance of Type II Manganese Sulfide on a Deep-Etched Surface [from 69]

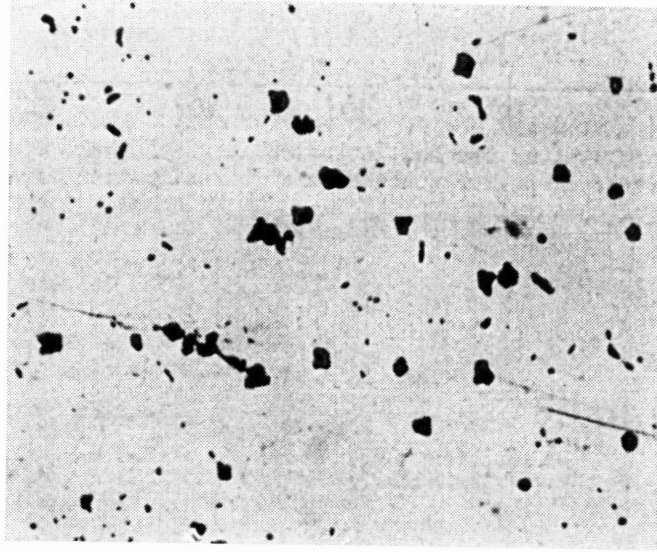


Figure 2.8 Appearance of Type III Manganese Sulfide on a Polished and Etched Surface [from 55]

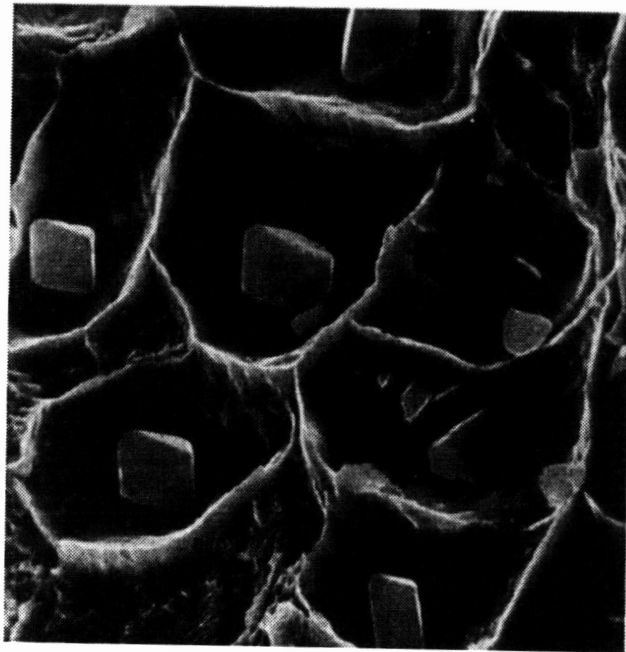


Figure 2.9 Appearance of Type III Manganese Sulfide on a Fracture Surface [from 69]

Figure 2.8. However SEM examination often reveals their true morphology to be perfect octahedra, as shown in Figure 2.9 [69]. Traditionally type III sulfides were thought to precipitate from the liquid at higher temperatures than type I [18] as a divorced eutectic [69]. However as for type I MnS, Ito and coworkers have suggested that type III sulfides may precipitate from solid solution during the  $\delta/\gamma$  transformation [18]. Concerning the micrograph reproduced in Figure 2.9, Baker comments that the cracks observed in some of the inclusions are "clearly occurring on (110) planes which have been shown to be preferential cleavage planes in MnS" [69], crediting Chao [97] for that result.

The preceding three morphologies have been supplemented by the work of Fredriksson and Hillert on synthetic low-oxygen F-Mn-S alloys. As summarized by Kiessling and Lange [46], the traditional Sims and Dahle classifications have been joined by a type IV crystalline ribbon morphology, illustrated in Figure 2.10, which forms by a cooperative eutectic reaction. In addition, Kiessling and Lange reproduce a previously unpublished micrograph of so-called "Widmanstätten MnS platelets" formed in a 0.13%C-0.039%S-0.51%Mn steel after being cooled at 20°C/min. from 1400°C to 1100°C. This micrograph is reproduced in Figure 2.11.

It is seen that MnS has been observed to occur in quite varied shapes. Concerning the prevalence of such precipitates, Kiessling [55] provides graphs which emphasize the number of inclusions which result for different sulfur contents. For example, even in a very clean low sulfur steel, e.g. 10 ppm, every ton of material can still contain on the order of  $10^{12}$  inclusions if they are each one  $\mu\text{m}$  in diameter. The possible influence on the properties of the steel for such a concentration of inclusions, depending on their sizes, shapes and distribution, is obvious. In the next section some of the effects of MnS on steel properties are reviewed.

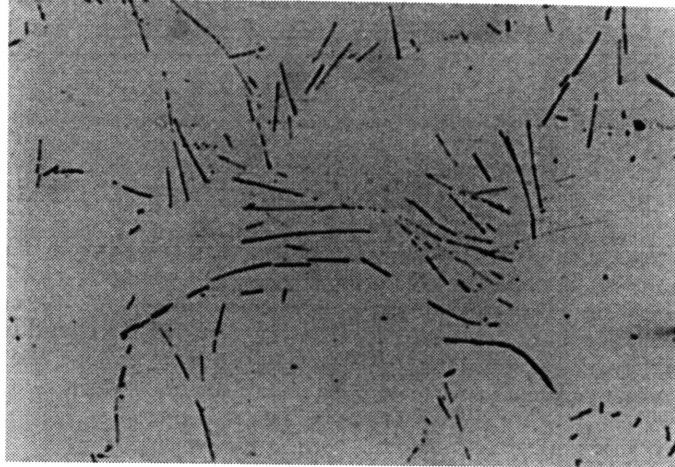


Figure 2.10 Type IV Ribbon Morphology Manganese Sulfide,  
Discovered by Kiessling and Lange [from 55]

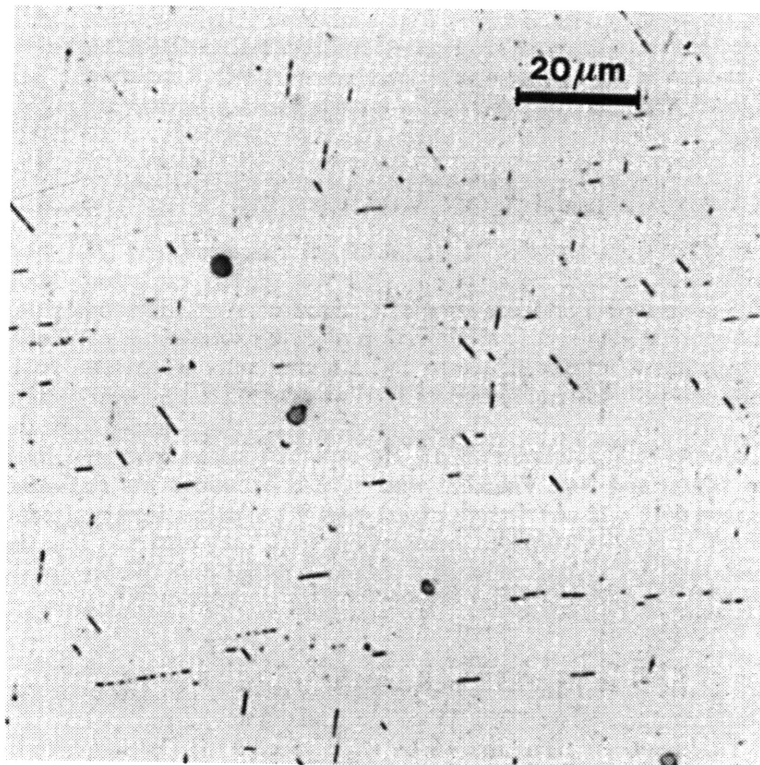


Figure 2.11 So-Called "Widmanstatten Platelets" of Manganese  
Sulfide [from 55]

### 2.2.3. MnS Influence on Material Performance in Low-Alloy Steels

The critical nature of the character of MnS inclusions, their sizes, shapes and distribution, is not restricted to low-alloy forging steels. On the contrary, it is a central factor in a broad range of steels and related processing problems. For example, loss of hot ductility is a serious problem in continuous cast strip mills. This phenomenon has been shown to be related to the relative amounts of iron and manganese sulfide developed during casting [98]. Another example is in the contribution of manganese sulfides to the so-called "free-machining" steels which contain additions of lead. MnS precipitated in these steels often forms duplex inclusions with metallic lead precipitates, which contributes substantially to machinability [36].

Similarly to these examples in carbon and free-machining steels, MnS precipitates and their characteristics are critical in a wide range of problems in the low-alloy forging steels, and this topic has been the focus of much research. One example of the interaction between sulfides and matrix is in creep-fatigue link-up of cavities nucleated at closely-spaced MnS inclusions. Large cracks initiated by this mechanism grew within the no. 2 IP/LP turbine rotor of the TVA Gallatin power station in the early 70s. They grew in-service to an extent that brittle fracture occurred during a subsequent cold start, destroying the unit and damaging much of the surrounding building and equipment [49-51]. It was later determined that the closely-spaced inclusions occurred in regions of inverse V segregation within the ingot, which enabled creep-fatigue cracks to initiate in a plane on both sides of the bore. This single failure has had a large impact on life-prediction and in-service inspection programs applied by utilities to their aging rotors. In particular, older 50s-era rotors with centers which are significantly dirty compared to modern standards are subject to rigorous inspection and analysis.

Another example is the role of MnS in stress corrosion cracking of low-alloy steels. This is a major concern in pressure vessel steels, such as for light water reactors. As the precipitates ahead of the advancing crack-tip are intersected by it, they release metallurgical sulfur into the solution, affecting the crevice chemistry and rate of material dissolution [52]. MnS inclusions dissolve easily in the water solution, freeing sulfur which remains in the crack environment,

ultimately forming hydrogen sulfide which maintains high rates of crack propagation [99]. The size, shape, distribution and orientation of the sulfides is recognized as a major uncertainty in the calculation of crack growth rates.

The topic of "stringers" in low-alloy rolled plate represents another instance of MnS precipitate shape strongly influencing material properties. However, in this case, the shape is developed by deformation processing after precipitation. As reviewed by Baker [69], the shape of an inclusion which results after deformation is a function of the relative plasticity ratio of the inclusion to the matrix. The yield strength of the matrix drops considerably at high forming temperatures, while the stable sulfides remain hard. In this situation the matrix deforms under stress rather than the inclusion. As the processing temperature is lowered, however, and the matrix hardens, the plasticity ratio of the sulfide to matrix drops and the inclusions deform along with the matrix. Type III inclusions are particularly deformable, possibly due to the hardening effect on the matrix of alloying elements which promote the formation of that type of MnS inclusion.

In any case, under heavy rolling equiaxed inclusions such as types I and III MnS can be flattened out into very high-aspect ratio "stringers", such as those shown in the micrograph provided by Baker [69], reproduced in Figure 2.12. An

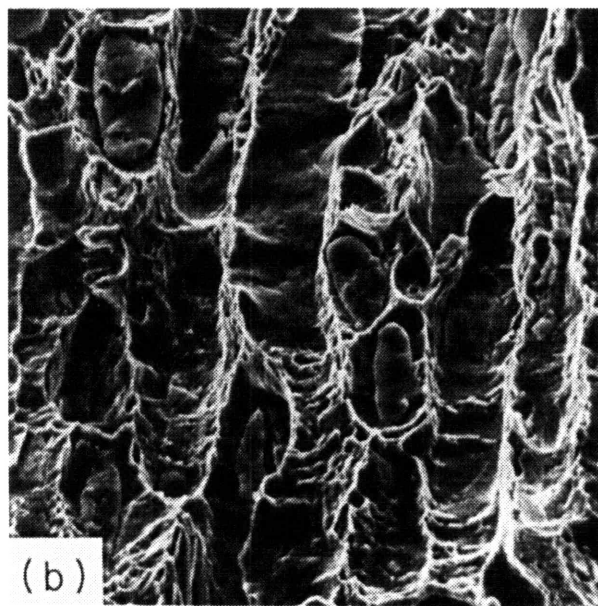


Figure 2.12 Equiaxed Type I/III MnS Flattened out into High-Aspect Ratio "Stringers" by Rolling [from 69]



example of the extremely high aspect ratios which can be developed is shown in Figure 2.13, from reference 100. The effect of these is to produce very poor through-thickness toughness in plate products. Fracture ductility in the through-thickness direction was correlated to the total projected area of the inclusions by Baker and Charles [101]. As noted by Baker, however, extremely large aspect ratios produce an inclusion whose large surface area, and thus large surface energy, presents a strong driving force for spheroidization during subsequent heat treatments [69]. Figure 2.14, reproduced from that reference, depicts a partially spheroidized stringer. Especially noteworthy are the ductile ridges developed during fracture between the coalescing portions of the sulfide.

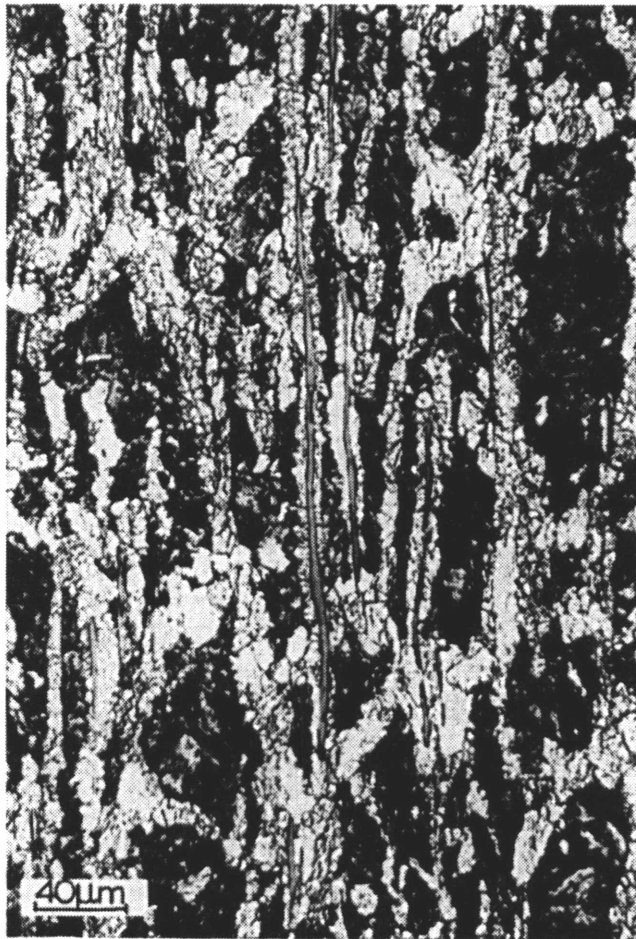


Figure 2.13 Extremely High Aspect Ratio Stringers [from 100]

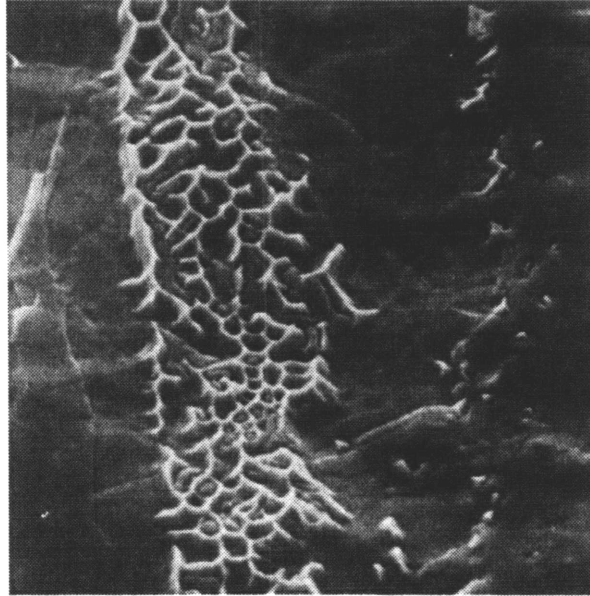


Figure 2.14 Partially Spheroidized Stringer [from 69]

This section has briefly summarized several phenomena in which the size, shape and distribution of MnS inclusions plays a major role in modifying the properties of low-alloy steels. The next section reviews in detail the history of investigation into another prime example, the phenomenon of overheating in low-alloy steel forgings.

#### 2.2.4. Overheating

As discussed briefly in the introduction, when forging steels are heated to temperatures above about 1250°C, the solubility limit of sulfur in the solid steel increases to the point that all of the available sulfur can be solutionized. During cooling, the austenite grain boundaries serve as nucleation sites for the re-precipitation of MnS. Depending on the cooling rate, dense arrays of fine manganese sulfides can precipitate at these boundaries. At room temperature, these arrays then serve as low-energy fracture paths, reducing fracture energy, as measured in an impact test such as the Charpy V-notch test, and producing facets on the fracture surface corresponding to the prior austenite grain boundaries. Paradoxically, it has been shown that in many cases reducing the sulfur content actually aggravates this problem. The reasons for this will be discussed later.

Early widespread observance of the phenomenon occurred during World War II, when higher forging temperatures were used to increase output of aircraft components. Overheating in these parts resulted in rejection of large numbers of them [102]. Early investigators struggled to distinguish the phenomenon from the more damaging "burning", during which grain boundary melting occurs [26,53,54]. The fundamental work on overheating was conducted by Preece, et. al. at Leeds in 1946 [26,54]. Preece performed fracture and etch tests of a large number of steels, after subjecting them to a high-temperature austenitization which simulated a forging heat. With this technique he was able to determine the "overheating temperature"  $T_{OH}$ , i.e., the temperature above which a particular steel must be austenitized to develop the characteristic matte faceted fracture morphology and low impact energy in an Izod test<sup>1</sup>. For the compositions that he evaluated, this temperature was found to be approximately 1250°C.

Although he showed that some etchants (particularly nitric-sulfuric) would reveal the overheated condition, indicated by a polygonal network corresponding to the prior austenite grain boundaries, Preece determined that

---

<sup>1</sup> An Izod test is an impact test similar to a Charpy test, however the specimen is fixed and struck in a cantilever position.

the fracture test was the more effective indicator of overheating. A decrease in impact energy of up to 90% was observed in severely overheated material. It was also shown that the effect was most severe in steels fully toughened by a quench and temper treatment after the high-temperature austenitization.

Among other observations, Preese noted that the rate of cooling through a narrow temperature range after the austenitization had a strong influence on the resulting extent of overheating. Either a gradual cool at about 3°C/min or a quench could suppress the effect. From this he concluded that overheating was due to some diffusional process, although the diffusing species were unknown. Further he made the seemingly paradoxical observation that dirty steels, with a high inclusion content, had a higher  $T_{OH}$  than cleaner steels<sup>2</sup>. Similarly open hearth steels had a higher  $T_{OH}$  than electric steels, which were typically distinguished from the former by their lower levels of impurities such as phosphorus and sulfur. Finally Preese showed that overheated steels could be "reclaimed" by heating to the same range as the previous austenitization and then slow cooling.

Woolman & Kirkby [53] proposed that overheating was a precipitation phenomenon in 1946. However it was Ko & Hansen [17] who by metallographic examination of the flat overheated facets identified precipitates on the fracture surfaces as manganese sulfides. They also attempted to explain the lower  $T_{OH}$  of high sulfur steels. Assuming that the solubility of sulfur in austenite increased with increasing temperature, as the soak temperature was raised more and more sulfur would be taken into solution. In a clean (low sulfur) steel, few intragranular sulfides would then remain as nucleation sites for subsequent reprecipitation, and thus relatively more would form at the austenite grain boundary. In contrast, more sulfides would remain at high temperature in a dirty steel, and these would compete with the grain boundary for sulfur during cooling, leaving relatively fewer sulfides formed there. The assumption of increasing sulfur solubility in austenitic Fe-Mn alloys was later confirmed by Turkdogan, et. al. [33] by measurements of the equilibration of hydrogen-sulfide/hydrogen mixtures with metal samples.

---

<sup>2</sup> That is, they had to be subjected to a higher temperature before they exhibited the effects of overheating.

Examination of overheated precipitates on the fracture surfaces of Izod specimens under scanning electron microscope was performed by Joy & Nutting in 1971 [15]. They observed what has come to be regarded as the characteristic morphology of overheating: fracture surface facets covered with numerous small ductile dimples nucleated at MnS inclusions. They also studied the effect of cooling rate, comparing inclusion sizes in a 50 ppm steel for cooling rates of 2 and 10°C/min. After observing no facets on the slower-cooled steel, and transgranular MnS particles on the 2°C/min specimens which were twice the size of those on the facets of the 10°C/min specimen, they theorized that slower cooling rates might mean larger and fewer PAGB sulfides, diminishing the overheating effect. Supporting this was their interpretation that the impact energy was undiminished by treatment at up to 1400°C in the 2°C/min specimens, while there was a distinct drop off in the energy of the 10°C/min specimens above 1250°C. Finally they proposed an additional explanation for the lower  $T_{OH}$  of low sulfur steel. They theorized that in a low sulfur steel the ratio of the matrix to overheated grain boundary toughness is greater, thus the propagating fracture is more likely to deviate to the grain boundary, exposing a facet. Figure 2.15 reproduces their classic graph demonstrating that the lower the sulfur content of the steel, the lower the austenitizing temperature at which the impact energy begins to decline.

Schulz & McMahon discovered a different form of overheating in a manganese-free steel after an austenitization temperature somewhat lower than that which would be expected to dissolve MnS [27]. Examining surfaces of notched bar fracture specimens they observed the characteristic fine ductile dimples. In this case, however, the microvoids apparently nucleated on chrome sulfides. A similar steel containing manganese did not exhibit this embrittlement. They explained this on the basis of the greater free energy of formation of MnS vs. CrS, i.e., the manganese sulfides could be expected to be stable to a higher temperature than the chrome sulfides. They cautioned against high-temperature forging of manganese-free steels, lest they develop this type of overheating.

An attempt was made to more rigorously quantify the effect of overheated sulfides by O'Brien, et. al. in 1976 [25]. They performed fracture testing of heat

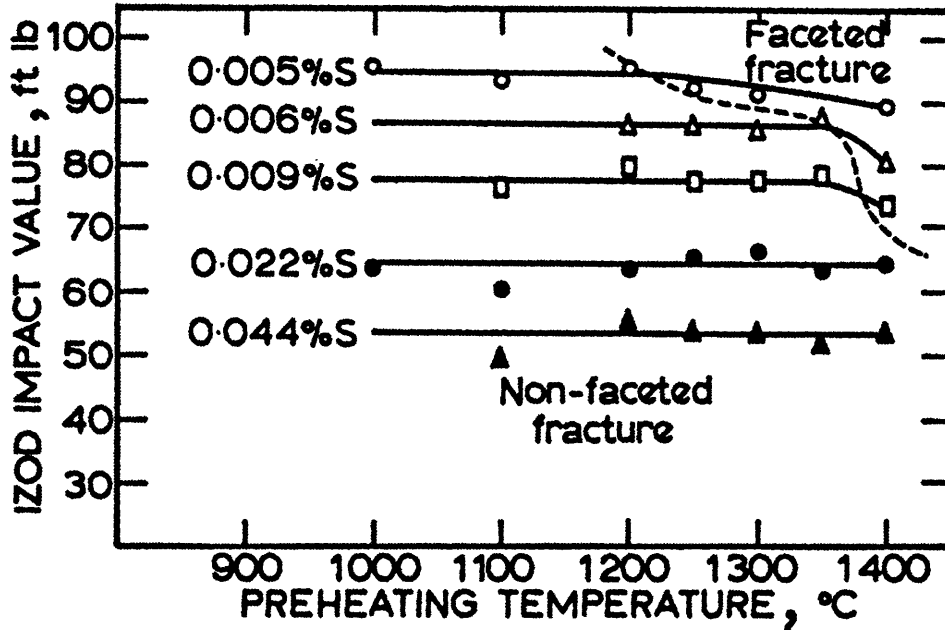


Figure 2.15 Impact Energy vs. Austenitizing Temperature for Steels of Various Sulfur Contents [from 15]

treated Charpy specimens of E39B, a 4%Ni-Cr steel and measured the resulting inclusion spacing. On the basis of their results they hypothesized that faceted fracture occurs when a critical value of the ratio of intra- to intergranular inclusion spacing is reached. Also studying the E39B grade, McLeod & Nutting investigated the effect of varying the manganese content on susceptibility to overheating, determining an optimum level for preventing the phenomenon [19]. They showed that higher manganese levels diminished susceptibility to overheating by limiting the amount of sulfur which is taken into solution at high temperature. Conversely, lower manganese levels left too little of the element available at the grain boundary for numerous MnS precipitates to form. However, intergranular failure was still obtained due to the presence of chrome sulfides similar to those observed by Schulz & McMahan.

Around this time Andrew, et. al., investigated the overheating phenomenon in low sulfur steels, including forged gun steels [1,2]. They treated 2.5Ni steels at temperatures up to 1400°C then cooled them at rates of about 12-14°C/min. They evaluated the effect of specimen orientation, determining that the effect was much more marked in specimens oriented longitudinally, i.e., parallel to grain

flow.<sup>3</sup> By examining etched sections of fracture surfaces, they confirmed that fracture in most cases proceeded by propagation along networks of fine MnS particles nucleated at prior austenite grain boundaries, to form the conventional flat, large facets. However, new to their results was the detection of sulfide precipitation on crystallographic planes in a higher sulfur steel heated to higher austenitizing temperatures. This was evident both in etch tests using the usual nitric-sulfuric etch recommended by Preece, as well as in the appearance of "numerous very small, regular, facets" on the fracture surface, much smaller than the PAGB facets. An example of such facets is reproduced in Figure 2.16.

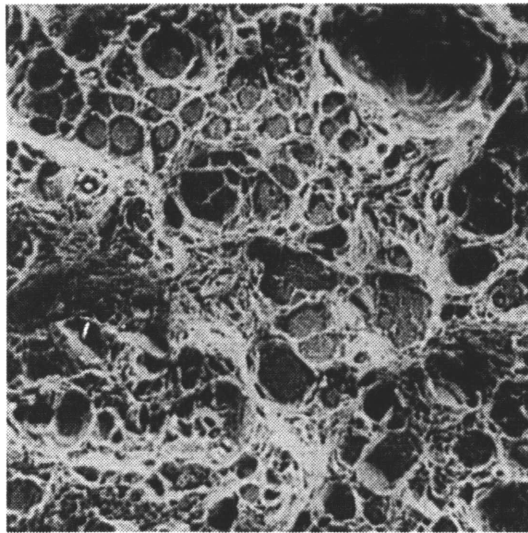


Figure 2.16 Microfacets Due to Transgranular Precipitation of Sulfides on Crystallographic Planes [from 2]

A summary opinion on the effect of overheating on material acceptability was provided by Hale and Nutting in their 1984 review of the subject [10]. In contrast to traditional practice, in which evidence of faceted fracture provided grounds for rejection of a forging, they argued that an overheated piece should be evaluated on the basis of results of materials properties tests.

---

<sup>3</sup> In other words, the fracture plane normal was parallel to the gun barrel axis and thus the direction of grain flow.

"It is reasonably clear that overheating only becomes a serious problem when the impact test shows a marked reduction in toughness and evidence of extensive faceting....It would be more realistic to say that mildly faceted components should be accepted for service if they meet the required property specifications." [10]

In their view, although fracture might occur along PAGBs containing networks of MnS precipitates, the work required in ductile failure of the tough, low-sulfur matrix around the precipitates was sufficient to give the material acceptable impact energy. In this regard, they echoed the earlier assertion by Baker that under the right circumstances overheating could be a tough mode of fracture [69]. In his view:

"[C]ontrary to widespread belief, overheating is a tough mode of fracture which results in only very minor reductions in impact toughness or plain strain fracture toughness... Large sulphide inclusions have a much more detrimental effect on toughness and in high sulphur steels, transgranular fracture via these large inclusions is a relatively low energy process... On the other hand, in very low sulphur steels, transgranular fracture is a very high energy process and even a small amount of sulphide precipitation at the grain boundaries is sufficient to produce an intergranular fracture." [69]

It should be emphasized that this revision of opinion was only possible due to development of steels with lower and lower sulfur content. It should not be taken to contradict results of earlier investigations, using dirtier steels, which showed that overheating could dramatically reduce properties. In any case, a conclusion which could be drawn from this line of thought was that the overheating regime, in terms of forging temperatures and cooling rates, could be entered as long as the steel chemistry was clean enough to provide acceptable impact energy values even in the overheated condition.

It should also be emphasized that such conclusions are based largely on evaluations of overheated material from a mechanical perspective, i.e., as regards strength, toughness, etc. Hale and Nutting note in their review that only two papers to-date had been published on the influence of overheating on susceptibility to stress corrosion cracking. They express surprise that more researchers had not addressed this issue, since in their view arrays of closely-



spaced MnS inclusions would constitute a preferential path for SCC. This is certainly a valid conclusion, in light of the previously mentioned dependence of SCC crack propagation rates on the size, shape and distribution of manganese sulfide.

Hale and Nutting [10] also confirmed that almost all investigations of overheating had demonstrated that for any given steel an intermediate cooling rate existed, neither too slow nor too fast, at which the overheating effect in terms of faceted fracture and diminished impact energy was most aggravated. They placed this rate typically in the range of 10-200°C/min, stating that for cooling rates faster than this the sulfur should stay in supersaturated solid solution, while for rates slower than this the MnS precipitates, although large, should be too few and far between to have much effect.

The EPRI-sponsored program to develop superclean steels resistant to temper embrittlement was discussed in the previous section. As mentioned there, this approach employs ladle refining and scrap control to produce steels low in residuals including sulfur and manganese, the critical elements in overheating. Thus the susceptibility of such steels to overheating could be questioned, and was duly investigated by Hale, Preston and Nutting as a subcomponent of the EPRI program [11]. They subjected commercial purity and superclean versions of 2.25Cr-1Mo, CrMoV and 3.5NiCrMoV to an overheating treatment consisting of one hour at 1300°C, followed by controlled cool at a rate of 2°C/min to 900°C and water quench. In the case of the 3.5NiCrMoV this was followed by a conventional quench and temper. CVN samples cut from the 20x20x75 mm blanks were fracture tested and examined using the SEM. No faceted fracture or drop in impact energy was observed in the superclean versions, even when heated to 1400°C. This was in contrast to commercial purity versions, which often experienced large drops in impact energy. They concluded the reason for this was that, even though the solubility limit equivalent to the low sulfur content of the superclean versions was reached at a low temperature, the amount of MnS available for reprecipitation during cooling was too insignificant to appreciably affect material properties.

An entirely new observation in their study of the 3.5NiCrMoV specifically was the development of rod-shaped MnS precipitates vs. the normal spherical

particles, as shown in Figure 2.17. As they noted, these had not been reported in the literature previously, and they listed the requirements they considered necessary for their formation, namely: 1) a large amount of sulfur in solid solution at high temperature, 2) a large austenite grain size during precipitation, and 3) a lack of intergranular sulfides to serve as competing nucleation sites [11]. In support of this hypothesis they noted the dramatic grain growth observed in this steel at temperatures above 1250°C, at which the entire sulfur content should have been solutionized. They recalled the work of Bodimeade demonstrating the pinning effect sulfides could have on a grain boundary [56]. Thus the overheating temperature  $T_{OH}$  could serve as a threshold. Once this temperature was exceeded all existing sulfides would be dissolved and the grains would be free to grow unhindered. With sufficient time spent above this temperature, they reasoned that the grains would be too large for diffusing sulfur to reach the

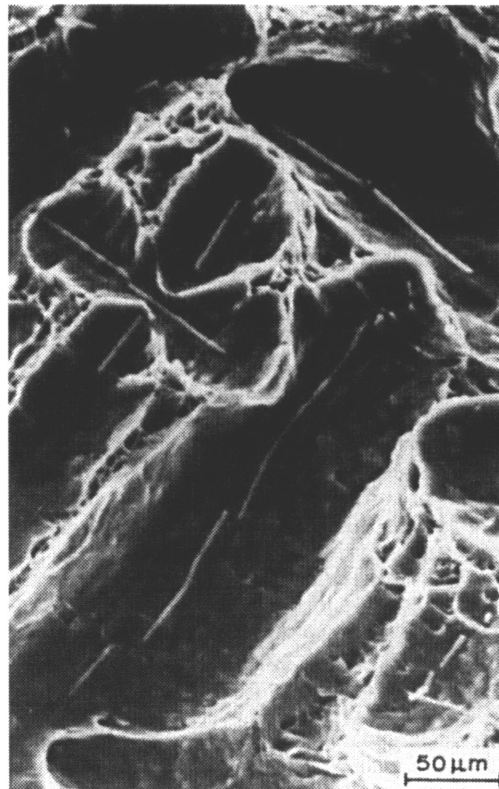


Figure 2.17 Rod-Shaped Sulfides Observed by Hale, Preston and Nutting in Overheated 3.5NiCrMoV [from 11]

boundaries upon cooling, producing intragranular precipitation, in this case in a rod-shaped morphology.

Katsumata et. al. also evaluated the effect of sulfur content and cooling rate on the overheating behavior of 3.5NiCrMoV steel specifically [16]. They determined a distinct trough in the overheating temperature, as measured by the Charpy V-notch upper shelf energy (CVN USE), at a sulfur content of about 50 ppm. They also noted that overheating in this material occurred over a wide range of cooling rates, from 0.5 to 300°C/min, with "especially remarkable" overheating between 2 and 170°C/min.

A mechanistic link between OH sulfides and PAGB cracking, possibly such as that observed in the flywheel, has been explored by several researchers. In particular this link has been explored as it relates to the previously mentioned problem of stress relief cracking. As summarized by McMahon [104] two cracking modes have commonly been identified with this phenomenon, one a brittle mode and one a cavitation mode. Middleton has been responsible for much of the progress made in understanding the role of prior austenite grain boundary sulfides in nucleating grain boundary cavities in the microvoid coalescence mode of cracking. A major advance was his investigation of the influence of PAGB MnS on cavitation cracking and grain boundary sliding during tensile tests at 700°C [23]. By testing steels of different compositions which had been subjected to an HAZ simulation treatment, Middleton was able to conclusively show that cavitation-mode reheat cracking resulted from two factors: 1) a dispersion of fine MnS inclusions which acted as cavity nucleators at the PAGB, and 2) a plastically weak zone which concentrated sliding deformation at the PAGB.

As for the brittle mode, McMahon reviewed the three models which have been proposed to explain this type of cracking: 1) simple segregation of impurity atoms such as sulfur to grain boundaries under tensile stress, embrittling them and enabling cracking, proposed by Hipsley and coworkers [105,106], 2) diffusive crack growth in which the ratio of grain boundary diffusion to surface diffusion is very high, advanced by Chen [107], and 3) decohesion due to an elevated concentration of sulfur atoms ahead of the crack tip, which has resulted from diffusion of the surface-active element from the cavity into the boundary,

leading to step-wise decohesion, developed by Shin, Bika and McMahon [4,29]. The third model was an outgrowth of the work of McMahon and coworkers on rationalizing the disparate susceptibilities to reheat cracking of A 508 Cl 2 and Cl 3, discussed previously.

This section has reviewed the literature on overheating, attempting to highlight results specific to the 3.5NiCrMoV grade as well as results which were anomalous in terms of the conventional wisdom regarding precipitation behavior of MnS. Of special significance in this regard are the rod-like sulfides observed by Hale, Preston and Nutting. As emphasized in much of the work on overheating, the nucleation advantage presented by the grain boundary to reprecipitating MnS has been the root cause of numerous later problems, such as reheat cavitation. Yet apparently that advantage is not operative during rod formation. By Wulff's theorem, generally precipitate dimensions are inverse to the interfacial energy in the plane defined by the direction of the dimension [108]. A transition to a morphology which is so distinct from the traditional three types of MnS implies a transition in the interfacial energy term in the nucleation and growth process. This, in turn, implies the possibility of a coherent boundary, or some other crystallographically-governed mechanism. Thus understanding this fundamental change in the MnS precipitation process requires understanding the influence of crystallography on precipitation, including any possible orientation relationship between matrix and sulfide. In the next and final section, literature relevant to this topic is reviewed, with special emphasis on experimental techniques to be employed in this thesis.

### 2.3. Precipitation Orientation Relationships

The concepts of precipitate/matrix orientation relationships and coherent boundaries are synonymous. As discussed by Porter and Easterling, coherent boundaries require close atomic matching, such that the crystal lattice is continuous across an interface [108]. Such a boundary is a comparatively low energy interface, and thus will be energetically favored in the nucleation and growth process. For a matrix and precipitate pair which have different structures, this matching will only be possible for certain planes and directions, when the two crystals are oriented properly to each other. The example they provide is Cu-Si alloys, when the hexagonal close-packed Si-rich  $\kappa$  phase and the face-centered cubic Cu-rich  $\alpha$  matrix are oriented with their close packed planes and directions parallel<sup>4</sup>. In this case there is virtually identical atomic matching across the interface.

Determination of such an orientation relationship (OR) obviously requires an experimental technique to detect the orientations of the crystal structures of the parent matrix and the precipitate. Physical features such as atomic planes, separated by angstroms, require a high-energy small-wavelength system to interact with them, namely X-rays or electrons. Since matrix grains and precipitates are usually too small for X-rays to be useful, diffraction under examination with a transmission electron microscope (TEM) has come to be the most commonly employed technique for revealing grain orientation.

The use of TEM diffraction for determination of ORs is exemplified by the work of Aaronson and coworkers on the characterization of FCC-BCC partially coherent interfaces, such as those developed in the austenite to ferrite transformation in steels [57-59]. A key obstacle in studying this system is the tendency towards complete transformation at room temperatures, leaving none of the parent austenite for examination. Rigsbee and Aaronson overcame this difficulty by employing a steel with high carbon content (an austenite stabilizer) to retain sufficient regions of the parent austenite for examination with high resolution TEM techniques. The orientations of adjacent austenite and ferrite

---

<sup>4</sup>  $(111)\alpha // (0001)\kappa$  and  $[110]\alpha // [1120]\kappa$

crystals were obtained by indexing their diffraction patterns [59]. This allowed them to determine the crystallographic orientations of linear features in the interface between the two crystals, confirming the hypothesis of Russell, et. al. [109] that coherency could be maximized, and thus interfacial energy minimized, if regular networks of structural ledges existed which allowed the interface to "skip" to a set of planes at which the adjacent crystals would more closely match [58]. When coupled with additional "misfit" dislocations perpendicular to these structural ledges, the resulting configuration is as depicted in their classic illustration, reproduced as Figure 2.18. While, due to the steps, the ferrite ( $\alpha$ ) and austenite ( $\gamma$ ) interface appears macroscopically irrational, at the microscopic scale of the ledge faces the closest packed planes of the two crystals are parallel.<sup>5</sup>

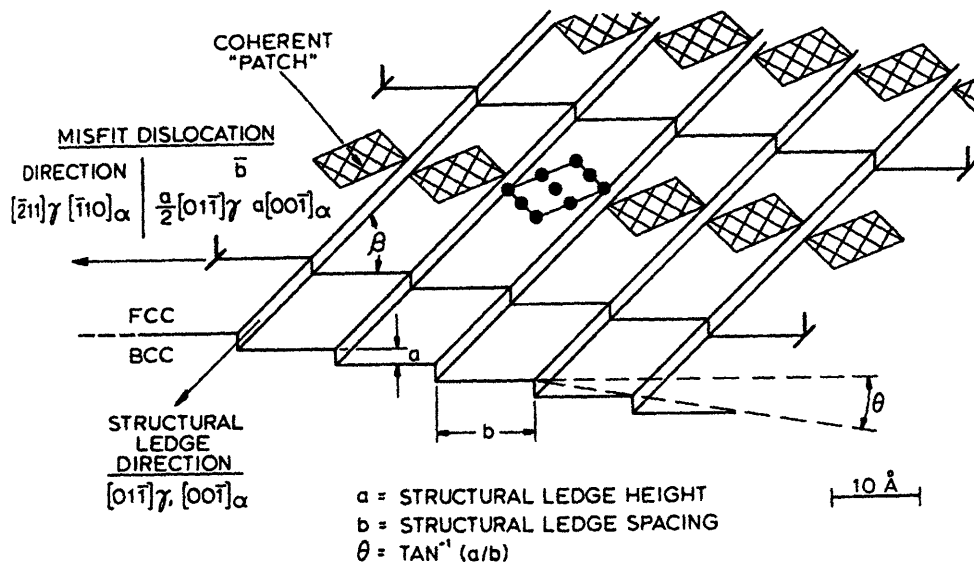


Figure 2.18 Structural Ledges Which Maximize Atomic Matching in Austenite-Ferrite Interface [from 58]

In the work by Rigsbee and Aaronson [59], the orientations of the linear features such as ledges were calculated using stereographic techniques and trace analysis. Barrett provides an overview of the use of the stereographic projection for solving such problems [72]. The stereographic projection is a graphical method

<sup>5</sup>  $(110)\alpha // (111)\gamma$

of depicting the orientation of a particular crystal structure. When manually manipulated along with "traces", i.e., lines in a specimen plane surface resulting from the intersection of that surface with another microstructural feature, such as a crystalline plane, the orientation of the microstructural feature can be determined with respect to the crystal structure. Barrett lists a number of crystallographic problems which can be solved with manual stereographic techniques, such as orientation of a crystal from the traces on one surface of four known planes. However the manual manipulation of stereographic projections and tracing papers is cumbersome and inaccurate. Tables and charts of solution orientations for given traces have been compiled in an attempt to facilitate the process [110,111]. Alternatively, some have developed exact procedures for solving problems such as those described in [72] as well as more complex ones, employing either exact geometric arguments or numerical techniques. For example, Drazin and Otte developed an analytical method of determining the orientation of a crystal from the nonparallel traces on a specimen surface of three octahedral {111} crystal planes [112]. Their method narrowed the possible orientations to either four or eight, and they recommended three implementations of the solution: a graphical procedure, an analytical procedure and a computer procedure. Subsequently Fong [113] reported an exact solution which determined crystal orientation to be either one of two possibilities, of which the correct one is "easily identified", for the problem of four traces of {111} planes observed on one surface. Reference 113 supplied a short program in BASIC to perform the calculation.

The traces of {111} planes are emphasized in the reported solution methods because of the frequent occurrence on them of microstructural features revealable by metallographic etching [113]. An example of such a feature is an annealing twin, a boundary which separates two twinned regions of a crystal, and which forms during exposure to elevated temperatures. These are commonly observed in FCC crystals, virtually always on {111} planes, and are easily identified since they are very low energy interfaces and thus have little effect, in terms of boundary tension, on other boundaries they intersect. Figure 2.19 is an example of annealing twins formed in annealed stainless steel [108]. As seen there, twin boundaries are extremely straight and exert little tension on the primary grain boundaries they intersect. The tendency of annealing twins to form from the

corners of primary grains, modeled by Fullman and Fisher [114], is also evident in Figure 2.19.

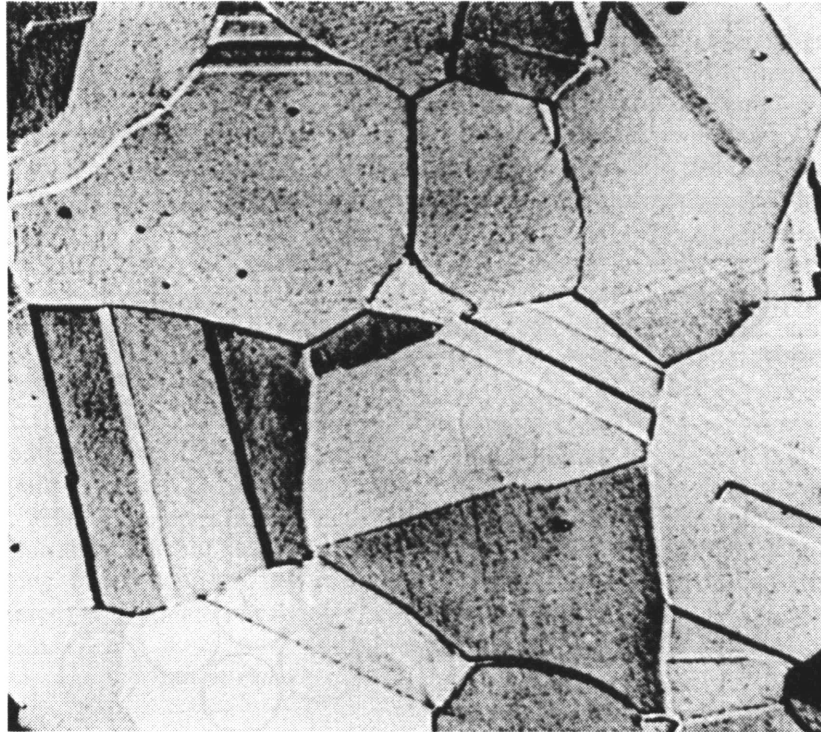


Figure 2.19 Annealing Twins Formed in Annealed Stainless Steel  
[from 108]



### 3.0 Research Objectives

In the review of the literature in the previous section, an attempt was made to highlight the following points:

- 3.5NiCrMoV is the material of choice for LP turbine rotors, including the very large monoblock forgings employed in nuclear power plants.
- A 508 Cl 4, which has a composition very similar to 3.5NiCrMoV, is the material of choice for naval nuclear reactor vessels, and could possibly be selected for next generation civilian reactor vessels.
- The commercial purity 3.5NiCrMoV has been shown to be very susceptible to conventional overheating, i.e., precipitation of numerous fine manganese sulfides at prior austenite grain boundaries after very high-temperature treatment.
- Several investigators have mechanistically linked conventional overheating to subsequent susceptibility to reheat cracking, and it is likely that this phenomenon was actually observed in the Alcator C-Mod flywheel, which had portions of the as-forged piece that were overheated due to its unusual size, shape and required heat temperature.
- The unusual shapes and large sizes of the forgings which are planned for the next generation of civilian reactor vessels, along with pressures to decrease press times, minimize heats and diversify vendors may lead forgemasters to employ unconventional procedures such as those used in making the flywheel.
- While formerly any evidence of overheating was cause for rejection of a forging, the argument is being advanced by some that a mildly overheated piece may be acceptable provided the properties are acceptable.
- Additional investigators have observed unconventional overheating modes in which sulfides did not form on PAGBs but in unusual intragranular morphologies, which were still highly embrittling. These morphologies included MnS rods observed in the 3.5NiCrMoV grade.
- The transition from the traditional MnS inclusion types to a radically different morphology such as rods implies a lower surface energy, which in turn implies a coherent boundary and crystallographic orientation relationship between the matrix and sulfides.

- The subject of the size, shape and distribution of manganese sulfide inclusions is central to a broad variety of material properties problems in steels, including a number which are of primary importance in low-alloy steel components employed in nuclear power plants.
- Although the developing "superclean steel" technologies are acknowledged to prevent overheating, there is ongoing debate in the industry as to the necessity of employing them on either rotors or vessels.

From the above points it is argued that:

- PAGB cracking resulting from overheating, such as that observed in the C-Mod flywheel, may be a concern in future LP rotor forgings and next-generation reactor vessels, due to their sizes and/or unusual shapes, compositions and processing procedures.
- A more thorough accounting of manganese sulfides precipitated from the solid state in low-alloy forging steels, both the precipitate types to be encountered and their dependence on temperature and cooling rate, may be essential in controlling such cracking.
- The widespread significance of MnS in mechanical behavior of steels, especially low-alloy steels employed in the nuclear industry, justifies further investigation of fundamental precipitation processes such as those involved in a change of morphology.

Thus a more thorough study of the overheating behavior of rotor and vessel steels is warranted, with the aim of mapping the precipitation behaviors which are likely to be encountered and the forging process parameters which induce them, as well as investigating the underlying mechanism of MnS rod formation and its implications. In particular this research will attempt to answer the following questions:

- What specific manganese sulfide inclusion types and precipitation phenomena are to be encountered in high-temperature treatment of 3.5NiCrMoV?
- What is the effect of variations in temperature and cooling rate on these phenomena, i.e., MnS size, shape and distribution?

- What is the effect of such fracture behavior on mechanical properties in 3.5NiCrMoV?
- How is the fracture behavior induced in 3.5NiCrMoV by various inclusion types affected by final microstructure?
- Are similar inclusion types and precipitation phenomena possible in A 508 Cl 4, and what is their effect on mechanical properties?
- What are the implications for the performance of A 508 Cl 4 in critical components such as reactor vessels?
- Is the crystal structure of the observed MnS precipitates uniform?
- What are the possible orientation relationships between low-alloy steel and MnS precipitates?
- What underlying mechanisms are responsible for orientation relationships which are encountered?

These are the goals of the research presented in this thesis. The next section will describe the experimental procedures and techniques employed to achieve them.

## 4.0 Experimental Procedure

### 4.1. Overheating Tests

The first half of the research program addressed mapping of the precipitation behaviors which are likely to be encountered versus the forging process parameters, namely temperature and cooling rate, which induce them. In general, the experimental procedures consist of:

- overheating heat treatments with varied cooling rate and austenitizing temperature, followed by quench and temper treatments to form the final microstructure
- impact tests to evaluate the effect on materials properties, and
- the use of microscopy and metallography to characterize the microstructure and state of MnS precipitation.

A matrix detailing the parameters for each material lot and test series is provided at the end of this section, however in general there were three main test series: 1) austenitization temperature tests (3.5NiCrMoV), 2) martensitic material tests (3.5NiCrMoV), and 3) cooling rate tests (3.5NiCrMoV and A 508).

#### 4.1.1. Material

Test material was taken from three sources: a test ring called-out on the diagram of the second flywheel forging (3.5NiCrMoV), a test coupon from a forged pressure vessel donated by a manufacturer (A 508 Cl 4), and a sample extracted from a dissected test forging of superclean vessel material (A 508 Cl 4).

The forging process employed on the second flywheel required a total of eight heats at temperatures between 1220 and 1280°C. The flywheel test ring was removed before the final quench and temper. Therefore, the starting microstructure is that achieved at the end of the preliminary heat treatment (PHT). The PHT profile is depicted in Figure 4.1. Material chemical composition as determined by a melt and check analysis performed by the manufacturer is given in Table 4.1. The test ring was cut from about the long journal of the

flywheel, with location within the as-forged piece as depicted in Figure 4.2. It was removed in four sections with nominal radius of 575 mm and cross section of 75x75 mm.

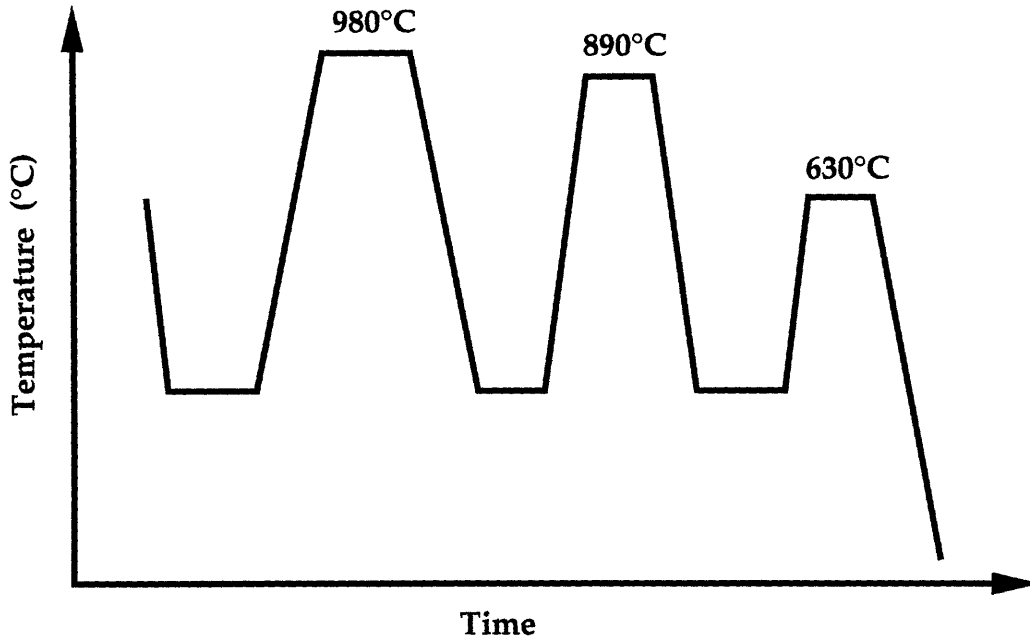


Figure 4.1 Flywheel 2 Preliminary Heat Treatment Schematic [after 45]

Less is known about the prior processing of the A 508 samples, although it is believed that they were obtained in the final as-forged and heat treated condition. Chemical content checks provided by the manufacturer for this material are also summarized in Table 4.1. Sawcut blocks of nominal dimension 20x30x82 mm of the commercial purity A 508 and 34x50x90 mm of the superclean version were provided by the manufacturer. The relatively smaller amount of material relative to the 3.5NiCr MoV necessitated far fewer specimens.

#### 4.1.2. Heat Treatment

All heat treatments were performed in air in a box furnace. The oxidation and decarburization expected was maintained at an acceptable minimum by using a

sufficiently large specimen and by inserting room temperature specimens directly into the preheated chamber, in order to quickly develop an insulating oxide layer. A chemical check verifying decarburization levels along with some discussion on this topic is provided in Appendix B. A Lindberg Model 51333 box furnace with silicon carbide heating elements capable of temperatures up to 1500°C was used for all treatments. The furnace was controlled by an Omega CN-2042 microprocessor-based PID controller capable of programmed ramps and soaks. The controller input was from a Pt/Pt-13%Rh (type R) thermocouple housed within a ceramic sheath mounted on the back wall of the furnace chamber. The controller output a 4-20 mA signal to an Omega SCR71Z silicon-controlled rectifier operating on 208V which powered the furnace.

Table 4.1 Chemical Composition of Subject Materials, As Determined by the Manufacturers

Analysis	C	Mn	P	S	Si	Ni	Cr	Mo	V
<u>Flywheel</u>									
A 470 Cl 5,6,7		0.20				3.25	1.25	0.25	0.05
Specification	0.28	0.60	0.012	0.015	0.10	4.00	2.00	0.60	0.15
Heat 1	0.28	0.41	0.007	0.004	0.09	3.52	1.63	0.40	0.17
Heat 2	0.27	0.35	0.005	0.003	0.06	3.53	1.70	0.39	0.07
Check, edge	0.27	0.38	0.006	0.005	0.08	3.55	1.65	0.39	0.12
Check, middle	0.27	0.38	0.006	0.004	0.07	3.51	1.64	0.39	0.12
Check, inside	0.28	0.37	0.005	0.004	0.07	3.51	1.64	0.38	0.11
<u>Reactor Vessel</u>									
A 508 Cl 4		0.20			0.150	2.75	1.50	0.40	
Specification	0.23	0.40	0.020	0.020	0.400	3.90	2.00	0.60	0.03
A (superclean)	0.20	0.09	0.007	0.002	0.04	3.48	1.62	0.56	0.03
B (commercial)	0.21	0.23	0.012	0.006	0.05	3.19	1.74	0.53	0.04

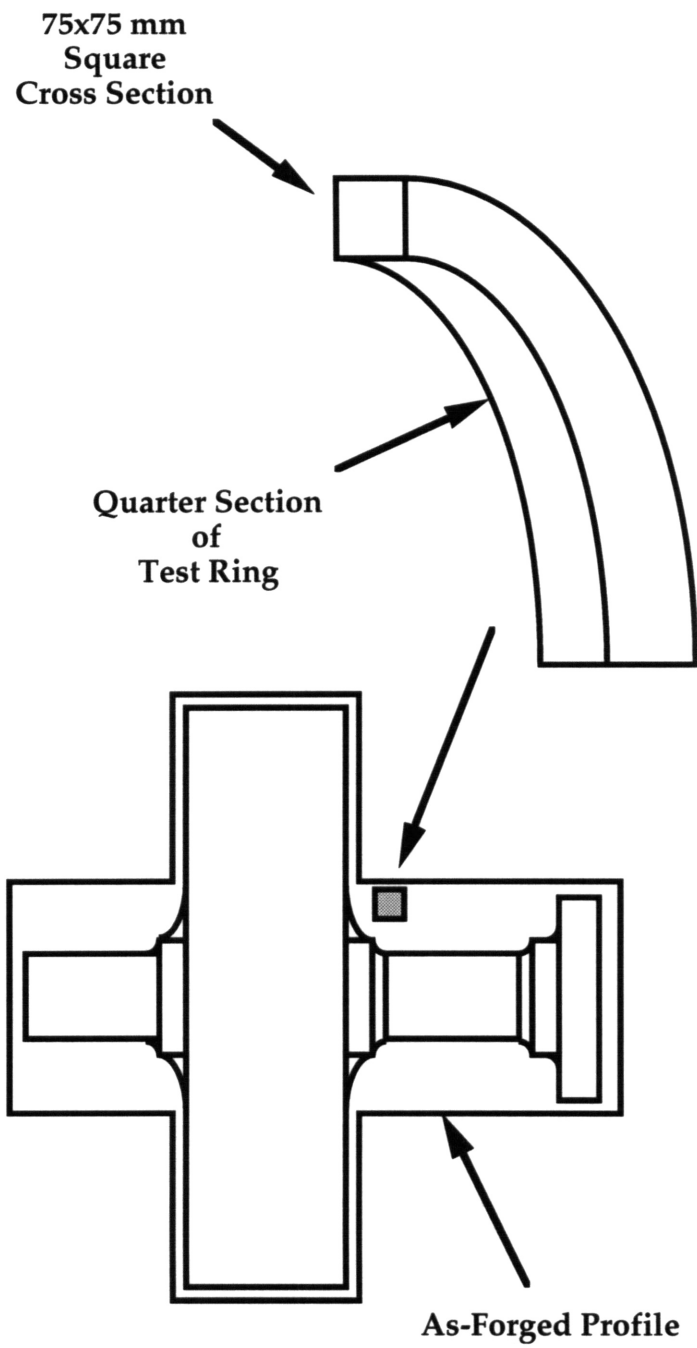
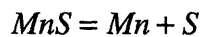


Figure 4.2 Test Ring Location on Piece and Within As-Forged Profile

#### 4.1.2.1. Austenitization Temperature Tests

The overheating heat treatments for the austenitization temperature tests followed the method of Hale, Preston & Nutting [11], a one-hour soak at the austenitizing temperature, a 2°C/min cool to 900°C then water quench. A blank design virtually identical to that of reference 11 was employed, 20x20 mm sections, 75 mm long, cut from the test ring in the axial direction of the forging. One specimen was obtainable from each such blank. In most cases four blanks were used for each temperature tested, two that experienced the controlled cool and two that were removed after the hour-long soak and air-quenched. Reference 11 states that the cooling rate in air for this size blank was determined in a separate experiment to be about 300°C/min. The intent of this air-quench was to provide a comparison material with an identical concentration of sulfur taken into solid solution as the controlled-cool specimens, which was then "locked-in" to the matrix and not allowed sufficient time during cooling to reprecipitate in a deleterious form.

Five temperatures were evaluated, every 50°C between 1200°C and 1400°C (3-1-X and 4-X-X series). This temperature range is typical of that investigated in past overheating studies of steels [10,16]. As mentioned previously, the solubility of sulfur in Fe-Mn alloys was investigated by Turkdogan, et. al. [33]. For the reaction:



the equilibrium constant defined by

$$K_2 = [Mn\%][S\%]f_S^{Mn}$$

was determined to have the form

$$\log K_2 = -\frac{9020}{T} + 2.929$$



where

$$\log f_S^{Mn} = \left(-\frac{215}{T} + 0.097\right)[Mn\%]$$

Although Turkdogan's work did not address the effect of alloying elements such as those in the flywheel steel, the equations above were expected to provide a reasonable prediction of the solubility. Table 4.2 provides values of sulfur solubility in the flywheel steel at various temperatures, calculated using the above model. As seen in the table, it is to be expected that the entire content of 40 ppm sulfur should be in solution by 1300°C. The temperature range evaluated in the austenitization temperature tests was selected to bracket this temperature.

Table 4.2 Sulfur Solubility vs. Temperature for Flywheel Steel, Determined Using Equations From Reference 33 For Manganese Content of 0.38% (Weight %)

T (deg C)	T (deg K)	f	Ks	%S (wt)
1100	1373	0.949	0.0002	0.0006
1125	1398	0.952	0.0003	0.0008
1150	1423	0.954	0.0004	0.0011
1175	1448	0.956	0.0005	0.0014
1200	1473	0.958	0.0006	0.0018
1225	1498	0.960	0.0008	0.0022
1250	1523	0.962	0.0010	0.0028
1275	1548	0.964	0.0013	0.0035
1300	1573	0.966	0.0016	0.0043
1325	1598	0.968	0.0019	0.0052
1350	1623	0.969	0.0024	0.0064
1375	1648	0.971	0.0029	0.0077
1400	1673	0.973	0.0034	0.0093

Since the sensitivity to overheating, as measured by the percent faceted fracture, is governed by the matrix/PAGB toughness ratio, it has become standard practice to test overheated materials in the fully toughened condition, i.e., after a quench and temper quality heat treatment [10]. Thus most blanks were

quenched and tempered as typical for this material: 840°C for one hour, oil quench,<sup>1</sup> 590°C for one hour, water quench [11, 37]. For comparison purposes, several were tempered at a higher temperature. As reviewed by Honeycombe [60], four stages are recognized for the tempering of martensite. The fourth, involving coarsening of carbides, takes place in the temperature range 300-700°C, and in the higher end of that range the martensite lathes are replaced by equiaxed ferrite grains in a recrystallization process. Thus several blanks were tempered at 650°C, providing an alternative quality heat treatment for evaluation which was expected to have a higher matrix toughness than material given the conventional heat treatment. Also for comparison purposes, six control specimens were included in this series. Four of them were tested in the as-received condition, while the other two were not overheated but were put through a quench and temper treatment.

#### **4.1.2.2. Martensitic Material Tests**

In addition to the above tests, several specimens were overheated but not subjected to a quench and temper, in order to evaluate the effect of the overheated precipitates on performance of material with fracture behavior fundamentally different than that of the very tough quenched and tempered material. The 3.5NiCrMoV grade was developed to provide good through hardening in thick sections. This is achieved by delaying the ferrite-pearlite reaction [60], so that martensite is formed easily, even at relatively slow cooling rates which would be considered a normalization for other steels.<sup>2</sup> To produce this microstructure, six specimens (5-1-X series) were subjected to an overheating treatment consisting of 1 hour at 1300°C, 2°C/min controlled cool to 900°C and then furnace-cooled to form martensite without subsequent tempering. For control comparison, three specimens were air-cooled from 1300°C, to yield martensite which did not contain overheated precipitates (6-5-X series).

---

<sup>1</sup> Some specimens were water quenched at this step. This was not believed to represent a significant difference due to the small blank size and good hardenability of this material.

<sup>2</sup> In very large structures (thickness greater than 1 m) with very slow cooling rates a "rimmed" structure is typically developed under quenching, with the outer region martensite and the inner core bainite [37].

#### 4.1.2.3. Cooling Rate Tests

Using the 3.5NiCrMoV material five cooling rates were investigated in the cooling rate tests: 0.5, 1, 5 and 10°C/min along with an undetermined rate believed to be about 50°C/min. The 0.5, 1 and 5°C/min rates were easily achieved using the microprocessor furnace controller. The 10°C/min rate was the maximum rate at which the furnace would cool once power was completely shut off. In order to achieve a more rapid rate between 10°C/min and the 300°C/min air quench, a quench within a bed of industrial ceramic insulation was employed yielding the estimated 50°C/min rate. For both the 10°C/min and ceramic quench tests, the time-temperature profiles were roughly exponential. However, during cooling through the precipitation range, (in the rapid early portion of the transient) they are approximately linear.

Heat treatments for the 1, 5 and 10°C/min tests were characterized by a relatively short high-temperature austenitization followed by controlled-cooling to 1100°C. For the 0.5°C/min test the method of reference 11 was employed; 1 hour at 1300°C, followed by cooling to 900°C then water quenching. The ceramic quench specimen was allowed to cool in the alundum bed to close to room temperature. The overheated blanks from all tests were then quenched and tempered, along with another un-overheated control blank.

Stricter temperature monitoring and a different blank design was employed for the 1, 5 and 10°C/min tests in this series. For these tests the box furnace was fitted with a removable plug door, with an Inconel tube atmosphere port penetrating it. This is illustrated in Figure 4.3. A system of alternating concentric Inconel and alumina tubes was fed through the port. The center alumina tube was a four-hole insulator, through which a Pt/Pt-10%Rh (type S) thermocouple was threaded with a junction formed by spot welding the lead wires. The outermost tube was alumina with an outer diameter slightly less than 12.7 mm (1/2") and a 9.5 mm (3/8") nominal wall thickness.

A 62 mm long (2.4", inner radius) section of the flywheel test ring was quartered to make specimen blanks for the 1, 5 and 10°C/min tests. A 12.7 mm (1/2") diameter hole was drilled axially down the blanks, so that they could be

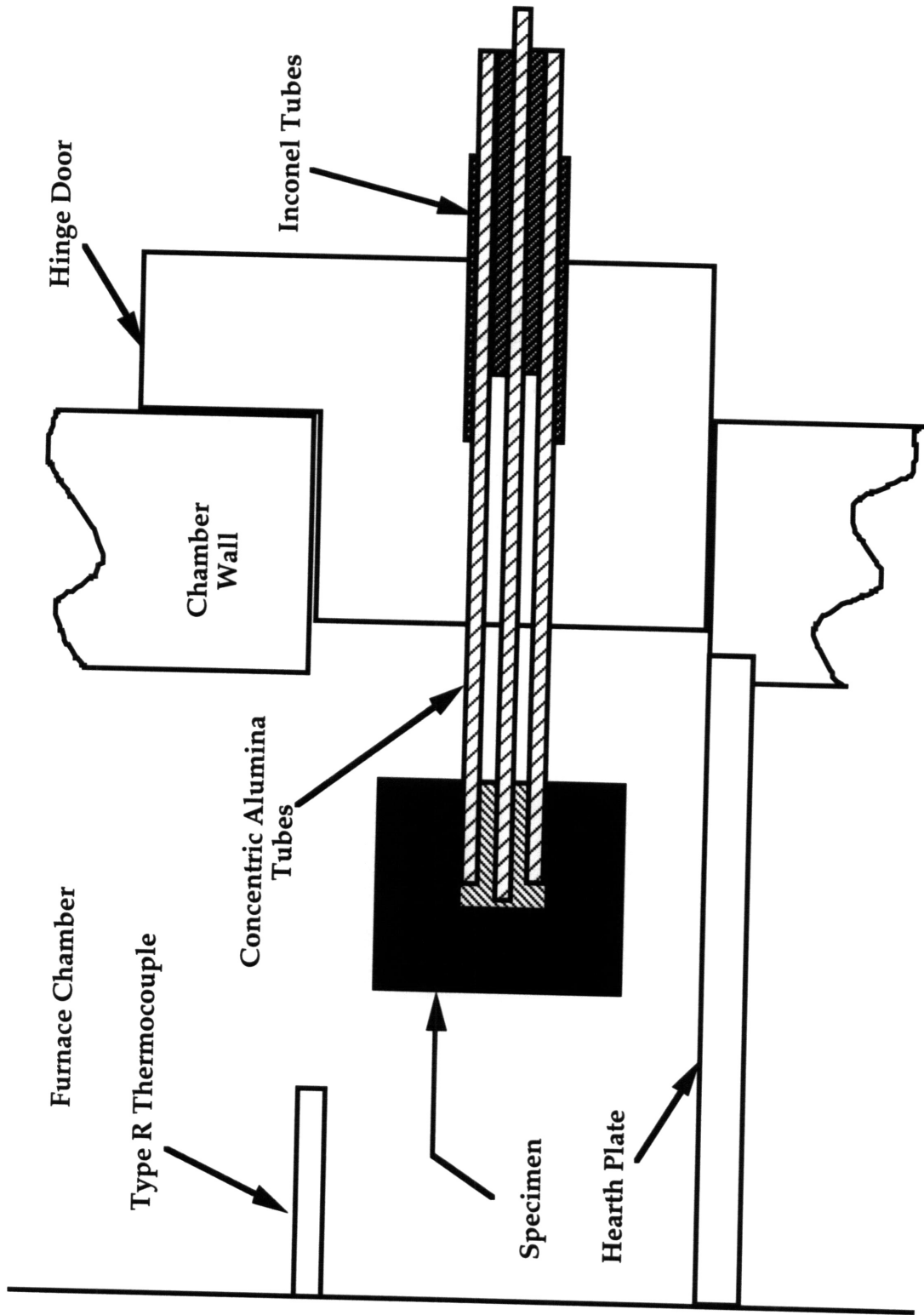


Figure 4.3 Furnace Apparatus for Cooling Rate Tests

supported cantilevered on the alumina rod with about 0.08 mm (3 mils) diametral clearance in the bore hole. Supported in this fashion the type S thermocouple was in contact with the inside of the bore hole. The thermocouple was read by an Omega DP-41TC high-performance digital meter, which relayed a scaled analog output to a voltage-reading chart recorder and a digital output to a Jameco XT-type microcomputer running a simple data acquisition routine written in GWBASIC. This enabled continuous monitoring of the core temperatures of the blanks during the overheating treatments. At least four, and in one case five, impact specimens could be obtained from this blank design.

In these treatments the furnace was heated to the austenitization temperature with the hinge door closed, then once the temperature had stabilized the hinge door was opened and the plug door with specimen attached was inserted directly into the hot chamber. When the temperature stabilized once again, the programmed profile was initiated, starting with a soak, followed by a controlled-rate furnace cool to 1100°C. At that point the furnace was shut off and the temperature allowed to free fall to room temperature.

The set-up for the ceramic quench test is as depicted in Figure 4.4. A one-gallon stainless steel can was filled with 5 pounds of coarse granulated alumina (no. 10 alundum from the Norton company). After one hour at 1300°C, the specimen was removed from the furnace and immediately placed on the surface of the alumina, at which point another 5 pounds was poured over it. A type K thermocouple probe was then inserted down the inside of the can at the surface of the bath and the temperature monitored over a period of several hours. A transient thermal finite element analysis was then performed for comparison to the recorded histories. On the basis of the results of this analysis, it is estimated that the ceramic/alumina quench cooling rate was approximately 50°C/min. Appendix C provides more details of this procedure. Three specimens were given this treatment and then quenched and tempered as indicated in Table 4.3.

The small amount of the A 508 material available necessitated evaluating fewer heat treatments. For these tests the method of reference 11 was again employed, 20x20x75 mm blanks, inserted in a preheated furnace and treated in the vertical position for one hour at 1300°C, followed by a controlled-cool at 1 or 2°C/min to 900°C, then water quenching. This was followed by a quench and temper

consisting of 840°C for one hour, water quench, one hour at 650°C, water quench. The size of the commercial purity specimen enabled cutting only two blanks, while the superclean version yielded six, of which three were used.

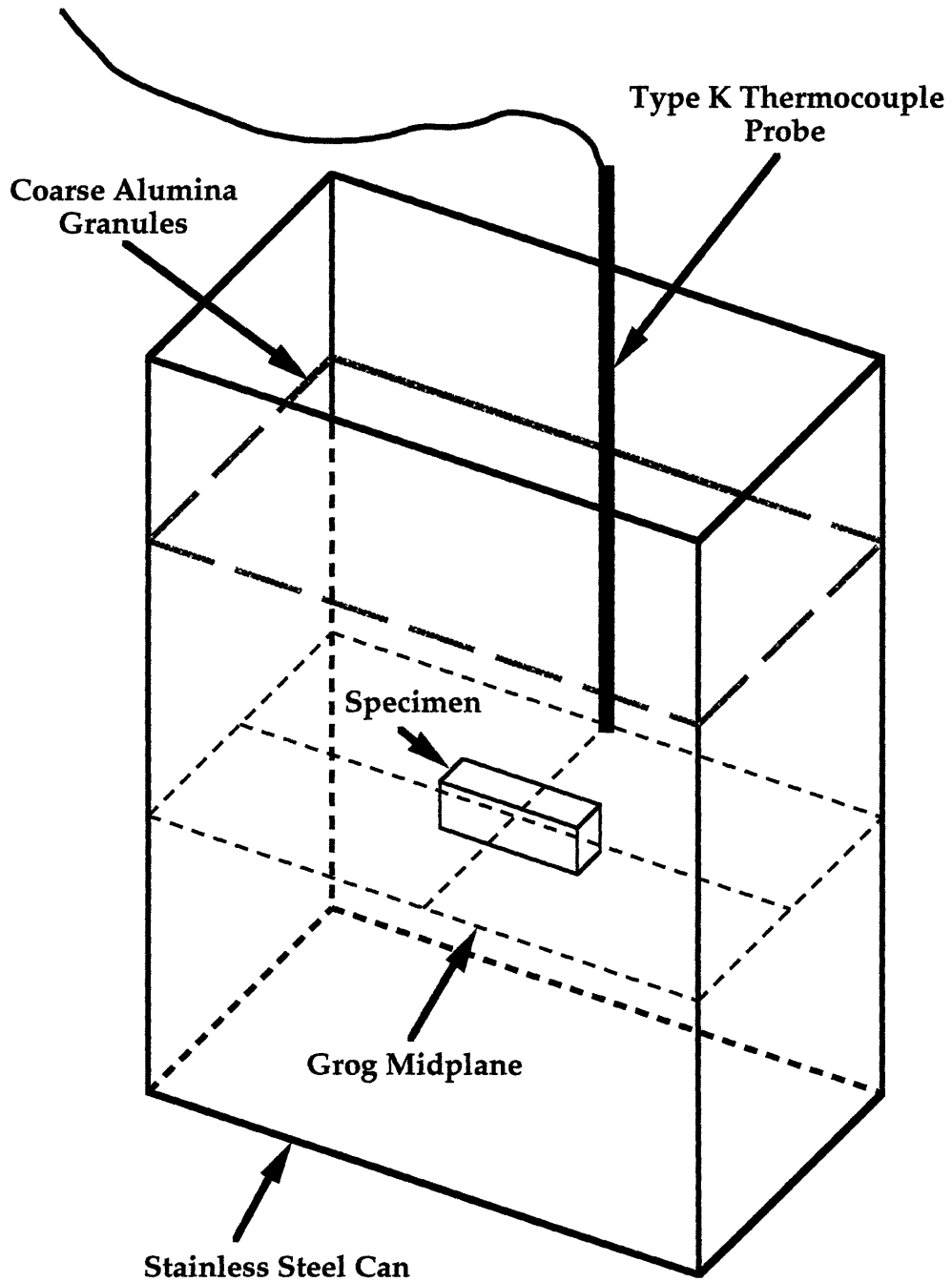


Figure 4.4 Configuration of Ceramic Bath Cooling Rate Test

#### 4.1.3. Test Matrix

Heat treatment parameters are provided for all specimens in Table 4.3. The fracture tests and microscopic and metallurgical examinations performed on them are provided in identical format in Table 4.4.

#### 4.1.4. Fracture Tests

Fracture behavior was assessed using Charpy V-Notch (CVN) impact testing. The intent of the testing was primarily to furnish fracture surfaces for inspection using electron microscope. Thus only a limited number of tests were performed on calibrated machines, while the remainder were performed on an uncalibrated machine described below. Only energy values from calibrated tests are reported in this thesis.

Impact specimens were either milled or ground from the heat treated blanks to standard size (10x10 mm cross section), as specified by ASTM E 23 92 [61]. All tests were performed at room temperature on one of three machines: 1) a 256 ft-lb Tinius-Olsen pendulum tester in the AMP Laboratory for the Mechanical Behavior of Materials in the MIT Mechanical Engineering Department, 2) a 128 ft-lb Physmet CIM-128 tester at the Altran Materials Engineering Inc.<sup>3</sup> in Cambridge, MA, or 3) a 264 ft-lb Tinius-Olsen machine at Mass Materials Research in West Boylston, MA. The MIT Mechanical Engineering machine is used by students for introductory coursework, and is not maintained in strict calibration. Although energy values for samples tested on this machine were recorded, they were not considered sufficiently reliable to report. The Altran Materials machine was within calibration for nearly all tests performed on it. Two tests were performed after the machine may have been put out of calibration by a failed strike. Impact energy values for these tests are not reported. The Tinius Olsen machines provide absorbed energy values directly from a sliding scale, while energy must be calculated from an angle indicator on

---

<sup>3</sup> Formerly Manlabs Testing Services.

Table 4.3 Heat Treatment Parameters For All Specimens,  
 Grouped By Test Series. Key: O - Oil, W - Water,  
 A - Air Quench, AL - Alundum, NA - Not Applicable

Specimen	Mater.	Overheating		Cooling Rate (C/min)	Quench and Temper			
		Temp. (deg C)	Time (min)		Quench Medium	Temper Temp. (deg C)	Temper Medium	
T E S T S	1-1-1	3.5Ni	NA	NA	NA	O	590	W
	1-1-2							
	1-1-3							
	1-1-4							
R A T E	1-2-1	3.5Ni	1290	25	5	O	590	W
	1-2-2							
	1-2-3							
	1-2-4							
	1-2-5							
C O O L I N G	1-3-1	3.5Ni	1300	12	1	O	590	W
	1-3-2							
	1-3-3							
	1-3-4							
A U S T .	1-4-1	3.5Ni	1280	18	10	O	590	W
	1-4-2							
	1-4-3							
	1-4-4							
	6-3-3	3.5Ni	1280	60	AL	W	590	W
	6-3-4							
	6-4-1							
	6-4-2	3.5Ni	1280	60	0.5	W	650	W
	6-4-3							
	6-4-4							
	3-1-1	3.5Ni	1300	60	2	W	590	W
	3-1-2				2			
3-1-3				A				
3-1-4				A				
3-1-5		NA	NA	NA	NA		NA	
3-1-6								



Table 4.3 cont. Heat Treatment Parameters For All Specimens,  
 Grouped By Test Series. Key: O - Oil, W - Water,  
 A - Air Quench, AL - Alundum, NA - Not Applicable

	Specimen	Overheating			Cooling Rate (C/min)	Quench and Temper		
		Mater.	Temp. (deg C)	Time (min)		Quench Medium	Temper Temp. (deg C)	Temper Medium
T E S T S	4-1-1	3.5Ni	1200	60	A	O	590	W
	4-1-2				A			
	4-1-3				2			
	4-1-4				2			
T E M P .	4-2-1	3.5Ni	1250	60	2	O	590	W
	4-2-2				2			
	4-2-3				A			
	4-2-4				A			
T E M P .	4-3-1	3.5Ni	1350	60	2	O	590	W
	4-3-2				2			
	4-3-3				A			
	4-3-4				A			
A U S T E N I T .	4-4-1	3.5Ni	1400	60	10	O	590	W
	4-4-2				10			
	4-4-3				A			
	4-4-4		1400	60	A	O		W
A U S T E N I T .	4-5-1	3.5Ni	NA	NA	NA	O	590	W
	4-5-2							
	4-5-3					NA	NA	NA
	4-5-4							
M A R T E N S .	5-1-S1	3.5Ni	1300	60	2	W	NA	NA
	5-1-S2							
	5-1-1							
	5-1-2							
	5-1-3							
	5-1-4							
	6-5-1				A			
	6-5-2							
	6-5-3							

Table 4.3 cont. Heat Treatment Parameters For All Specimens,  
Grouped By Test Series. Key: O - Oil, W - Water,  
A - Air Quench, AL - Alundum, NA - Not Applicable

Specimen	Overheating			Cooling Rate (C/min)	Quench and Temper		
	Mater.	Temp. (deg C)	Time (min)		Quench Medium	Temper Temp. (deg C)	Temper Medium
F - A - 1	508	1300	60	2	W	650	W
F - A - 2							
F - A - 3							
F - B - 1							
F - B - 2				1			

the Physmet machine, using the following equation:

$$E = 127.54 - 128.52 \sin^2 (\theta / 2)$$

where E is in ft-lbs and  $\theta$  is in degrees.

#### 4.1.5. Microscopy

Initial assessment of most fracture surfaces was conducted using an optical stereoscope. Detailed examination was then performed by scanning electron microscopy (SEM). Material microstructure and sulfide precipitation characteristics were further evaluated with an optical metallograph after chemical and electrolytic etching. Each of these techniques is described in turn below.

##### 4.1.5.1. Optical Fractography

One of the fundamental characteristics of overheating is the presence of flat, matte facets observable on a fracture surface. As would be expected these are more apparent with a larger prior austenite grain size. At the scale of grains achieved in this material during one hour at temperatures above 1250°C (about 1-5 mm), they are difficult to view effectively in the SEM. Thus prior to

Table 4.4 Mechanical Tests and Microscopic and Metallurgical Examinations For All Specimens, Grouped By Test Series

	Specimen	Impact Chem		Microscopy			Etching	
		Test	Check	SEM	TEM	Aug	Micro.	PAGB
COOLING RATE TESTS	1-1-1							
	1-1-2			■				■
	1-1-3			■				
	1-1-4			■				
	1-2-1			■				■
	1-2-2			■				■
	1-2-3			■				
	1-2-4			■				
	1-2-5			■				
	1-3-1			■				
	1-3-2			■				
	1-3-3			■				
	1-3-4			■				■
	1-4-1			■				
	1-4-2			■				
	1-4-3			■				
1-4-4			■					
AUST.	6-3-3	■						
	6-3-4	■						
	6-4-1							
	6-4-2	■						
	6-4-3	■						
	6-4-4							
	3-1-1	■		■				
	3-1-2	■		■				■
3-1-3	■		■				■	
3-1-4	■		■				■	
3-1-5	■		■				■	
3-1-6	■		■				■	

Key: ■ - valid test      ||||| - unreportable test



Table 4.4. cont. Mechanical Tests and Microscopic and Metallurgical Examinations For All Specimens, Grouped By Test Series

	Specimen	Impact Test	Chem Check	Microscopy			Etching		
				SEM	TEM	Aug	Micro.	PAGB	MnS
T E M P . T E S T S	4-1-1								
	4-1-2								
	4-1-3								
	4-1-4								
	4-2-1								
	4-2-2								
	4-2-3								
	4-2-4								
	4-3-1								
	4-3-2								
	4-3-3								
	4-3-4								
	4-4-1								
	4-4-2								
	4-4-3								
	4-4-4								
A U S T E N I T . T E S T S	4-5-1								
	4-5-2								
	4-5-3								
	4-5-4								
M A R T E N S . T E S T S	5-1-S1								
	5-1-S2								
	5-1-1								
	5-1-2								
	5-1-3								
	5-1-4								
	6-5-1								
	6-5-2								
	6-5-3								

Key:  - valid test       - unreportable test

Table 4.4 cont. Mechanical Tests and Microscopic and Metallurgical Examinations For All Specimens, Grouped By Test Series

Specimen	Impact Test	Chem Check	Microscopy			Etching		
			SEM	TEM	Aug	Micro.	PAGB	MnS
C R .	F - A - 1							
	F - A - 2							
	F - A - 3							
	F - B - 1							
	F - B - 2							

Key:  - valid test       - unreportable test

examination in that instrument, fracture surfaces were first examined using a Zeiss stereoscope with possible magnifications of 20, 40 and 80X. Sketched maps of interesting features and facets were constructed to guide later examination using the SEM. No measurement of percent faceted fracture was calculated, since it was considered that there was an insufficient number of specimens in each heat to enable a statistically significant measurement.

**4.1.5.2. SEM Fractography**

After optical fractography, fracture surfaces were protected from corrosion with Microstop polymeric coating and cut from the remainder of the CVN bar with a Buehler Isomet 2000 high-speed, fluid-cooled abrasive metallographic saw. The cut surfaces were cleaned and Microstop removed ultrasonically in acetone. The cleaned surfaces were then examined without coating in one of two SEMs: the Cambridge Instruments Stereoscan 250Mk3 SEM in the microscopy facility of MIT's Center for Materials Science and Engineering (CMSE), or the Topcon ABT-150S SEM in the Materials Group facility of the Plasma Fusion Center. The Topcon was equipped to do EDS analysis with a Noran Voyager II X-ray Quantitative Microanalysis System. Viewing was always done in secondary electron mode, generally at acceleration voltages between 20 and 40 kV.

### 4.1.5.3. Optical Metallography

In this phase, material from the fracture specimens was ground, polished and etched, employing a variety of conventional chemical and electrolytic etches. Table 4.5 summarizes the etchants, their compositions, source references and

Table 4.5 Metallographic Etchants: References, Compositions and Subject Specimens

Etchant	Ref.	Composition	Specimen Series
Nital	[68]	100 mL ethanol	3-1-X
		2,4,8 mL nitric acid	4-X-X
			5-1-X
Picral	[68]	100 mL ethanol	3-1-2
		4 g picric acid	
Bechet & Beaujard's	[65]	150 mL distilled water	5-1-X
		2.25 g picric acid	
		1 g cupreous chloride (CuCl <sub>2</sub> )	
		3 mL wetting agent	
Villela's Reagent	[65]	100 mL ethanol	5-1-X
		5 mL hydrochloric acid	
		1 g picric acid	
Struer's Perchloric (modified Knuth-Winterfeldt's reagent)	[66]	90 mL distilled water	1-2-2
		730 mL ethanol	1-3-4
		100 mL butylcellusolve	
		78 mL perchloric acid	
CrO <sub>3</sub>	[65]	25 g CrO <sub>3</sub>	1-2-2
		133 mL acetic acid	1-3-4
		7 mL distilled water	
Nitric Deep Etch	[67]	125 mL nitric acid	4-2-2
		125 mL tap water	

subject specimens. There were three basic goals: 1) characterization of the final microstructure, 2) investigation of the prior austenite grain structure, and 3) determination of the nature and distribution of the overheated sulfides. In most cases, cross sections of the CVN bars about 2-6 mm in width were cut from beneath the fracture surfaces using the high-speed metallographic saw. These were mounted in epoxy or phenolic and ground and polished. Grinding was done to 600 grit and polishing to 3  $\mu\text{m}$  diamond solution, both on a Beuhler Ecomet 3/4 automatic polishing wheel.

Final microstructure of specimens from the austenitization temperature test series, both overheated and control, was determined by etching with 2-8% nital, by swabbing with a cotton ball. This was done for overheated and air-quenched specimens for temperatures of 1200-1350°C, as well as for as-received and quenched and tempered control specimens.

Several picric acid-based etchants, recommended for revealing prior austenite grain structure, were evaluated, including: 1) warm (35°C) and room-temperature picral, 2) modified Bechet & Beaujard's etch, and 3) Villela's HCl/picric reagent. The warm picral was applied by immersion in a 100 mL solution in a glass container, itself immersed in a continuously running hot tap-water bath for periods of 2-4 minutes, preceded by 2 minutes at room temperature. The other etchants were applied as was the nital, swabbed with a cotton ball until sufficient attack was achieved, judged visually.

Electrolytic etching with perchloric and chrome trioxide electrolytes was performed using a Struers Polectrol electrolytic polishing and etching apparatus. The perchloric solution is a generally applicable electrolyte for irons and steels, while the chrome trioxide solution is recommended for attacking and revealing inclusions such as the overheating inclusions. These specimens were ground to 600 grit and then etched with the Polectrol using strong bath agitation. Voltage and time were varied over the ranges 20-40V and 10-15 seconds, respectively. A hard plastic mask was employed which supported the mounted specimen while exposing the entire CVN cross section (1  $\text{cm}^2$ ) to the bath.

As described previously, type II MnS precipitates form interdendritically from the melt. Their three-dimensional morphology is difficult to observe with

conventional plane-surface etching [69]. Baker and Charles [67] overcame this problem by deep-etching using a warm 50% nitric acid solution which attacked the matrix much more rapidly than the sulfides, leaving a relief structure well-suited for examination under SEM. One of their classic micrographs of a typical "parallel fence" structure of type II MnS is reproduced as Figure 4.5.

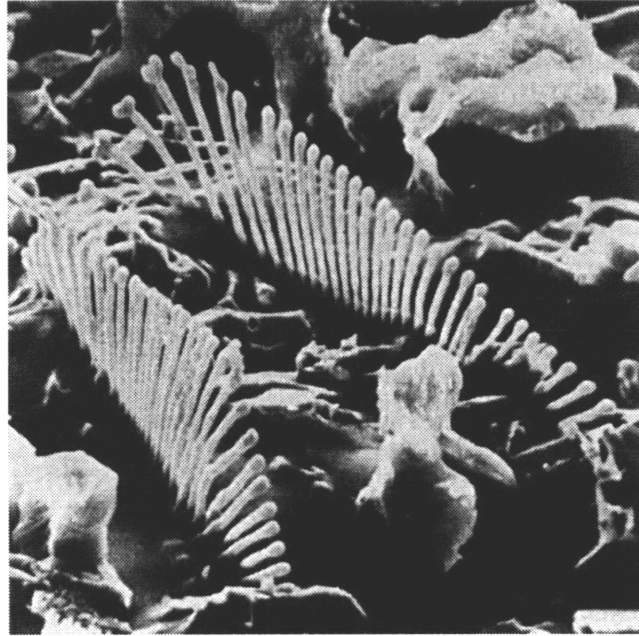


Figure 4.5 Parallel Fence Structure of Type II MnS, Revealed by Warm 50% Nitric Acid [from 67]

This technique was used on a specimen (no. 4-2-2) from the austenitization temperature tests which developed rod manganese sulfides on the fracture surface. The nitric acid was held in a 300 ml beaker supported atop a wide rubber stopper within a 600 ml beaker containing a continuously flowing hot tap-water bath. Bath temperature was maintained at 50°C, monitored with a mercury thermometer. Mounted specimens were quick-dipped in the hot etchant for periods ranging from instantaneously to 15 seconds, then ultrasonically cleaned in either methanol, ethanol, isopropyl alcohol or acetone. They were then dried and examined in the SEM.



#### **4.1.5.4. Auger Spectroscopy**

As will be described in the Results section, precipitate-free PAGB facets were found to occur with various overheating heat treatments. To evaluate whether a mechanism such as interfacial segregation was the cause, examination of specimens fractured in vacuo within an Auger microscope was conducted. No results of value were obtained, however, since it was found to be impossible to induce fracture at the PAGBs within the extremely small but tough specimens required for the microscope.

## 4.2. Sulfide-Rod Orientation Relationship

The purpose of this part of the research program was to investigate the crystallography of the sulfide rods and their relationship to the parent matrix. The experimental procedure consisted of two main components: 1) transmission electron microscope (TEM) examination of extracted sulfide rods to determine their crystal structure and the relationship between that structure and their exterior morphology, and 2) trace analysis of etched samples containing rods to determine the orientation of the rod morphology with respect to the original austenite.

### 4.2.1. TEM of MnS Rod Extractions

Based on the results of the SEM examination of the CVN fracture surfaces, a specimen was selected which displayed a dense population of rods. Extraction was performed by wetting the fracture with acetone and overlaying a small strip of biotin polymer tape. A low pressure was applied to the tape while the acetone dried to promote forming to the fracture contour. Once dry, the tape was torn rapidly from the surface. The area of the tape retaining the fracture mold, approximately 10x10 mm, was cut out and coated with a layer of carbon in a Denton DV-502A carbon evaporator. The coated film was then examined in the SEM to verify that rods were successfully extracted, and to map their locations.

Areas of the film which had a number of rods were scissor-cut into small (< 3 mm) squares under the optical stereoscope. The acetone float method was used to dissolve the biotin from beneath the carbon film. In this method, a fine mesh stainless steel screen with square shape is bent into a low platform and placed in a petri dish, as depicted in Figure 4.6. Several 3 mm copper TEM grids are laid on the grid and the film squares are laid on top of them, biotin side down. The petri dish is then slowly filled with acetone until the meniscus contacts the bottom of the TEM disks, wetting the biotin film. The acetone dissolves the biotin, leaving the carbon film with precipitates attached to be stretched across the disks. This procedure is repeated as necessary.

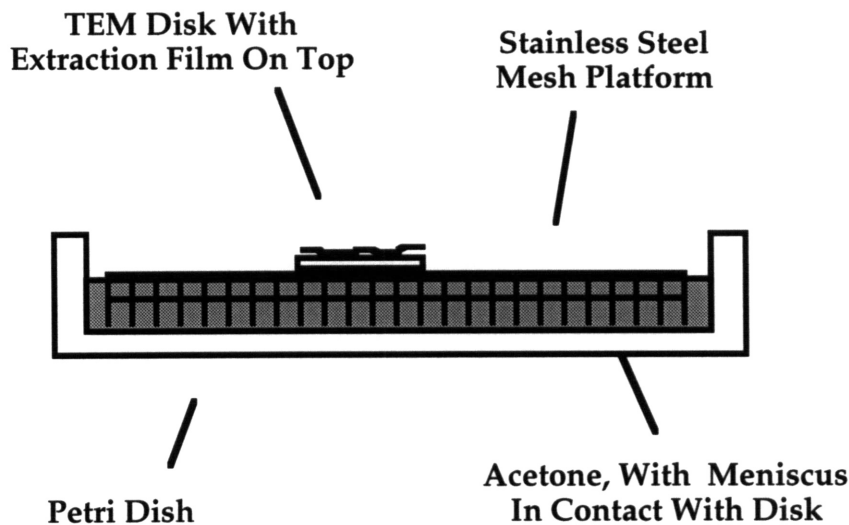


Figure 4.6 Apparatus for Removing Extraction Replica Film Via the Acetone Float Method

The prepared disks were then examined in either of two of the transmission electron microscopes in the microscopy facility of MIT's Center for Materials Science and Engineering (CMSE). The first is a Japan Electron Optics Laboratory (JEOL) 200CX, with accelerating voltages to 200 kV and resolution capability to 2.9 Å. The second is a custom-built Topcon 002B with accelerating voltages to 200 kV and resolution capability to 1.8 Å. Specimens were examined using both single and double-tilt stages. Bright-field images, diffraction patterns, and dark-field images of the rods were obtained. An effort was made to obtain corresponding bright-field images and diffraction patterns in order to enable correlating the zone axis of the pattern with the physical morphology of the rod.

Initial indexing of the diffraction images was performed by inspection of catalogued patterns [62], and then confirmed using the Desktop Microscopist computer program, running on a Macintosh IICi. Desktop Microscopist [63] is a graphical interface program which enables plotting diffraction images which would be produced from a given crystal structure by illumination with an electron or X-ray beam of given characteristics. Essential inputs are crystal structure (specified through space group or discrete unit cell definition), camera

length and zone axis. The plotted patterns were then printed and checked against the overlaid TEM negatives, in order to verify that the structure and zone axes determined by inspection were correct.

#### **4.2.2. Trace Analysis**

As determined during the metallographic phase of the first half of the work, annealing twins formed in austenite grains which grew large during the overheating treatments were clearly observable, both with the naked eye and under the microscope, after chemical etching with several different etchants. Since the sulfide rods were also revealed by the same etchants, it was possible to perform a trace analysis relating rod direction to the {111} planes represented by the twins. This enabled orienting the rod axes with respect to the parent austenite crystal, provided that traces of features in the correct configurations were present on the etched surfaces, as described below.

##### **4.2.2.1. Geometry and Analysis**

In the literature review, several methods of stereographic trace analysis were described, which require different types of input information. Two factors made these techniques inappropriate for application here: 1) the failure of any examined grains to display twins in more than two nonparallel directions (a requirement for single surface analysis), and 2) the difficulty of cutting a single prior austenite grain to produce more than two nonparallel surfaces. It was found, however, that upon inspection of the etched surfaces occasionally a grain could be found which had two nonparallel twin traces, one of which was of sufficient size and oriented appropriately to enable exposing it on a second, perpendicular surface produced by cutting on a metallographic saw. This configuration is depicted in Figure 4.7. The information provided by this configuration, termed hereinafter a "two-one" trace analysis since one feature is observable on two surfaces while the other only on one, is sufficient to determine the orientation of the austenite crystal to within six possible positions. The method underlying this analysis is described now.

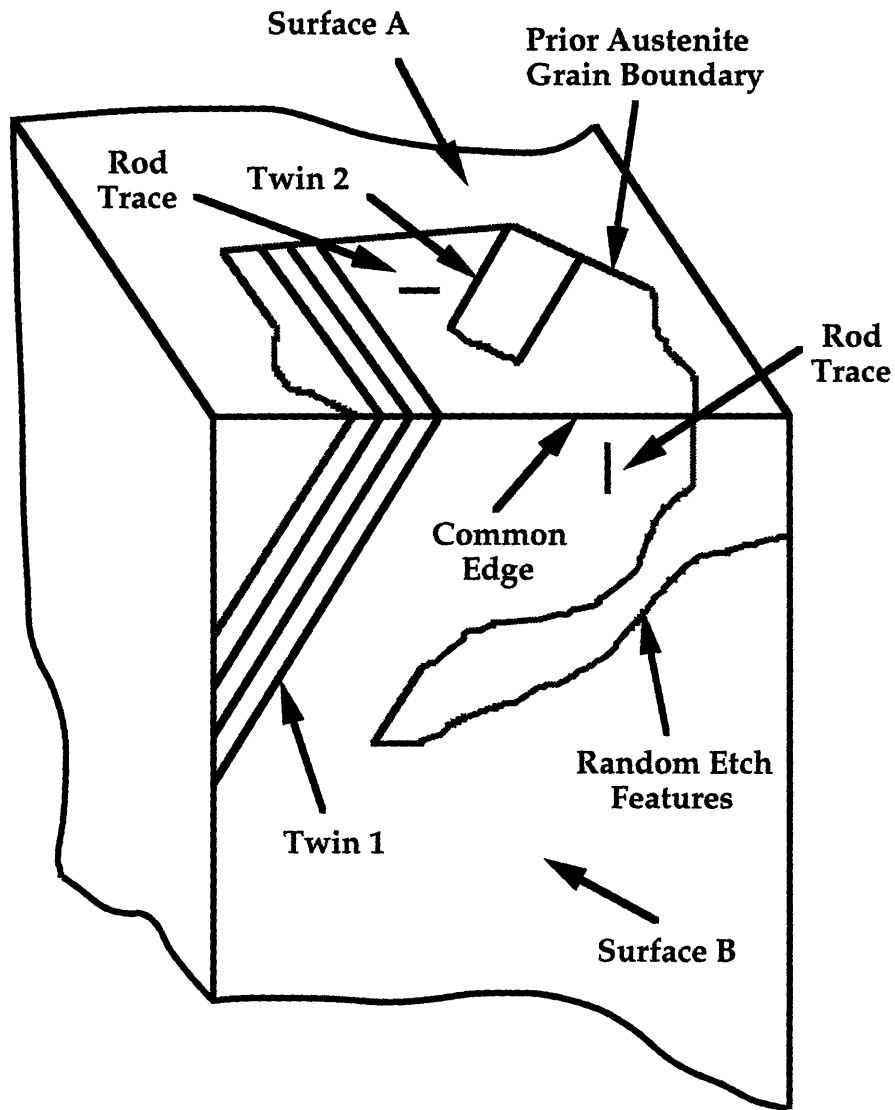


Figure 4.7 Specimen Appropriate for Two-One Trace Analysis (Specimen 5-1-S1)

Figure 4.8 depicts the geometry of the problem. Various elements of the problem are:

- A - first surface of the specimen
- B - second surface
- $\vec{n}_A$  - unit normal vector defining surface A
- $\vec{n}_B$  - unit normal vector defining surface B

$\phi$	-	included angle between surfaces A and B
$\vec{T}_{A1}$	-	vector representing the trace of twin 1 on surface A
$\vec{T}_{B1}$	-	vector representing the trace of twin 1 on surface B
$\vec{T}_{A2}$	-	vector representing the trace of twin 2 on surface A
$\vec{E}$	-	edge vector along intersection of surfaces A and B
$\psi_{A1}$	-	angle on surface A between edge and twin 1 trace
$\psi_{B1}$	-	angle on surface B between edge and twin 1 trace
$\psi_{A2}$	-	angle on surface A between edge and twin 2 trace
$\vec{n}_1$	-	normal vector defining {111} plane of twin 1
$\vec{n}_2$	-	normal vector defining {111} plane of twin 2

All of the vectors listed above are expressed in terms of the specimen coordinate system, with axes as depicted in Figure 4.8.

The orientation in specimen coordinates of the plane of twin 1 is completely specified by the normal vector  $\vec{n}_1$ , calculated as the normalized cross product of  $\vec{T}_{A1}$  and  $\vec{T}_{B1}$ . All possible orientations of the austenite crystal are then constructable by orienting a (111) plane of the FCC lattice parallel to the plane defined by the vector  $\vec{n}_1$ , and then rotating the lattice about this normal. A natural numerical solution procedure consists of rotating this lattice, starting from an assumed initial orientation, and calculating at each step the traces on surface A of the other six (only three of which are unique) nonparallel octahedral planes. Any orientation which yields a trace on A parallel to the vector  $\vec{T}_{A2}$  is a possible solution.

A distinct advantage of this procedure is that, by plotting all possible configurations of the austenite crystal, the uniqueness of the obtained solutions is determined, as well as information on the degree to which the problem is "well-posed" by the metallographic input. It will be seen that, generally, the behavior of the three other nonparallel octahedral planes is identical and 120 degrees out of phase. Such an observation is not intuitively obvious, but is readily demonstrated using this "brute force" numerical technique. The calculation procedure is described now.

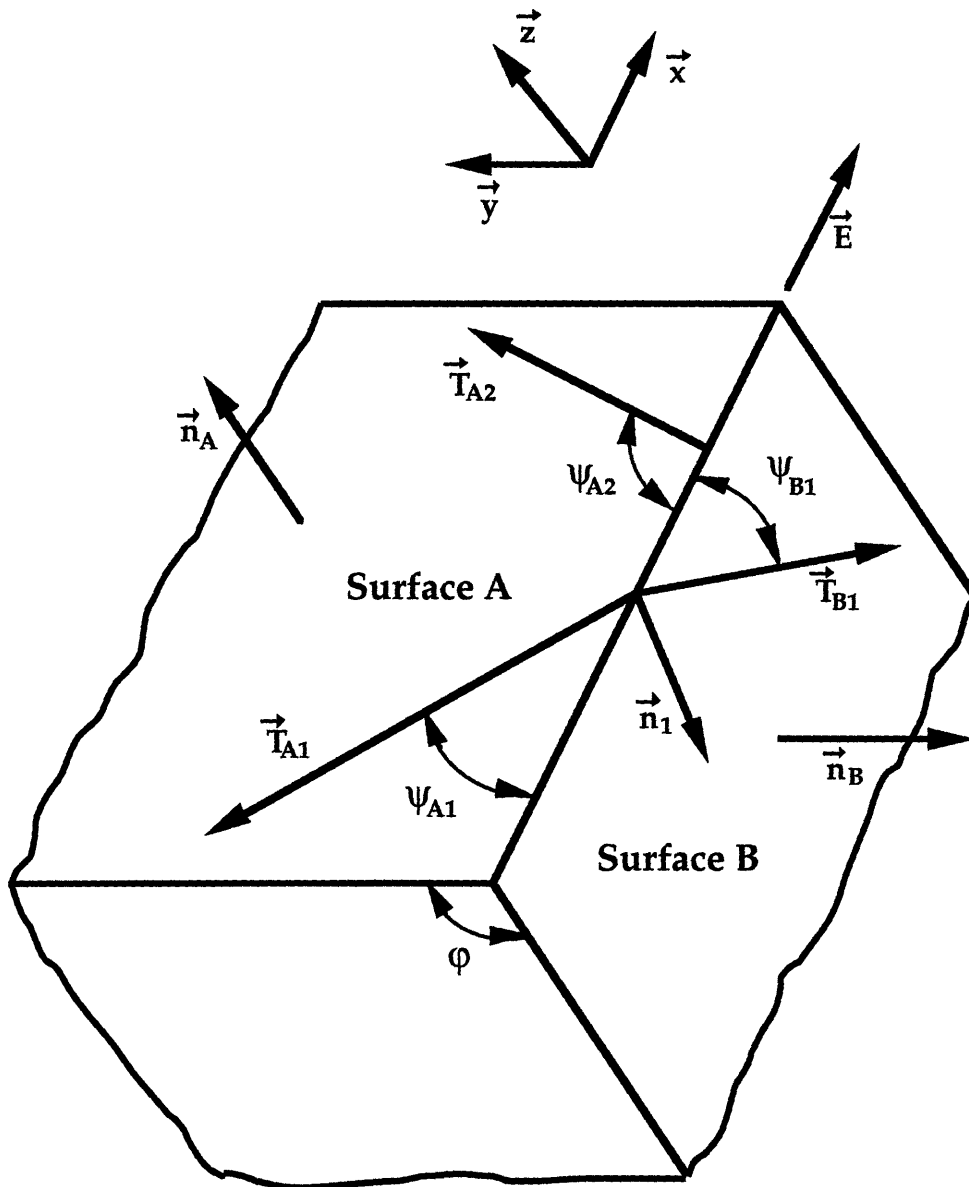


Figure 4.8 Geometry of Two-One Trace Analysis

Input data from the metallography consists of the angles  $\psi_{A1}$ ,  $\psi_{B1}$  and  $\psi_{A2}$ . The trace vectors are calculated from:

$$\vec{T}_{A1} = (-\cos \psi_{A1}, \sin \psi_{A1}, 0)$$

$$\vec{T}_{B1} = (\cos \psi_{B1}, 0, -\sin \psi_{B1})$$

The normal vector to the plane of twin 1 is calculated by the cross product of the two trace vectors:

$$\vec{n}_1 = \vec{T}_{A1} \times \vec{T}_{B1} = \begin{vmatrix} \vec{i} & \vec{j} & \vec{k} \\ -\cos \psi_{A1} & \sin \psi_{A1} & 0 \\ \cos \psi_{B1} & 0 & -\sin \psi_{B1} \end{vmatrix}$$

The process of constructing all possible orientations of the austenite crystal consists of rotating the "pyramid" defined by the upper octahedral planes about the axis  $\vec{n}_1$ , with face 1 corresponding to the plane of twin 1, as depicted in Figure 4.9. An initial position is assumed in which the base edge of face 1, represented by vector  $\vec{B}_1$ , is parallel to the vector  $\vec{T}_{A1}$ . Defining a vector  $\vec{T}_{P1}$  which lies in the plane of twin 1 and is perpendicular to  $\vec{T}_{A1}$  yields a pair of orthogonal vectors lying in the plane of twin 1. Rotation of the austenite octahedron is accomplished by transforming the base vector  $\vec{B}_1$  by an angle  $\omega$  in

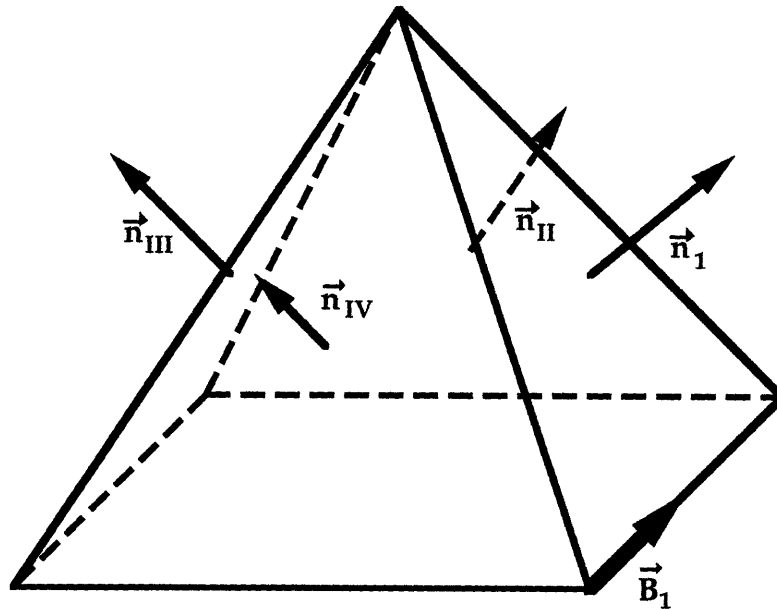


Figure 4.9 Austenite Crystal Orientation Represented by "Pyramid" Defined by the Upper Octahedral Planes



the local coordinate system defined by these vectors, as shown in Figure 4.10. This is easily done numerically, an increment  $d\omega$  at a time. The orientation of the

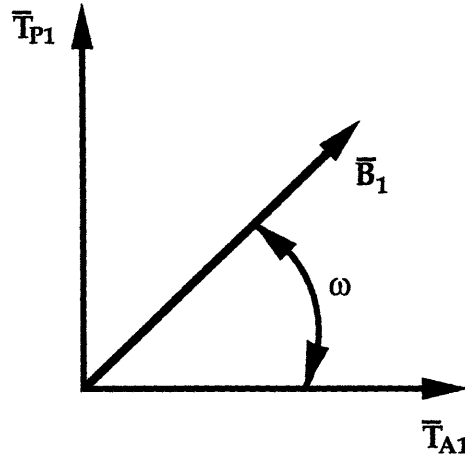


Figure 4.10 Austenite Crystal Orientation Rotation Geometry

normal vectors defining the other three faces of the octahedral pyramid, faces II, III and IV,<sup>4</sup> are then calculated by straightforward geometry and vector algebra, as shown in Figure 4.11. The calculation details are as follows:

$$\vec{T}_{P1} = \vec{T}_{A1} \times \vec{n}_1$$

$$\vec{B}_1 = \cos \omega \cdot \vec{T}_{A1} + \sin \omega \cdot \vec{T}_{P1}$$

$$\vec{R}_1 = \vec{n}_1 \times \vec{B}_1$$

$$\vec{n}_{III} = \cos(2\theta - \pi/2) \cdot \vec{R}_1 - \sin(2\theta - \pi/2) \cdot \vec{n}_1$$

$$\vec{V} = \frac{\vec{n}_1 + \vec{n}_{III}}{|\vec{n}_1 + \vec{n}_{III}|}$$

---

<sup>4</sup> An arabic numeral 1 designates the octahedral plane whose orientation is completely determined by the traces of twin 1 on surfaces A and B. Roman numerals II, III and IV designate the other three octahedral planes, whose orientations vary as the transformation angle  $\omega$  varies.

$$\begin{aligned}\vec{n}_{II} &= \cos(\pi/2 - \theta) \cdot \vec{R}_1 + \sin(\pi/2 - \theta) \cdot \vec{n}_1 \\ &= \sin \theta \cdot \vec{B}_1 + \cos \theta \cdot \vec{V}_1\end{aligned}$$

$$\begin{aligned}\vec{n}_{IV} &= -\cos(\pi/2 - \theta) \cdot \vec{B}_1 + \sin(\pi/2 - \theta) \cdot \vec{V}_1 \\ &= -\sin \theta \cdot \vec{B}_1 + \cos \theta \cdot \vec{V}_1\end{aligned}$$

where  $\theta$  is the base angle of the octahedral pyramid as indicated in Figure 4.11b.

As the normals for faces II, III and IV are calculated at each step of the rotation, the traces they would make on surface A are represented by the cross products of their normals with the normal to A. These traces can be evaluated for the degree to which they are parallel to the observed trace of twin 2 by calculating the dot product, designated DP here, of their trace vectors with the vector  $\vec{T}_{A2}$ . For example, for the II face of the octahedron:

$$\vec{T}_{AII} = \vec{n}_A \times \vec{n}_{II}$$

$$DP = \vec{T}_{AII} \cdot \vec{T}_{A2}$$

and similarly for faces III and IV.

A FORTRAN program titled TRACE was written to perform the above calculations numerically. The program requires the angles  $\psi_{A1}$ ,  $\psi_{B1}$  and  $\psi_{A2}$  as input data. Then, as in the above, starting from an assumed initial orientation it determines all possible austenite lattice orientations by systematically rotating the FCC crystal an increment  $d\omega$  at a time. At each orientation it calculates the normal and trace vector components for the other three octahedral planes, writing them to a solution file if the trace vector dot product is within a specified tolerance of unity. In addition, at each step of the rotation it writes the dot product for all three faces to a file which can be plotted versus angle of rotation. This second file provides useful information on the nature of the crystallographic problem, as will be shown in the Results section. A copy of the code of the program TRACE is provided in Appendix A.1.

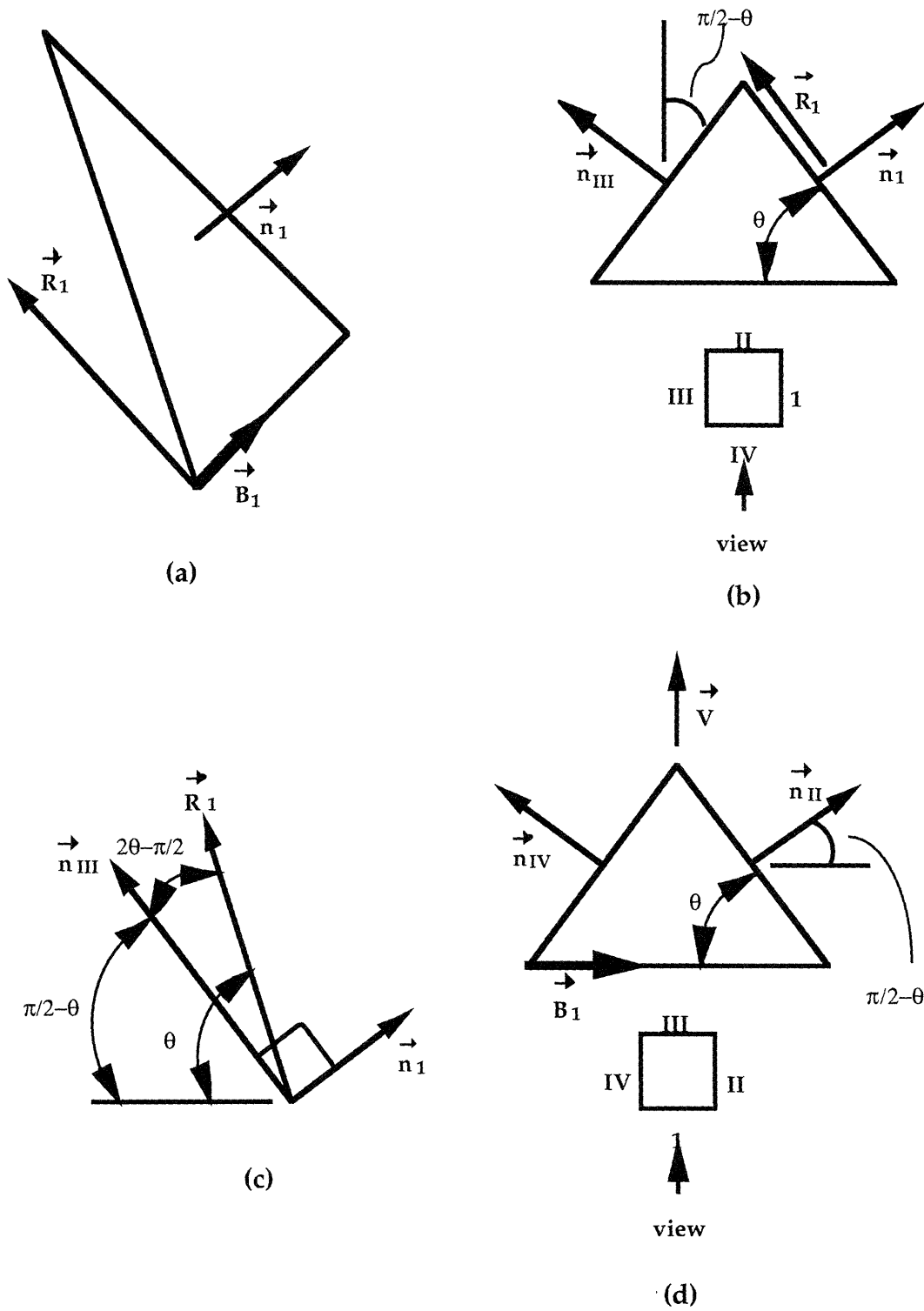


Figure 4.11 Directions of Normal Vectors of the Other Three Octahedral Planes

Orientations of the austenite, represented by rotations about the normal to face 1, for which the trace vector dot product is close to unity are possible solutions. For each of these orientations the orientation of the axis of an observed rod within the austenite crystal can be determined by calculating the 3x3 matrix representing the 3-dimensional transformation between vectors expressed in specimen coordinates (i.e.,  $\vec{n}_2$ ) and the corresponding vectors expressed in the local coordinates of the austenite crystal, depicted in Figure 4.9 (i.e.,  $\vec{m}_2$ ). This transformation has the form:

$$\vec{m}_1 = \tilde{A}\vec{n}_1$$

where the transformation matrix  $\tilde{A}$  has elements:

$$\tilde{A} = \begin{bmatrix} \lambda_1 & \mu_1 & \nu_1 \\ \lambda_2 & \mu_2 & \nu_2 \\ \lambda_3 & \mu_3 & \nu_3 \end{bmatrix}$$

Specifying the elements of  $\tilde{A}$  requires solving a set of nine simultaneous equations with nine unknowns. A linearly-independent set of such equations can be constructed by forming the cross product of each face normal with the normal to face 1, forming a basis set of three orthogonal vectors. This set in specimen coordinates is easily determined for each solution orientation determined by the TRACE program, while in the local coordinates of the austenite crystal the set is constant-valued for each of the other three octahedral planes. Figure 4.12 depicts the directions of the face normals in local austenite coordinates. (Since austenite is FCC, a cubic system, directions expressed in the local coordinate system with rational coordinates are identically expressed in Miller indicial notation.) The cross products which form the third vector in the basis sets are, for faces 1 and II:

$$\begin{vmatrix} \vec{i} & \vec{j} & \vec{k} \\ 1 & 1 & 1 \\ -1 & 1 & 1 \end{vmatrix} = (0, -2, 2) = (0, -0.7071, 0.7071)$$

and for faces 1 and III:

$$\begin{vmatrix} \vec{i} & \vec{j} & \vec{k} \\ 1 & 1 & 1 \\ -1 & -1 & 1 \end{vmatrix} = (2, -2, 0) = (0.7071, -0.7071, 0)$$

and for faces 1 and IV:

$$\begin{vmatrix} \vec{i} & \vec{j} & \vec{k} \\ 1 & 1 & 1 \\ 1 & -1 & 1 \end{vmatrix} = (2, 0, -2) = (0.7071, 0, -0.7071)$$

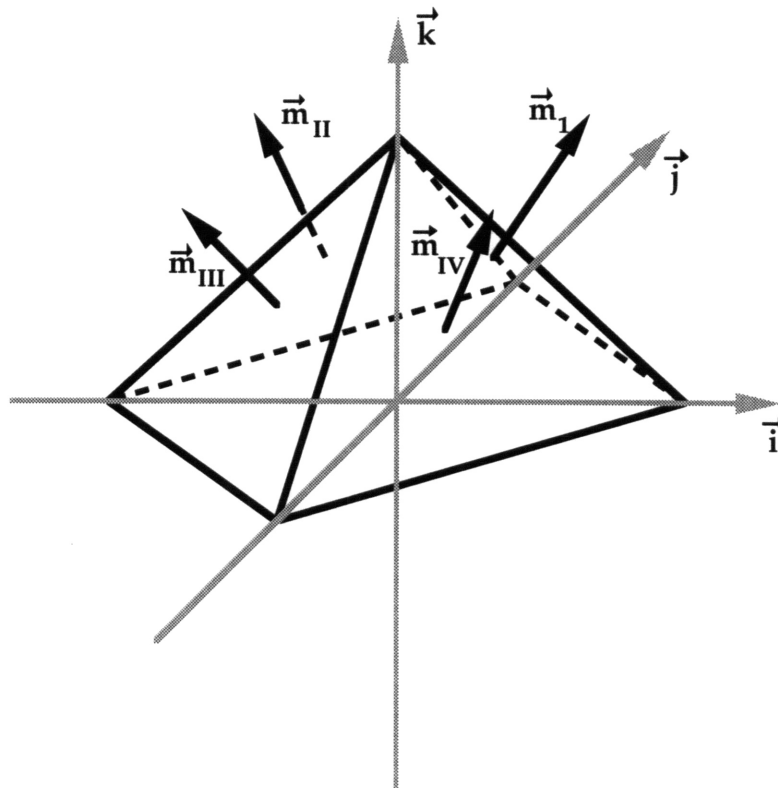


Figure 4.12 Geometry of Local/Specimen Coordinate Transformation

The equations resulting from the transformations of these known vectors yield the required nine equations. An example of the resulting equations for the case of octahedral face I is:

$$\begin{bmatrix}
 n_{11} & n_{12} & n_{13} \\
 n_{II1} & n_{II2} & n_{II3} \\
 n_{III1} & n_{III2} & n_{III3} \\
 & & & n_{11} & n_{12} & n_{13} \\
 & & & n_{II1} & n_{II2} & n_{II3} \\
 & & & n_{III1} & n_{III2} & n_{III3} \\
 & & & & & & n_{11} & n_{12} & n_{13} \\
 & & & & & & n_{II1} & n_{II2} & n_{II3} \\
 & & & & & & n_{III1} & n_{III2} & n_{III3}
 \end{bmatrix}
 \begin{bmatrix}
 \lambda_1 \\
 \mu_1 \\
 \nu_1 \\
 \lambda_2 \\
 \mu_2 \\
 \nu_2 \\
 \lambda_3 \\
 \mu_3 \\
 \nu_3
 \end{bmatrix}
 =
 \begin{bmatrix}
 m_{11} \\
 m_{III1} \\
 m_{111} \\
 m_{12} \\
 m_{II2} \\
 m_{1112} \\
 m_{13} \\
 m_{1113} \\
 m_{1113}
 \end{bmatrix}$$

In the coefficient matrix above, all terms vanish other than those shown. It is then a straight-forward matter to solve these equations by standard Gaussian reduction, yielding a column vector containing the terms of the 3x3 transformation matrix  $\tilde{A}$ . Local coordinate expressions, and thus Miller indices, of the traces of observed rods are then calculated for the given orientation by a simple multiplication of the transformation matrix times the trace vector in specimen coordinates.

A FORTRAN program titled RODS was written to perform the above calculations. The program requires as input the angles  $\xi_A$  and  $\xi_B$  between the axes of a rod on each surface and the edge intersection, measured metallographically as shown in Figure 4.8, along with the file of solution orientations output by the TRACE routine. The code calculates the Miller indices of the observed traces for each orientation and prints them to a file. A copy of the RODS code is provided in Appendix A.3.

As mentioned previously, the behavior of the other three octahedral planes as rotated through space is identical and out-of-phase by 120°. Thus more than one

of these planes can be a valid solution, and the observed trace of twin 2 could be caused by more than one octahedral plane, giving multiple possible Miller indices for the rod traces. Consideration of the consistency of the resulting solutions will reveal the true orientation, as will be demonstrated in the Results section.

#### 4.2.2.2. Experimental Procedure

A "two-one" trace analysis as described above was conducted on material containing sulfide rods from the austenitization temperature tests. Material chosen was from the 5-1-X tests which were not given a post-overheating quench and temper, so that the microstructure was closer to that which existed during precipitation of the rods. One long side of each of the CVN halves dissected for metallography was mounted in phenolic, ground to 600 grit, polished to 3  $\mu\text{m}$  and etched using Vilella's reagent.<sup>5</sup> The etched specimens were then examined visually and under the stereoscope to identify prior austenite grains with two nonparallel twin traces. Grains with suitable twins were coated with microstop, sectioned out, and cut on the abrasive saw with a diamond blade to produce a second surface intersecting one of the two twins. The specimens were fixed in the saw chuck in a manner to yield a second surface which was nominally perpendicular to the first, to correspond to the analytical development of the previous section. The second surface was then ground and polished identically to the first. The first surface was lightly repolished as needed. Finally the specimen with both polished surfaces exposed was re-etched with Vilella's reagent to reveal both twin features and rods.

The matrix within the grains surrounding the twins was then searched on the metallograph for rod traces which exhibited a high aspect ratio. The closer the lengths of etched rod traces to the lengths of rods observed on fracture surfaces, the more valid the assumption that they lay within the etch plane, and thus their orientations could be specified completely by their angles within that plane. If suitable rod traces were found, preferably on both surfaces, the specimen was included in the analysis. In the course of the metallography stage, it was

---

<sup>5</sup> As will be discussed in the Results section, this etchant was found to most clearly reveal the prior austenite grain structure from the overheating treatments.

observed that frequently annealing twins which could not be imaged on the high-magnification metallograph were clearly discernible on the stereoscope. For this reason, and to minimize measurement errors which might result from fine-scale local variations in the twin boundary trace, twin angles  $\Psi_{A1}$ ,  $\Psi_{B1}$ , and  $\Psi_{A2}$  were measured from low magnification micrographs of the etched surfaces taken on the stereoscope. Rod angles had to be measured from high magnification micrographs taken on the metallograph. The measured angle data was input to the TRACE and RODS programs, yielding for each specimen: 1) a file of solution orientations, 2) a file of dot product values vs. austenite orientation, and 3) a file of Miller indices for each rod at each orientation. The resulting indices were plotted on the stereographic triangle for evaluation of the consistency of results.



## 5.0 Results

### 5.1. Overheating Tests

Results pertaining to the first half of the research program, investigating general overheating behavior of the subject steel and consisting of fracture tests, microscopy and metallography, are presented here.

#### 5.1.1. Impact Energy

As discussed in the section on experimental procedure, impact energy was of secondary concern to fracture appearance. Some tests, however, were run on calibrated machines, and the energies recorded in those tests are summarized in Table 5.1. Among the interesting points exhibited by the data in that table are:

1. The impact energy of the 3.5NiCrMoV material which was slow-cooled at 2°C/min from 1300°C, quenched, and tempered at 590°C was exactly half that of the corresponding material which was air-quenched (41 ft-lbs vs. 82 ft-lbs, respectively).
2. Similarly, the impact energy of the 3.5NiCrMoV material which was slow-cooled at 0.5°C/min from 1280°C quenched, and tempered at 650°C was exactly half that of the same material which was alumina-quenched (63 ft-lbs vs. 127 ft-lbs).
3. The impact energy of the 3.5NiCrMoV which was tempered at 650°C was 1.5 times that of the material tempered at 590°C. This was true for both slow-cooled and quenched specimens.
4. The impact energy of the slow-cooled 3.5NiCrMoV material in the martensitic state was about 25% less than that of the air-quenched martensitic 3.5NiCrMoV (17 ft-lbs vs. 23 ft-lbs).
5. The A 508 Cl 4 superclean material was over 2.5 times tougher than the commercial purity A 508 after slow-cooling from 1300 at 2 (152 ft-lbs vs. 59 ft-lbs).

Table 5.1 Impact Energies for All Valid Charpy V-Notch Tests

	Specimen	Material	Heat Treatment			Impact Energy	
			Temp. (deg C)	Cool. Rate (C/min)	QT (Y/N)	Each (ft-lbs)	Average (ft-lbs)
C R	6-3-3	3.5Ni	1280	AL	Y	131	
	6-3-4					122	127
	6-4-2	3.5Ni	1280	0.5	Y	56	
	6-4-3					70	63
A U S T .	3-1-1	3.5Ni	1300	2	Y	39	
	3-1-2			2		42	41
	3-1-3			A		78	
	3-1-4			A		86	82
	3-1-5		NA	NA	N	60	
	3-1-6					52	56
M A R T E N S .	5-1-S1	3.5Ni	1300	2	N	16	
	5-1-S2					15	
	5-1-1					20	
	5-1-2					17	
	5-1-3					17	
	5-1-4					17	17
	6-5-1		1300	A		21	
	6-5-2					27	
	6-5-3					22	23
C R	F-A-1	508	1300	2	Y	158	158
	F-A-2					146	146
	F-B-1					59	
	F-B-2			1		69	64

## 5.1.2. Microscopy and Metallography

Results from the microscopy examinations and metallography, consisting of representative micrographs, are presented here, and their salient features discussed. The last line of the micrograph captions provides a summary of the vital statistics: specimen number, heat treatment condition (AR - as-received, QT - quenched and tempered, otherwise soak temperature and cooling rate), camera or microscope, and magnification if not indicated on the specimen.

### 5.1.2.1. Optical and SEM Fractography

Results of optical and SEM microscopy techniques, both concerned with the three dimensional morphology of the fracture, will be addressed in this section. Results for the cooling-rate series of tests on 3.5NiCrMoV material are presented first.

#### 3.5NiCrMoV Cooling Rate Tests

As described previously, one of the classical indications of overheating is the development of flat, matte facets on the fracture surface. Under low magnification optical examination, what appeared to be facets were visible on the fracture surfaces for many of the specimens, including those of the control materials, although they were never predominant. Under SEM examination, however, distinct differences in the fracture and precipitate morphologies were apparent.

Facets were observed on the control material from the cooling rate tests, which was not overheated but was quenched and tempered. However sometimes they were flat like a classical facet while other times they were significantly distorted. Figure 5.1 shows a 1 mm facet on the fracture surface of control material (specimen 1-1-3). Figure 5.2 is a higher magnification micrograph of the facet surface, clearly showing the fine, regular 3-4  $\mu\text{m}$  ductile dimples nucleated on 1  $\mu\text{m}$  and smaller inclusions which are characteristic of an overheated condition. Facets with similar and smaller dimples and inclusions were repeatedly observed on surfaces of the control material. Meanwhile Figure 5.3 is an optical fractograph of the highly distorted facets on the surface of other control material

with identical treatment (specimen 1-1-2). Figure 5.4 is an SEM micrograph of the same feature as in Figure 5.3. The same fine precipitates as on the flat facet of figures 5.1 and 5.2 are observable in the higher magnification micrograph of the distorted facets in Figure 5.5.

Large facets which obviously corresponded to prior austenite grain boundaries were observed on the surfaces of the 3.5NiCrMoV material quenched in alumina, as seen in Figure 5.6. The PAGB triple point is obvious in the lower left portion of the figure. Unlike the facets observed on the control material surfaces, however, the dimple-like features on these facets were coarser (10-20  $\mu\text{m}$ ) and were usually free of corresponding inclusions, as seen in Figure 5.7. The fracture surrounding the facets was very rough and fibrous, typical of a tough, ductile, intragranular failure, as shown in Figure 5.8.

A facet which includes a grain boundary edge is visible on material control-cooled at 10°C/min from preheating (specimen 1-4-2), as shown in Figure 5.9. Figure 5.10 is a higher magnification micrograph, again showing the characteristic fine dimples and precipitates. Here the average dimple and inclusion size is about 4 and 0.5-1  $\mu\text{m}$ , respectively. Like the facet in Figure 5.1, the grain boundary edge depicted in Figure 5.9 is about 1 mm long. Also evident on this same material (specimen 1-4-2) are numerous microfacets, such as those reported by Andrew, et. al. [2], seen to the left side of Figure 5.11. (Figure 2.16 reproduced a micrograph from reference 2 illustrating such features.) These were not found on the surfaces of the control material, and thus are products of the overheating treatment.

A facet which is also clearly an opened prior austenite grain boundary was visible on the surface of material cooled somewhat slower (5°C/min, specimen 1-2-2) as shown in Figure 5.12. The grain boundary edges and triple point are obvious. The dimples and sulfides are in general larger than on the more rapidly cooled material (10  $\mu\text{m}$  dimples, 1.5-2  $\mu\text{m}$  sulfides). Figure 5.13, a higher magnification micrograph of the facet surface, shows a different feature however: two rod-shaped sulfides with aspect ratios of approximately 10:1. Figure 5.14, a closer view of one, shows that it has fractured in several places and is split down the axis. EDS was performed on this inclusion to confirm that it was indeed manganese sulfide. The resulting spectrum is shown in Figure 5.15. Material

from other tests cooled at the same rate (specimen 1-2-4) also displayed larger dimple/sulfides and random small rods. Other interesting features evident on the surfaces of 5°C/min material were the sulfide "rafts" shown in Figure 5.16 (specimen 1-2-4). The figure shows the large "super dimples" formed around these inclusion structures during fracture. Their detailed appearance is seen to be dendritic in Figure 5.17.

Figure 5.18 shows a large facet from material cooled at a still slower rate of 1°C/min (specimen 1-3-1). Closer inspection of the facet surface revealed that it was free of the usual round dimples nucleated at spherical sulfides, such as the classical precipitates found on the control material. Rather, it exhibited a low-ductility morphology similar to quasi-cleavage, as shown in Figure 5.19. The large size of the facet (1.5 mm) indicates that it also is probably related to an austenite grain formed in the long final heat during the forging process. The rough and irregular fracture surface about the facet is seen to contain numerous elongated dimples nucleated on very high-aspect ratio (50:1) rods. These apparently are the rod morphologies reported by Hale, Preston and Nutting [11]. Figures 5.20 and 5.21 are higher magnification micrographs of these rods, which display numerous fractures along their length. Figure 5.22 depicts a similar facet from material also cooled at this rate (specimen 1-3-4). Higher magnification, shown in Figure 5.23, reveals that its surface exhibits even less ductile deformation than the previous facet. Surrounding this facet are again the same elongated dimples and inclusion rods, shown in Figure 5.24. Most significantly, the rods/dimples are clearly seen in Figure 5.24 to be aligned in a regular crossweave-type pattern, particularly in the central portion of the figure, in which the dimples are all arranged parallel or at right angles to each other.

Finally, Figure 5.25 depicts a fracture surface from material cooled at the slowest rate of 0.5°C/min (specimen 6-4-4). This surface, as with that of all the material cooled at this rate, was covered with the same "basket weave" pattern of elongated dimples containing sulfide rods. A high-magnification micrograph of a clean cleavage fracture in one rod is shown in Figure 5.26. In contrast to the more rapidly cooled material, no low-ductility PAGB facets were observed on any of the material cooled at this rate.

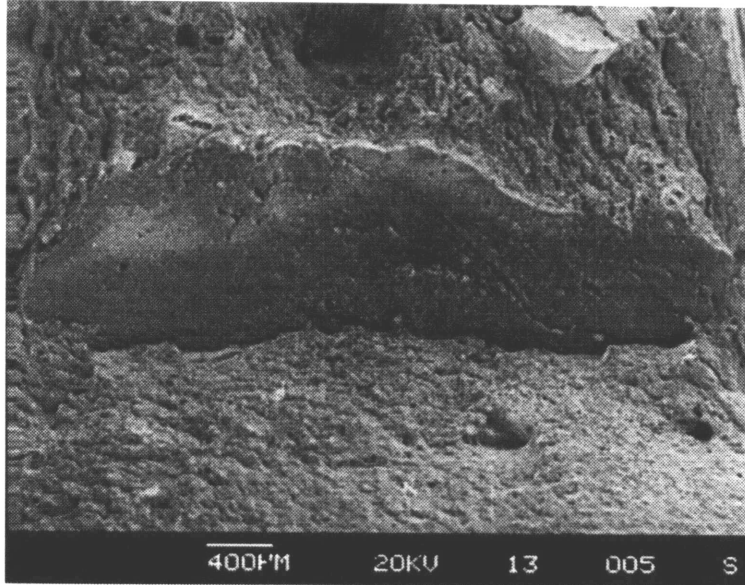


Figure 5.1 Flat Facet on As-Received Control Material  
Spec. 1-1-3, AR, SEM

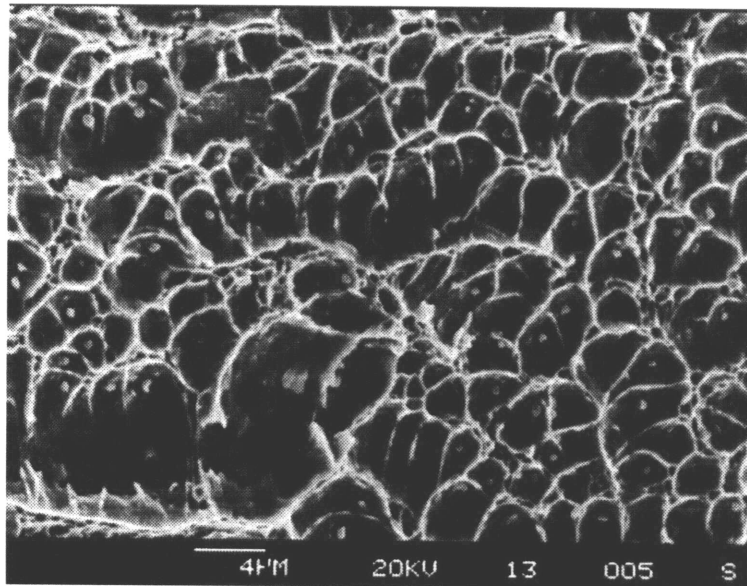


Figure 5.2 Higher Magnification of Dimples and Sulfides on Facet in Figure  
5.1  
Spec. 1-1-3, AR, SEM



Figure 5.3 Optical Micrograph of Distorted Facets on As-Received Control Material  
Spec. 1-1-2, AR, Optical Fractograph, 20X

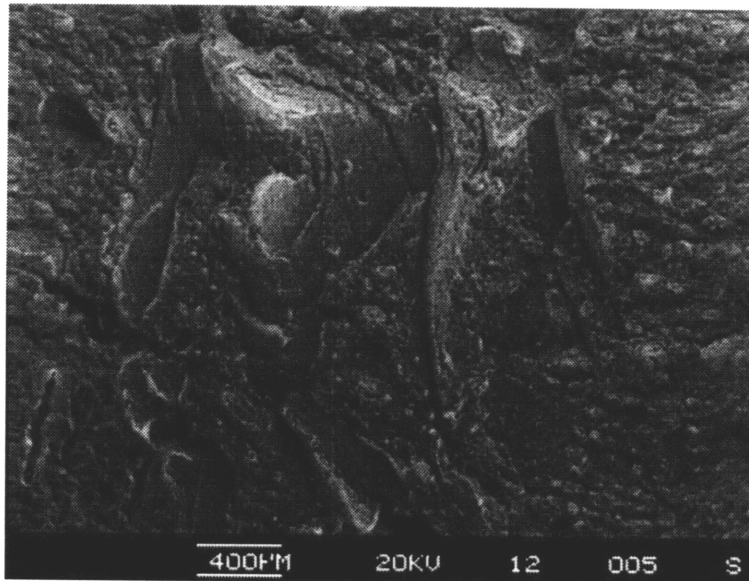


Figure 5.4 SEM Micrograph of Distorted Facets in Figure 5.3  
Spec. 1-1-2, AR, SEM

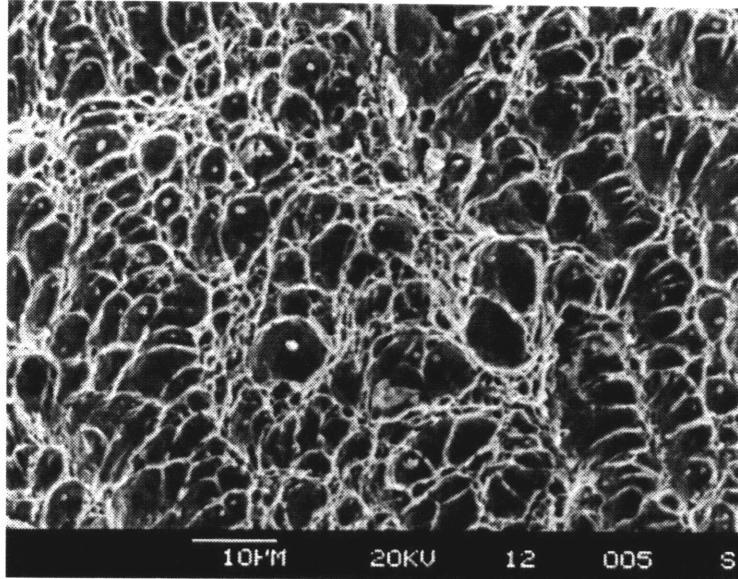


Figure 5.5 Higher Magnification Micrograph of Distorted Facets in Figure 5.3  
Spec. 1-1-2, AR, SEM

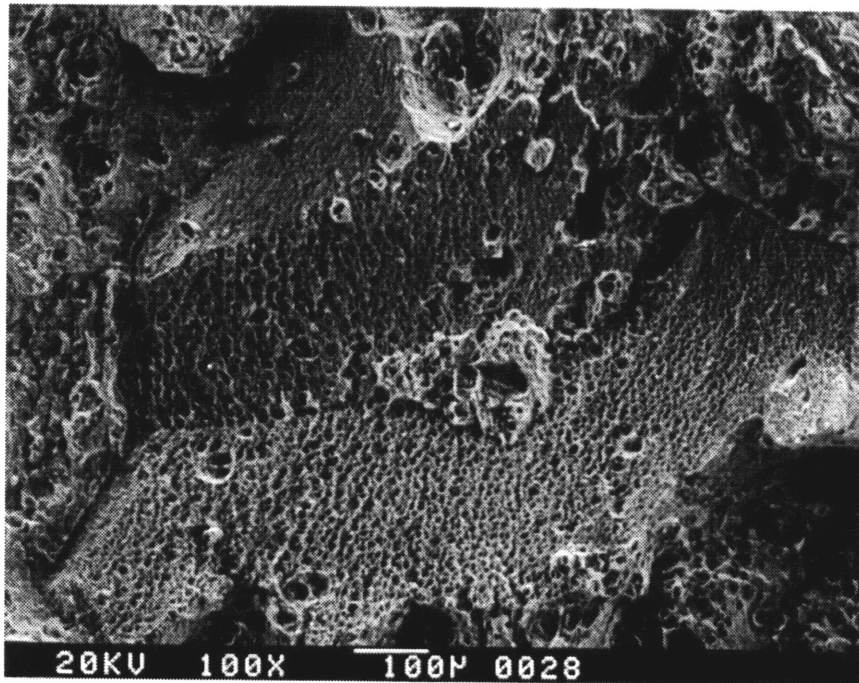


Figure 5.6 Large PAGB Facet on Fracture Surface of Alumina-Quenched  
Material  
Spec. 6-4-1, 1280°C, Alum-Quench, SEM



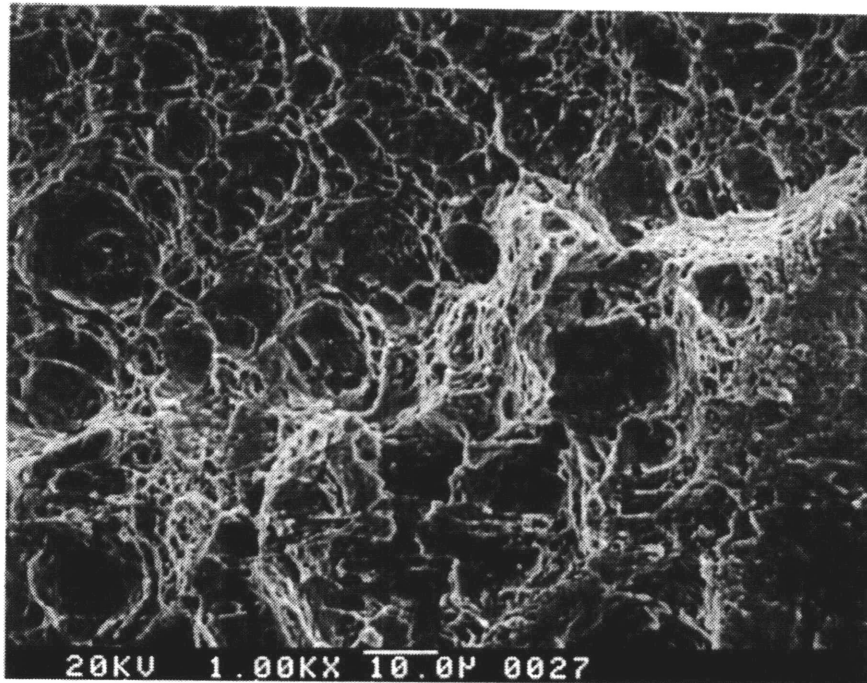


Figure 5.7 Inclusion-Free Dimples on Facet in Figure 5.6  
Spec. 6-4-1, 1280°C, Alum-Quench, SEM

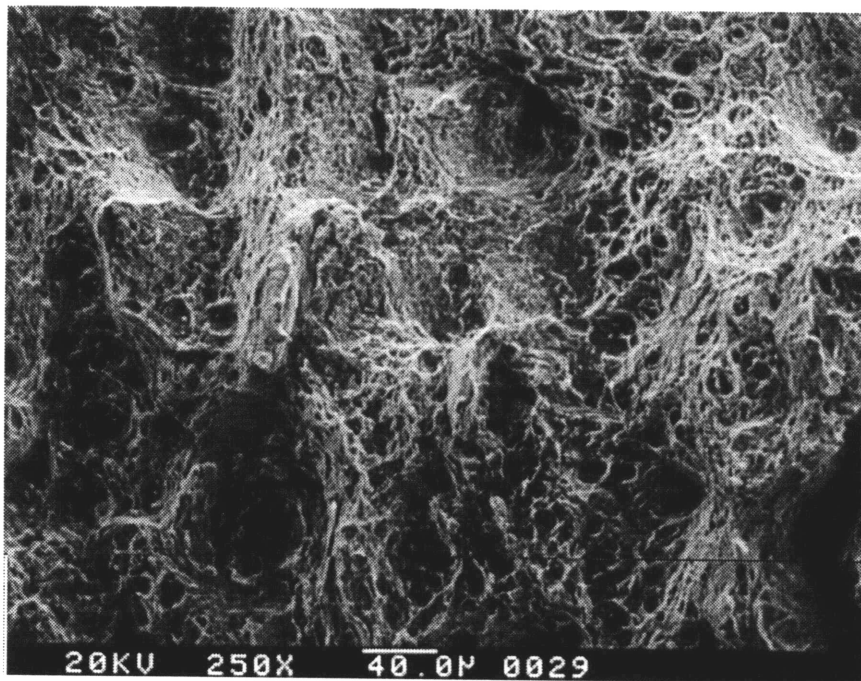


Figure 5.8 Fracture Surface Surrounding Facet of Figure 5.6, Typical of Tough,  
Ductile, Intragranular Failure  
Spec. 6-4-1, 1280°C, Alum-Quench, SEM

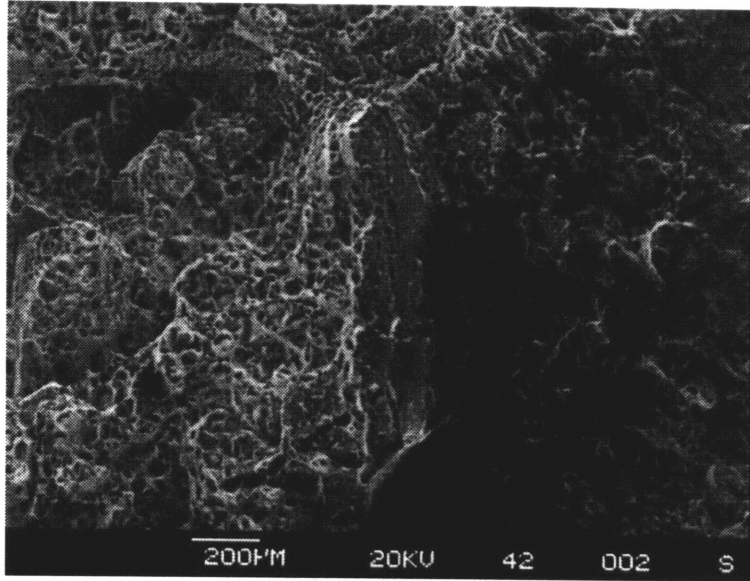


Figure 5.9 Elevated Facet Containing a Prior Austenite Grain Boundary Edge in a 10°C/min Control-Cooled Material  
Spec. 1-4-2, 1280°C, 10°C/min, SEM

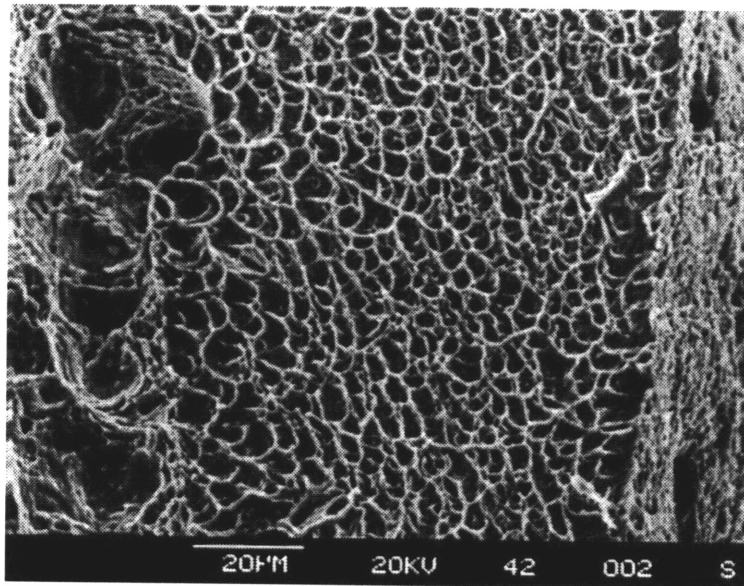


Figure 5.10 Higher Magnification Micrograph of Inclusions and Dimples on Facet of Figure 5.9  
Spec. 1-4-2, 1280°C, 10°C/min, SEM

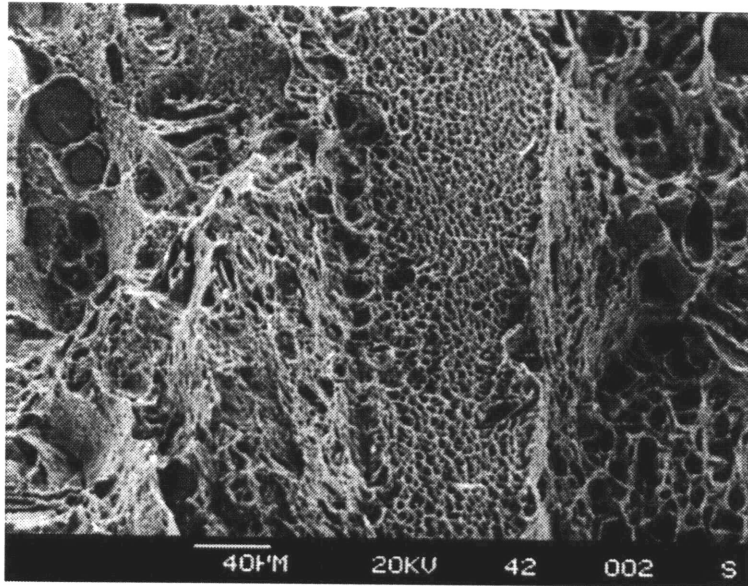


Figure 5.11 Microfacets Adjacent to Edge Facet of Figure 5.9  
Spec. 1-4-2, 1280°C, 10°C/min, SEM

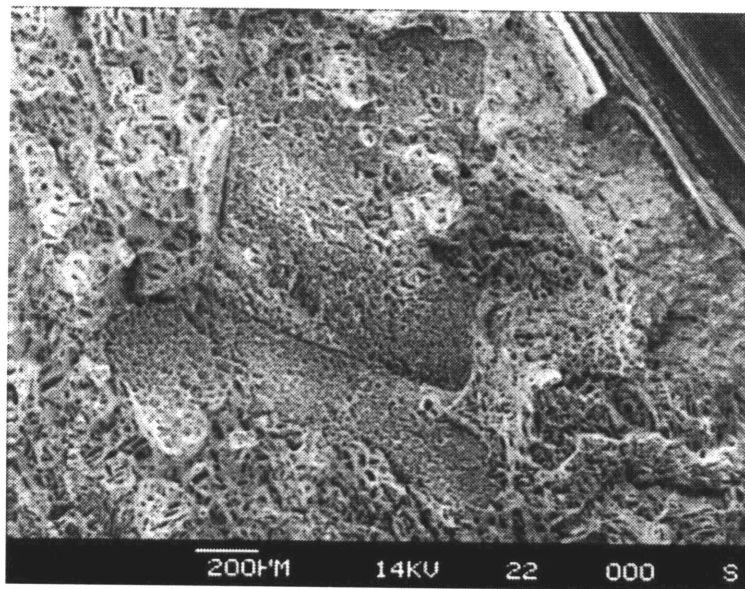


Figure 5.12 Opened Grain Boundary Triple Point on Surface of 5°C/min  
Control-Cooled Material  
Spec. 1-2-2, 1290°C, 5°C/min, SEM

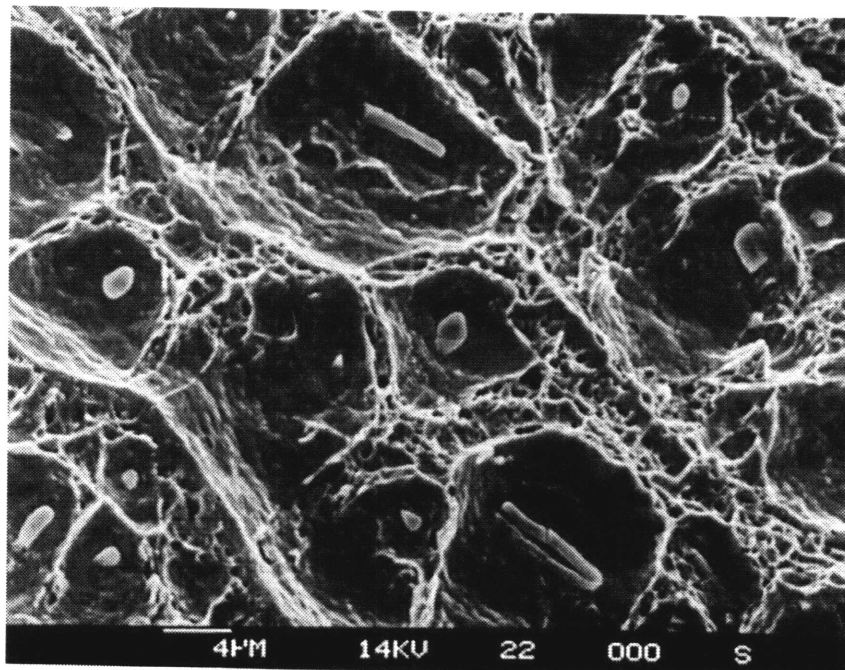


Figure 5.13 Higher Magnification Micrograph of Inclusions and Dimples on Facet of Figure 5.12  
Spec. 1-2-2, 1290°C, 5°C/min, SEM

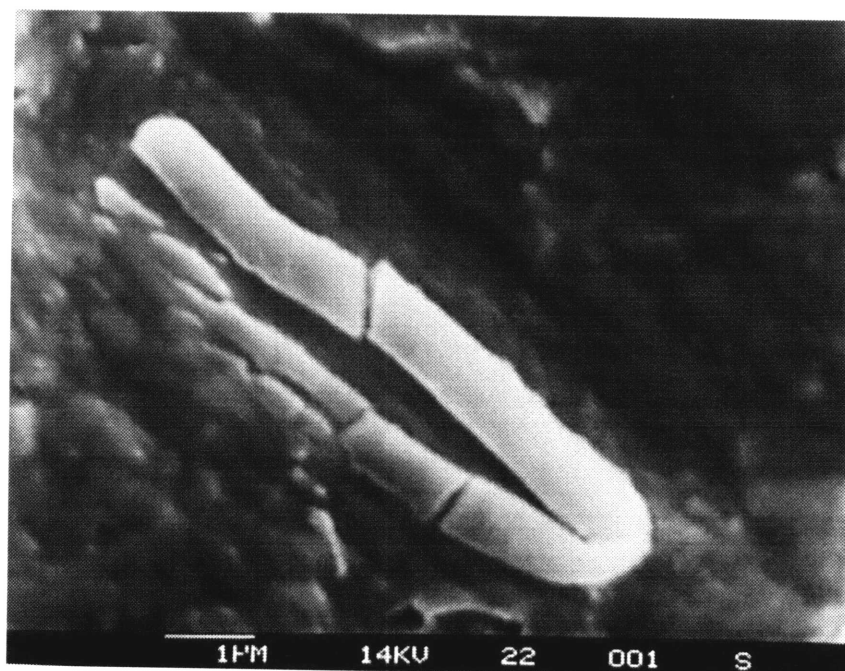


Figure 5.14 Higher Magnification Micrograph of Split Rod Precipitate in Figure 5.13  
Spec. 1-2-2, 1290°C, 5°C/min, SEM

TN-5500  
Cursor 10.230keV = 7

THU 14-OCT-93 15:37

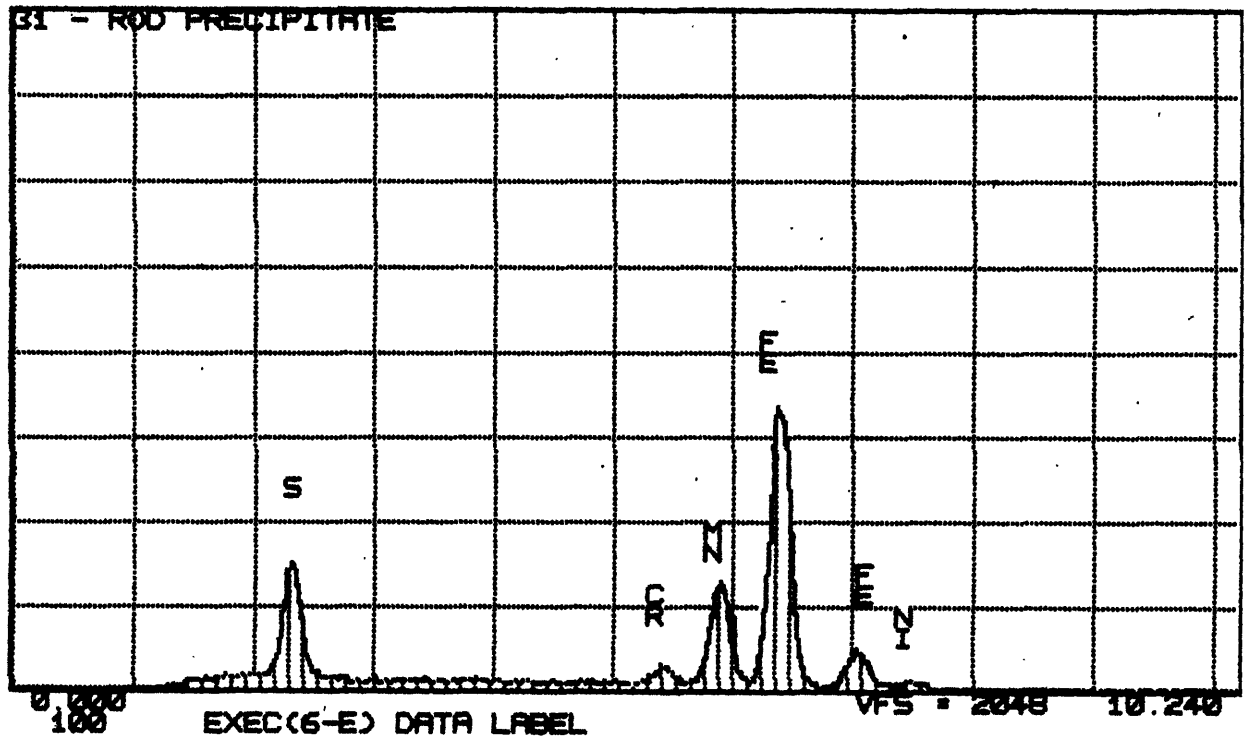


Figure 5.15 EDS Spectrum of Rod Precipitate in Figure 5.21

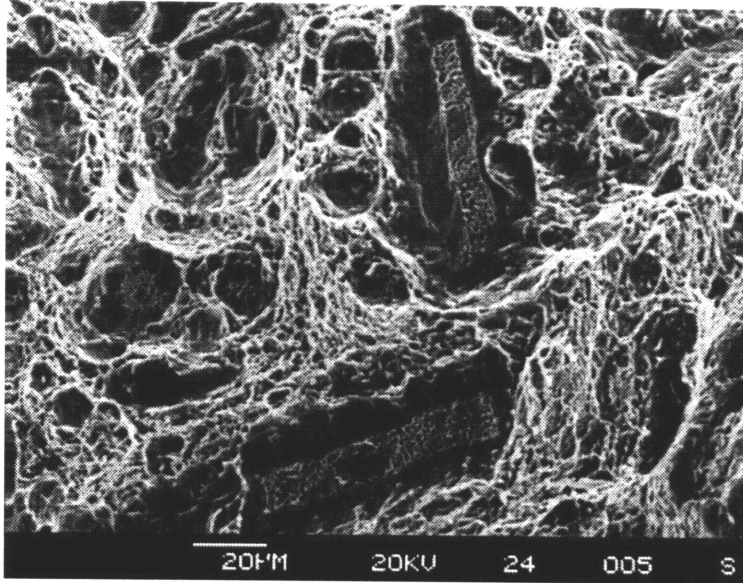


Figure 5.16 Sulfide "Rafts" Developed on 5°C/min Control-Cooled Material  
Spec. 1-2-4, 1290°C, 5°C/min, SEM

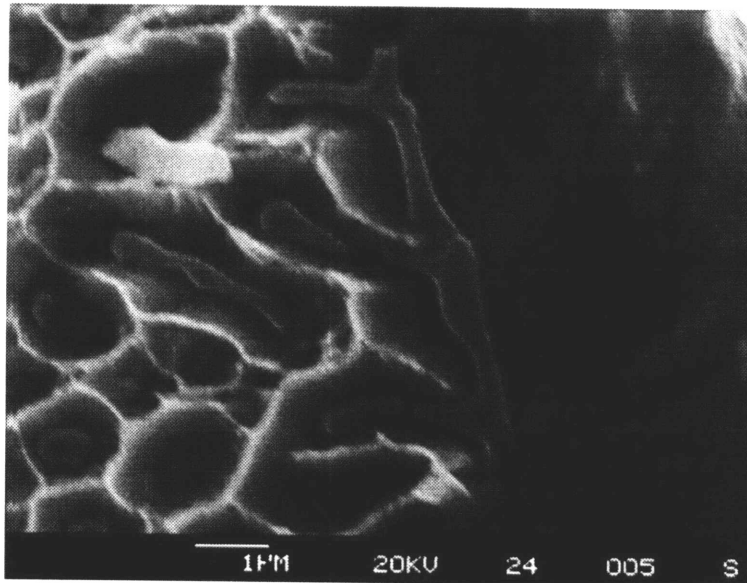


Figure 5.17 Fine Dendritic Structure of Sulfide Rafts in Figure 5.16  
Spec. 1-2-4, 1290°C, 5°C/min, SEM



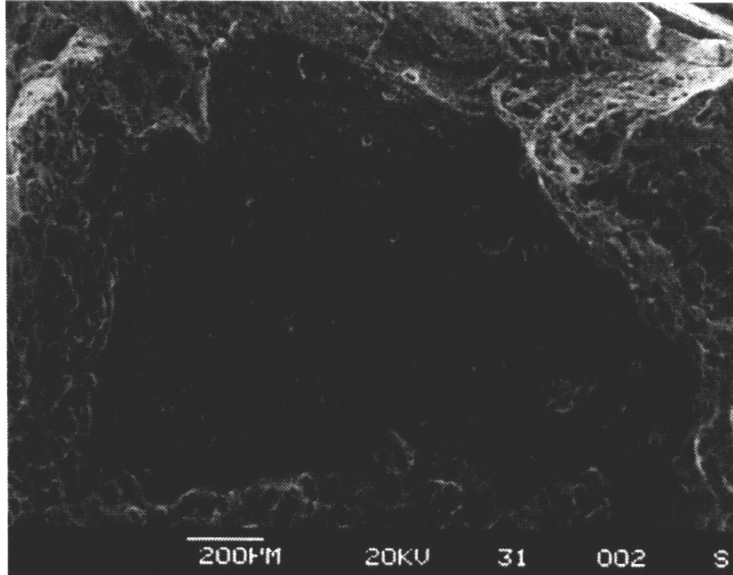


Figure 5.18 Large Low-Ductility Facet on Surface of 1°C/min Control-Cooled Material  
Spec. 1-3-1, 1300°C, 1°C/min, SEM

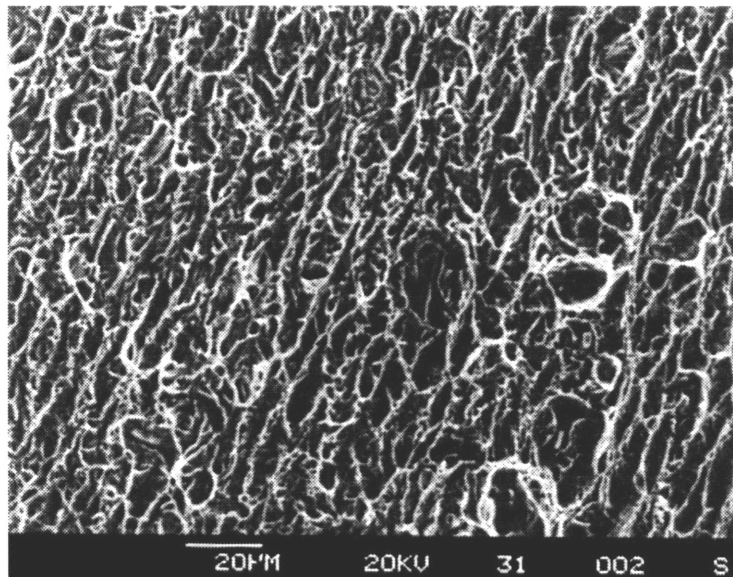


Figure 5.19 Higher Magnification View Showing Low-Ductility Nature of Surface of Large Facet in Figure 5.18  
Spec. 1-3-1, 1300°C, 1°C/min, SEM

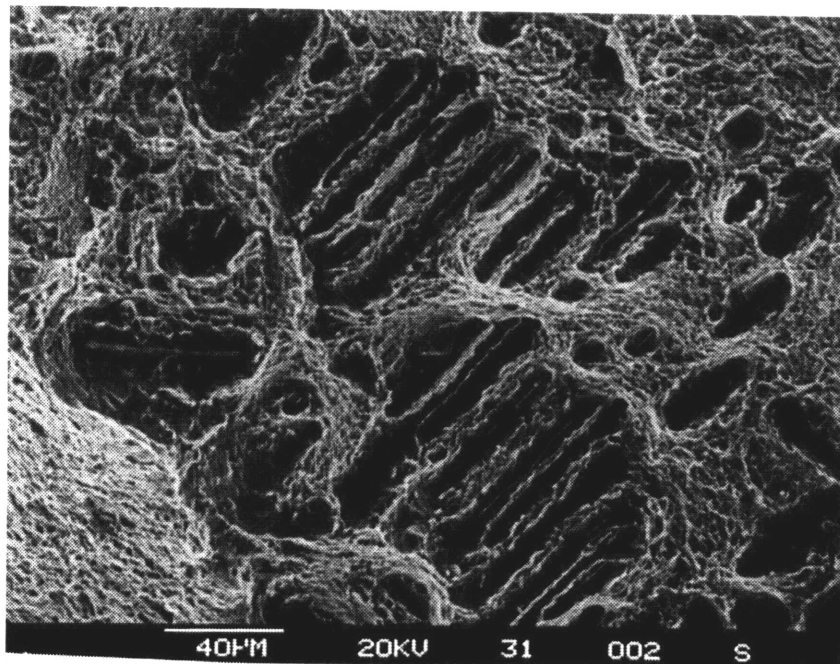


Figure 5.20 Elongated Dimples and High-Aspect Ratio Sulfide Rods Surrounding Large Facet in Figure 5.18  
Spec. 1-3-1, 1300°C, 1°C/min, SEM

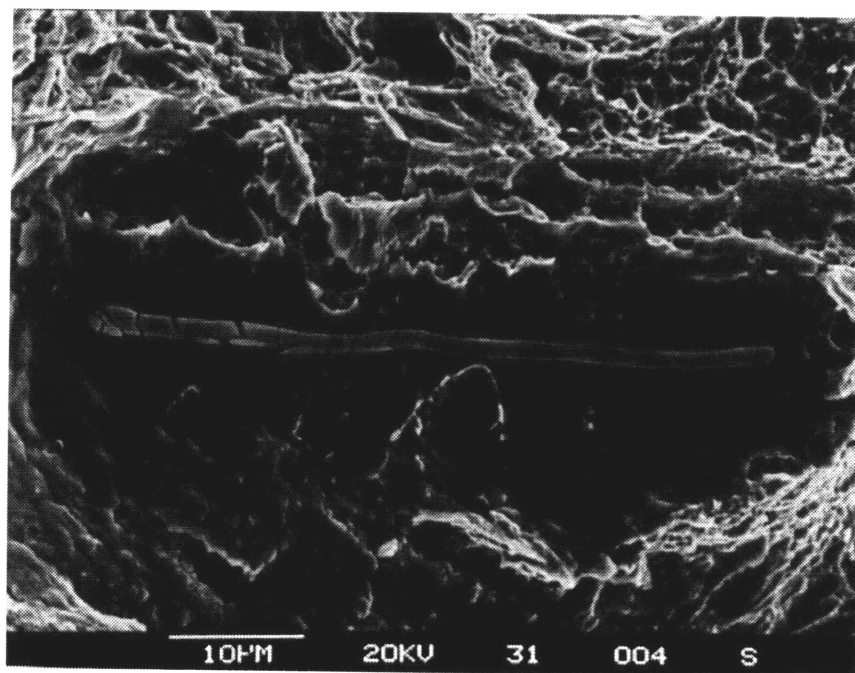


Figure 5.21 Typical High-Aspect Ratio Sulfide Rod From Region About Large Facet in Figure 5.18  
Spec. 1-3-1, 1300°C, 1°C/min, SEM



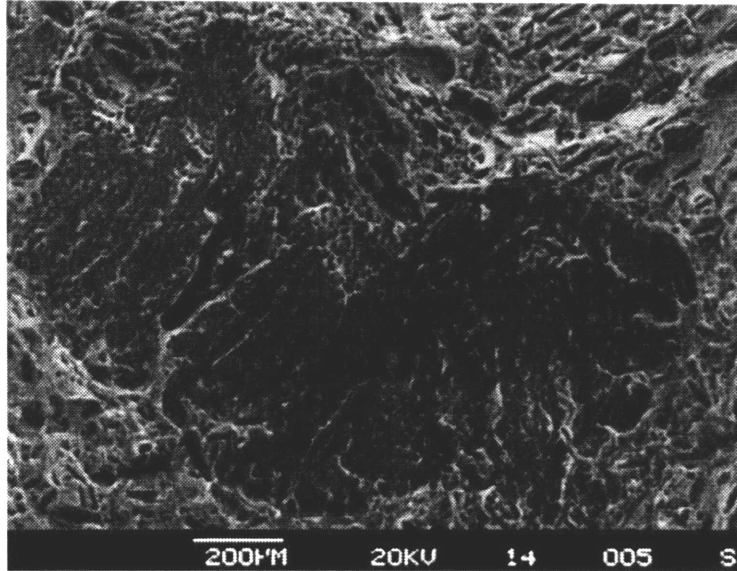


Figure 5.22 Large Facet on Surface of 1°C/min Control-Cooled Material  
Spec. 1-3-4, 1300°C, 1°C/min, SEM

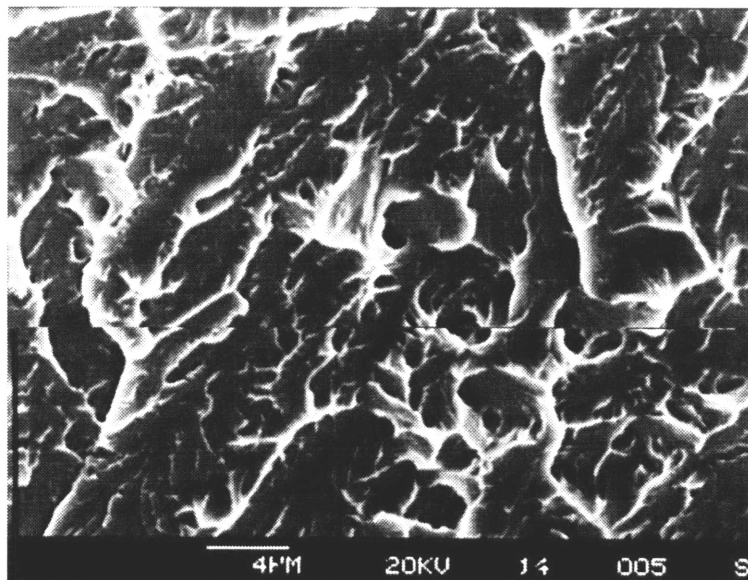


Figure 5.23 Higher Magnification Micrograph Of Low-Ductility Nature of  
Large Facet in Figure 5.22  
Spec. 1-3-4, 1300°C, 1°C/min, SEM

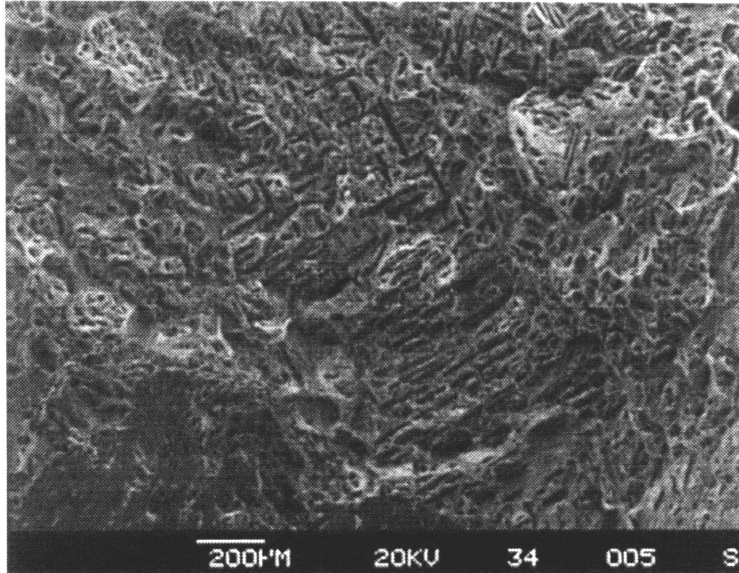


Figure 5.24 Long Sulfide Rods and Dimples in "Basket-Weave" Distribution About Large Facet in Figure 5.18  
Spec. 1-3-1, 1300°C, 1°C/min, SEM

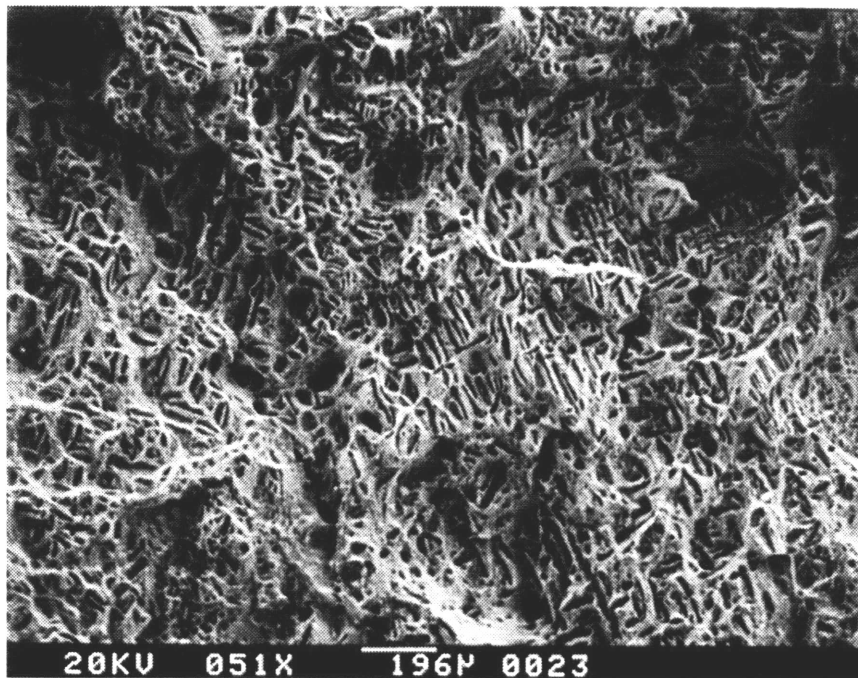


Figure 5.25 "Basket-Weave" Pattern of Sulfide Rods on Fracture Surface of Material Cooled at Slowest Rate of 0.5°C/min  
Spec. 6-4-4, 1300°C, 0.5°C/min, SEM

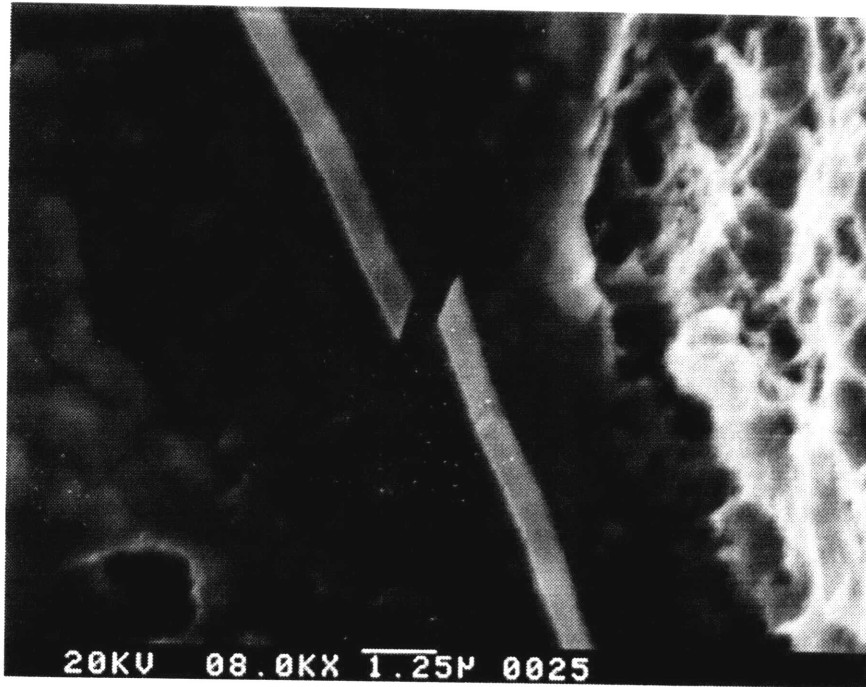


Figure 5.26 High-Magnification Micrograph of Clean Cleavage Fracture in Sulfide Rod  
Spec. 6-4-4, 1300°C, 0.5°C/min, SEM

### 3.5NiCrMoV Austenitization Temperature Tests

Results from the austenitization temperature tests will be presented now. In this series of tests, fracture surfaces of control material which was tested in the as-received (AR) condition appeared quite shiny under the optical stereoscope, in contrast to the duller appearing quenched and tempered (QT) material. This is evident in Figure 5.27, a low-magnification photograph of the specimen surfaces taken with a stage camera. Scanning electron microscopy revealed that both AR and QT controls also had large (about mm) facets with the same fine dimples and sulfides as on quenched and tempered controls in the cooling-rate tests. An example of this type of large facet on the surface of the AR material is shown in Figure 5.28. However in the AR controls the surrounding typical fracture had a quasi-cleavage appearance, while in the QT controls it appeared very fibrous and ductile. Figure 5.29 is a micrograph of the AR material surface, while Figure 5.30 is a micrograph of the QT material.

On the material control-cooled from the lowest preheating temperature (4-1-X, 1200°C), large PAGB facets were again observed, as illustrated in Figure 5.31. However, scattered among the usual fine spherical MnS inclusions were very small embryonic rods of aspect ratio about 2:1. Figure 5.32 is a micrograph which shows several such rods. As with the fully-developed rods, observed in the cooling-rate tests, the embryo axes were aligned with each other in all cases observed. In contrast, by the next preheating temperature evaluated, 1250°C, control-cooled material surfaces were characterized by extensive regions of transgranular fracture, densely populated by long dimples and rods, in the same aligned basket-weave pattern as observed on the material in slowest of the cooling rate tests. These are illustrated in Figures 5.33 and 5.34. Frequently subregions existed on the surface within which all rods were arranged either parallel or at right angles to each other. These regions were very rough and irregular, indicating transgranular fracture, in contrast to the flat PAGB facets on earlier overheated material. In addition, large, flat PAGB facets appeared on the material control-cooled from a preheating temperature of 1250°C, however they were now free of ductile dimples or sulfides, similar to those observed in the cooling rate tests.

Transgranular aligned rods and low-ductility PAGB facets continued to be prevalent on 1300°C-preheat control-cooled material, as shown in Figure 5.35. A particularly interesting example is shown in Figure 5.36, in which a rod is seen to "turn a corner", changing from one direction to another. That this shape preceded the fracture process is indicated by the matching shape of the surrounding dimple. Further, the two directions of this angled rod match the directions of surrounding straight rods. Also at preheating temperatures of 1300°C, rod precipitates in the rough, transgranular fracture were interspersed with numerous microfacets, illustrated in Figure 5.37, which were not present at lower temperature.

Fracture surface features on material preheated at 1350°C and control-cooled were similar to those at 1300°C, characterized by: 1) intragranular aligned rods, 2) large, low-ductility, precipitate-free PAGB facets, and 3) intragranular microfacets. Figure 5.38 provides a good composite view of these features. The horizontal rift in the center of the facet is likely a perpendicular twin boundary, opened partially during the fracture process. Figure 5.39 provides a high magnification view of a microfacet. The fine structure of the precipitation resembles a fractal image, with similarly-shaped yet smaller and denser islands of precipitates scattered throughout the overall microfacet.

The 1400°C overheating treatment was of questionable success. Qualitatively, material from these tests exhibited the lowest impact energy of any of the heat treatments. However it is possible that this was due to a phenomenon other than overheating. The fracture surfaces were dominated by large PAGB facets, whose fine structure was unusual, appearing unlike either ductile dimples or quasi-cleavage, resembling the surface of a sponge in appearance. This is shown in Figure 5.40. It is well known that early investigations of overheating were hampered by confusion with the more severe "burning" in which actual melting of the austenite grain boundary occurs [10]. This is generally attributed to the segregation of sulfur, phosphorus and carbon to the grain boundary, and usually occurs at preheating temperatures above 1400°C. Thus it is possible that the behavior of this material is characteristic of burning rather than overheating. An additional influence may be due to formation on the material of an unanticipated iron oxide which melts at 1371°C [64]. The oxide flowed off the specimens while in the furnace and attacked the ceramic hearthplate. The resulting reduction

reaction may have contributed to material degradation of the steel as well. When the molten oxide was observed, furnace power was shut off, so that the actual cooling rate experienced was 10°C/min, rather than the 2°C/min planned. The possibility of burning is discussed more in the section on optical metallography.

None of the unconventional precipitation phenomena described above (i.e., inter- or transgranular rods, rafts, low-ductility facets or microfacets) were observed on the air-cooled material. PAGB facets were observed on material throughout the preheating temperature range 1200-1300°C. However in the lower temperature range these were covered with very fine dimples correlated almost one-to-one with fine inclusions, illustrated in Figure 5.41, while at the higher temperature range they were covered with dimples which commonly lacked a nucleating sulfide, illustrated in Figures 5.42 and 5.43. Outside of the PAGB facets, the fracture surface exhibited a fibrous morphology typical of a normal, tough steel, which is shown in Figure 5.44.

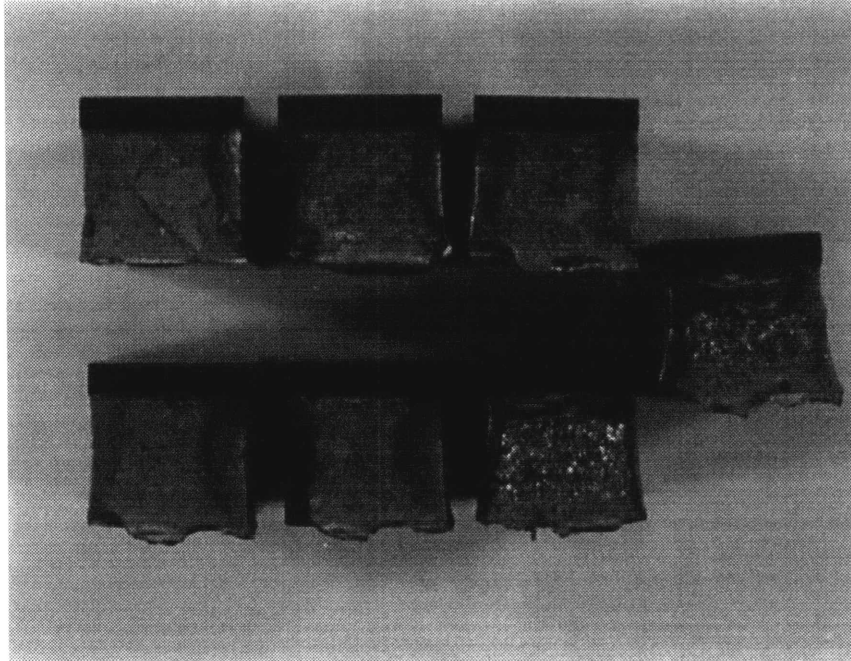


Figure 5.27 Shiny and Dull Fracture Surfaces of As-Received and Quenched and Tempered Material, Respectively  
Specs. 4-5-X, AR and AR+QT, MP-4 Stage Camera

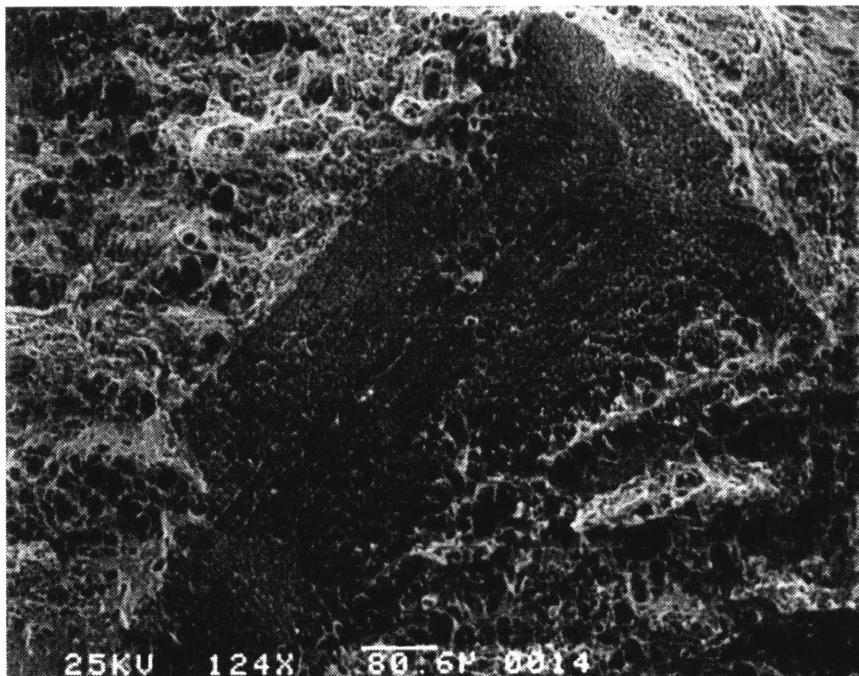


Figure 5.28 Large Facet With Fine Dimples and Sulfides on Austenitization Temperature Test As-Received Material  
Spec. 3-1-5, AR, SEM



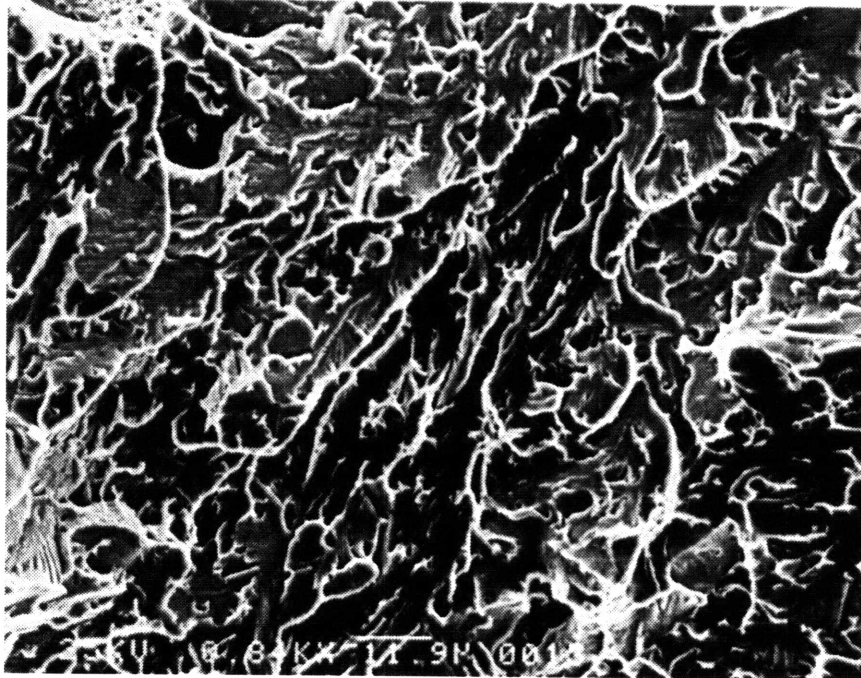


Figure 5.29 Typical Fracture Surrounding Large Facets on Austenitization Temperature Test As-Received Material  
Spec. 3-1-5, AR, SEM

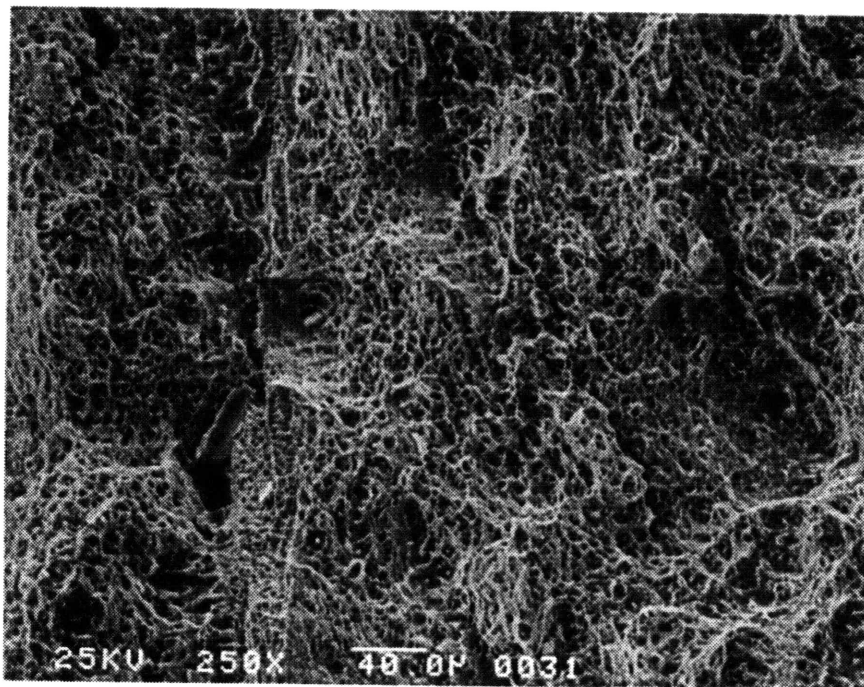


Figure 5.30 Typical Fracture Surface of Austenitization Temperature Test Quenched and Tempered Material  
Spec. 3-1-5, AR, SEM



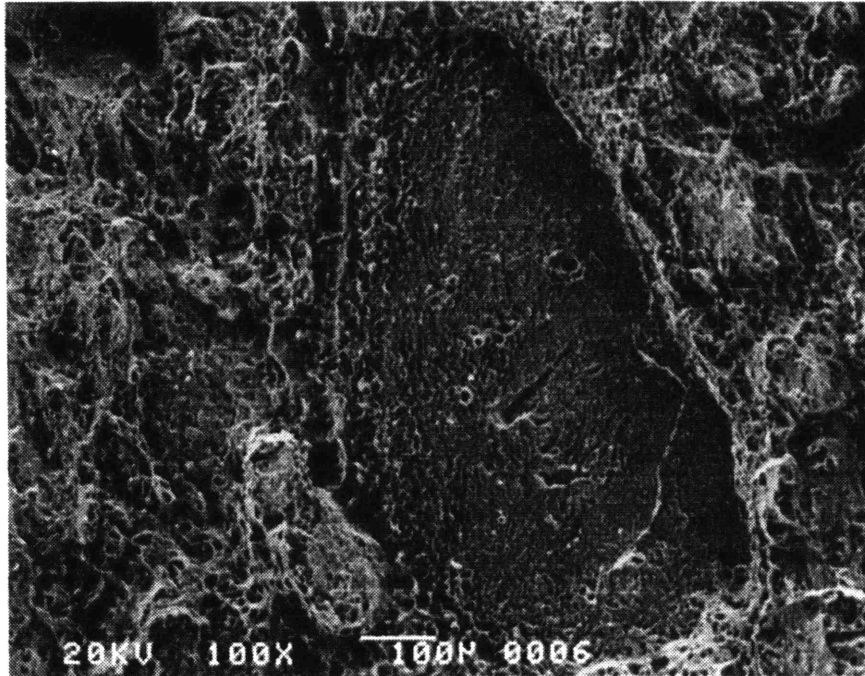


Figure 5.31 Large PAGB Facet on 1200°C Control-Cooled Material  
Spec. 4-1-3, 1200°C, 2°C/min, SEM

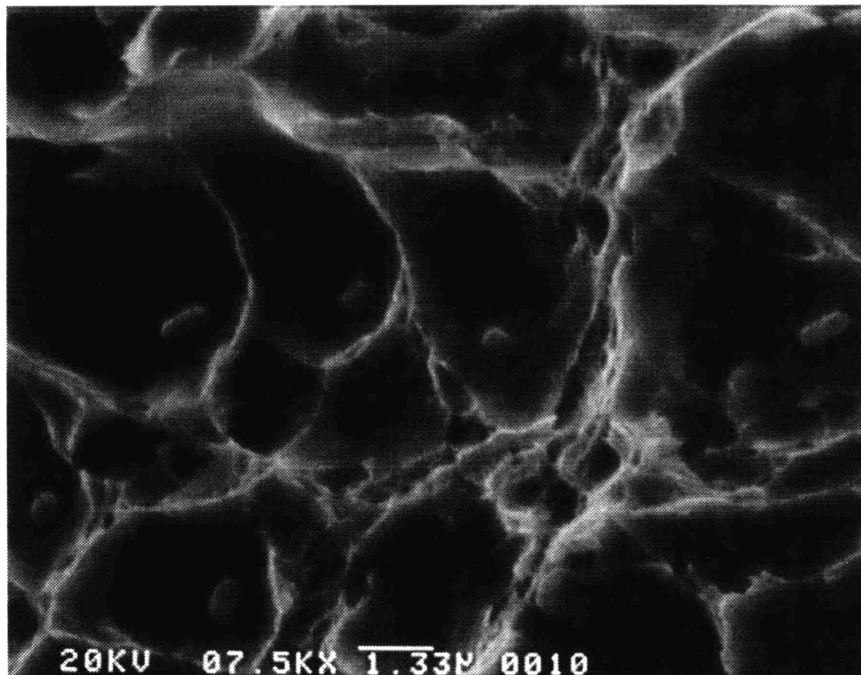


Figure 5.32 Higher Magnification Micrograph of Aligned Embryonic Rod  
Sulfides on PAGB Facet in Figure 5.31  
Spec. 4-1-3, 1200°C, 2°C/min, SEM

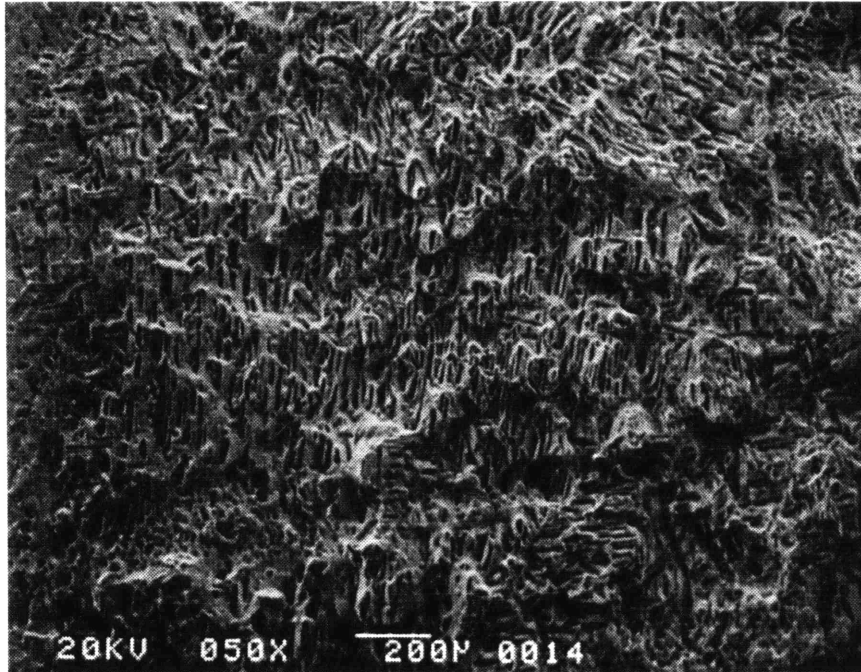


Figure 5.33 Dense Region of High-Aspect Ratio Dimples and Rods, Aligned Within Subregions, on 1250°C- Control-Cooled Material  
Spec. 4-2-1, 1250°C, 2°C/min, SEM

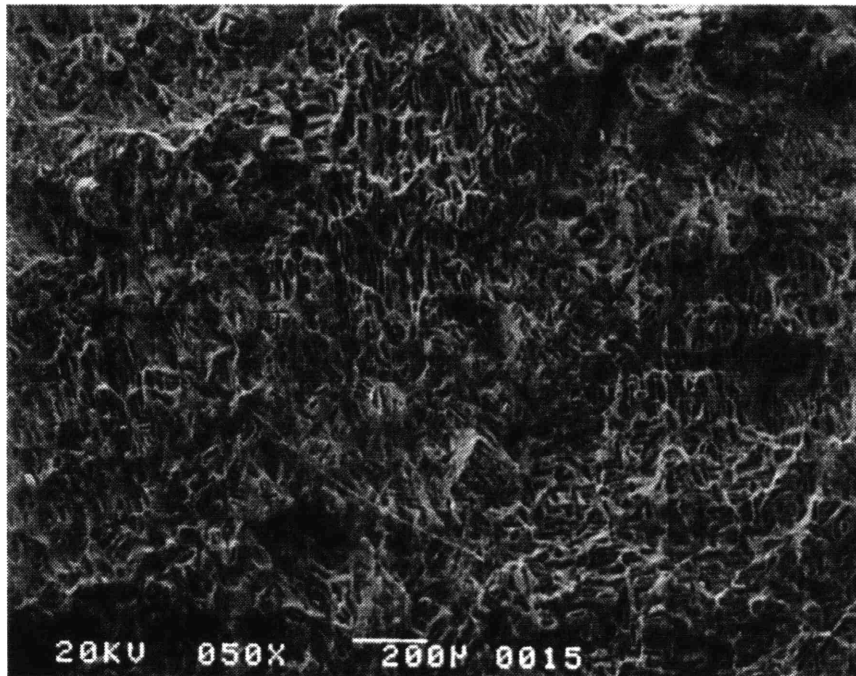


Figure 5.34 More Aligned High-Aspect Ratio Dimples and Rods on Additional 1250°C Material  
Spec. 4-2-2, 1250°C, 2°C/min, SEM

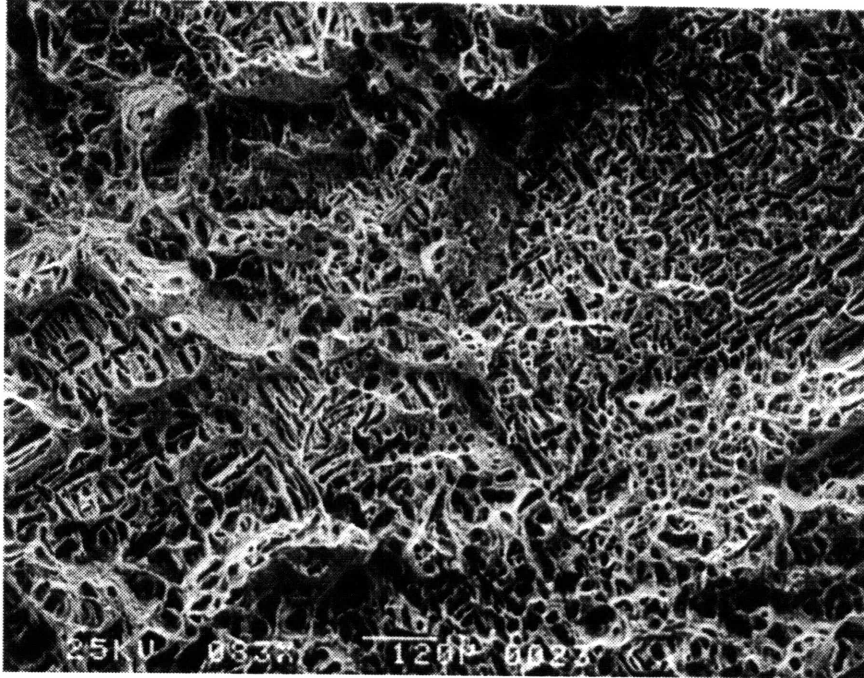


Figure 5.35 Aligned High-Aspect Ratio Dimples and Rods on 1300°C Material  
Spec. 3-1-2, 1300°C, 2°C/min, SEM

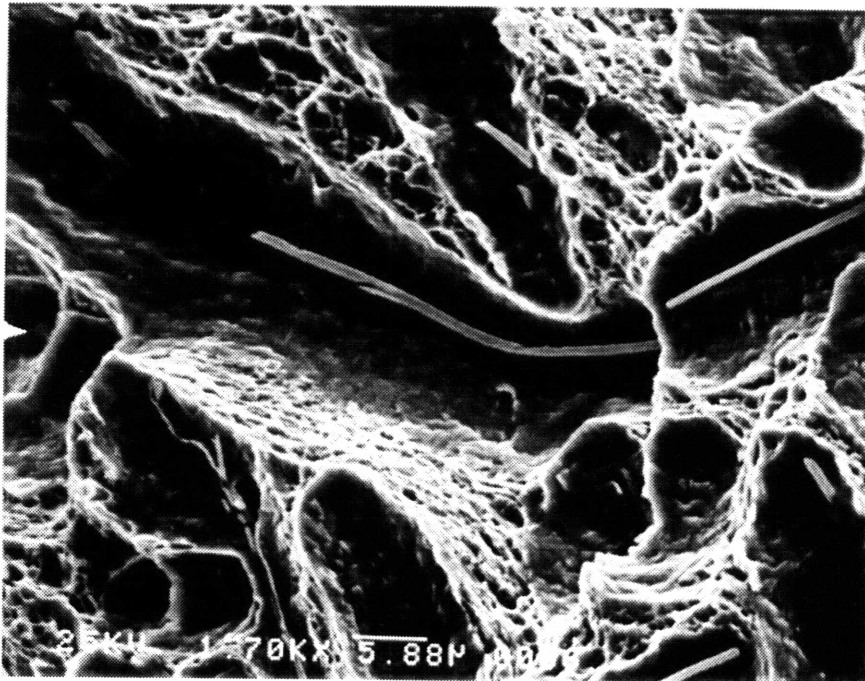


Figure 5.36 Sulfide Rod "Turning the Corner" on 1300°C Control-Cooled  
Material  
Spec. 3-1-2, 1300°C, 2°C/min, SEM

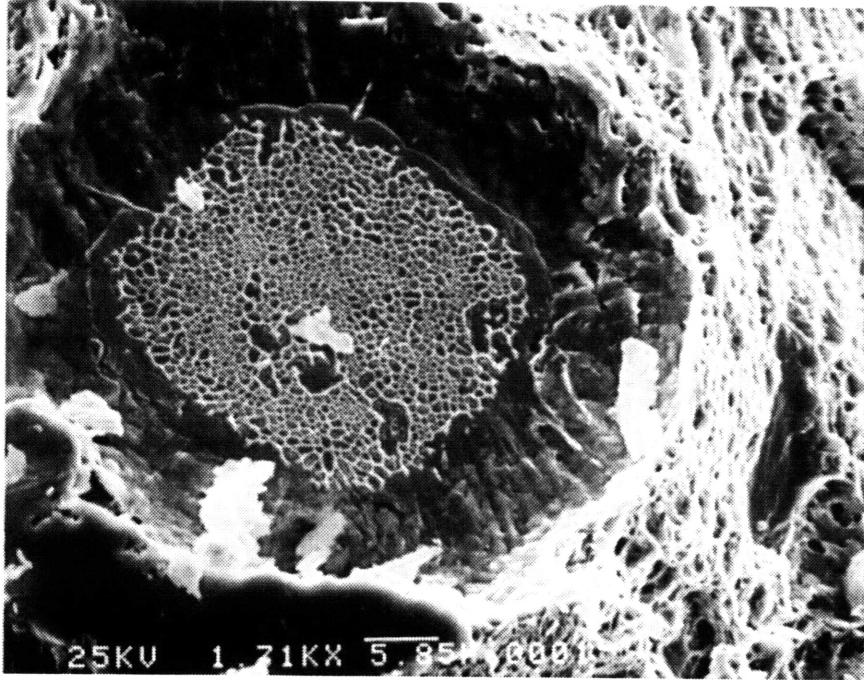


Figure 5.37 Microfacet on 1300°C Control-Cooled Material  
Spec. 3-1-1, 1300°C, 2°C/min, SEM

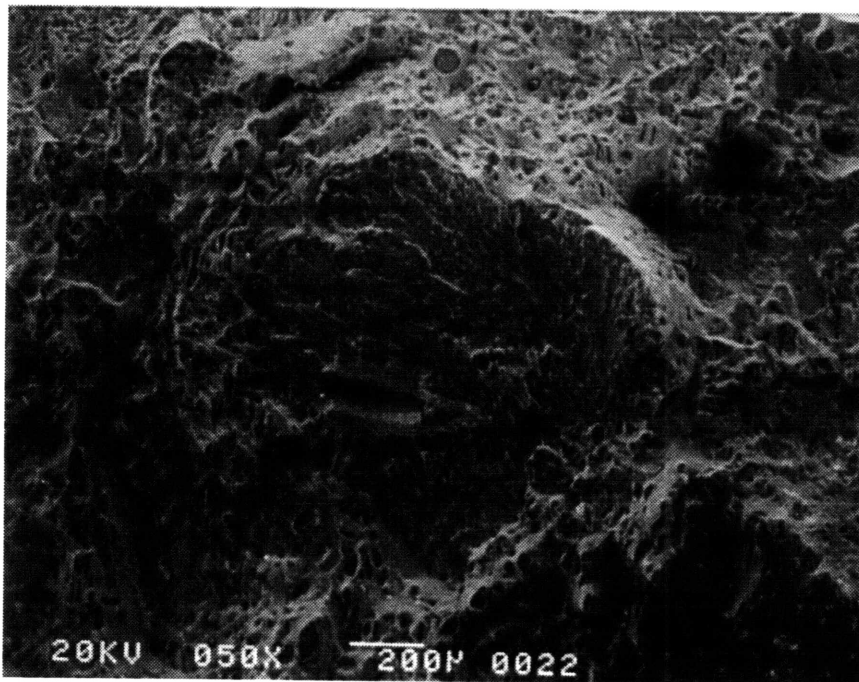


Figure 5.38 Large Low-Ductility PAGB Facet Surrounded by Microfacets and Aligned Rods on 1350°C Control-Cooled Material  
Spec. 4-3-1, 1350°C, 2°C/min, SEM



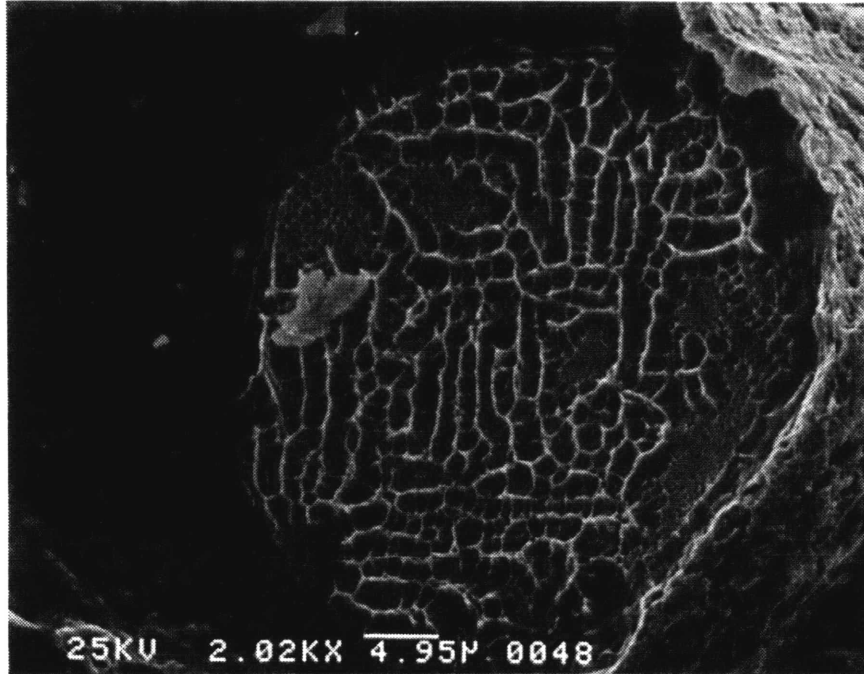


Figure 55. High-Magnification Micrograph of Microfacet, Indicating Fractal-Like Structure  
Spec. 4-3-2, 1350°C, 2°C/min, SEM

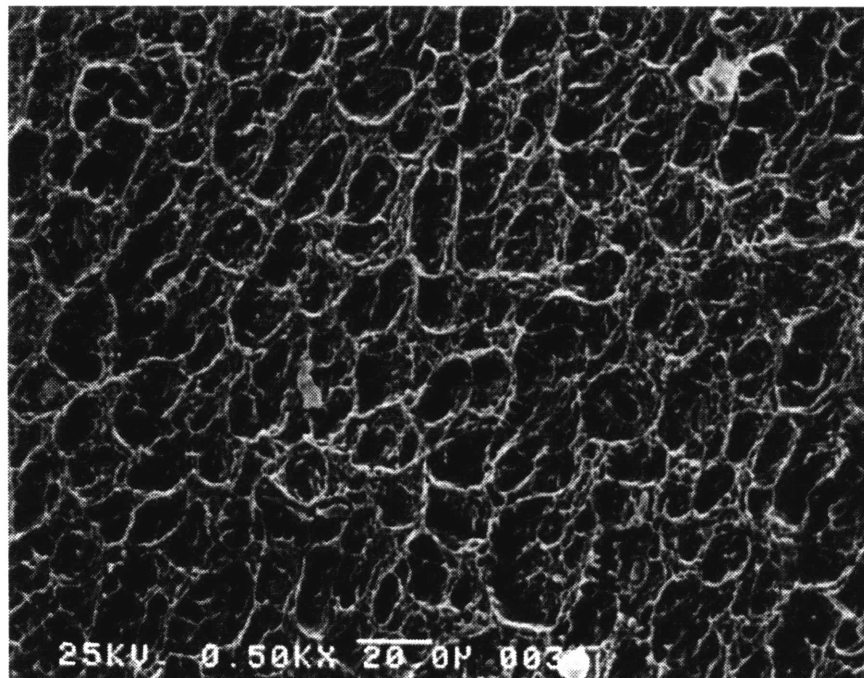


Figure 56. High-Magnification View of Sponge-Like Morphology of 1400°C Slow-Cooled Material  
Spec. 4-4-2, 1400°C, 10°C/min, SEM

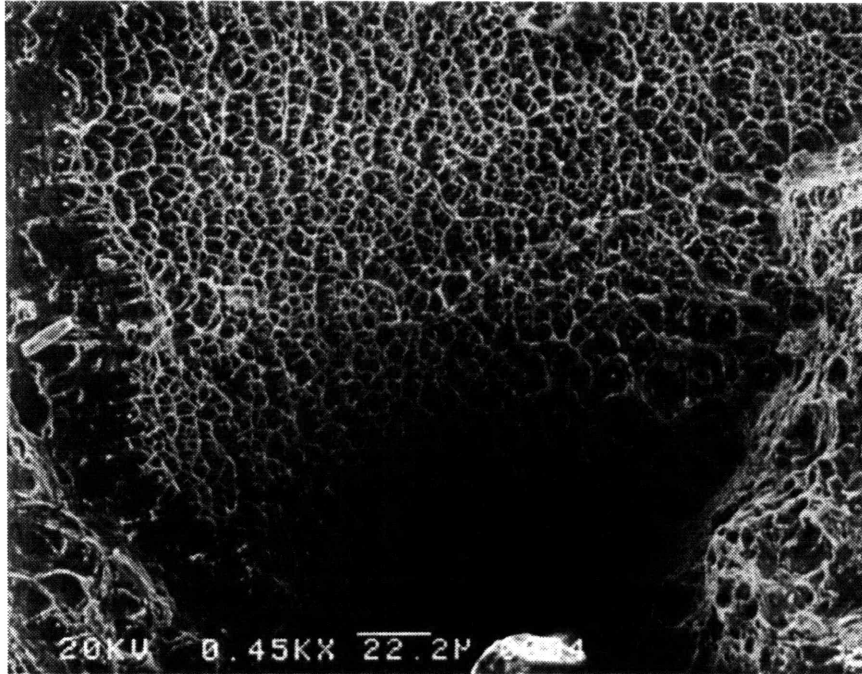


Figure 5.41 Large PAGB Facet With Ductile Dimples Nucleated at Fine Sulfides on 1200°C Air-Quenched Material  
Spec. 4-1-2, 1200°C, AQ, SEM

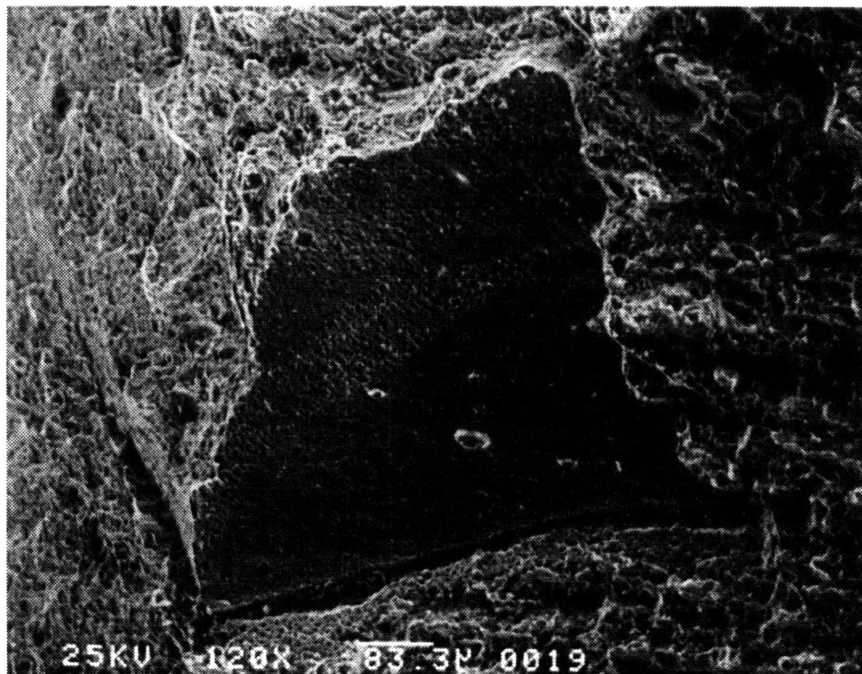


Figure 5.42 Large PAGB Facet With Ductile Dimples But Without Sulfide Nucleators  
Spec. 3-1-3, 1300°C, AQ, SEM

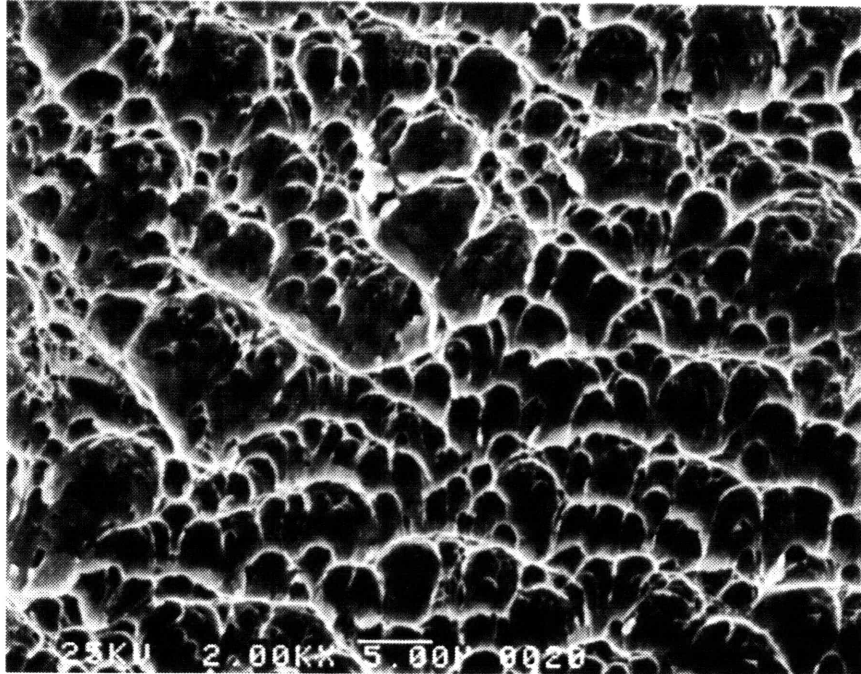


Figure 5.43 Inclusion-Free Ductile Dimples on Facet of Figure 5.42  
Spec. 3-1-3, 1300°C, AQ, SEM

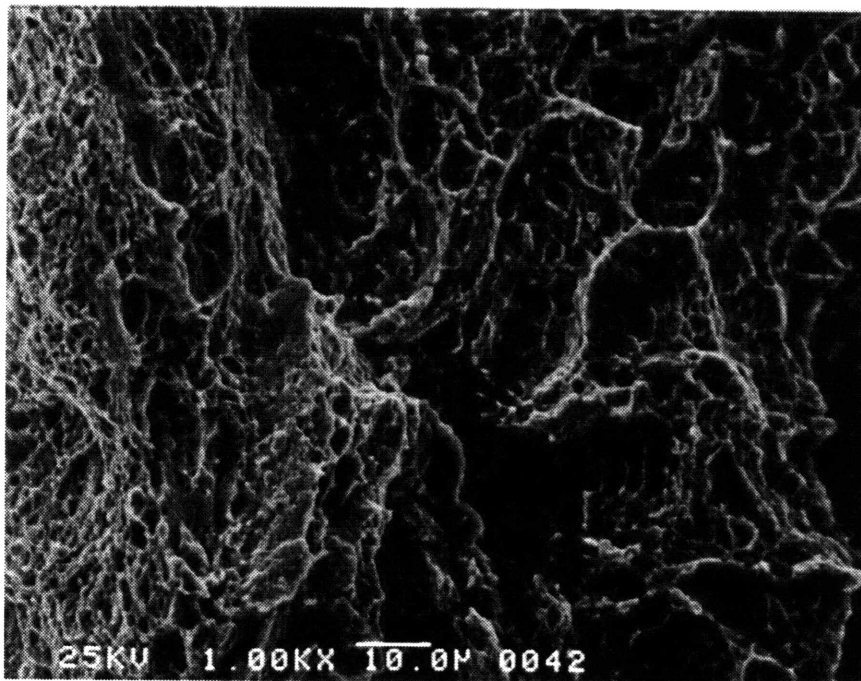


Figure 5.44 Tough, Fibrous Fracture Outside of PAGB Facets on 1350°C Air-  
Quenched Material  
Spec. 4-3-4, 1350°C, AQ, SEM

### 3.5NiCrMoV Martensitic Tests

Material in the 5-1-X test series was subjected to an overheating treatment consisting of preheating at 1300°C followed by controlled-cooling at 2°C/min. However it was then quenched prior to transformation and tested in the martensitic condition. Large PAGB facets were again present on the fracture surfaces, as shown in Figure 5.45. Several artifacts of austenite triple points and grain edges were discernible on the surface of Figure 5.45, as well as the image of martensite lathes or plates formed at the austenite boundary on the facet itself. These are illustrated in the micrograph of Figure 5.46. The surrounding intragranular fracture exhibited a planar morphology typical of brittle cleavage. However, scattered throughout this region were slit-like "troughs" similar in shape to the high-aspect ratio ductile dimples observed in the previous tests. Closer inspection of these showed that they did not have any ductile character but rather were formed by the same cleavage fracture mechanism as in the surrounding area. Figure 5.47 shows several such troughs, displaying the alignment expected of the nucleating rod inclusions, amid a field characterized by cleavage fracture. Figure 5.48 is a high magnification micrograph of one such trough.

Material in the 6-5-X test series was also subjected to a high-temperature austenitization, but was then air-quenched rather than control-cooled and similarly tested in the martensitic state. Again large PAGB facets were observed on the fracture surface, shown in Figure 5.49, but with detailed structure as shown in the high-magnification micrograph in Figure 5.50. The surrounding region exhibited a planar cleavage morphology which was finer than that in the 5-1-X material, illustrated in Figure 5.51. However, as expected, no evidence of rod-related troughs was observed.



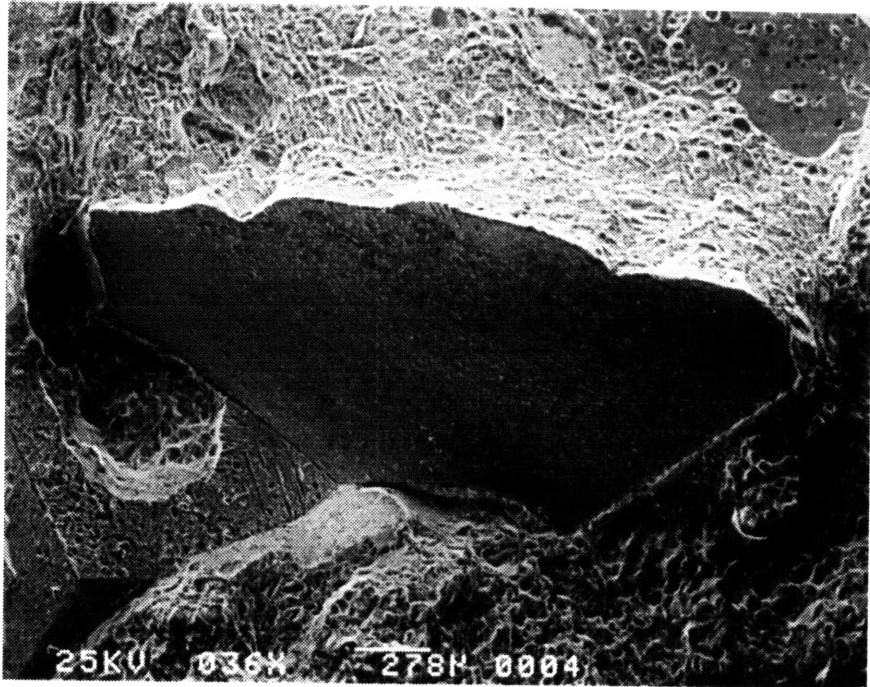


Figure 5.45 Large PAGB Facet on Fracture Surface of Control-Cooled Martensitic Material  
Spec. 5-1-S1, 1300°C, 2°C/min, SEM

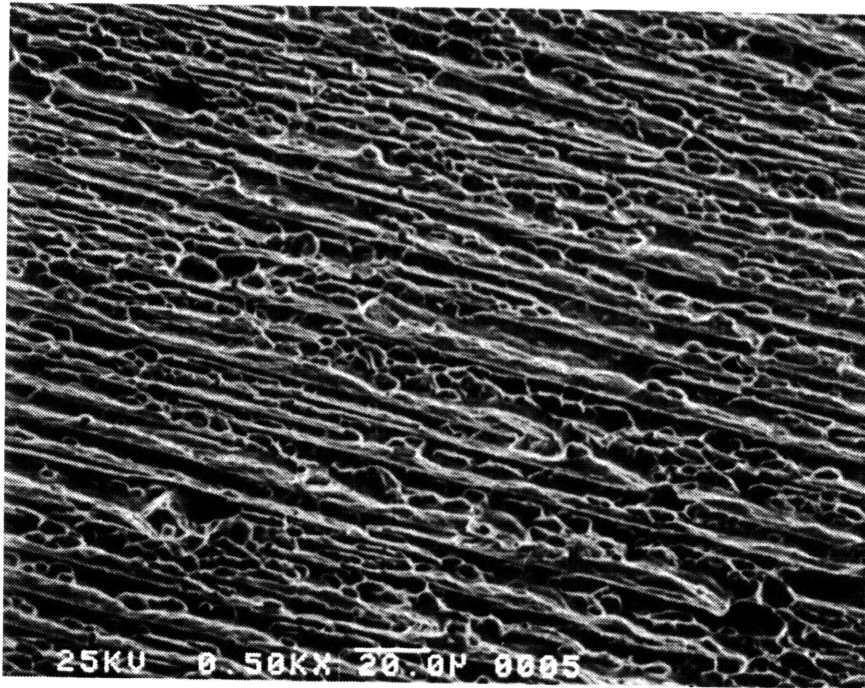


Figure 5.46 Impression of Martensite Lathes or Plates Formed at the Austenite Boundary on Facet of Figure 5.45  
Spec. 5-1-S1, 1300°C, 2°C/min, SEM

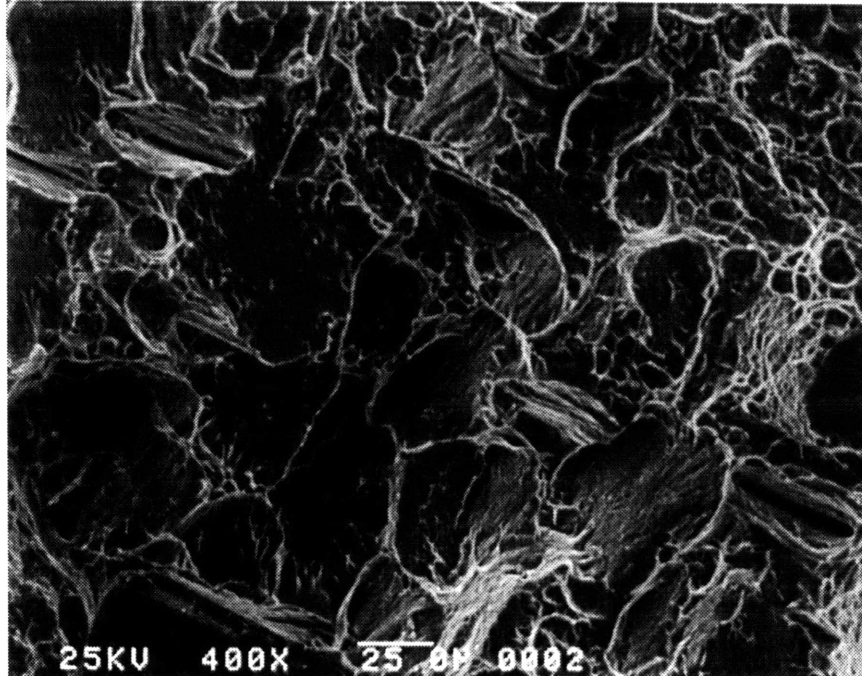


Figure 5.47 Aligned Troughs Amid Cleavage Fracture Field in Martensitic Material of Figure 5.45  
Spec. 5-1-S1, 1300°C, 2°C/min, SEM

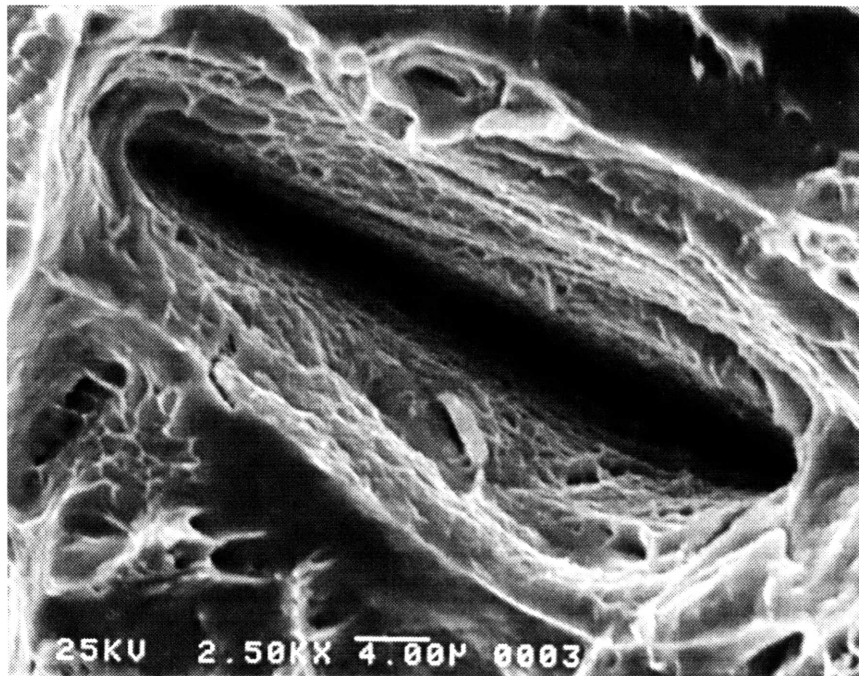


Figure 5.48 High-Magnification Micrograph of Rod Trough in Figure 5.47  
Spec. 5-1-S1, 1300°C, 2°C/min, SEM

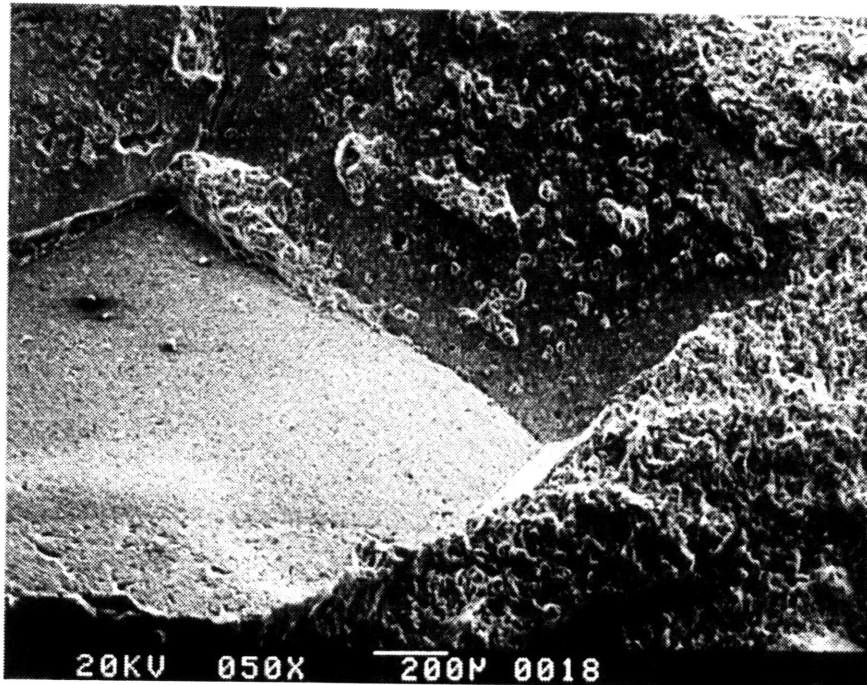


Figure 5.49 Large PAGB Facet on Fracture Surface of Air-Quenched Martensitic Material  
Spec. 6-5-3, 1300°C, AQ, SEM

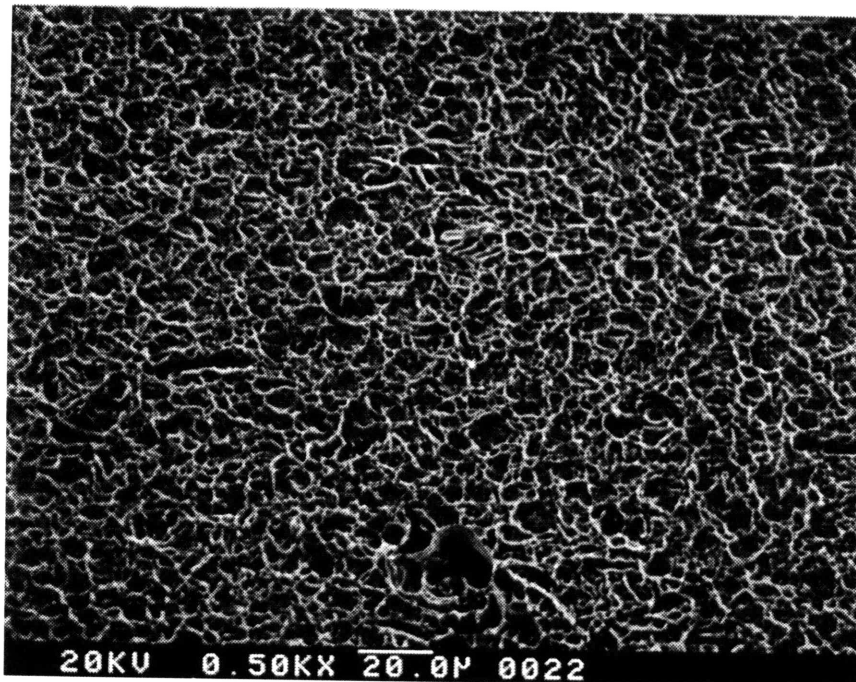


Figure 5.50 Detailed Structure of Air-Quenched Martensitic Material PAGB Facet in Figure 5.49  
Spec. 6-5-3, 1300°C, AQ, SEM

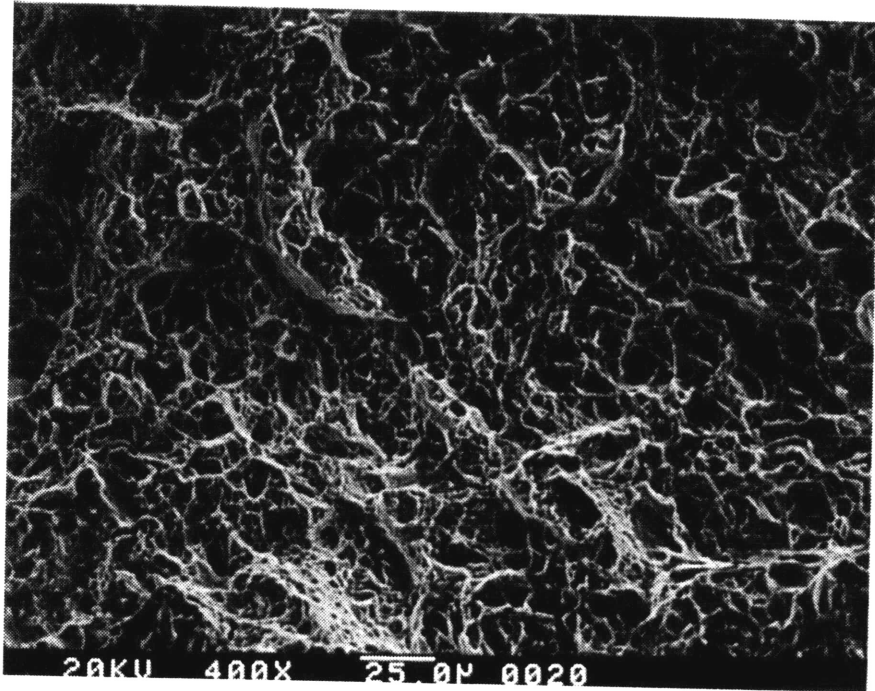


Figure 5.51 Finer Cleavage Morphology in Air-Quenched Martensitic Material  
Spec. 6-5-3, 1300°C, AQ, SEM

## A 508 Cl 4 Tests

Fractographic results for the A 508 Cl 4 material are presented now. The commercial purity material was preheated at 1300°C and control-cooled at either 1 or 2°C/min, then quenched and tempered (650°C). The fracture surfaces associated with both treatments were almost completely characterized by intergranular failure, as seen in Figures 5.52 and 5.54. The dramatic decohesion of individual prior austenite grains is especially evident in Figure 5.52, along with the almost one-to-one correlation of ductile dimples and fine inclusions on the prior austenite grain boundaries. Close examination of these dimples on surfaces of material with both treatments reveals that many of them are embryonic rods similar to those observed on the facets of the 1200°C-preheat 3.5NiCrMoV material, as seen in Figures 5.53 and 5.55. The alignment of the rods with each other is evident in both figures, particularly in Figure 5.53. Another interesting feature of Figure 5.53 is that the inclusions which are not rods are virtually all globular type I MnS whose diameters are greater than the typical rod diameters.

The fracture behavior of the superclean A 508 offered a striking contrast to that of the commercial purity composition. All material was preheated at 1300°C and control-cooled at 2°C/min, then quenched and tempered (650°C). The fracture appearance was typified by rough intragranular ductile failure, with large dimples and almost no evidence of sulfide inclusions, as seen in Figure 5.56. The faint facet of a prior austenite grain boundary was only rarely observed. One such occurrence is shown in Figure 5.57. In this case, the facet surface contains a very small number of sulfides, of which some exhibit a globular type I morphology while others appear to be in the incipient stage of rod development.



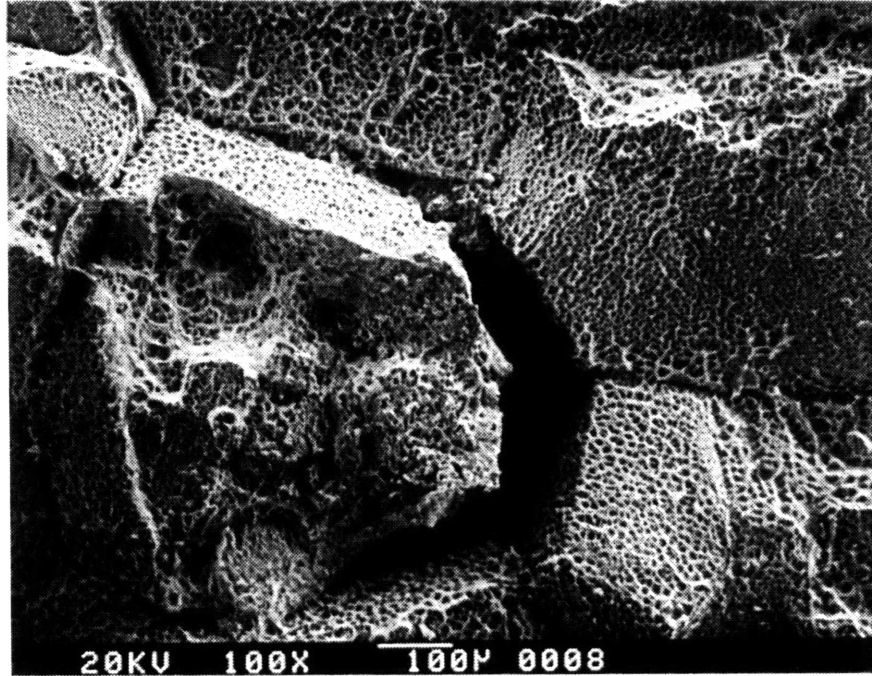


Figure 5.52 Intergranular Failure Morphology of Control-Cooled Commercial Purity A 508 Cl 4 Material  
Spec. F-B-1, 1300°C, 2°C/min, SEM

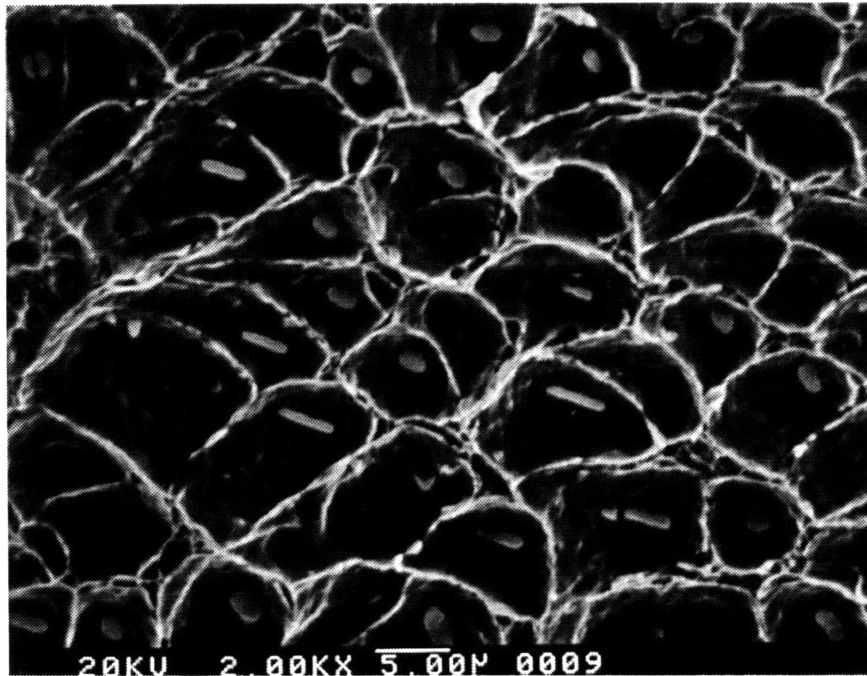


Figure 5.53 Embryonic Rods on Prior Austenite Grain Boundaries of Control-Cooled A 508 Cl 4 Material in Figure 5.52  
Spec. F-B-1, 1300°C, 2°C/min, SEM

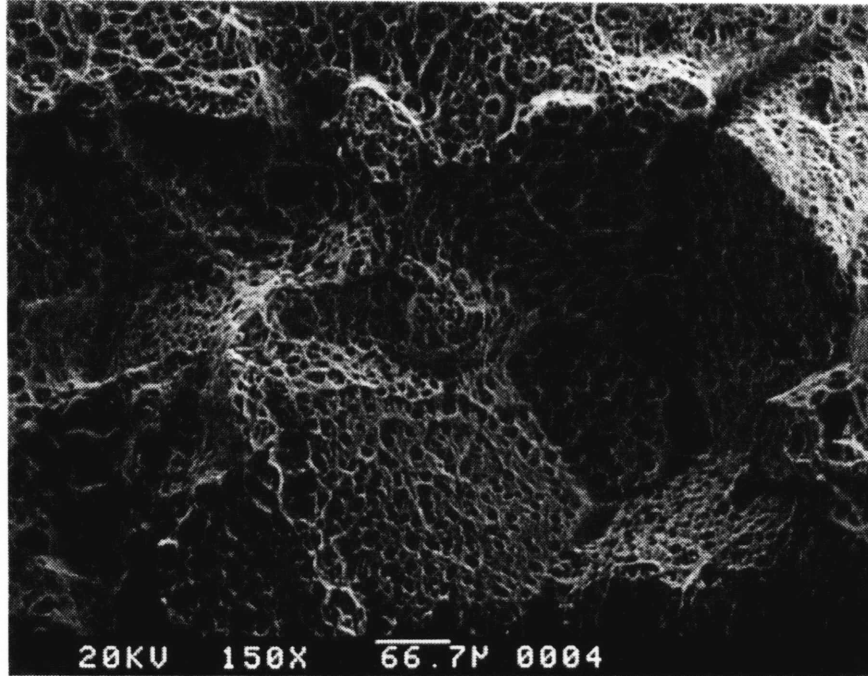


Figure 5.54 Intergranular Failure Morphology of Control-Cooled Commercial Purity A 508 Cl 4 Material  
Spec. F-B-2, 1300°C, 1°C/min, SEM

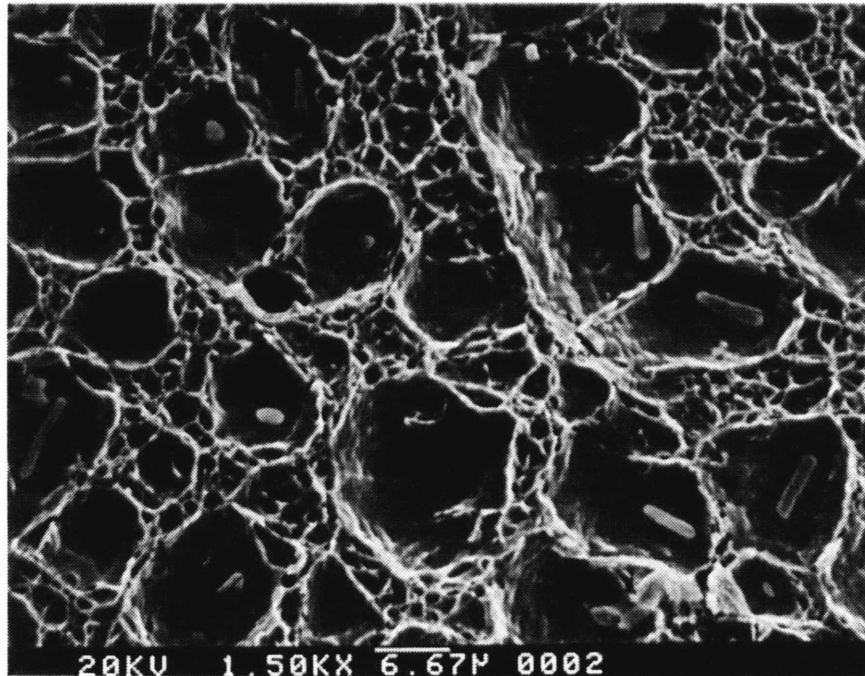


Figure 5.55 Embryonic Rods on Prior Austenite Grain Boundaries of Control-Cooled A 508 Cl 4 Material in Figure 5.54  
Spec. F-B-2, 1300°C, 1°C/min, SEM

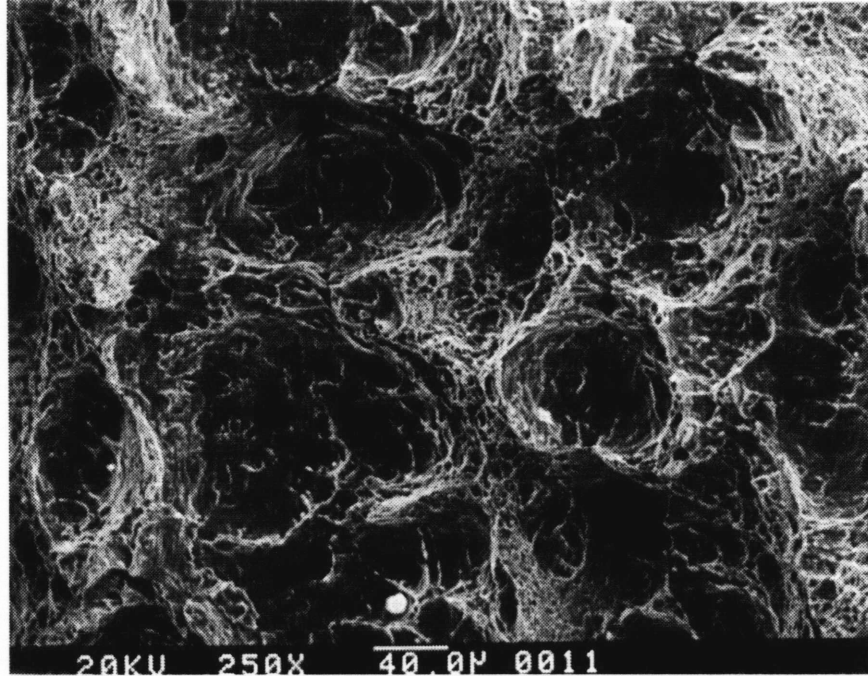


Figure 5.56 Rough, Ductile, Intragranular Failure on Surface of Control-Cooled Superclean A 508 Cl 4 Material  
Spec. F-A-3, 1300°C, 2°C/min, SEM

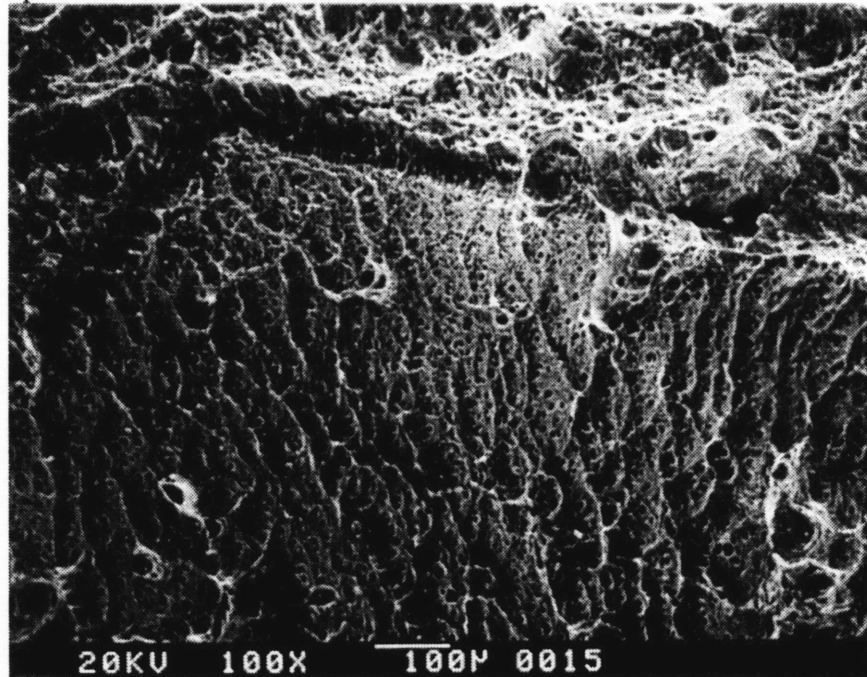


Figure 5.57 Faint Facet of Prior Austenite Grain Boundary on Surface of Control-Cooled Superclean A 508 Cl 4 Material  
Spec. F-A-3, 1300°C, 2°C/min, SEM



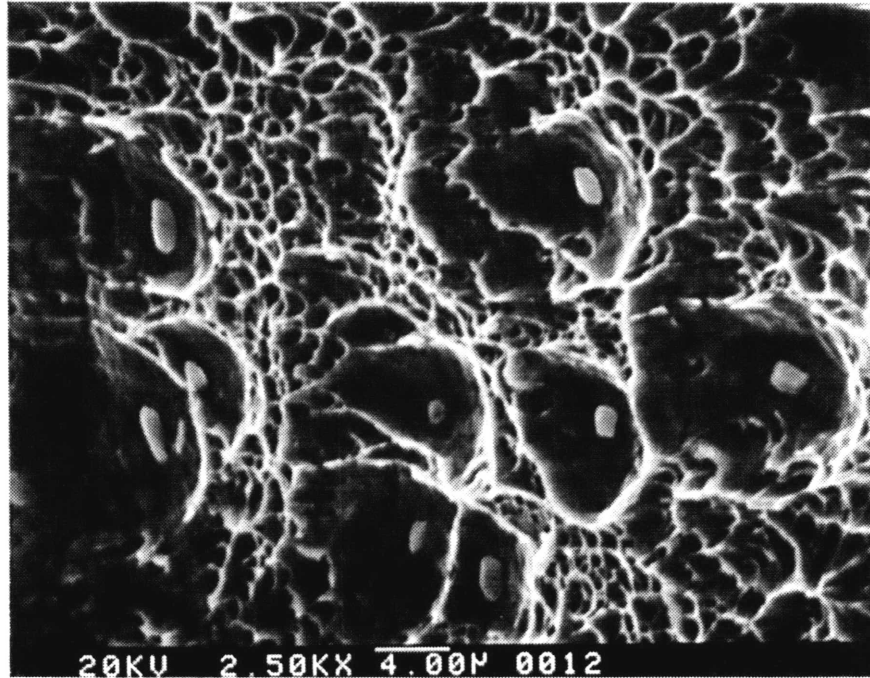


Figure 5.58 Sparse Sulfides on Faint Facet of Figure 5.57, Surface of Control-Cooled Superclean A 508 Cl 4 Material  
Spec. F-A-3, 1300°C, 2°C/min, SEM

### 5.1.2.2. Optical Metallography

#### Final Microstructural Characterization

The microstructure of the as-received 3.5NiCrMoV as revealed by etching with nital is illustrated in the low- and high-magnification micrographs of figures 5.59 and 5.60 (4-5-X series). The prior austenite grain structure is revealed even with nital, as seen in Figure 5.59. It should be emphasized here that this microstructure is established by the last austenitization experienced by this material, an unspecified time at 890°C, followed by a temper at 690°C, also of unknown length [45]. This grain structure is distinct from the much larger structure developed during forging, which is revealed by facets which form due to MnS precipitation. This MnS structure is unaffected by the 890°C treatment, and thus survives to indicate the forging grain size. The actual final microstructure is believed to be tempered martensite, as shown by comparing Figure 5.60 with Figure 5.61 which reproduces an example of tempered martensite provided by reference 40. The lighter areas are ferrite, while the dark points and clusters are probably coarsened cementite. The microstructure resulting from the quench and temper performed in this work as revealed by etching with nital is illustrated in the low- and high-magnification micrographs of figures 5.62 and 5.63 (also 4-5-X series). The much finer austenite grains and carbide distribution developed during this treatment, as compared to that in the as-received material, is evident.

Very large austenite grains grown during the control-cooled overheating treatments, which would be similar to those developed during forging, are revealed with a nital etch, as shown in Figure 5.64. The fine structure of this tempered martensite structure is shown in the high magnification view in Figure 5.65. There is virtually no difference between the final microstructures of the control-cooled versus air-quenched materials, save for larger prior austenite grains in the control-cooled material, as shown in figures 5.66 and 5.67, which are identical in magnification to figures 5.64 and 5.65, respectively. The microstructures depicted in figures 5.64-67 were characteristic of austenitization temperature treatments throughout the 1250-1350°C range. By contrast, Figure 5.68 shows a low-magnification view of material subjected to a 1200°C preheat then control-cooled, in which the very large austenite grains are not as obvious.

The martensite morphology material which was tested directly after the overheating treatment (5-1-X series) is clearly shown in Figure 5.69, as etched with nital. It is likely that this is  $(557)_\alpha$  lath martensite, which forms in steels with carbon content below 0.4% [71]. Figure 5.69 is the two-dimensional analog to the three-dimensional lath impressions seen under SEM examination of the facet in Figure 5.46. Lath martensite frequently develops with a specific orientation relationship to the parent austenite [71]. Figure 5.70 is a good example of the resulting crystallographically-oriented appearance. Of special significance in that figure are the traces of rods aligned in three different directions, which on this surface appear parallel to traces of the martensite lathes themselves.



Figure 5.59 Microstructure of As-Received Material, Revealed by Etching with Nital  
Spec. 4-5-3, AR, Nital, Metallograph, 50X

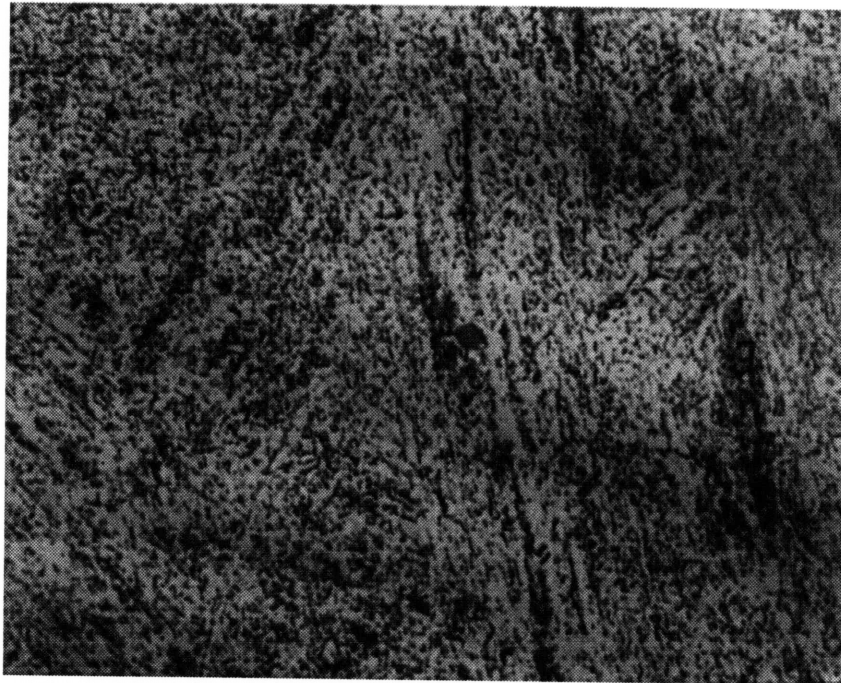


Figure 5.60 High-Magnification View of As-Received Microstructure  
Spec. 4-5-3, AR, Nital, Metallograph, 500X

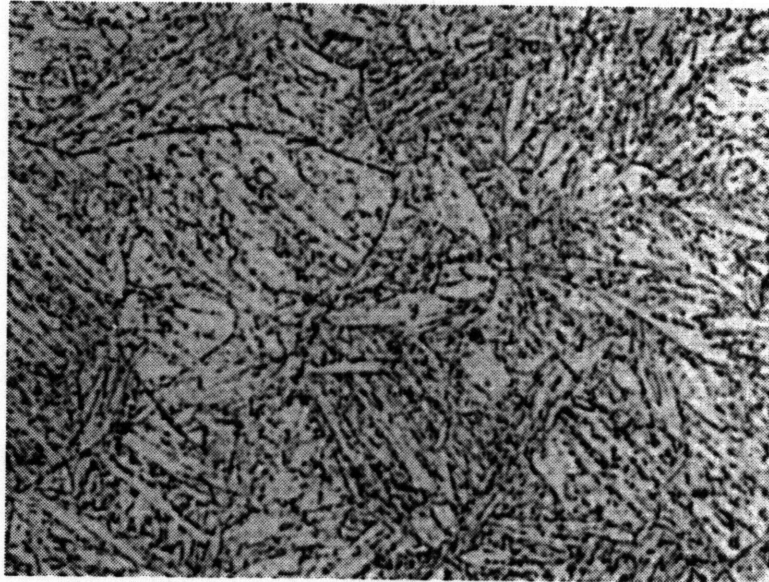


Figure 5.61 Tempered Martensite Structure Achieved by Quenching and Tempering 10B35 Steel, 2% Nital, 1000X Reduced by 10%, [from 70]

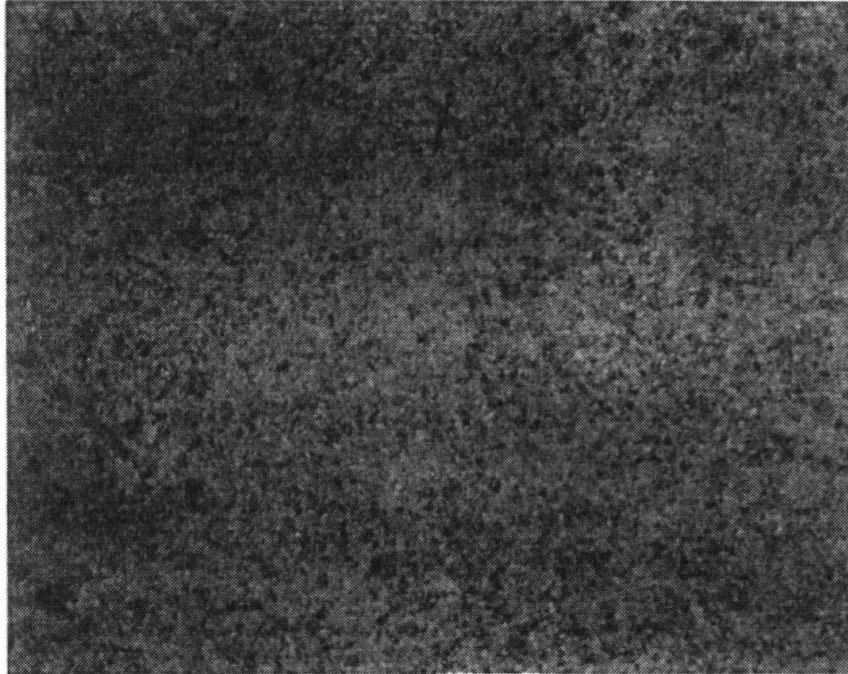


Figure 5.62 Microstructure of Quenched and Tempered Control Material  
Spec. 4-5-2, AR+QT, Nital, Metallograph, 50X



Figure 5.63 High-Magnification View of Microstructure of Quenched and Tempered Control Material  
Spec. 4-5-2, AR+QT, Nital, Metallograph, 500X





Figure 5.64 Prior Austenite Grain Structure of Control-Cooled Material,  
Revealed by Etching with Nital  
Spec. 4-2-2, 1250°C, 2°C/min, Nital, Metallograph, 50X



Figure 5.65 High-Magnification View of Structure of Control-Cooled Material,  
Revealed by Etching with Nital  
Spec. 4-2-2, 1250°C, 2°C/min, Nital, Metallograph, 1000X

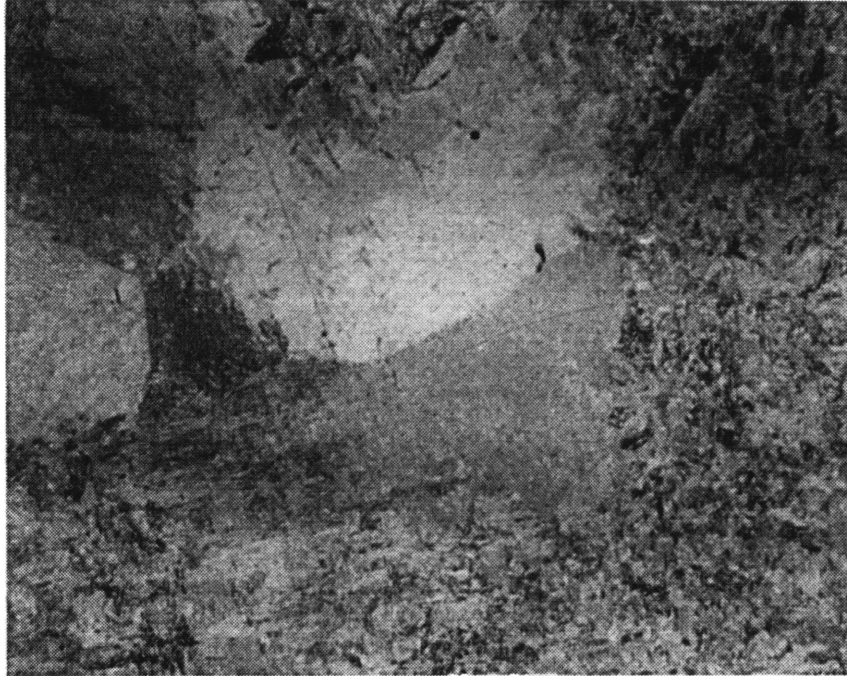


Figure 5.66 Prior Austenite Grain Structure of Air-Quenched Material,  
Revealed by Etching with Nital  
Spec. 4-2-3, 1250°C, AQ, Nital, Metallograph, 50X



Figure 5.67 High-Magnification View of Structure of Air-Quenched Material,  
Revealed by Etching with Nital  
Spec. 4-2-3, 1250°C, AQ, Nital, Metallograph, 1000X





Figure 5.68 Low-Magnification View of 1200°C Control-Cooled Material With Small Prior Austenite Grains, Revealed by Etching with Nital  
Spec. 4-1-3, 1200°C, 2°C/min, Nital, Metallograph, 50X



Figure 5.69 Lathe Martensite Morphology Revealed by Etching with Nital  
Spec. 5-1-1, 1300°C, 2°C/min, Nital, Metallograph, 200X

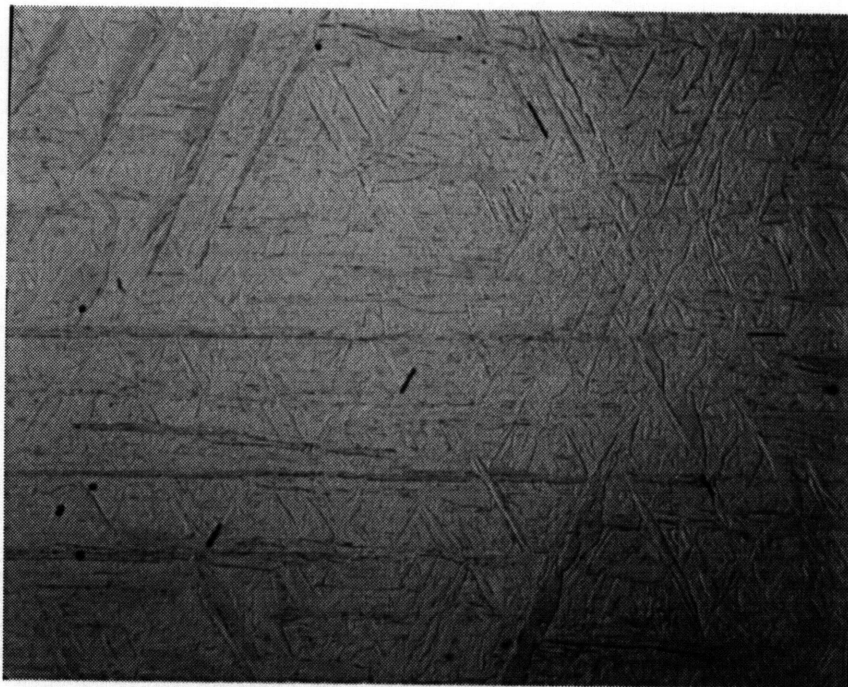


Figure 5.70 Alignment of Martensite Lathes and MnS Rods, Revealed by  
Etching with Nital  
Spec. 5-1-3, 1300°C, 2°C/min, Nital, Metallograph, 1000X

## **Prior Austenite Grain Structure**

In contrast to nital, the picral etchant generally performed poorly in revealing prior austenite grain structure. This was true of both room temperature and warm tests. At high magnification, however, aligned rods were frequently observable after etching with picral. An example of this is shown in Figure 5.71, etched two minutes at room temperature followed by 4 minutes at 35°C. This figure shows three parallel or perpendicular rods lying in the plane of the micrograph, and several features which may be cross sections of rods whose axes point out of the page. The preserved condition of manganese sulfides after etching with picral is believed to be due to the alcohol base, versus water in other etchants. Poor results were also obtained with Bechet & Beaujard's etch, even though it is generally considered to be a prime candidate for revealing prior austenite grain structure. In contrast, good results were obtained with Villela's picric acid-based reagent, which not only clearly revealed prior austenite grain boundaries, but also repeatedly displayed annealing twins associated with that structure. An example of this is shown in Figure 5.72, a low-magnification micrograph (taken with the optical stereoscope) of a mounted section.

Electrolytic etching with a modified version of Knuth & Winterfeldt's perchloric acid-based etchant was shown to be effective in revealing both overheated sulfides at prior austenite grain boundaries as well as the current microstructure. Figure 5.73 is a micrograph of material preheated to 1290°C and control-cooled at 5°C/min (specimen 1-2-2), then etched at 30V for 10 seconds, yielding a current density of 5.5 A/cm<sup>2</sup>. The PAGB sulfides are clearly revealed as a network of fine pits. It is recalled that fracture surfaces in material from this series (1-2-X) typically displayed fine spherical precipitates along with some low-aspect ratio rods on large facets.

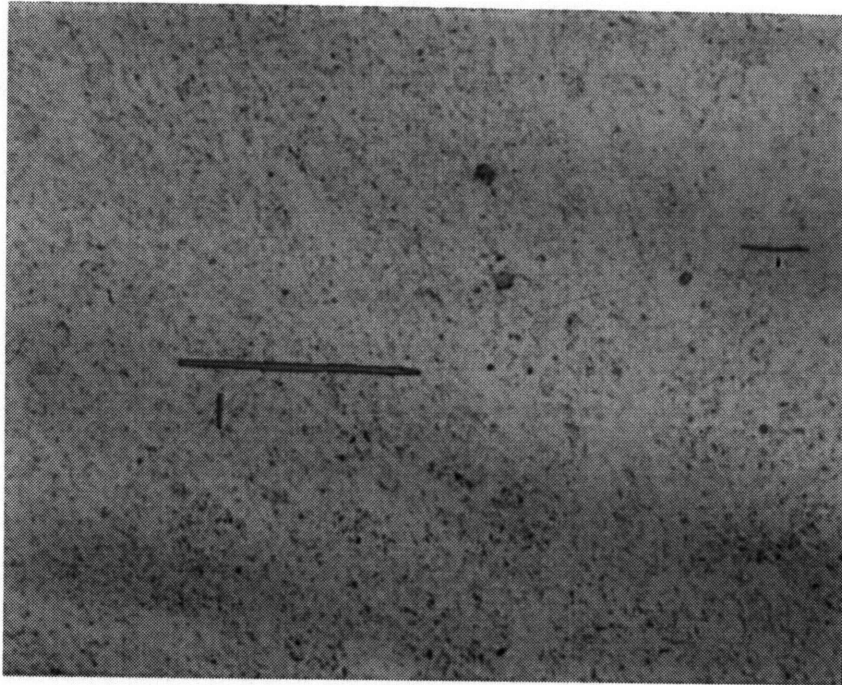


Figure 5.71 Aligned Rods in Slow-Cooled Material, Revealed by Etching With Picral  
Spec. 3-1-2, 1300°C, 2°C/min, Picral, Metallograph, 1000X

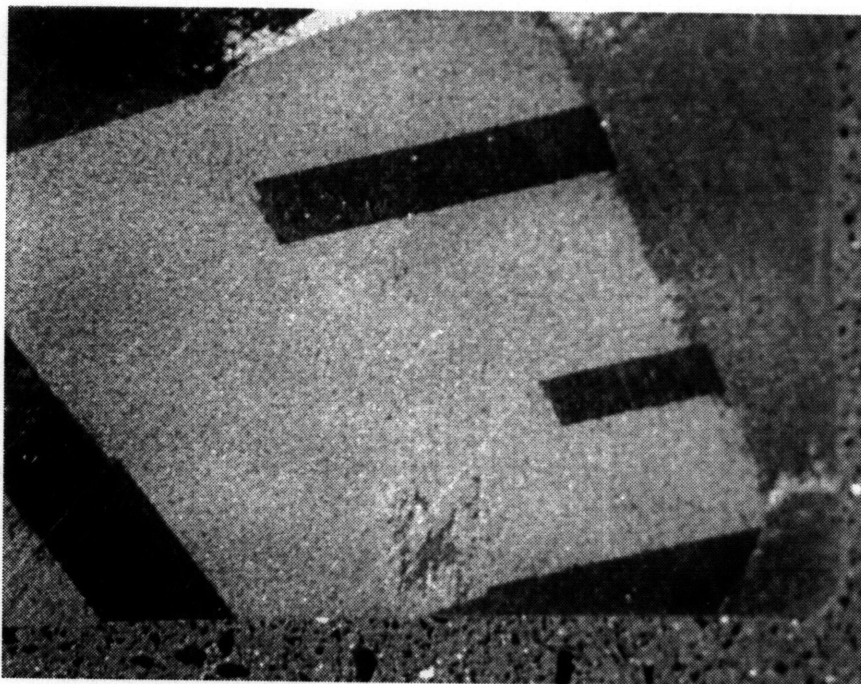


Figure 5.72 Prior Austenite Grain Boundaries and Twins in Martensitic Material, Revealed by Etching With Villela's Reagent  
Spec. 5-1-2, 1300°C, 2°C/min, Villela's, Fractograph, 20X

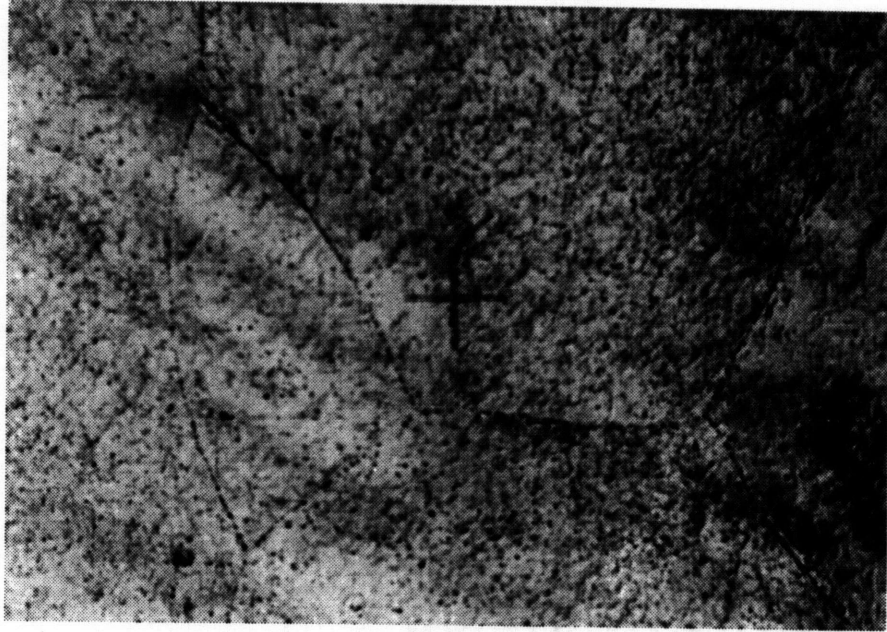


Figure 5.73 MnS Network on Prior Austenite Grain Boundary Revealed by Electrolytic Etching With Modified Knuth & Winterfeldt's Reagent  
Spec. 1-2-2, 1290°C, 5°C/min, Knuth & Winterfeldt's Reagent, Metallograph, 50X

## Inclusion Characteristics

The chrome trioxide etch was very effective at revealing the inclusions, especially MnS rods, while leaving the matrix untouched as seen in figures 5.74 and 5.75. The etch procedure for these micrographs consisted of a 20V, 20 sec, 0.1A/cm<sup>2</sup> electropolish, followed by a 5V, 0.04A/cm<sup>2</sup> electropolish for 1.5 minutes for Figure 5.74 and 2.5 minutes for Figure 5.75. The alignment of several sets of high-aspect ratio rods are clearly revealed there. When nonparallel rods lie entirely in the etched plane it becomes possible to measure the included angle between them. As the length of a rod trace decreases, however, the error involved in assuming that the direction of its axis lies in the plane of the micrograph increases.

Assuming that the rods seen in figures 5.74 and 5.75 lay entirely in the etch plane, the included angles were determined for different sets of rod directions. Figures 5.76 and 5.77 reproduce figures 5.74 and 5.75 with trace directions and their included angles overlaid<sup>1</sup>. From these and similar measurements made on other micrographs, it was seen that the included angle between groups of nonperpendicular rods was consistently in the range of 114 to 130°, as summarized in Table 5.2. A very rough measure of the accuracy of assuming the rods lie entirely in the etch plane is provided by calculating the angle of inclination  $\phi$  to the plane, assuming that all rods are 1.5  $\mu\text{m}$  in diameter<sup>2</sup>. The calculated angle of inclination  $\phi$  is also included in Table 5.2, determined from:

$$\phi = \arctan(1.5 / l)$$

where  $l$  is the length in microns of the rod trace in the etch plane.

The warm nitric acid deep etch was effective in revealing the morphology and alignment of the MnS rods. Figure 5.78 is an SEM micrograph of a sample immersed for 10 seconds and then cleaned in isopropyl alcohol. The figure

---

<sup>1</sup> The overlaid directions and angle diagrams are merely schematics. The actual angle values depicted in these diagrams were determined manually from photocopies of the original micrographs.

<sup>2</sup> Slightly greater than that of the rod in figure 5.21. A larger diameter overestimates error.



shows the heavy attack of the matrix along with several MnS rods exposed, with their alignment preserved. The rod morphology is obvious in these micrographs. Higher magnification images of the exposed rods suffered from "transparency", i.e., it was impossible not to obtain features of the hidden matrix surface due to electron transmission through and/or around the narrow rod, as seen in Figure 5.79. Coating of the surface with gold or carbon might eliminate this problem and render a better image.

A significant feature revealed by this technique was the clustering of rod precipitates within narrow intragranular bands. Figure 5.80 is a low-magnification composite image of such banding, appearing as dark, continuous streaks running across the images. Within the dark streaks are numerous etch pits, usually with a rod jutting from each, as shown in Figure 5.81. (Extensive examination of another specimen revealed virtually one-to-one correspondence between the pits and exposed rods.) It is obvious from the structure of the bands that they do not correspond to prior austenite grain boundaries, which are much straighter and would not exhibit the acute angle intersections seen in Figure 5.80.

A final observation is the occurrence of cracking along boundaries of the austenite grains developed during the overheating treatment. An example of this is seen in the micrograph of Figure 5.82, an SEM image of an as-polished section mounted in epoxy. A relatively thick oxide layer on the interior of the crack is evidence that it developed during heat treatment. Such cracking was observed a number of times on cut and polished faces of specimens in another phase of the work, running in from the as-treated surfaces towards the interior. The fact that the crack corresponds to a large prior austenite grain boundary was established using a separate etch.

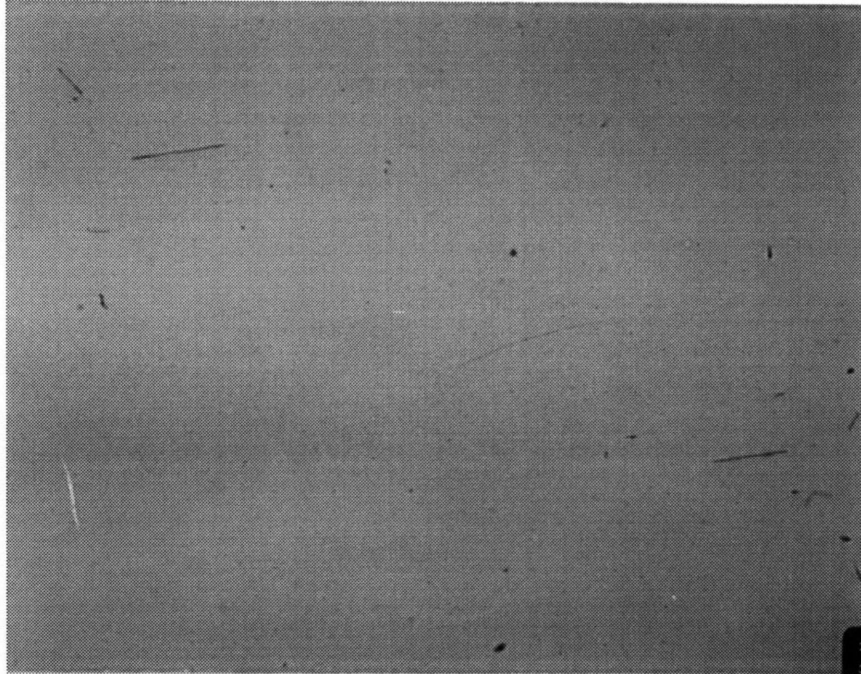


Figure 5.74 Aligned Rods As Revealed by  $\text{CrO}_3$  Etch  
Spec. 1-3-4,  $1300^\circ\text{C}$ ,  $1^\circ\text{C}/\text{min}$ ,  $\text{CrO}_3$ , Metallograph, 200X

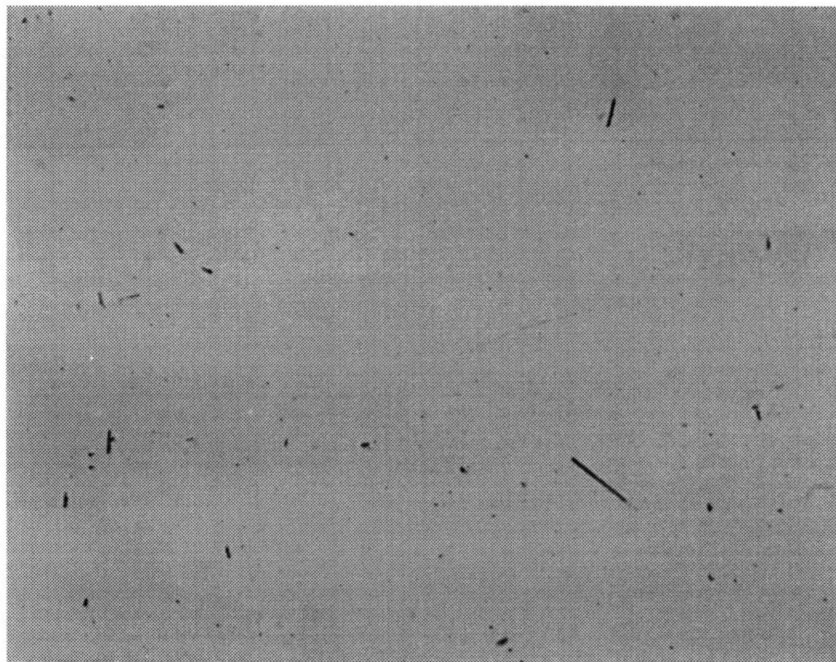


Figure 5.75 Aligned Rods As Revealed by  $\text{CrO}_3$  Etch  
Spec. 1-3-4,  $1300^\circ\text{C}$ ,  $1^\circ\text{C}/\text{min}$ ,  $\text{CrO}_3$ , Metallograph, 500X



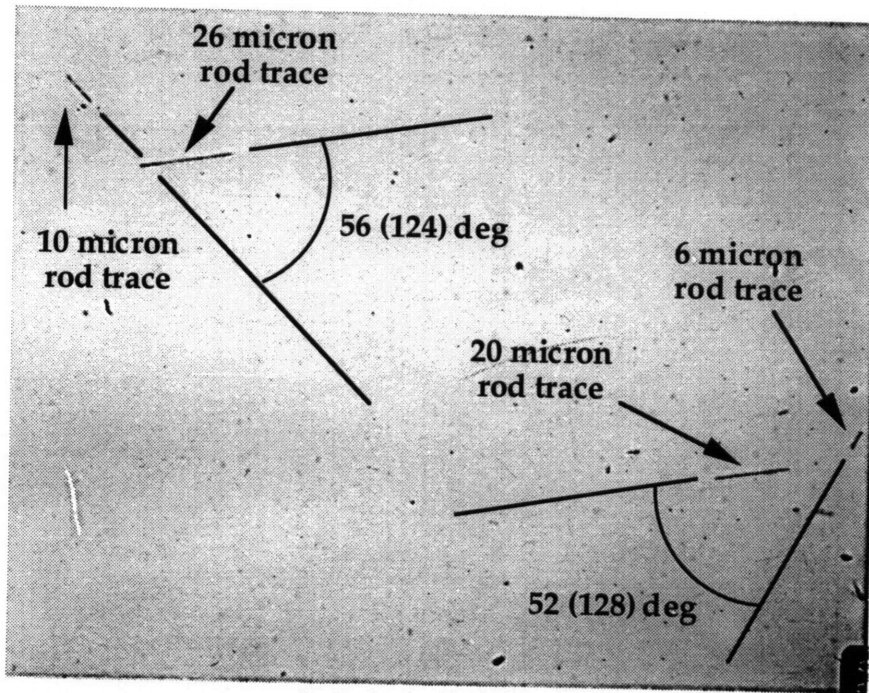


Figure 5.76 Aligned Rods From Figure 5.74, With Overlaid Trace Directions and Included Angles  
Spec. 1-3-4, 1300°C, 1°C/min, CrO<sub>3</sub>, Metallograph, 200X

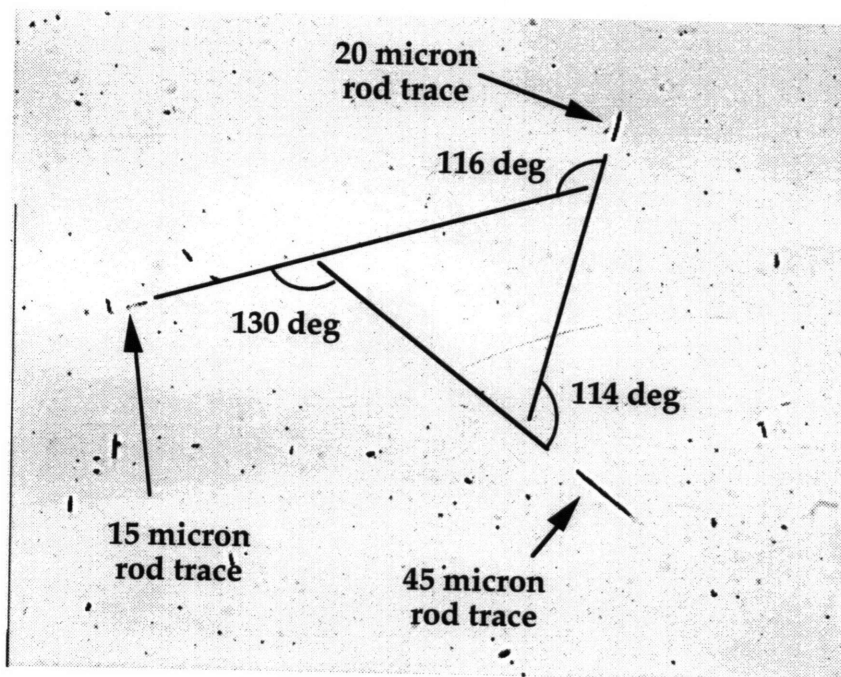


Figure 5.77 Aligned Rods From Figure 5.75, With Overlaid Trace Directions and Included Angles (Schematic)  
Spec. 1-3-4, 1300°C, 1°C/min, CrO<sub>3</sub>, Metallograph, 500X

Specimen	Micrograph	Rod Lengths (microns)	Estimated Inclination to Surface (deg)	Included Angle (deg)
1-3-4	2	26 10	3 9	124
1-3-4	2	20 6	4 14	128
1-3-4	3	45 20	2 4	114
1-3-4	3	45 15	2 6	130
1-3-4	3	20 15	4 6	116
1-3-4	10	30 10	3 9	89

Table 5.2 Included Angles Between MnS Rods, Measured From Chrome Trioxide Etch Micrographs, With Estimated Angle of Inclination to Etch Plane

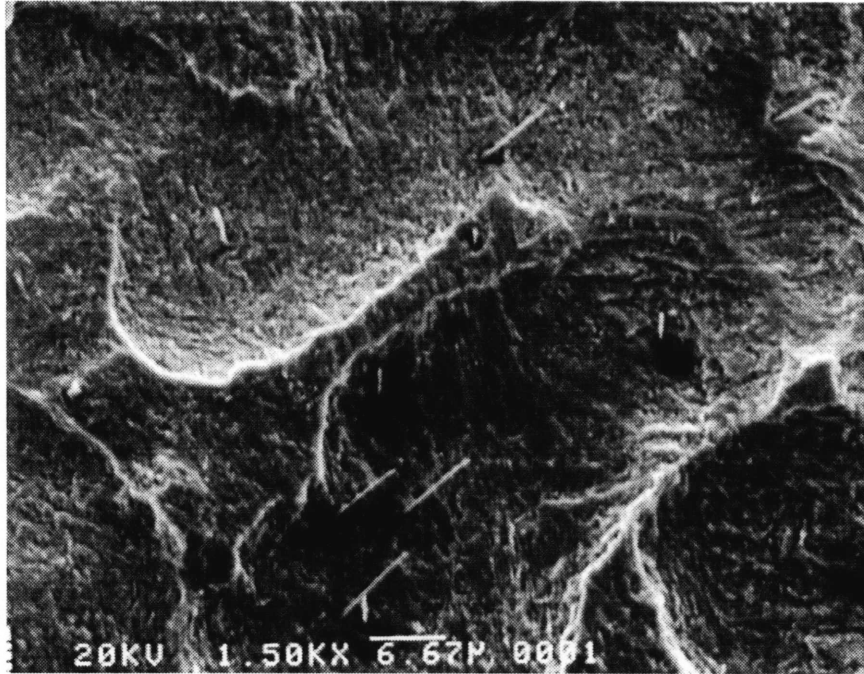


Figure 5.78 Aligned Rods As Revealed by Warm 50% Nitric Acid Deep Etch  
Spec. 4-2-2, 1250°C, 2°C/min, Warm Nitric, SEM



Figure 5.79 High-Magnification View of Rods As Revealed by Warm 50% Nitric Acid Deep Etch  
Spec. 4-2-2, 1250°C, 2°C/min, Warm Nitric, SEM

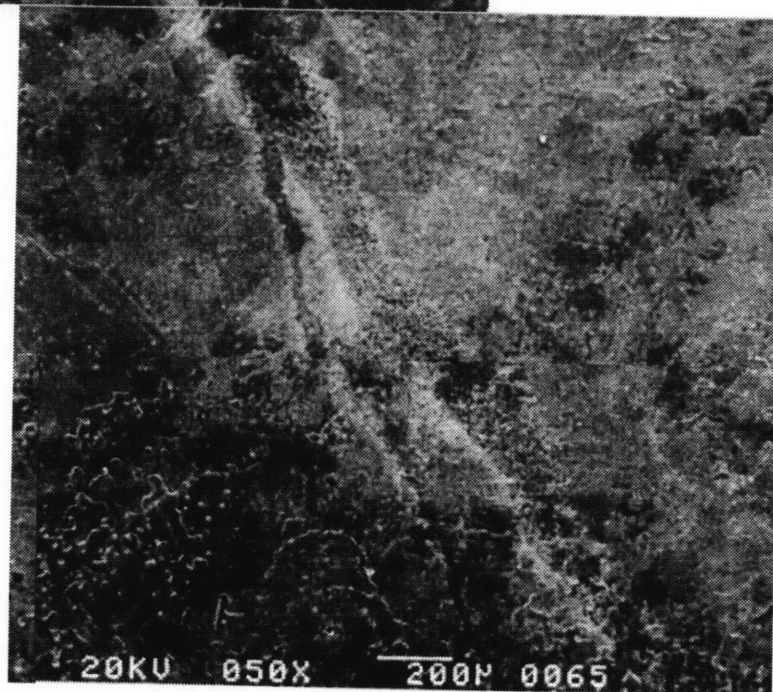


Figure 5.80 Low-Magnification Composite Image of Band Distribution of Rod Precipitates  
Spec. 4-2-2, 1250°C, 2°C/min, Warm Nitric, SEM



Figure 5.81 High-Magnification View of Rod Precipitates Within Etch Pits in Bands of Figure 5.80  
Spec. 4-2-2, 1250°C, 2°C/min, Warm Nitric, SEM

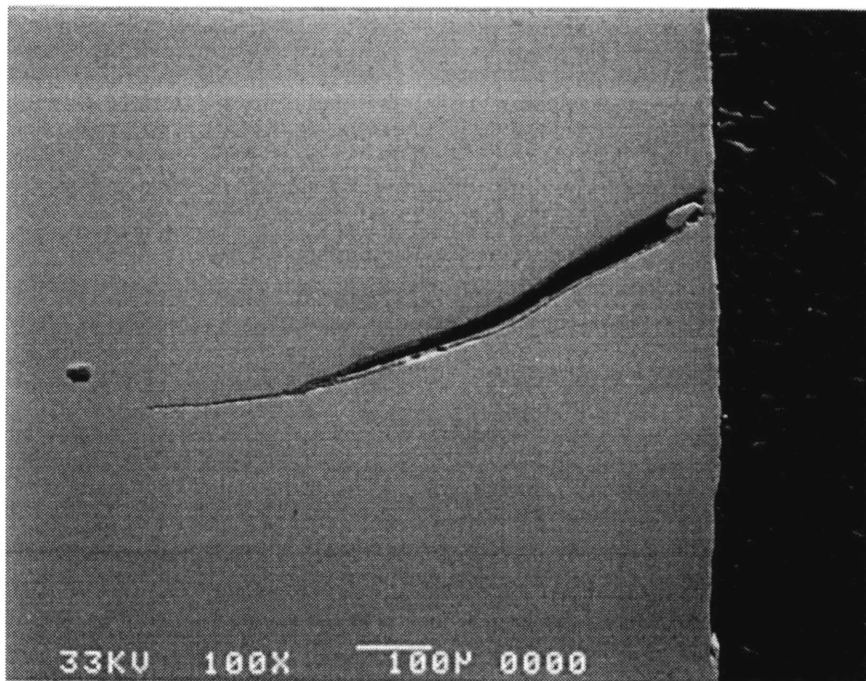


Figure 5.82 As-Polished Surface With Oxidized Crack Along Boundary of Austenite Grain Developed During Overheating Treatment  
Spec. 4-3-2, 1350°C, 2°C/min, As-Polished, SEM



## 5.2. Sulfide-Rod Orientation Relationship

Results pertaining to the second half of the work, investigating the crystallography of the sulfide rods and their relationship to the matrix are presented now. The order of presentation is first the TEM of extracted sulfide rods, followed by the trace analysis of etched samples.

### 5.2.1. Extraction Replicas

The fracture surface of specimen 4-2-1 (preheat temperature of 1250°C, cooling rate of 2°C/min) displayed a very dense population of rods (see Figure 5.33), and thus was chosen for making extraction replicas. SEM examination of the removed extraction film showed several regions in which the surface morphology of elongated ductile dimples was replicated, as shown in Figure 5.83. Close inspection was required, however, to ensure that the corresponding sulfide was actually extracted, since many replica dimples were found to be empty. Two regions of the replica were found to have extracted a number of rods, as shown in Figure 5.84, and these were cut into small squares and processed as described in the Experimental Procedure section. One square was lost during processing, but one was successfully transferred to a TEM disk and examined.

Upon examination, it was seen that the biotin film was not entirely removed by the acetone float treatment, however images and diffraction patterns were still obtainable. This was true even though the rods were examined as extracted, without any attempt at thinning. Figure 5.85 is a bright-field image of one portion of a rod, showing the surrounding film. The impression of another portion of the rod which was apparently lost in removing the film from the fracture surface is apparent at the top of the figure. A dark-field image of this rod was obtainable from one of the diffraction pattern spots, and is reproduced as Figure 5.86. As seen there, the entire rod is illuminated by imaging this spot, indicating that the image zone axis is common to the entire rod crystal structure. Figure 5.87 provides a bright-field image of another rod, however, in which a boundary is apparent oriented perpendicular to the rod axis, with one side

brightly illuminated and the other dark. It is likely that this is a grain boundary, since no other reasonable cause of such contrast is plausible.

Diffraction patterns were obtained from a number of rods. Bright-field images were obtained for most of these patterns, for correlating zone axis with rod morphology. An example of an image and the corresponding diffraction pattern is presented in figures 5.88 and 5.89, respectively. As described in the Procedures section, the diffraction patterns were indexed with plotted patterns generated using the Desktop Microscopist computer program. The indexed pattern for Figure 5.89 is shown in Figure 5.90, generated for a MnS alpha crystal with zone axis [100]. Table 5.3 summarizes the diffraction images obtained<sup>1</sup>, the zone axes predicted by the indexed patterns, and the characteristics of the corresponding bright-field image, when available.

All indexed patterns could be generated from the alpha modification of MnS, which has the NaCl rock-salt structure. Further, as seen in Table 5.3, all but two of the indexed patterns had zone axes in which one or more of the Miller indices was zero. In other words, the zone axes for these images were perpendicular to one of the principal axes of the MnS alpha structure. Most images were obtained from large portions of rod, for which it was reasonable to assume that the rod axis was approximately perpendicular to the indexed zone axis. Of the two patterns indexed to zone axes with three non-zero indices, one (diffraction images 903 and 904, [123] zone axis) was taken from an area of the rod which had fractured, in an attempt to find a naturally thin portion of the precipitate. The other pattern (diffraction image 957, [111] zone axis) did not have a corresponding bright-field image, however it is noted that the pattern itself exhibits some degree of asymmetry, and thus it is possible the indexed zone axis is not exactly perpendicular to the projected plane of the subject rod. Thus for both of these images the relationship of the indexed pattern to the rod morphology is uncertain.

---

<sup>1</sup> In Table 5.3 images are designated by the frame number automatically assigned each negative by the TEM instrument. This number designation is used merely for convenience.

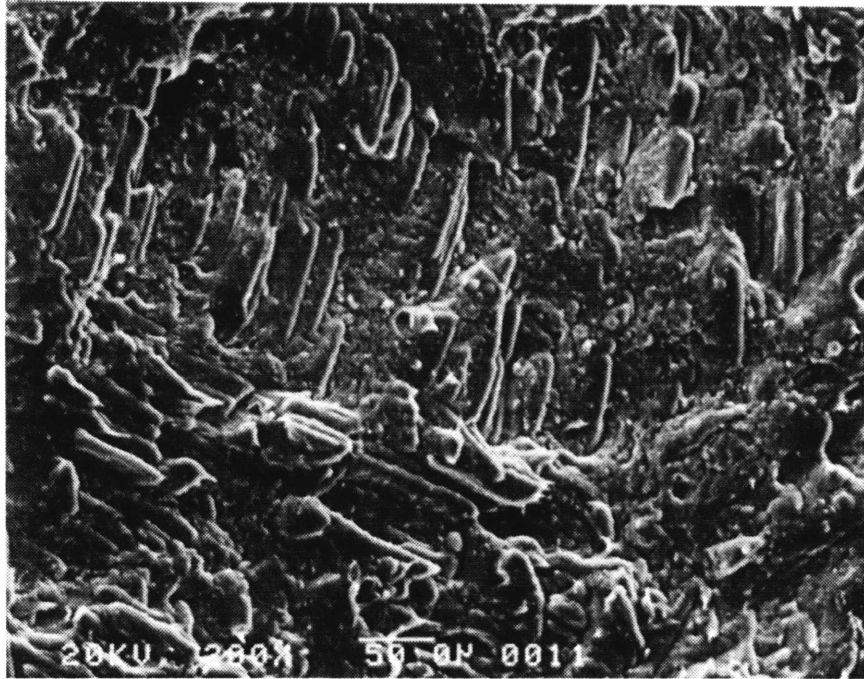


Figure 5.83 Region of Extraction Replica Film Exhibiting Elongated Ductile Dimple Morphology  
Spec. 4-2-1, 1250°C, 2°C/min, SEM

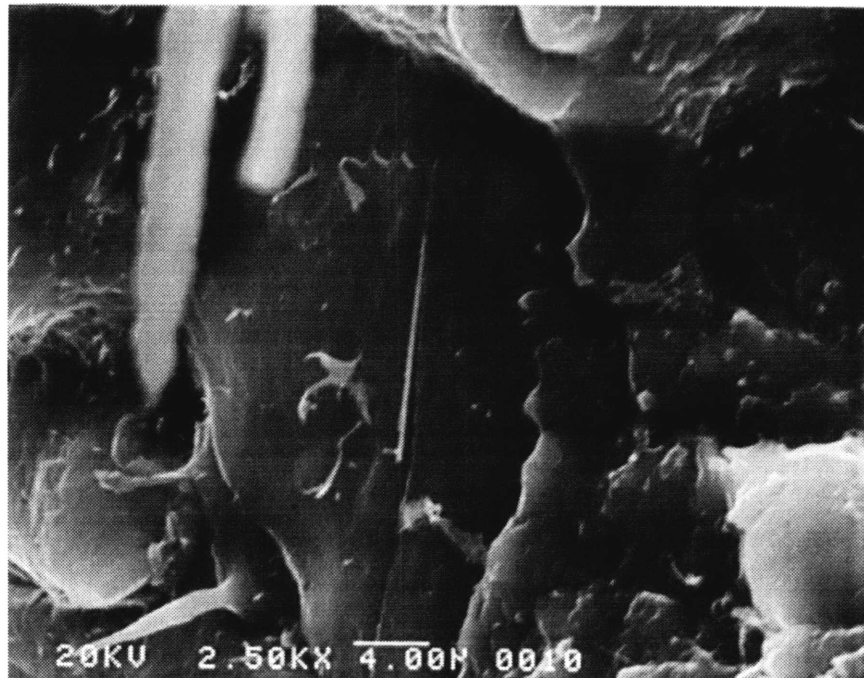


Figure 5.84 Extracted Rod Captured Within Replica Film  
Spec. 4-2-1, 1250°C, 2°C/min, SEM



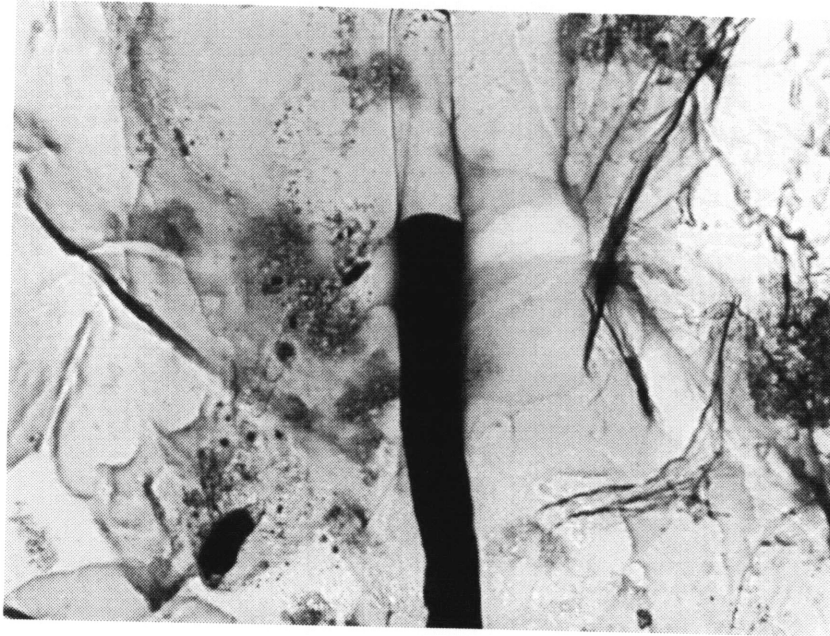


Figure 5.85 Bright-Field Image of Portion of Extracted Rod in Biotin Film  
Spec. 4-2-1, 1250°C, 2°C/min, TEM



Figure 5.86 Dark-Field Image of Entire Rod of Figure 5.85  
Spec. 4-2-1, 1250°C, 2°C/min, TEM



Figure 5.87 Dark-Field Image of Extracted Rod Exhibiting Contrast Boundary Possibly Due to Crystal Grain Boundary  
Spec. 4-2-1, 1250°C, 2°C/min, TEM

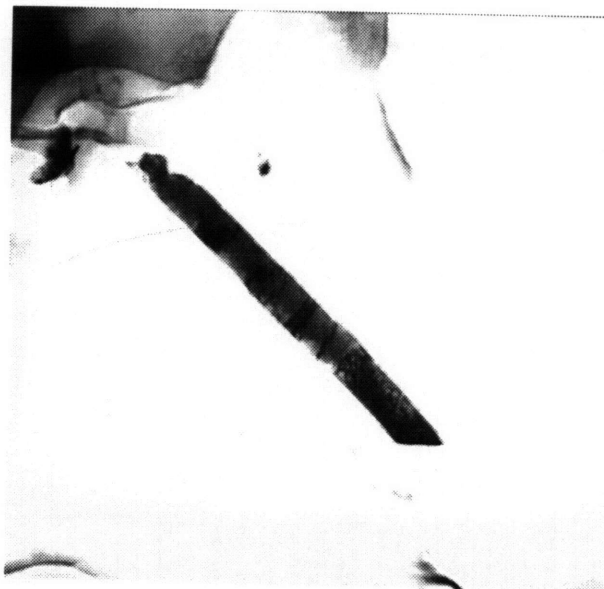


Figure 5.88 Bright-Field Image of a Typical Rod  
Spec. 4-2-1, 1250°C, 2°C/min, TEM

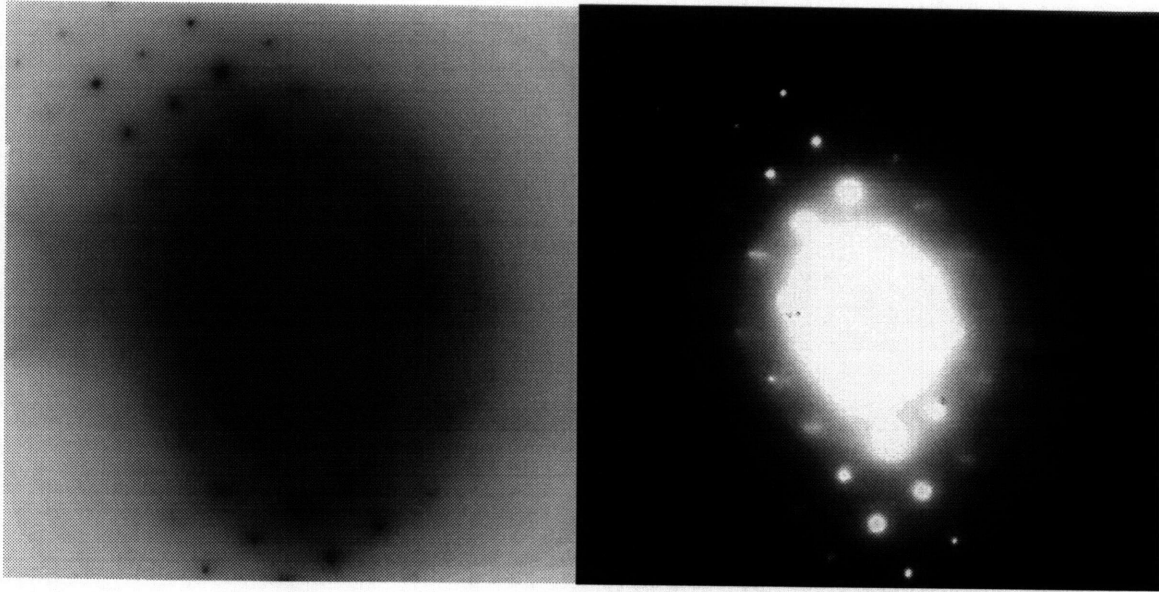


Figure 5.89 Diffraction Pattern Corresponding to Image of Figure 5.88, Scanned Negative (Left) and Printed Negative (Right)  
Spec. 4-2-1, 1250°C, 2°C/min, TEM

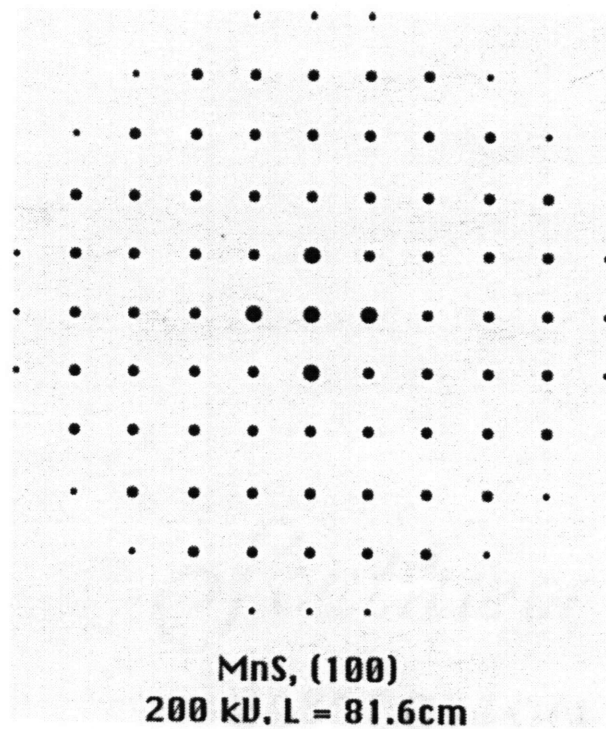


Figure 5.90 Indexed Diffraction Pattern Generated by Desktop Microscopist for Alpha MnS and [100] Zone Axis

Table 5.3 Summary of Indexing of TEM Diffraction Patterns From Extraction Replicas

Photo	Zone Axis	Image Orientation	Comment
896	[110]	perpendicular	very difficult to index
902	[100]	perpendicular	difficult to index
903/904	[123]	near broken area	
957	[111]	no image	asymmetric
958/959	[100]	perpendicular	
963	[100]	no image	
964	[100]	no image	

## 5.2.2. Trace Analysis

This section describes results obtained from the trace analysis of rods and annealing twins in the etched martensitic samples. The metallographic data will be addressed first, followed by the analysis results obtained from the TRACE and RODS codes for the input data. Finally a summary of the analysis results regarding precipitate/matrix orientation relationship is provided.

### 5.2.2.1. Metallography for Input Data

After processing the martensitic material samples (5-1-X series) as described in the Procedures section, it was possible to obtain four twin extractions which fulfilled all the metallographic requirements for a trace analysis. Micrographs from which the analysis input data was obtained for one specimen, no. 5-1-S1, are provided as an example in figures 5.91-96. (Figure 4.7 in the Procedures section is actually a sketch of the geometry of this specimen.) The original sectioned and mounted Charpy V-Notch specimen, etched with Villela's reagent, is shown in Figure 5.91, in which a large prior austenite grain containing two nonparallel annealing twins is clearly visible. Figure 5.92 shows the surface from the previous figure, designated surface A for the analysis, re-etched after the sawcut intersecting twin 2 was made. Figure 5.93 is, in turn, a micrograph of the new surface (surface B) resulting from this cut, after etching with Villela's reagent. Figure 5.94 is a micrograph of the etched surface A, with a rod trace adjacent to the trace of twin 2, while Figure 5.95 is a composite micrograph of the etched surface B, with a rod trace in the lower middle portion of the image, and the edge common to the two surfaces at the top. Geometric parameters required as input data to the analysis were measured directly from these micrographs. Parameters for the other three analyses were measured from similar micrographs. Table 5.4 summarizes the input data obtained for all specimens.

### 5.2.2.2. Computer Model Results

Input data as summarized in Table 5.4 was processed using the TRACE code which, as described previously, outputs a file of normal and trace vectors for each of the other three octahedral planes in any orientation which parallels the trace of the second twin within a specified tolerance, as measured by the dot

product criterion. It also outputs a file of dot product values for all three octahedral planes for all angles of rotation. The output files generated by TRACE for all specimens are provided in Appendix A.2, including the output for specimen 5-1-S1, using a dot product criterion of 0.0001. The variation of the dot product vs. angle of rotation for this specimen is plotted for the other three octahedral planes in Figure 5.96.

The geometric behavior of the other three octahedral planes during the rotation required by the solution process is not intuitively obvious, but it becomes apparent upon examination of Figure 5.96. As seen in that figure, the transient pattern of traces which planes 2, 3 and 4 would make on surface A are identical, but out of phase by  $120^\circ$ . Although at first glance the curve for plane 3 appears dissimilar, inverting it produces a curve identical to that of planes 2 and 4. This inversion is completely acceptable, since the sign of the dot product is artificial, a result of retaining an arbitrary sense of the normal vector defining plane 3. Also, as seen in Figure 5.96, the absolute value of the dot product is unity twice during the rotation for each of the three other octahedral planes. In other words, there are six possible orientations of the austenite crystal which could produce the observed traces.<sup>1</sup> In fact, however, the six solution orientations output by TRACE represent only two crystallographically unique orientations. Thus it is to be expected that the six orientation solutions will only predict two crystallographically distinct directions for the rod axis.

Plots similar to Figure 5.96 are provided in figures 5.97-99 for the analyses performed on metallographic data from specimens 5-1-S2, 5-1-1 and 5-1-2. A useful feature of curves such as these is illustrated by comparing figures 5.96 and 5.98. In Figure 5.96 the domains in rotation angle over which the absolute value of the dot product is close to unity are small. This implies that a narrow range of austenite orientations would produce traces such as those measured for the metallography input data, and that small errors in measurement of metallographic quantities are unlikely to produce large errors in the orientation solutions. In other words, the crystallographic problem represented by the

---

<sup>1</sup> TRACE outputs all orientations which satisfy the dot product criterion, which in the case of the 5-1-S1 analysis amounts to 55 orientations. These envelope the six true solutions, so the output file is edited to retain only the "closest" for input to the RODS program.

annealing twin traces on specimen 5-1-S1 is well-posed. In contrast, the dot products of Figure 5.98 approach unity over large domains of rotation angle. It is clear that a wide variety of austenite orientations could produce the traces observed on specimen 5-1-1. Small errors in measuring metallographic quantities could have a large influence on which orientation within this domain is the "closest". Thus the rod orientations determined from the 5-1-S1 analysis are likely to be significantly more accurate than those determined from the 5-1-1 analysis. This is also true of the traces of specimen 5-1-2, which exhibit the same large solution domains, as seen in Figure 5.99. For this reason specimens 5-1-1 and 5-1-2 were not retained in the analysis.

Continuing the example of specimen 5-1-S1, an input file containing the six closest orientations edited from the output of the TRACE program was input to the RODS program. The set of axis directions, in the form of unit vectors in the cubic crystal system, output by the code for the two observed rods is included in Appendix A.4.<sup>2</sup> These unit vectors must then be rationalized to yield Miller indices, which is done by normalizing the components of each vector and taking their absolute value. This calculation is performed on the RODS output for specimen 5-1-S1 in Table 5.5. The fact that the six austenite orientations determined by TRACE represent only two crystallographically unique orientations is demonstrated by the fact that the rod directions determined by RODS for rod A can all be grouped into two families of indices:  $[1\ 1\ 0]$  and  $[1\ 14\ 23]$ .

The sets of Miller indices calculated by RODS for the rod directions observed on the other specimens are also summarized in Table 5.5. As seen there, the six sets for each rod on the other specimens can also be grouped into only two distinct families of directions. The task of determining in each case which of the resulting two sets is the correct one is accomplished by considering the consistency of the data. By inspection, the distinct sets for each rod include one direction which is close to  $[1\ 1\ 0]$  and one which is not. First the directions which are not close to  $[1\ 1\ 0]$  are plotted on the stereographic triangle. Direction cosines are calculated for

---

<sup>2</sup> The input files for both the TRACE and RODS programs for all analyses are provided in Appendix A as well.

each set of Miller indices [i j k] by:

$$l = i / (i^2 + j^2 + k^2)$$

$$m = j / (i^2 + j^2 + k^2)$$

$$n = k / (i^2 + j^2 + k^2)$$

Then the location on the stereographic triangle of the direction cosines l, m and n, expressed as x and y coordinates in a Cartesian coordinate system centered on the pole of the projection, is calculated by [72]:

$$x = l / (1 + n)$$

$$y = m / (1 + n)$$

Figure 5.100 depicts the cubic system stereographic triangle with the directions not close to [1 1 0] plotted. A fairly large scatter in the predicted directions is apparent in that figure. Figure 5.101 reproduces this plot selecting the directions from Table 5.5 which are close to [1 1 0]. As seen there, these directions show fairly good agreement centered about the [1 1 0] direction. It should be recalled that these directions were determined for the four rods observed on specimens for which the crystallographic problem was well-posed, namely specimens 5-1-S1 and 5-1-S2.



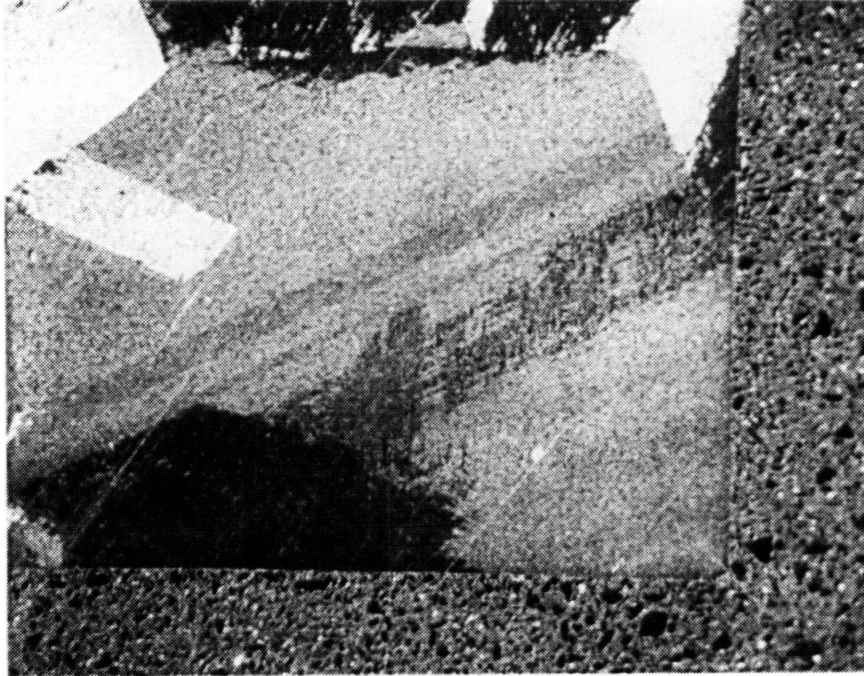


Figure 5.91 Dark-Field Image of Extracted Rod Exhibiting Contrast Boundary Possibly Due to Crystal Grain Boundary  
Spec. 5-1-S1, 1300°C, 2°C/min, Fractograph, 20X

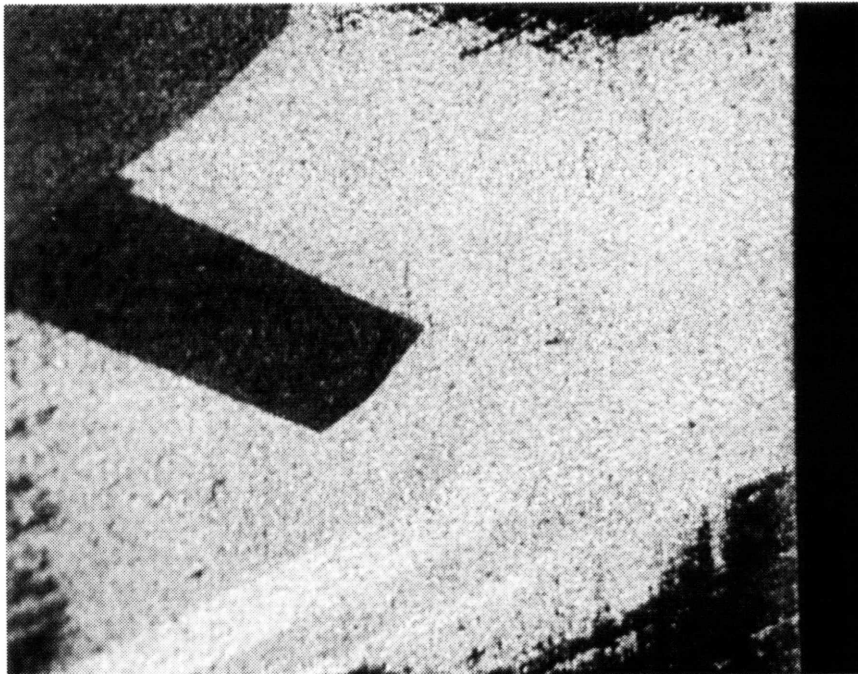


Figure 5.92 Surface of Figure 5.91 (Surface A) After Sawcut to Intersect Twin 1 is Made, Re-Etched With Villela's Reagent  
Spec. 5-1-S1, 1300°C, 2°C/min, Fractograph, 40X

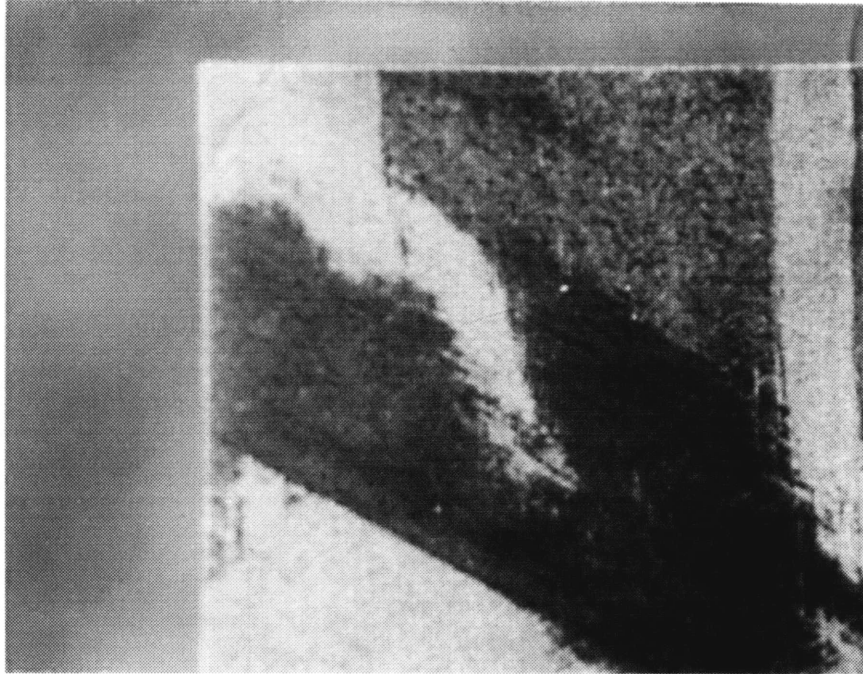


Figure 5.93 New Surface Produced by Sawcut to Intersect Twin (Surface B), Etched With Villela's Reagent  
Spec. 5-1-S1, 1300°C, 2°C/min, Fractograph, 20X

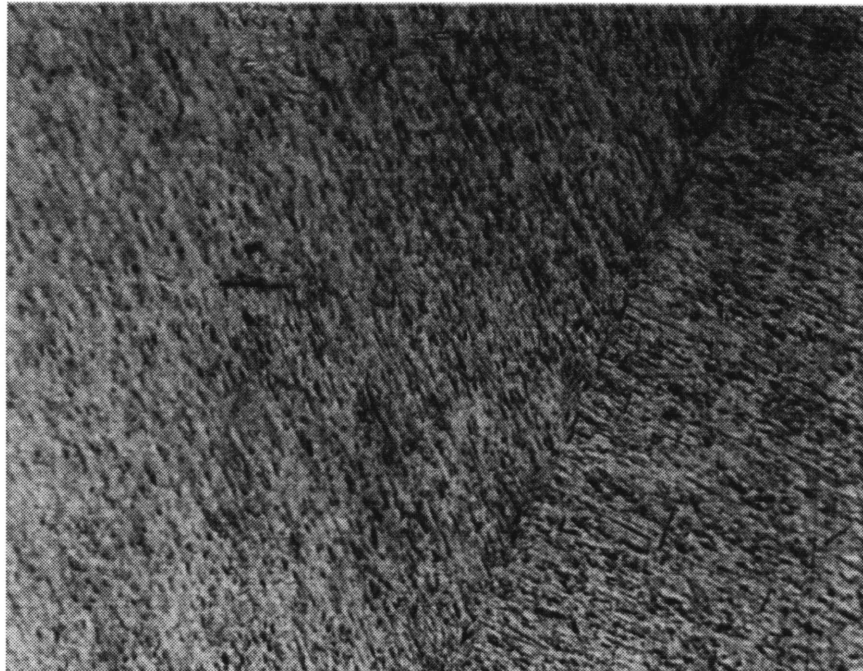


Figure 5.94 Micrograph of Etched Surface of Figure 5.91 (Surface A), Etched With Villela's Reagent, Showing Rod Adjacent to Twin Trace  
Spec. 5-1-S1, 1300°C, 2°C/min, Metallograph, 200X



Figure 5.95 Composite Micrograph of Etched Surface of Figure 5.91 (Surface B), Etched With Vilella's Reagent, Showing Common Edge at Top and Rod Trace at Lower Center

Spec. 5-1-S1, 1300°C, 2°C/min, Metallograph, 500X

Table 5.4 Trace Analysis Input Data for All Specimens

Specimen	PsiA1	PsiB1	PsiA2	PsiB2	XiA	XiB
5-1-S1	65.0	119.0	112.0	N/A	-1.0	58.0
5-1-S2	96.5	62.5	22.0	N/A	19.5	67.5
5-1-1	49.0	82.0	118.5	106.5	N/A	138.0
5-1-2M	53.0	70.5	169.5	129.5	21.0	N/A

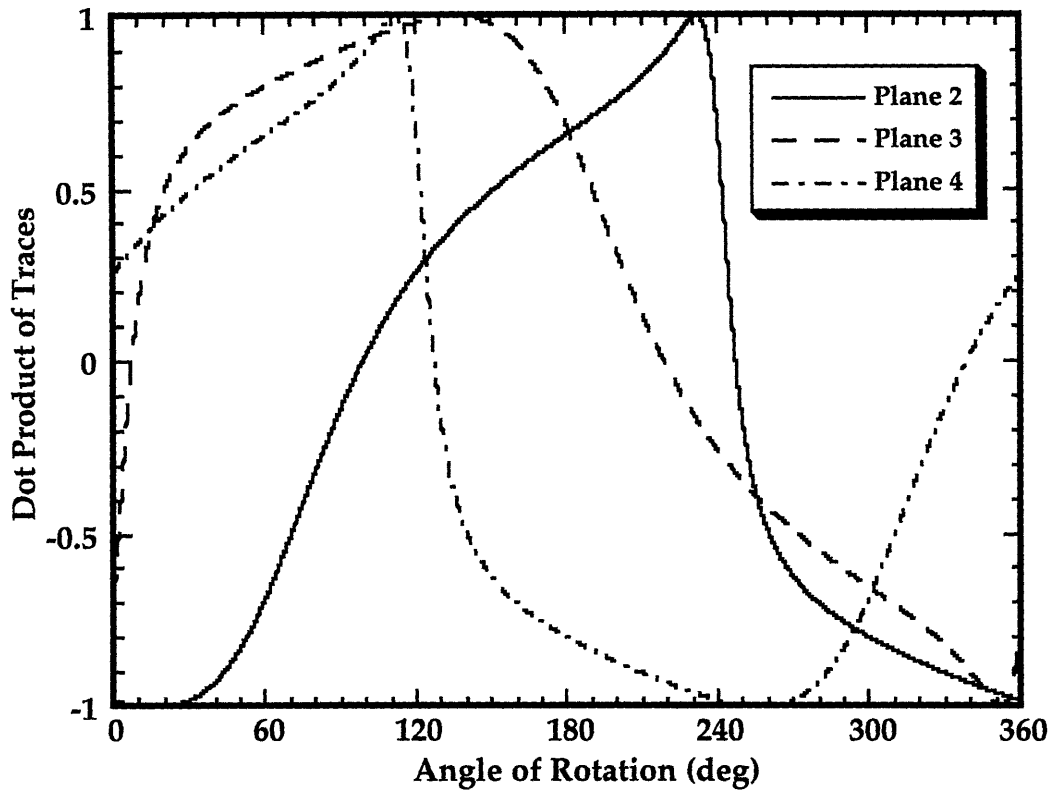


Figure 5.96 Dot Product Solution Curves for Remaining Octahedral Planes Versus Analysis Rotation Angle for Specimen 5-1-S1

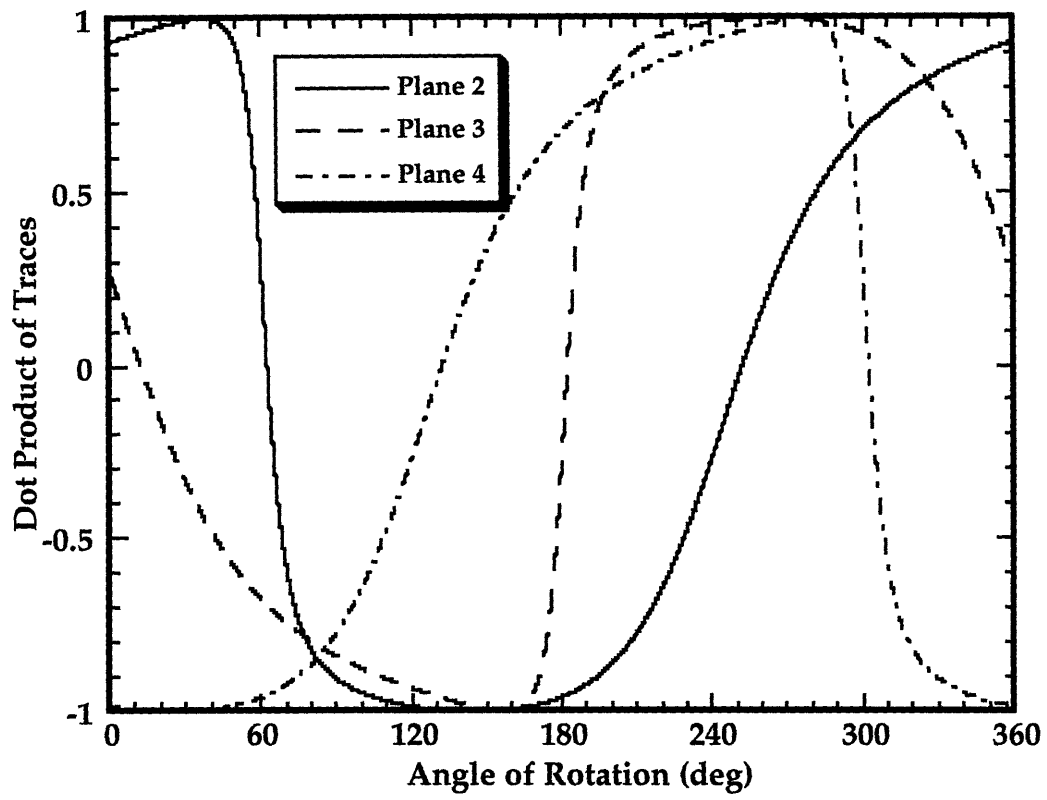


Figure 5.97 Dot Product Solution Curves for Remaining Octahedral Planes Versus Analysis Rotation Angle for Specimen 5-1-S2

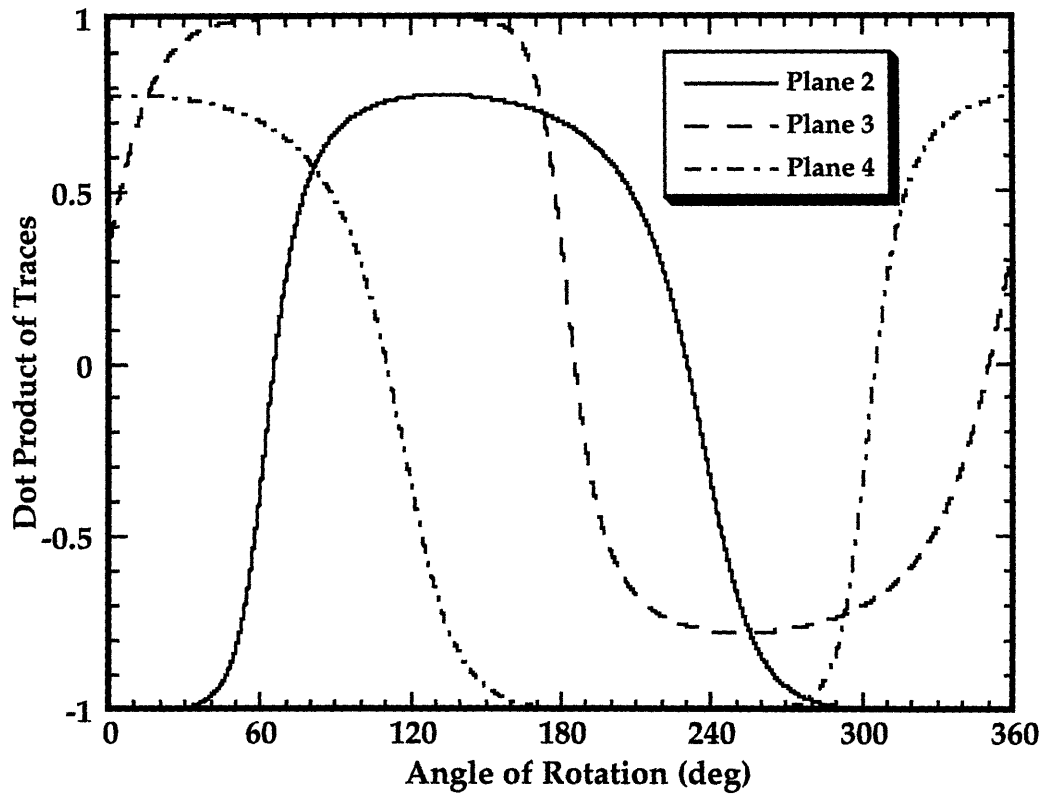


Figure 5.98 Dot Product Solution Curves for Remaining Octahedral Planes Versus Analysis Rotation Angle for Specimen 5-1-1

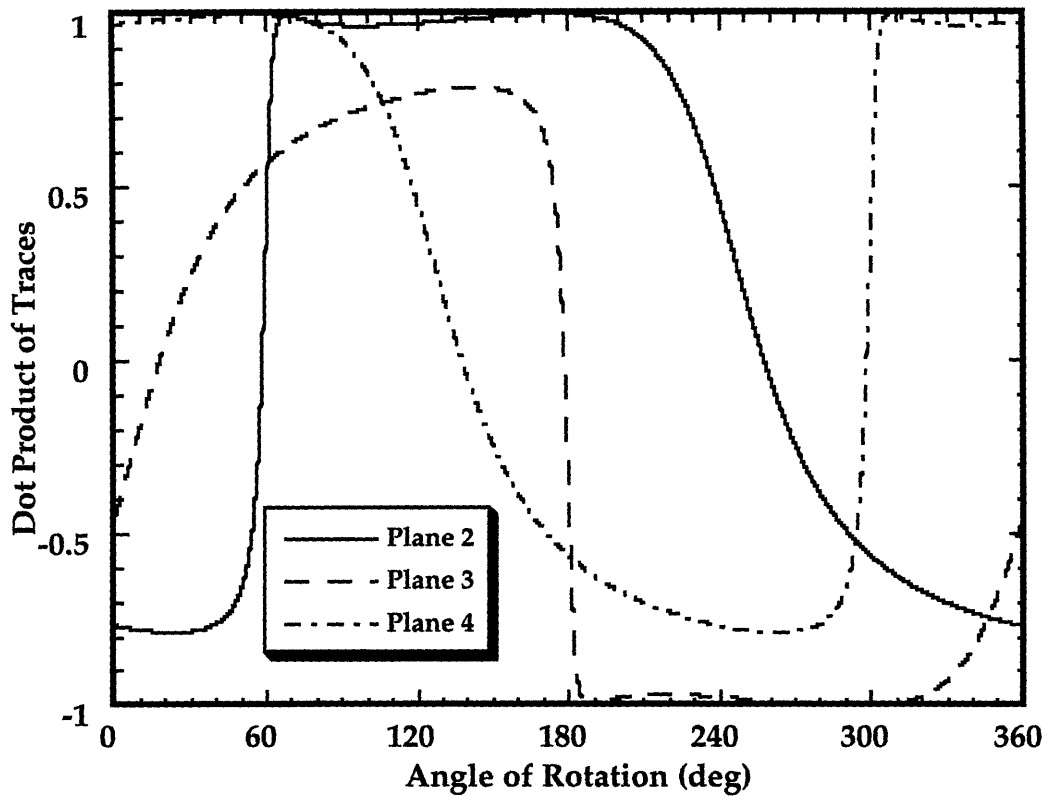


Figure 5.99 Dot Product Solution Curves for Remaining Octahedral Planes Versus Analysis Rotation Angle for Specimen 5-1-2



Table 5.5 Cubic System Unit Vectors and Rationalized Miller Indices for the Rod Traces,  
As Determined by the RODS Code

Angle of Rotation	Oct. Plane	Rod A Direction (unit vector)	Rod B Direction (unit vector)	Rod A Direction (rationalized)	Rod B Direction (rationalized)								
5-1-S1													
16	2	0.000	0.716	0.698	-0.663	-0.749	0.009	0.0	1.0	0.9	1.0	0.0	
112	4	0.528	0.849	0.038	-0.884	-0.054	-0.465	14.0	22.5	1.0	1.0	0.1	0.5
137	3	0.716	0.698	0.000	-0.749	0.009	-0.663	1.0	1.0	0.0	1.0	0.0	0.9
232	2	0.849	0.038	0.528	-0.054	-0.465	-0.884	22.5	1.0	14.0	0.1	0.5	1.0
257	4	0.698	0.000	0.716	0.009	-0.663	-0.749	1.0	0.0	1.0	0.0	0.9	1.0
352	3	0.038	0.528	0.849	-0.465	-0.884	-0.054	1.0	14.0	22.5	0.5	1.0	0.1
5-1-S2													
25	4	0.696	0.713	0.091	-0.638	0.019	0.770	7.7	7.9	1.0	1.0	0.0	-1.2
37	2	0.764	0.638	0.097	-0.711	0.183	0.679	7.9	6.6	1.0	1.0	-0.3	-1.0
145	2	0.713	0.091	0.696	0.019	0.770	-0.638	7.9	1.0	7.7	0.0	-1.2	1.0
157	3	0.638	0.097	0.764	0.183	0.679	-0.711	6.6	1.0	7.9	-0.3	-1.0	1.0
265	3	0.091	0.696	0.713	0.770	-0.638	0.019	1.0	7.7	7.9	-1.2	1.0	0.0
277	4	0.097	0.764	0.638	0.679	-0.711	0.183	1.0	7.9	6.6	-1.0	1.0	-0.3

Table 5.5 Cont. Cubic System Unit Vectors and Rationalized Miller Indices for the Rod Traces,  
As Determined by the RODS Code

Angle of Rotation	Oct. Plane	Rod A Direction (unit vector)	Rod B Direction (unit vector)	Rod A Direction (rationalized)	Rod B Direction (rationalized)
5-1-1					
11	2		-0.262 0.577 0.774		1.0 -2.2 -3.0
81	3		0.040 0.998 0.051		1.0 25.3 1.3
131	3		0.577 0.774 -0.262		-2.2 -3.0 1.0
201	4		0.998 0.051 0.040		25.3 1.3 1.0
251	4		0.774 -0.262 0.577		-3.0 1.0 -2.2
321	2		0.051 0.039 0.998		1.3 1.0 25.4
5-1-2M					
55	4	0.346 0.875 -0.338		-1.0 -2.6 1.0	
68	2	0.510 0.766 -0.392		-1.3 -2.0 1.0	
175	2	0.875 -0.338 0.346		-2.6 1.0 -1.0	
188	3	0.767 -0.392 0.509		-2.0 1.0 -1.3	
295	3	-0.338 0.346 0.875		1.0 -1.0 -2.6	
308	4	-0.392 0.510 0.766		1.0 -1.3 -2.0	

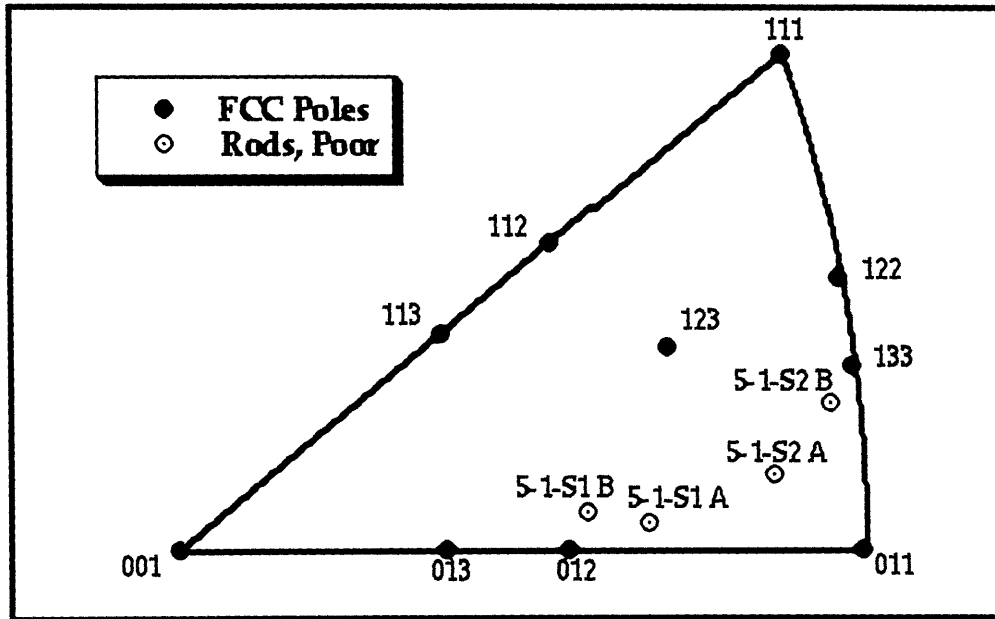


Figure 5.100 Face-Centered Cubic (FCC) System Stereographic Triangle With Widely Scattered Results of Trace Analysis

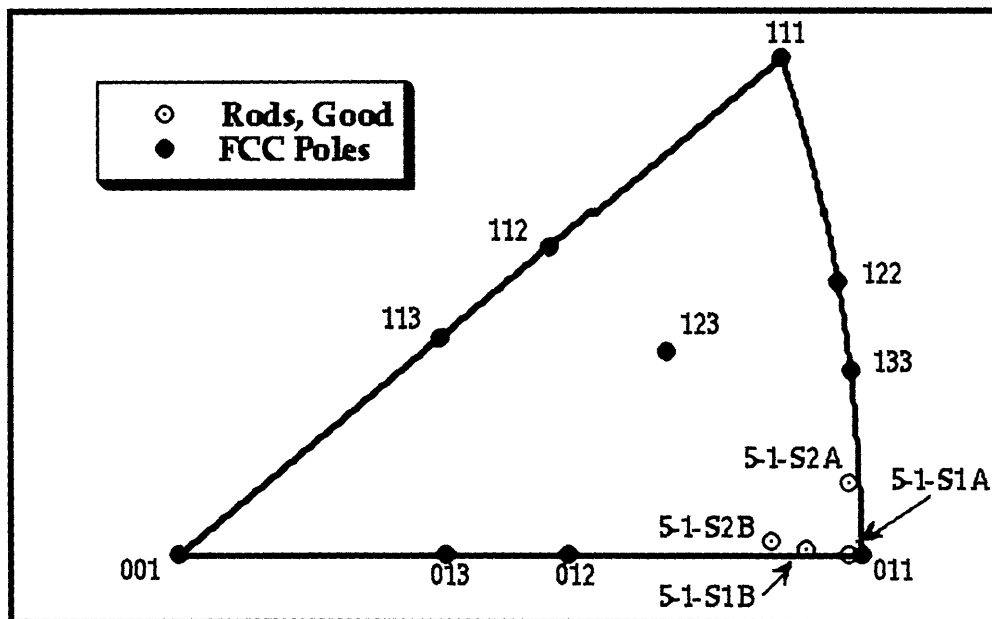


Figure 5.101 Face-Centered Cubic (FCC) System Stereographic Triangle With Closely Agreeing Results of Trace Analysis

## 6.0 Discussion

### 6.1 Overheating Tests

#### 6.1.1 Initial Material Condition

The first point of discussion concerns the as-received condition of the 3.5NiCrMoV material. Overheated facets with the classical morphology of numerous ductile dimples nucleated on fine sulfides were observed in fracture tests of control samples of this material. Since no overheating treatment was performed on this material, it is clear that the sample material as received already possessed some degree of overheating due to the forging treatment. This is supported by the large facet size, 1 mm and greater, characteristic of the size of grains which would form during a long forging heat.

The location of the test ring on the flywheel forging, from which the subject 3.5NiCrMoV was obtained, was at the transition between the long journal and the disk. The journal was known to be severely overheated since it had been through a furnace heat after it was forged. The disk, however, exhibited no cracks, which were the end product of overheating in the journals, and thus was believed to be free of overheating. Thus the as-received material may represent a transition state, characteristic of a material for which deformation after high-temperature treatment has only partially prevented overheating. In particular, the distorted facets shown in Figure 5.3 appear to be overheated PAGB facets which were not deformed sufficiently to prevent their MnS network structure from serving as an advantageous fracture path. In any case, it is evident that the deformation which did occur took place after the overheated MnS networks had already precipitated at the austenite grain boundaries.

The test ring was relatively close to the as-forged surface, compared to other regions of the final piece, thus it should have experienced more rapid cooling on the press after the last heat, allowing overheating to occur before deformation. **The implication of this result is that, if temperatures in the overheating regime are to be employed during forging of steels with a susceptible composition, the beneficial effect of dynamic recrystallization during forging while cooling**

through the precipitation range may only be realized in the inner, more slowly-cooled regions. Thus post-heat deformation alone may not be sufficient to prevent overheating in components with a small size and/or a high yield<sup>1</sup>.

### 6.1.2 Precipitation Phenomena Variation with Temperature and Cooling Rate

Figure 6.1 summarizes the occurrence of the various precipitation phenomena over the temperature/cooling rate domain as observed in this work. Phenomena are plotted vs. nominal temperature and cooling rates, e.g., the results of the cooling rate tests which used a 1280°C preheat temperature are included in the 1300°C subdomain. Trends in the fundamental precipitation behavior can be elucidated by examining constant temperature or cooling rate "slices" of this diagram. An attempt is made now to suggest physical models which can rationalize these trends.

#### 6.1.2.1 Phenomena Versus Cooling Rate

Consider a constant temperature slice at a preheating temperature of 1300°C. At the extremely rapid cooling rate of an air quench no unusual sulfide precipitates are observed, thus it is likely that the assertion by Hale & Nutting [10] that solutionized sulfur remains "locked into" supersaturated solution is valid. However even without the presence of fine overheated sulfides apparently the prior austenite grain boundaries remain a low energy fracture path, yielding the large inclusion-free facets observed during this work. Although these facets are inclusion-free, they are not dimple-free. Rather they are covered with the fine scale (< 5 µm) ductile dimples which are associated with a classically overheated piece. The underlying cause of this phenomenon is unknown, however it is proposed that this morphology might be a form of "void sheeting". The mechanism is as follows.

---

<sup>1</sup> Yield is the percentage of forged material retained in the final machined piece.

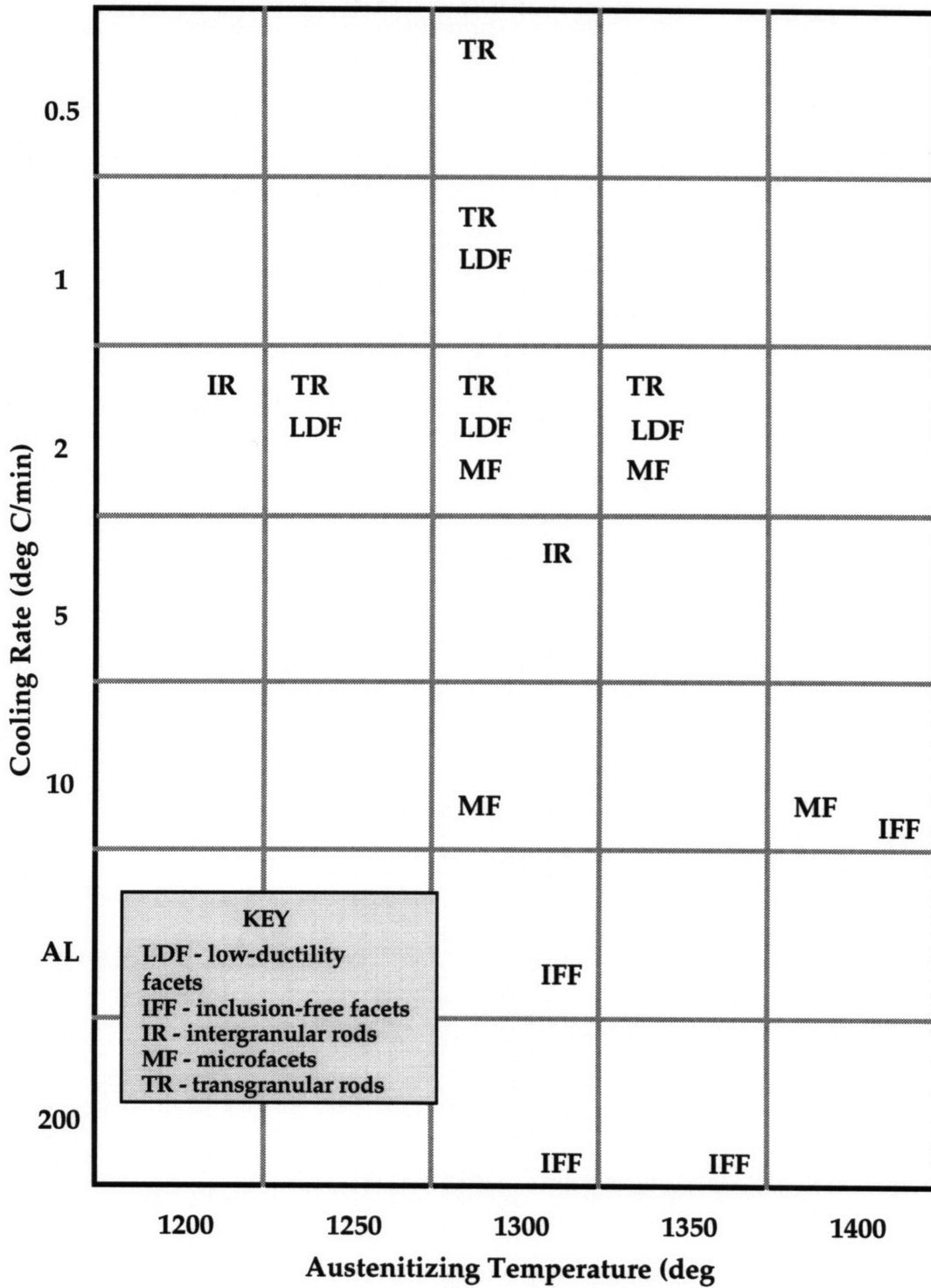


Figure 6.1 Summary Diagram of Precipitation Phenomena Observed in 3.5NiCrMoV

During the high-temperature austenitization the overheated manganese sulfides which existed at the prior austenite grain boundaries in the as-received material are dissolved. The sulfur and manganese atoms diffuse to some degree into the austenite matrix, leaving behind cavities corresponding to the location and size of the precipitates. These cavities either 1) shrink, due to vacancies "boiling off" into the matrix, 2) remain stable, or 3) are "filled" to some extent with impurity atoms which have segregated at the boundary. Provided the cavity survives the one-hour treatment and cool-down period in some form, it will be fixed at room-temperature, either empty or containing some amount of impurity atoms. Central to this model is the requirement that interstitial sulfur and substitutional manganese atoms diffuse more rapidly through the matrix than do vacancies. The cavities should be stabilized by the surface-active nature of sulfur. While most sulfur will diffuse into the matrix, the tendency of sulfur to segregate at free surfaces will ensure that some will be retained on the cavity wall. This, in turn, lowers the surface energy of the cavity, helping to stabilize it from collapse. The mechanical effect of a sheet of such cavities is equivalent to a network of overheating sulfides, serving to minimize the work of fracture required along the interface. This produces fracture by microvoid coalescence along the PAGB, yielding a ductile dimple morphology which is free of sulfide inclusions.

Continuing to move along the constant temperature slice in the direction of slower cooling rates, the first fracture feature to be observed is that of intragranular microfacets, observed in this work at a cooling rate of  $10^{\circ}\text{C}/\text{min}$  and below. At these rates, time-at-temperature is sufficient to allow the close-range sulfur diffusion required for nucleation and growth of the extremely small sulfides observed within the microfacets. The time is not sufficient, however, to allow longer range diffusion for growth of larger sulfides such as rods. Further, the rate is rapid enough that the degree of undercooling at the onset of precipitation is large, i.e., there is a large driving force for the supersaturated sulfur in solution within the austenite grain interior to precipitate out.

As noted in the literature review section, Andrew et. al. [2] determined that these facets formed as a result of sulfide precipitation on crystallographic planes of the austenite. Although the exact physical mechanism underlying this phenomenon is once again unknown, a model is suggested. The large undercooling implies the sulfide has a strong incentive to form as an inclusion within the matrix,

before the matrix can completely accommodate it by self-diffusion. Consider the first sulfide inclusion formed within an austenite grain, as shown in Figure 6.2. The volume free energy change induces it to form, despite the constraint of the surrounding matrix. The resulting inclusion is compressed inward by the matrix, while the matrix is expanded outward by the presence of the inclusion. The interior of the austenite grain is elastically anisotropic due to its crystal structure, i.e., some directions are stiffer than others. Thus the strain field around the inclusion is asymmetric, with the greatest strain in the softest direction. This produces an elastically accommodating zone adjacent to the inclusion along planes perpendicular to the soft direction which in turn provides a preferential nucleation site for further sulfide precipitation. This is illustrated in Figure 6.3.

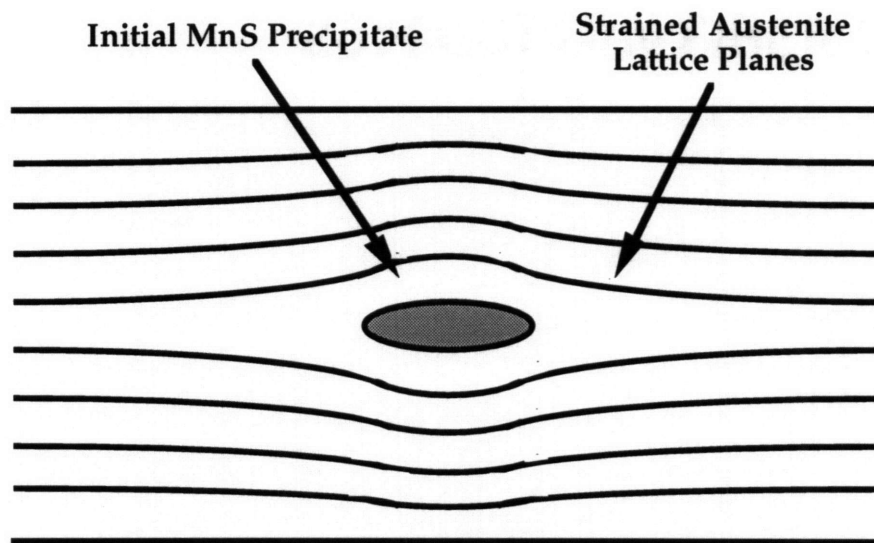


Figure 6.2 Rapidly-Formed Precipitate Straining Austenite Lattice Planes

The elastically accommodating zone is to a first approximation circular in shape about the initial inclusion, decaying spatially away from the inclusion but expanding temporally as the sulfide grows. This model might explain the "fractal" appearance of the microfacets. As seen in Figure 5.39, some microfacets appear to contain several smaller "micro-microfacets" which appear similarly structured. This might develop as the elastically accommodating zones



surrounding several nearby, growing micro-microfacets coalesce to yield a single larger microfacet with a greater tensile strain field. Subsequent precipitates can now form outside of the zones of the original micro-microfacets but within the zone of the new encompassing microfacet, filling it in with inclusions which are larger due to the greater magnitude of the tensile strain. The planar nature of the tensile field around the inclusions will favor planar growth of the later inclusions which nucleate and grow within it.

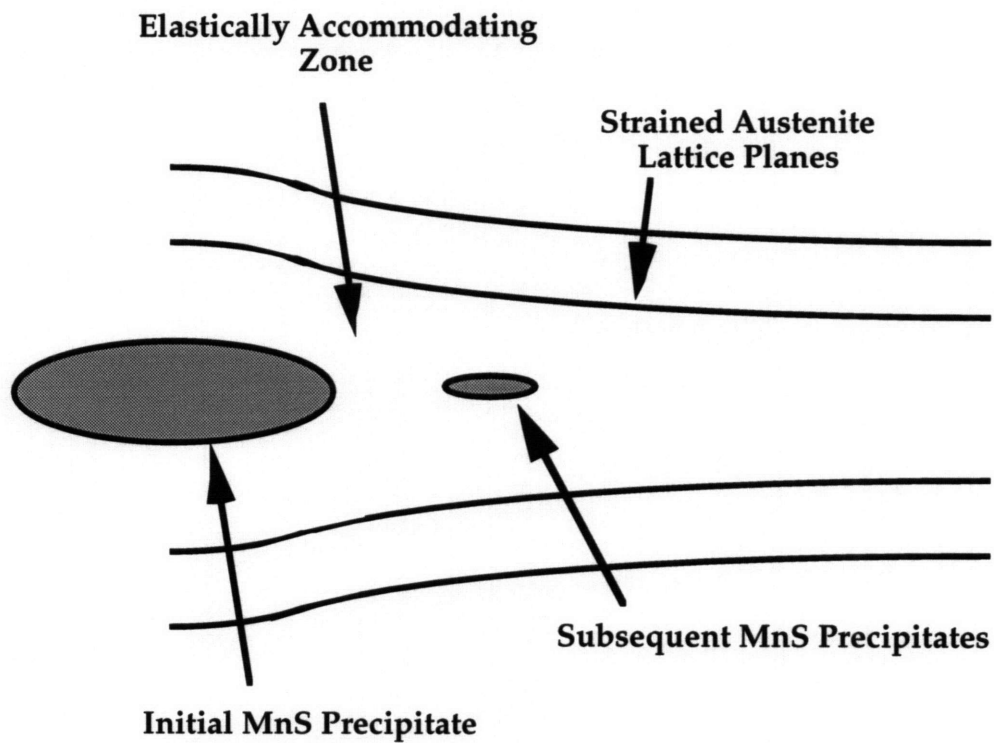


Figure 6.3 Subsequent Precipitates Forming in Elastically Accommodating Zone Adjacent to Initial Precipitate

Further slowing the cooling rate within the constant temperature slice of the temperature-rate precipitation diagram, the next sulfide morphology encountered is that of intragranular rods in conjunction with low-ductility PAGB facets, at a rate of 2°C/min. (The material cooled at 5°C/min will be discussed later.) At this stage, time-at-temperature is now sufficient to allow the long range diffusion required by larger sulfide morphologies. The slower cooling also

implies that the degree of undercooling at any point during nucleation and growth is very small compared to that during precipitation at the higher rates investigated. The volume free energy change in the precipitation process is lowered and thus this term becomes a less significant portion of the nucleation and growth thermodynamics, allowing other terms to assume a greater significance in determining the kinetics.

The dominant factors governing the thermodynamics of nucleation and growth at high-temperature are volume free energy change and interfacial energy. Diffusion rates are high at these temperatures, thus elastic strain energy is not a significant factor. At rapid cooling rates, there is significant undercooling, and thus the volume free energy change dominates, while the interfacial energy is minor in comparison. This means that sulfide inclusions whose orientations yield lower energy interfaces are not much more advantageous than those with higher energy interfaces. In contrast, at the slower cooling rates, morphologies and orientations with lower energy interfaces become more and more energetically favored as the volume free energy change term drops in relative significance. The precipitating sulfur has both the incentive and mobility to attach to a growing inclusion in a growth direction which yields the lowest energy interface. This is proposed to be the mechanism underlying the development of intragranular rods as the predominant sulfide type at cooling rates of 2°C/min and below. The nature of the low-energy interface will be discussed in section 6.2.

At the more rapid end of the cooling rate range in which rods are encountered, they form in conjunction with prior austenite grain boundary facets which have a low-ductility, quasi-cleavage morphology. These are in contrast to the PAGB facets encountered in air-cooled material, which were covered with ductile dimples. Returning to the model discussed in conjunction with the air-cooled material, after prior overheating sulfides dissolve during high-temperature heat treatment. PAGB cavities are left behind which are either vacant or contain some amount of impurity atoms. In the air-cooled material they remain after being quickly cooled to room temperature. The slowly-cooled material, however, experiences more time-at-temperature, during which the cavities can disappear due to boiling off of vacancies, creep, self-diffusion, etc. Once the cavities have disappeared to a sufficient degree, room temperature fracture will no longer take

place by microvoid coalescence. It is clear, however, that the PAGB is still embrittled to some degree relative to the matrix, since it appears as a facet on the fracture surface. The nature of this embrittlement is unknown although it could result from segregation of impurities, for example sulfur.

As noted in reference 104, in steels such as those investigated here there is little equilibrium segregation of sulfur to grain boundaries at lower temperatures. However as described in the above model, PAGB voids whose surfaces are covered with free sulfur will release it into the matrix as they disappear during cooling. This could be a source of an excess nonequilibrium concentration of sulfur at the PAGB, which is then locked in when quenched from 900°C. Whether such a concentration remains would then depend on the extent of void collapse/disappearance which has occurred by the time room temperature is reached. This, in turn, depends on the cooling rate. It is significant then that although extensive intragranular rods were observed, no accompanying low-ductility PAGB facets were in evidence on the surfaces of specimens cooled at the slowest rate of 0.5°C/min. This would fit with the hypothesized model, implying that the voids had sufficient time-at-temperature to collapse completely, releasing their entire content of sulfur into the matrix, where it would have time to diffuse to uniform distribution.

At a cooling rate of 5°C/min, PAGB facets were observed, but with a variety of inclusions within ductile dimples. These included globular type I inclusions, angular type III inclusions and small intergranular rods. Most investigations of overheating have indicated cooling rates between 10 and 200°C/min were the most detrimental to materials properties and produced the most faceted fractures [10]. It is believed that the PAGB sulfides observed in the 5°C/min specimens represent the low (i.e., slow) end of the cooling rate range at which reprecipitating MnS will nucleate first at the austenite grain boundary. As seen on the fracture surfaces of these specimens, at this rate a transition is in process to the rod morphology. The austenite grain boundary is still an advantageous nucleating site, however the undercooling and growth rates are low enough that nuclei grow in a rod morphology.

It should be noted here, however, that the austenitizing soak times employed in the cooling rate tests were only  $1/4$  to  $1/3$  as long as those employed in the

austenitizing temperature tests. The control of the soak temperature was also not as precise in these tests as in the austenitizing temperature tests. Thus it is possible that the sulfur content was not uniformly solutionized. Thus, for example, the globular and angular PAGB sulfides observed in material cooled at 5°C/min tests should also be expected in that cooled at 10°C/min tests as well.

The intergranular rod precipitates are an interesting phenomenon. The growth of intragranular rods is obviously governed by a uniform crystallographic environment. Rods at the austenite grain boundary, however, have different crystal surroundings on either side of the boundary. The question could be posed as to whether sulfide nuclei at the austenite grain boundary might not grow preferentially into one or another grain. Extending this line of argument further, one could ask whether the intragranular rods observed on other specimens had not in fact nucleated at a grain boundary and then grown into a grain. In that case they might be exposed on the fracture surface by virtue of having an optimal orientation with respect to the CVN specimen, while the boundary from which they originated might not. However, the intergranular rods which were observed appeared to lie in the plane of the PAGB facet. They were also uniformly much shorter than any of the intergranular rods. Finally, PAGB facets which were observed in conjunction with extensive intragranular rods exhibited little ductility, without the intergranular rods which should also appear were this line of argument valid. **Thus it seems likely that there is a genuine transition in morphology from intergranular to intragranular rods starting at a cooling rate of around 5°C/min.**

#### 6.1.2.2 Phenomena Versus Austenitizing Temperature

Next consider a constant cooling rate slice at 2°C/min. At the lowest austenitizing temperature (1200°C), large PAGB facets were observed whose surfaces were covered with ductile dimples nucleated on globular type I and angular type III MnS, as well as on intergranular rods. At this temperature it was expected that not all sulfur would be resolutionized, thus it is likely that some sulfides will remain at the PAGB from the prior overheating in the as-received material. During cooling, the solutionized MnS would precipitate at these boundaries, on the remaining very small sulfides which now serve as nuclei. Since sulfides in material from the 1300°C-2°C/min tests consisted virtually

entirely of intragranular rods, it is likely that the rod growth mechanism is also the dominant one in material undergoing a  $1200^{\circ}\text{C}-2^{\circ}\text{C}/\text{min}$  treatment. In this case, the non-rod morphologies may be vestiges of undissolved prior overheating sulfides. In any case, the significant observation is that at the lower austenitizing temperatures, prior overheated sulfides will remain which will serve as nucleation sites for reprecipitating sulfur, preventing the formation of the fully intragranular rods observed at the higher temperatures.

Figure 6.4 reproduces the format of the summary diagram of Figure 6.3 while generalizing the dependence of the observed precipitation phenomena on temperature and cooling rate. This diagram should be considered a very approximate map of the different morphologies to be expected in cooling 3.5NiCrMoV from forging temperatures. Arrows on the boundaries of some zones indicate it is likely that they extend further than indicated here, although there is not enough data in this work for predicting so with certainty. It should also be emphasized that this figure is specific to a sulfur level of 40 ppm, and is likely to vary widely for other concentrations. Some measure of the variation possible is provided by considering the A 508 material, with 60 ppm S, discussed in the next section.

### **6.1.3 A 508 Cl 4 Material Tests**

The condition and underlying processes of the A 508 Cl 4 specimens is in many ways similar to the  $1200^{\circ}\text{C}$  3.5NiCrMoV tests just discussed. Most apparent on the fracture surfaces of the commercial purity material is the much smaller prior austenite grain size. As noted by Hale and Nutting [10], sulfides can have a significant grain-pinning effect. Thus it is possible that not all manganese sulfides were dissolved in this material at  $1300^{\circ}\text{C}$ , and that these undissolved precipitates served to prevent the dramatic grain growth observed in the 3.5NiCrMoV material. The sulfur content is 60 ppm in the commercial purity material, 1.5 times that of the flywheel steel, so it is to be expected that the overheating temperature will be higher. This contention is supported by the much larger size of the prior austenite grain features which are barely observable in the superclean A 508 material, indicating that without the presence of sulfides the grains were free to grow unhindered.

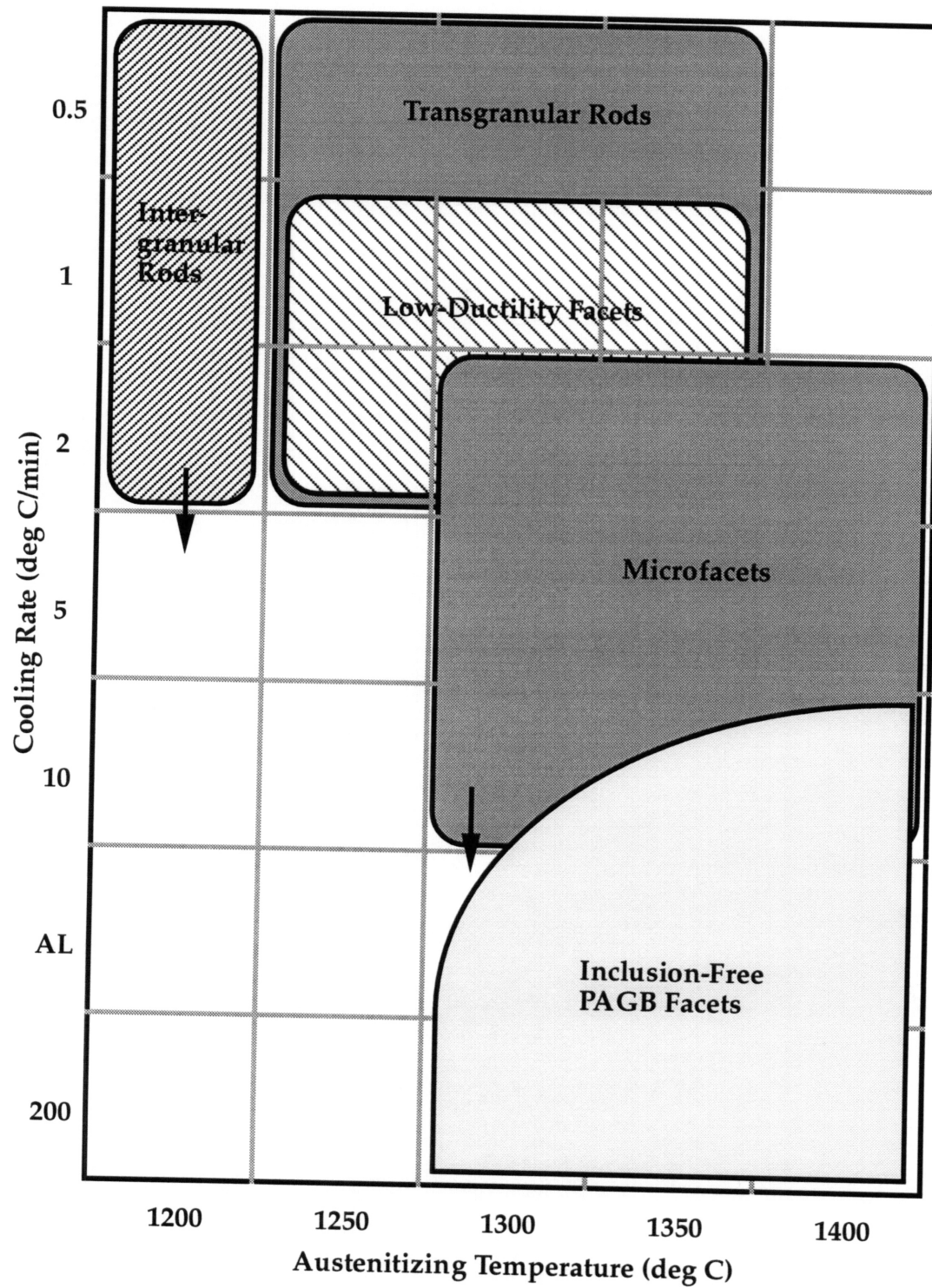


Figure 6.4 Generalized Diagram of Precipitation Phenomena Possible in 3.5NiCrMoV With 40 PPM Sulfur

Thus it is concluded that not all the sulfides were dissolved in these tests, and those remaining undissolved could serve as nuclei for further precipitation as the material cooled. The appearance of the same types of PAGB precipitates as observed in the 3.5NiCrMoV preheated at 1200°C; globular type I and angular type III MnS, as well as on intergranular rods, is understandable since neither material had exceeded its overheating temperature. The one main difference between the two is that the 3.5NiCrMoV material had prior overheating, while the A 508 Cl 4 probably did not. Thus the facets upon which the MnS precipitates appear are much larger in the 3.5NiCrMoV than in the A 508, since the undissolved sulfides in that material were remains of overheated precipitates on very large forging grains, while the sulfides in the A 508 were likely to be conventional, randomly-distributed inclusions from the melt.

#### 6.1.4 Implications for Forging Procedure

Frequently past investigations have studied whether overheated material could be "reclaimed" through some heat treatment, such as is possible with temper embrittled material. It has generally been the conclusion that a high temperature treatment followed by fast or slow cooling, or deformation, could significantly reduce the effect of previous overheating [10]. **However, considering the phenomenological model discussed above for PAGB facets resulting from coalescence of microvoids left by dissolution of prior overheated sulfides, it may not be sufficient to merely exceed the overheating temperature, since the embrittled grain boundary will still remain as a low energy fracture path. Rather, it is necessary to provide sufficient time-at-temperature for the microvoids and segregated impurities to disappear from the grain boundary in order to completely remove the effect of overheating.** Achieving this requires either a sufficiently long soak time above the overheating temperature, or a sufficiently slow cooling rate, both of which entail furnace costs and loss to scaling. This point, in conjunction with that previously mentioned on the possible risks of relying on post-heat deformation to remove the effects of overheating, points up the difficulties which may be encountered both in reclaiming a truly overheated piece as well as in forging within the overheating regime.

## 6.1.5 Implications for Material Performance

### 6.1.5.1 Rod Morphology Transition

The transition to an intragranular rod morphology for manganese sulfide inclusions can affect material properties in two basic ways. The first is due to the sulfide shape change. It is instructive to compare this to the work of Baker and Charles on the effect of MnS shape on the through-thickness toughness of hot-rolled steel [101]. In that study, they found a strong correlation between total sulfide length per area and loss of toughness, as measured by crack opening displacement required to produce fracture. However, the variable they evaluated was the greater projected length for a given amount of sulfide. In other words, greater rolling reductions forced a given volume of sulfide to project a greater length in the rolling plane, diminishing the toughness. This is in contrast to the rod sulfides studied here, in which the shape is the result of solid state precipitation. In this case, it was observed that rod diameters were in most cases not significantly different from the diameters of other globular sulfides, thus a given amount of sulfide precipitated in rod versus spherical form will not project significantly different area.

The more serious effect of rods on toughness results from their banded distribution within the austenite grain interior as well as their appearance in conjunction with low-ductility precipitate-free prior austenite grain boundaries. Figure 6.5 depicts these effects. In a conventionally overheated piece, in which the sulfur content of the steel is contained in uniformly distributed PAGB sulfides, fracture occurs by a mixture of transgranular ductile rupture and intergranular microvoid coalescence. In a piece which has been heat-treated in a manner to yield both intragranular rods and low-ductility PAGB facets, such as a 1300°C soak followed by a 2°C/min cool, both the narrow bands within which the rods precipitate and the prior austenite grain boundaries are low-energy fracture paths, as depicted in Figure 6.5. A propagating fracture can include both, which is the fracture surface morphology seen on the 3.5NiCrMoV material cooled at 1 and 2°C/min. **The aggravating effect of the rod precipitates is seen then to result from: 1) their concentration of total inclusion volume, which would normally be spread out over the grain boundary area, within narrow bands in the grain interior, and 2) the possible participation of embrittled**



**PAGBs occurring in conjunction with them in the fracture process.** The extent to which toughness is diminished is dependent on factors such as the width of the precipitation bands and whether the PAGB facets experience sufficient time-at-temperature to become de-embrittled, such as in the material cooled at 0.5°C/min.

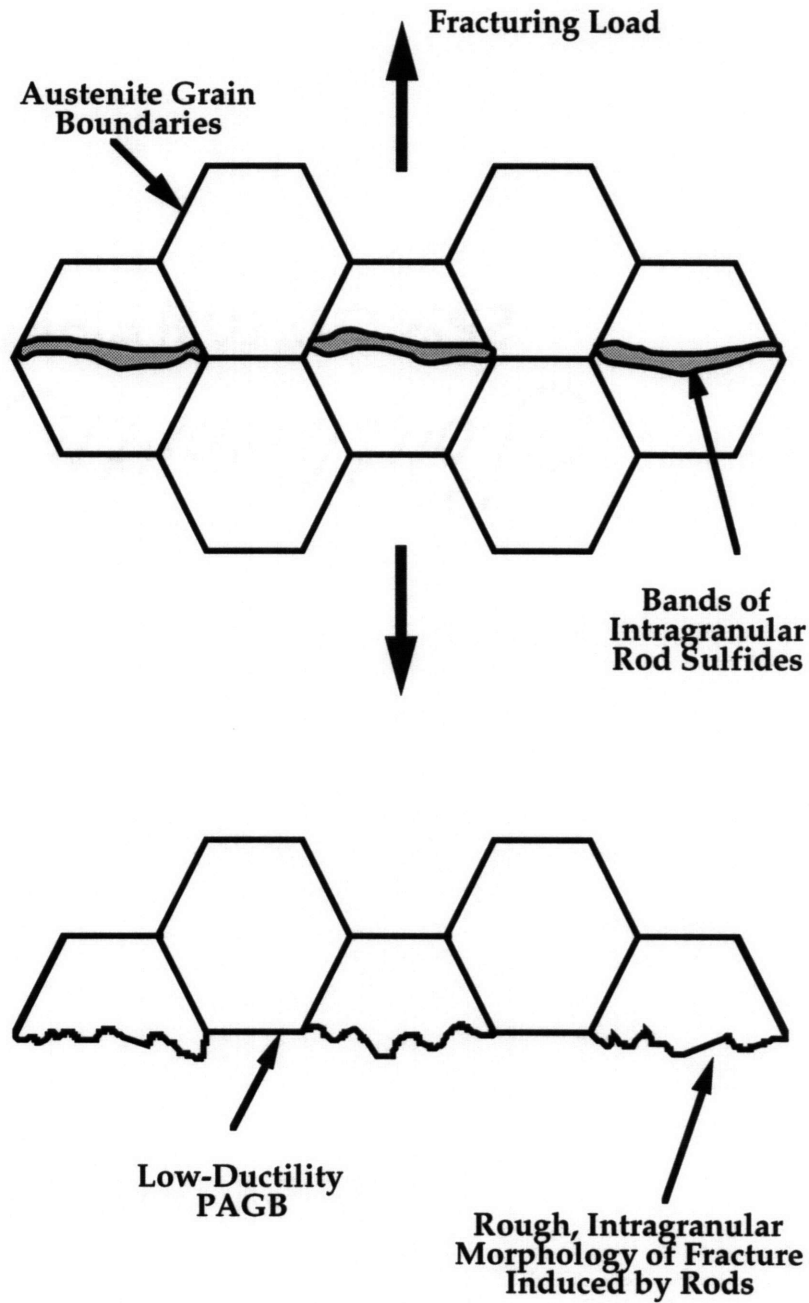


Figure 6.5 Affect on Fracture Propagation of Rod Bands and Low-Ductility PAGB

### 6.1.5.2 Necessity for Superclean Specification

As mentioned in the Literature Review section, there is serious debate within the forging industry concerning the need for specifying superclean compositions in forgings. This discussion usually centers on the possible benefits of producing a forging which can survive the higher temperatures of the temper embrittlement regime, e.g., turbine temperatures above 350°C. However as pointed out by J. Nutting during a comment session at a recent conference [116], the superclean specification was intended to prevent overheating as well as temper embrittlement. The effectiveness of this steelmaking technique is evident in the tests of the A 508 Cl 4 material.

Toughness is a critical property for steels used for reactor pressure vessels. The U.S. Nuclear Regulatory Commission sets a lower limit of 68 J (50 ft-lbs) on the upper shelf energy (USE), as measured by the Charpy V-Notch impact test, of the vessel material through the life of the reactor. The vessel as fabricated must have a sufficiently great margin of toughness to accommodate the radiation embrittlement which accumulates during service, while still remaining above this minimum. Thus a material which has an USE in the as-fabricated condition which is already close to this minimum value would be unacceptable.

As reported in the Results section, commercial purity A 508 Cl 4 which was slow-cooled from 1300°C had an USE of only 80 J (59 ft-lbs) due to the effects of overheating. Comparison to un-overheated material is difficult, since there is usually a significant effect due to orientation on the impact energy, and the orientation of the material specimens within the original material is unknown. However reference 12 provides typical impact energy values for commercial purity A 508 Cl 4 of about 183 J (135 ft-lbs) for longitudinal specimens and about 95 J (70 ft-lbs) for transverse specimens. **Thus in this material with this sulfur composition it must be considered possible for the overheated condition to yield a reduction in impact energy of at least 30%, and possibly up to 60-65%.** In contrast, the superclean A 508 material which experienced identical overheating treatment to the commercial purity material retained toughness levels which were almost three times those of the latter.

The development of materials properties as poor as those of the commercial purity A 508 is contingent upon employing a forging procedure which allows some portion of a finished forging to remain in the overheated state. The reasons that may lead future fabricators to employ such a procedure again include: 1) larger forgings requiring greater workability (and thus higher temperatures), 2) desire to lower press times (again by higher temperature), 3) desire to diversify vendors, and thus utilize producers with smaller presses (again greater workability, and thus higher temperature), and 4) larger forgings with unusual configurations, which necessarily leave some parts unforged after the final heat. **Should it prove unavoidable to employ such procedures, a superclean composition may be required to mitigate the otherwise unacceptable degradation of material properties.**

### **6.1.5.3 Susceptibility of Overheated Material to Environmental Cracking**

As discussed previously, the overheating behavior of the A 508 Cl 4 commercial purity material preheated at 1300°C was very similar to that of the 3.5NiCrMoV material preheated at 1200°C, i.e., formation of globular and incipient rod-type manganese sulfides at the austenite grain boundary. The sulfide morphologies and distributions in both materials are characteristic of a material which has had a large portion, but not all, of the sulfur content solutionized and then reprecipitated under slow-cooling conditions. In conventional overheating terms, this is material which has come close to but not exceeded the overheating temperature, equal to the temperature at which the solubility limit of sulfur equals the sulfur concentration. It is seen that even without exceeding the overheating temperature, an extensive network of PAGB sulfides, including aligned rods, will develop if the material is slow-cooled from preheating. As noted by Hale and Nutting, it is likely that networks such as these will form advantageous paths for environmental cracking, such as SCC. This is considered especially true when the PAGB network contains a large number of aligned incipient rods. **The implication of this result is that even if components are forged at temperatures considered below the overheating regime, their resistance to environmental cracking may be affected if they are of sufficient size to produce slow cooling and thus aligned PAGB rods.**

## 6.2 Manganese Sulfide Inclusion Characteristics

### 6.2.1 Rod-Matrix Orientation Relationship

The results concerning the orientation relationship of the rod-shaped sulfides with the austenite matrix are worth reviewing. The primary data for the orientation of the rod axis with respect to the austenite parent crystal is the results of the trace analysis performed on etched specimens. As described in the Results section, when it is assumed that of the two possible orientations determined the correct one is that which provides the most consistent results, **the four data points obtained predict a direction for the rod axis parallel to the [110] direction within the austenite crystal**, within the bounds of error considered reasonable with this method.

If the rods are consistently oriented along the [110] directions of the austenite crystal, the included angle between pairs of rods should necessarily be equal to that between pairs of [110] $\gamma$  directions. Figure 6.6 depicts a cubic crystal and the possible pairs of [110] directions within it. As seen there, the included angles for pairs of nonparallel directions are either 90° for coplanar directions or 120°/60° for noncoplanar directions. (Note that sets of noncoplanar directions form isosceles triangles, thus the 120°/60° included angle.) As reported in the Results section, the included angle was measured metallographically between six sets of rods. Of these, five were non-perpendicular, i.e., their included angle was not close to 90°. The average included angle for these five was 122°, and none was more than 10° from 120°. The one included angle for a perpendicular-type rod pair was measured to be 89°. Thus the results of this method give strong support to the conclusion from the trace analysis that the rod axes are parallel to the austenite [110] direction.

The results concerning the orientation of the MnS crystal with respect to the rod morphology, determined from TEM of the extracted rod, are less clear. As described in the Results section, five of the seven diffraction images obtained yielded zone axes in which one or more of the Miller indices was zero, i.e., they were perpendicular to a principal axis of the MnS lattice. The other two yielded zone axes which were significantly different, [111] and [123]. Most images were

obtained from large portions of rod, for which it was reasonable to assume that the rod axis was approximately perpendicular to the indexed zone axis. Of the two patterns indexed to zone axes with three non-zero indices, one (photo 903/904, [123] zone axis) was taken from an area of the rod which had fractured, in an attempt to find a naturally thin portion of the precipitate. The other pattern (photo 957, [111] zone axis) unfortunately did not have a corresponding bright-field image, however it is noted that the pattern itself exhibits some degree of asymmetry, and thus it is possible the indexed zone axis is not exactly perpendicular to the projected plane of the subject rod. Thus for both of these images the relationship of the indexed pattern to the rod morphology is not clear.

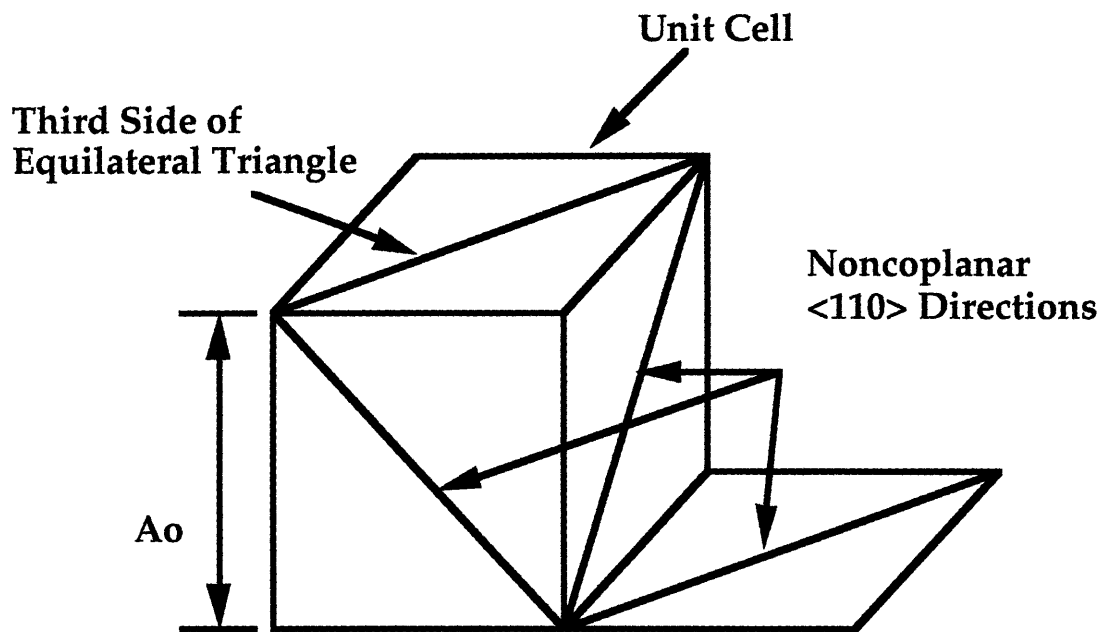


Figure 6.6 Included Angles Between Cubic Crystal [110] Directions

There are two ways to interpret these results. In the first, it is assumed that the MnS crystal lattices are uniformly oriented with one principal axis parallel to the rod axis. In this case the two anomalous patterns result from viewing the extracted rods, or pieces of them, with the TEM beam direction skewed with respect to the rod axis. In the second interpretation, more than one orientation is possible, and the two anomalous patterns represent rods with some minority orientation. **It seems reasonable to conclude then that the orientation of the**

**MnS crystal structure within the rod in which a principal axis of the lattice is parallel to the rod axis is at least the predominant orientation, if not the only one.**

Study of the austenite and MnS crystal lattices provides an explanation for the observed orientations of rod-to-austenite and MnS lattice-to-rod. As described previously, the MnS lattice consists of two interpenetrating face-centered cubic structures, with a nominal lattice constant of 5.22Å. The austenite crystal is face-centered cubic, with a nominal lattice constant of 3.65Å. As shown in Figure 6.7, this implies an atom-to-atom distance in the principal direction of the MnS lattice of 2.61Å, and in the [110] direction of the austenite lattice of 2.58Å. Calculating the unconstrained misfit using the atom-to-atom distances yields [after 108]:

$$\delta = \frac{a_{MnS} - a_{\gamma}}{a_{\gamma}} = 1.2\%$$

The low value of this parameter indicates the high degree of atomic matching possible when the two lattices are oriented in this direction. Only widely-spaced misfit dislocations would be required in the matrix/rod interface in the axial direction. **Therefore good atomic matching, yielding a virtually coherent interface and thus low interfacial energy along the sides of the rod, is proposed to be the underlying cause of the transition to a rod morphology.**

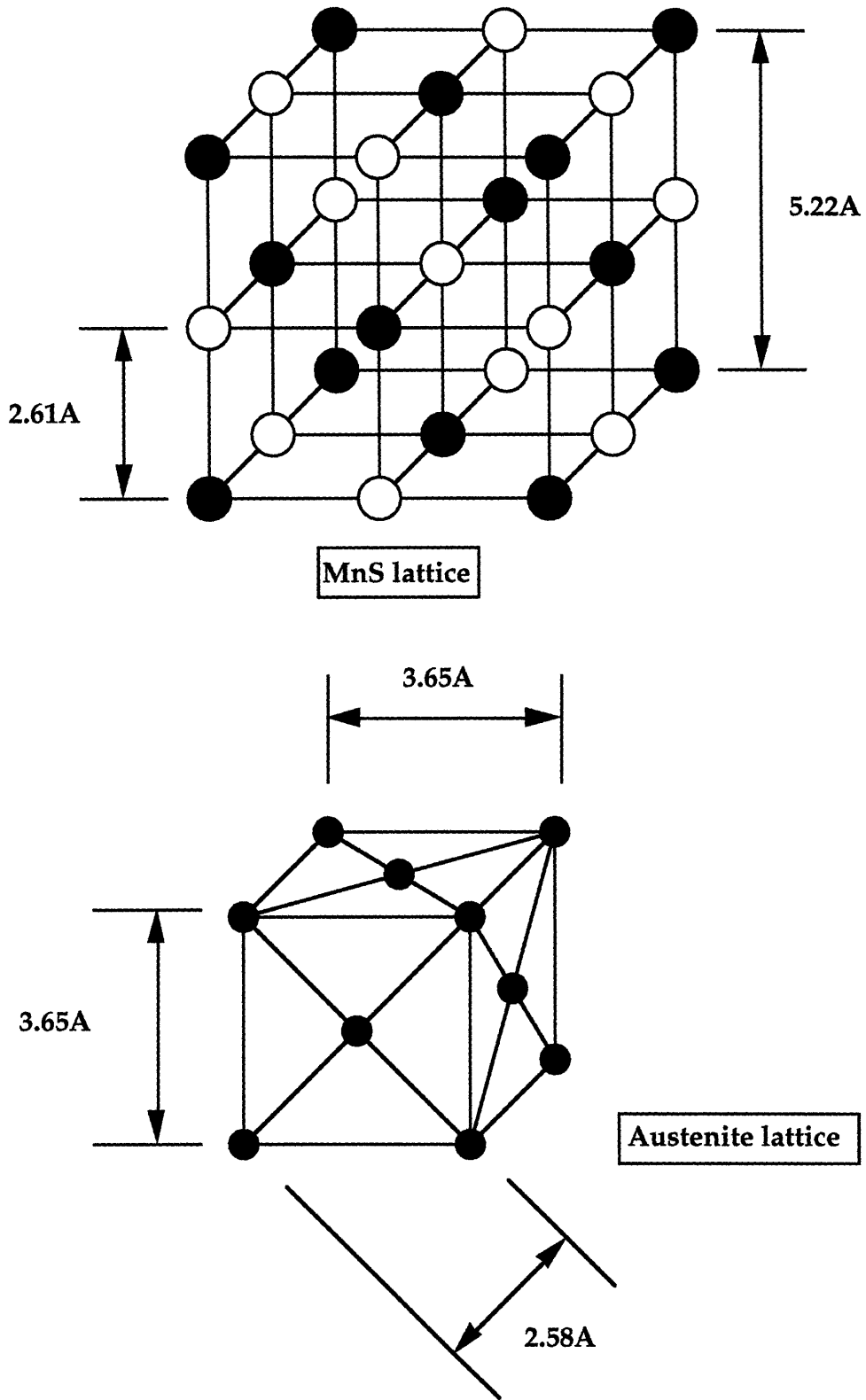


Figure 6.7 Atomic Matching Between [100] MnS Direction and [110] Austenite Direction

### 6.2.2 Implications for Other MnS Morphologies

As discussed in the Literature Review, Ito et. al. have advanced the view that angular type III MnS precipitates in solid steel, rather than from the melt as has been traditionally believed [103]. Included among the evidence for this view is their observation that the number of type III MnS precipitates developed during their solidification tests was independent of the sulfur content. They also evaluated the effect of cooling rate on the number and volume fraction of each MnS type developed in the solidified ingot. At cooling rates below 1°C/min, they observed a dramatic decrease in the number of type III sulfides at the same time as a continual increase in the volume fraction of these precipitates. In other words, there were fewer but much larger type III sulfides. Type III growth rates increased while nucleation rates decreased for these cooling conditions.

It is suggested that this behavior is consistent with development of a coherent boundary, similar to that developed on the rod MnS studied here. The octahedral regularity of this type of MnS has traditionally been considered to be due to development of a perfect crystal from the melt. However it is suggested that this morphology may be due to an atomic matching mechanism between the sulfide precipitate and the parent matrix, such as that responsible for rod growth. In support of this hypothesis is the alignment of the type III octahedra evident in the micrograph of Figure 2.9, from reference 69. This is quite similar to the alignment of embryonic rods, such as in the micrograph of Figure 5.32. It is further questioned whether the mechanism proposed here to explain the rod morphology is not also responsible for the so-called "Widmanstätten MnS platelets" reported in reference 46 (see Figure 2.11).



## 7.0 Summary, Conclusions and Future Work

This section summarizes the thesis and the conclusions which were drawn. Suggestions are then made for future work to continue this line of research.

### 7.1 Summary and Conclusions

This thesis studied the precipitation behavior of manganese sulfide in 3.5NiCrMoV and A 508 Cl 4 low-alloy forging steels when cooled from high temperatures. A program of heat-treatments was developed which varied austenitizing temperature, cooling rate and final microstructure. Impact tests of heat-treated material were conducted to measure impact energy and provide fracture surfaces for microscopic evaluation. Extensive examination under SEM was performed to fully characterize the various precipitation phenomena which are possible. Microstructural characterization by electrolytic and chemical etching was performed. TEM diffraction patterns of rod-shaped sulfides were obtained and indexed. Trace analysis of etched specimens was performed to orient the rod precipitates with respect to artifacts of the parent austenite matrix. A computer simulation of the geometry of the trace analysis was developed and coded. The routine was employed, in conjunction with diffraction patterns obtained from the extracted rods, to determine the orientation relationship of the rod sulfides and the austenite matrix. The simulation technique provided valuable information as to the degree to which the crystallographic orientation problems were well-posed, and thus the results obtained precise.

Among the conclusions which were drawn from this work are:

#### **MnS Precipitation Behavior**

- The manganese sulfide inclusion types and precipitation phenomena which can be encountered when low-alloy forging steels are subjected to high-temperature treatments are: transgranular rods with crystallographic alignment, intergranular incipient rods, intergranular low-ductility facets, intergranular inclusion-free facets covered with ductile dimples, and intragranular crystalline plane microfacets.

- Different phenomena are favored in different ranges of the temperature and cooling rate domains. For a given austenitizing temperature, as cooling rates are depressed the manganese sulfide morphology undergoes a transition from intergranular globular sulfides and incipient rods to crystallographic microfacets and then to intragranular rods. Concurrently prior austenite grain boundary facets appear, change morphology from ductile dimpled to low-ductility, and then disappear again.
- The rod sulfide precipitate crystal structure is alpha MnS, with a "rock-salt" NaCl structure of two interpenetrating FCC lattices, identical to that of manganese sulfides usually reported in steel.
- In the rod-shaped sulfides, the manganese sulfide lattice is at least predominantly, if not solely, oriented with a principal direction parallel to the rod axis. The rod precipitate axis is oriented parallel to the [110] direction in the austenite parent matrix.
- An atomic matching argument is proposed for the mechanism underlying the rod precipitation phenomenon.

### **Material Performance**

- In 3.5NiCrMoV slowly-cooled (1-2°C/min) from 1300°C, transgranular rods and intergranular brittle facets occur in conjunction, and can depress the room-temperature impact energy by over 50% in comparison to rod and facet-free air-quenched material.
- Rod-shaped MnS also depresses the impact energy of 3.5NiCrMoV in the martensitic state, although not to as great a degree as in fully toughened quenched and tempered material. Martensitic samples which had been subjected to the slow-cooling treatment described above experienced about a 25% drop in impact energy. While the fracture mechanism of martensitic samples is still cleavage, as in a tougher matrix rod sulfides are still a low energy fracture path and appear as brittle "troughs" on the fracture surface.
- The same transition to rod-shaped sulfides is encountered in slowly-cooled commercial purity A 508 Cl 4. Intergranular globular and incipient rod sulfides are observed on prior austenite grain boundaries when cooled from 1300°C at 1-2°C/min. The impact energy in these specimens is also approximately halved from that expected for un-overheated material.

- In the overheated state described above, A 508 Cl 4 can have CVN upper shelf energy values as low as 59 ft-lbs, unacceptably close to the minimum value required by the U.S. NRC for reactor pressure vessel materials.

## 7.2 Future Work

Among the open issues remaining in this work are: 1) the nature of the embrittlement of the PAGB facets occurring in conjunction with the intragranular rods, 2) the cause of the distribution of the sulfide rods within narrow bands in the austenite grain interior, and 3) the overheating temperature of the higher sulfur A 508 Cl 4 material.

As mentioned in the Experimental Methods section, fracture of material containing intragranular rods and PAGB facets was attempted in vacuo within an Auger electron microscope. Although the fracture attempts failed to reveal the embrittled facets as desired, the technique of Auger spectroscopy is still considered to be potentially useful in investigating the underlying cause of the facet embrittlement, particularly if it is a segregation-type mechanism. Brittle PAGB facets were regularly revealed in standard size Charpy V-Notch tests, thus it would be useful to devise a method of examining one which had been adequately preserved after fracture. A possible method might be immersion in an acetone and dry ice solution immediately after breaking, to slow surface diffusion rates and prevent oxidation. Condensation during loading of the chilled specimen would be a problem, however.

It is possible that the occurrence of the intragranular rods in a banded distribution is due to segregation of the component species, such as manganese. EDS mapping with an SEM may be a useful tool to detect this. It is observed in the deep-etched specimens that the matrix surrounding these rod sulfides was preferentially attacked, thus if segregation is the underlying cause it may still be detectable in specimens quenched to room temperature. Long-time EDS maps were not attempted in this work. A possible procedure might be to locate the distribution bands on the etched surface with hardness indentations, repolish the surface, and then conduct a long-time map for manganese and sulfur. It might also be worth mapping elements which are known to cosegregate with manganese in temper embrittlement.

More commercial purity A 508 Cl 4 material is required, in order to determine the overheating temperature through an austenitization temperature-

varying test series such as that conducted on the 3.5NiCrMoV material in this work. Obviously temperatures above 1300°C must be evaluated, at least up to 1350°C. Careful attention to calibration of the impact testing machine is obviously required in order to correlate the drop in impact energy with the expected appearance of completely intragranular sulfide rods, indicating the overheating temperature has been reached.

More general questions are still unanswered. Specifically, the mechanism by which cracks result from overheated PAGBs is still unknown. On the basis of observations made during this work, it is hypothesized that cracking may be related to the nucleation of ferrite grain boundary allotriomorphs on overheated sulfides. Nucleation of ferrite islands on manganese sulfide inclusions was observed during long-time isothermal transformation tests conducted in support of the work reported here. Material with classical overheating, in which the grain boundaries are decorated with dense fine sulfides, may be appropriate for testing this hypothesis.

Finally, the affect of overheating on the susceptibility of a material to environmental cracking such as SCC is particularly worthy of investigation. Monoblock rotors forged from 3.5NiCrMoV are designed to avoid problems such as stress corrosion cracking in 3.5NiCrMoV shrunk-on disks. However inherently they entail larger sizes and slower cooling rates, thus the influence on SCC susceptibility of the MnS precipitate morphologies developed under slow cooling is worthy of investigation.

## References

1. Andrew, R. C. and Weston, G. M. "The Effect of Overheating on the Toughness of Low Sulphur ESR Steels," Journal of the Australasian Institute of Metals, v22, n3-4, Sep-Dec, 1977, pp. 171-176.
2. Andrew, R. C., Weston, G. M. and Southin, R. T. "Overheating in Low-Sulphur Steels," Journal of the Australasian Institute of Metals, v21, n2-3, Jun-Sep, 1976, pp. 126-131.
3. Austel, W. and Korbe, H. "Integral Forged Pump Casing for the Primary Coolant Circuit of a Nuclear Reactor: Development in Design, Forging Technology and Material," Steel Forgings, ASTM STP 903, E. G. Nisbett and A. S. Melilli, Eds., American Society for Testing and Materials, Philadelphia, 1986, pp. 385-397.
4. Bika, D. Dissertation for PhD, University of Pennsylvania, 1992, cited in ref. 104, p. 8.
5. Bodnar, R.L., Ohhashi, T. and Jaffee, R.I. "Effects of Mn, Si, and Purity on the Design of 3.5NiCrMoV, 1CrMoV, and 2.25Cr-1Mo Bainitic Alloy Steels," Metallurgical Transactions A, 20A, Oct, 1989, pp. 2197-2212.
6. Bodnar, R.L., Taylor, K.A., Albano, K.S. and Helm, S.A. "Improving the Toughness of 3-1/2NiCrMoV Steam Turbine Disc Forgings," Recent Developments in Rotor Forging Steels, Bodnar, R.L., ed., Iron and Steel Society, Inc., 1990, pp. 9-21.
7. Edwards, B.C. "Interfacial Fracture in Alloy Steels," Defects and Fracture: Proceedings of First International Symposium on Defects and Fracture, G. C. Sih and H. Zorski, eds., 1980, pp. 39-49.
8. Erve, M., Papouschek, F., Fischer, K. and Maidorn, C. "State of the Art in the Manufacture of Heavy Forgings for Reactor Components in the Federal Republic of Germany," Nuclear Engineering and Design, v108, 1988, pp. 485-495.
9. Glue, D.R., Jones, C.H. and Lloyd, H.K.M. "Effect of Composition and Thermal Treatment on the Overheating Characteristics of Low-Alloy Steels," Metals Technology, 9/75, Sep, 1975, pp. 416-421.
10. Hale, G.E. and Nutting, J. "Overheating of Low-Alloy Steels," International Metals Reviews, v29, n4, 1984, pp. 273-298.

11. Hale, G.E., Preston, S. and Nutting, J. "Influence of Manganese and Sulphur on Overheating of Some Low-Alloy Steels," Materials Science and Technology, v2, Jun, 1986, pp. 571-575.
12. Hinkel, A.V., Handerhan, K.J., Manzo, G.J., Simkins, G.P. "Processing and Properties of Superclean ASTM A508 Cl. 4 Forgings," Proceedings of the 11th International Forgemasters Meeting, 1992.
13. Hipsley, C.A., Knott, J.F. and Edwards, B.C. "A Study of Stress Relief Cracking in 2-1/4 Cr 1Mo Steel - II. The Effects of P Segregation," Acta Metallurgica, v28, 1980, pp. 869-885.
14. Hipsley, C.A., Knott, J.F. and Edwards, B.C. "A Study of Stress Relief Cracking in 2-1/4 Cr 1Mo Steel - II. The Effects of Multi-Component Segregation," Acta Metallurgica, v30, 1982, pp. 641-654.
15. Joy, G.D. and Nutting, J. "Influence of Intermetallic Phases and Non-Metallic Inclusions Upon the Ductility and Fracture Behavior of Some Alloy Steels," Effect of Second-Phase Particles on the Mechanical Properties of Steel, The Iron and Steel Institute, London, 1971, pp. 95-100.
16. Katsumata, M., Takagi, I. and Kaji, H. "Effect of Chemical Composition and Manufacturing Condition on Overheating in Steel for Low Pressure Turbine Rotor," Iron and Steel Institute of Japan, 1990, pp. 230-237.
17. Ko, T. and Hanson, D. "Grain-Boundary Phenomena in Severely Heated Steels," Journal of the Iron and Steel Institute, v164, Jan, 1950, pp. 51-62.
18. Leslie, W.C. "Inclusions and Mechanical Properties," ISS Transactions, v2, 1983, pp. 1-24.
19. McLeod, N.P. and Nutting, J. "Influence of Manganese on Susceptibility of Low-Alloy Steel to Overheating," Metals Technology, v9, Oct, 1982, pp. 399-404.
20. McMahon, C.J., Dobbs, R.J. and Gentner, D.H. "Stress Relief Cracking in MnMoNi and MnMoNiCr Pressure Vessel Steels," Materials Science and Engineering, v37, 1979, pp. 179-186.
21. McMahon, Jr., C.J. "High-Temperature Brittle Fracture in Low Alloy Steels," Zeitschrift Fur Metallkunde, Bd. 75, H. 7, 1984, pp. 496-509.
22. Meitzner, C.F. "Stress-Relief Cracking in Steel Weldments," Welding Research Council Bulletin 211, Nov, 1975.

23. Middleton, C.J. "Reheat Cavity Nucleation and Nucleation Control in Bainitic Creep-Resisting Low-Alloy Steels: Roles of Manganese Sulphide, Residual, and Sulphur-Stabilizing Elements," Metal Science, Apr, 1981, pp. 154-167.
24. Murphy, J.T., Ballinger, R.G., Becker, H., Gwinn, D.A. and Mathew, S. "Turbogenerator Flywheel for Alcator C-Mod," paper submitted to 14th IEEE/NPSS Symposium on Fusion Engineering, San Diego, 1991.
25. O'Brien, R.N., Jack, D.H. and Nutting, J. "Effect of MnS Distribution on the Fracture Properties of Heat-Treated Low-Alloy Steels," Heat Treatment '76: Proceedings of the 16th International Heat Treatment Conference, The Metals Society, 1976, pp. 161-168.
26. Preece, A., Hartley, A., Mayer, S.E. and Nutting, J. "The Overheating and Burning of Steels, Parts I & II," Journal of the Iron and Steel Institute, v153, 1946, pp. 237-254.
27. Schulz, B.J. and McMahon Jr., C.J. "Fracture of Alloy Steels by Intergranular Microvoid Coalescence as Influenced by Composition and Heat Treatment," Metallurgical Transactions, v4, Oct, 1973, pp. 2485-2489.
28. Shin, J., Kameda, J. and McMahon, C.J. "Mechanisms of Stress Relief Cracking in MnMoNi and MnMoNiCr Pressure Vessel Steels," Micro and Macro Mechanics of Crack Growth, K. Sadananada, B.B. Rath and D.J. Michel eds., The Metallurgical Society of AIME, 1984, pp. 149-161.
29. Shin, J. and McMahon, Jr., C.J. "Mechanisms of Stress Relief Cracking in a Ferritic Steel," Acta Metallurgica, v32, n9, 1984, pp. 1535-1552.
30. Shin, J. and McMahon, Jr., C.J. "Comparison of Stress Relief Cracking in A 508 2 and A 533 B Pressure Vessel Steels," Metal Science, 18, Aug, 1984, pp. 403-410.
31. Solomon, H.D. "Embrittlement of Welds," Treatise on Materials Science and Technology, C.L. Briant and S.K. Banerji, eds., v25, 1983.
32. Sun, J., Zaiss, R., Menyhard, M. and McMahon, Jr., C.J. "Impurity Effects in Stress Relief Cracking of a Mn-Cr-Mo-Ni Steel," Materials Science and Technology, v3, Feb, 1987, pp. 139-145.
33. Turkdogan, E.T., Ignatowicz, S. and Pearson, J. "The Solubility of Sulphur in Iron and Iron-Manganese Alloys," Journal of the Iron and Steel Institute, Aug, 1955, pp. 349-354.



34. Vinckier, A.G. and Pense, A.W. "A Review of Underclad Cracking in Pressure-Vessel Components," Welding Research Council Bulletin 197, Aug, 1974.
35. Viswanathan, R. Damage Mechanisms and Life Assessment of High-Temperature Components, ASM International, Metals Park, 1989.
36. Watson, J.D. "Microscopy and the Development of Free-Machining Steels," Applied Metallography, G. F. Vander Voort, ed., Van Nostrand Reinhold, New York, 1986.
37. LLewellyn, D. T. Steels: Metallurgy and Applications, Butterworth-Heinemann Ltd., Oxford, 1992.
38. Curran, R.W. "The Development of Improved Forgings for Modern Steam Turbines," Steel Forgings, ASTM STP 903, E. G. Nisbett and A. S. Melilli, Eds., American Society for Testing and Materials, Philadelphia, 1986, pp. 9-32.
39. Bodnar, R.L. and Cappellini, R.F. "Effects of Residual Elements in Heavy Forgings: Past, Present, and Future," MiCon 86: Optimization of Processing, Properties, and Service Performance Through Microstructural Control, ASTM STP 979, B.L. Bramfitt, R.C. Benn, C.R. Brinkman and G.F. Vander Voort, Eds., American Society for Testing and Materials, Philadelphia, 1988, pp. 47-82.
40. EPRI CS/EL-5593, Life Assessment Methodology for Turbogenerator Rotors, Volume 2: SAFER Code Engineering Tutorial, Electric Power Research Institute, Palo Alto, Mar, 1988.
41. ASTM A 470 - 91 Standard Specification for Vacuum-Treated Carbon and Alloy Steel Forgings For Turbine Rotors and Shafts, American Society of Testing and Materials, Philadelphia, 1991.
42. ASTM A 508/A 508M - 92 Standard Specification for Quenched and Tempered Vacuum-Treated Carbon and Alloy Steel Forgings for Pressure Vessels, American Society of Testing and Materials, Philadelphia, 1992.
43. ASME Boiler and Pressure Vessel Code, Section XI, "Rules for Inservice Inspection of Nuclear Power Plant Components", American Society of Mechanical Engineers, New York.
44. Ekeroth, D.E. "Forging Design for Westinghouse Advanced Nuclear Plants Components," Proceedings of the 12th International Forgemasters Meeting, Forging Industry Education and Research Foundation, Cleveland, Sep, 1994.

45. Bokelmann, D., Forch, K. and Haverkamp, K.D. "Forging Technique for the Manufacture of a Heavy Flywheel With 108 t Forging Weight," Proceedings of the 11th International Forgemasters Meeting, Jun, 1991.
46. Kiessling, R. and Lange, N. Non-Metallic Inclusions in Steel, Parts I -IV, The Metals Society, London, 1978.
47. Moore, C. and Marshall, R.I. Steelmaking, The Institute of Metals, London, 1991.
48. Sims, E.E. and Dahle, F.B. "Effect of Aluminum on the Properties of Medium Carbon Cast Steel", Transactions of the American Foundrymen's Association, v46, 1938, pp. 65-132.
49. Schmerling, J.M. and Hammon, J.C. "Investigation of the Tennessee Valley Authority Gallatin Unit No. 2 Turbine Rotor Burst", Presentation before the 38th Annual Meeting of the American Power Conference, Chicago, Illinois, April 21, 1976, in Proceedings of the American Power Conference, v38, 1976, pp. 545-554.
50. Kramer, L.D. and Randolph, D.D. "Analysis of the Tennessee Valley Authority Gallatin No. 2 Unit Turbine Rotor Burst, Part I - Metallurgical Considerations", Presentation before the Winter Annual Meeting of the ASME, New York, December 5-10, 1976, reprinted in Creep-Fatigue Interaction, R.M. Curran, ed., The American Society of Mechanical Engineers, New York, pp. 1-24.
51. Weisz, D.A. "Analysis of the Tennessee Valley Authority Gallatin No. 2 Unit Turbine Rotor Burst, Part II - Mechanical Analysis," Presentation before the Winter Annual Meeting of the ASME, New York, December 5-10, 1976, reprinted in Creep-Fatigue Interaction, R.M. Curran, ed., The American Society of Mechanical Engineers, New York, pp. 25-39.
52. EPRI NP-7473-L, Environmentally Assisted Cracking of Low-Alloy Steels, Electric Power Research Institute, Palo Alto, Jan, 1992.
53. Woolman, J. and Kirkby, H.W. "Some Experiments on Overheating," Journal of the Iron and Steel Institute, v153, 1946, pp. 265-279.
54. Preece, A., Hartley, A., Mayer, S.E. and Nutting, J. "The Overheating and Burning of Steel, Part III," Journal of the Iron and Steel Institute, v164, Jan, 1950, pp. 37-45.
55. Kiessling, R. "Sulfide Inclusions: A Summary and Study of Sulfides in Resulfurized Ferritic ELI-Steels of the 18:2 Type," Sulfide Inclusions in

- Steel, Proceedings of an International Symposium, J.J. deBarbadillo and E. Snape, eds., American Society for Metals, Metals Park, 1975, pp. 104-122.
56. Bodimeade, A.H., O'Brien, R.N., Jack, D.H. and Nutting, J. Proceedings of a Conference on Inclusions and Their Effect on Steel Properties, British Steel Corporation, Leeds, 1974.
  57. Hall, M.G., Aaronson, H.I. and Kinsma, K.R. "The Structure of Nearly Coherent fcc:bcc Boundaries in a Cu-Cr Alloy," Surface Science, v31, 1972, pp. 257-274.
  58. Rigsbee, J.M. and Aaronson, H.I. "A Computer Modeling Study of Partially Coherent F.C.C.:B.C.C. Boundaries," Acta Metallurgica, v27, 1979, pp. 351-363.
  59. Rigsbee, J.M. and Aaronson, H.I. "The Interfacial Structure of the Broad Faces of Ferrite Plates," Acta Metallurgica, v27, 1979, pp. 365-376.
  60. Honeycombe, R.W.K. Steels, Microstructure and Properties, Edward Arnold Ltd., London, 1981.
  61. ASTM E 23- 92 Standard Test Methods for Notched Bar Impact Testing of Metallic Materials, American Society of Testing and Materials, Philadelphia.
  62. Hirsch, P., Howie, A., Nicholson, R., Pashley, E.W. and Whelan, M.J. Electron Microscopy of Thin Crystals, Robert E. Krieger, Malabar, FL, 1977.
  63. Desktop Microscopist: Diffraction Simulation and Analysis for the Macintosh, Software Version 1.0, Manual Version 1.0, Virtual Laboratories, Albuquerque, NM.
  64. Elliott, J.F. "Physical Chemistry of High Temperature Reactions," Chapter 20 in Electric Furnace Steelmaking, C.R. Taylor and C.C. Custer, eds., Iron and Steel Society of the AIME, Warrendale, 1985.
  65. Vander Voort, G.F. Metallography, Principles and Practice, McGraw-Hill, New York, 1984.
  66. Recipes for Electrolytes, The Struers Company.
  67. Baker, T.J. and Charles, J.A. "Morphology of Manganese Sulphide in Steel", Journal of the Iron and Steel Institute, Sep, 1972, pp. 702-706.

68. Petzow, G. Metallographic Etching: Metallographic and Ceramographic Methods for Revealing Microstructure, American Society for Metals, Metals Park, 1976.
69. Baker, T.J. "Use of Scanning Electron Microscopy in Studying Sulphide Morphology on Fracture Surfaces," Sulfide Inclusions in Steel, Proceedings of an International Symposium, J.J. deBarbadillo and E. Snape, eds., American Society for Metals, Metals Park, pp. 135-158.
70. "Carbon and Alloy Steels," article in Metallography and Microstructures, Volume 9, Metals Handbook, 9th Edition, ASM, Metals Park, 1985.
71. McDougall, P.G. and Wayman, C.M. "The Crystallography and Morphology of Ferrous Martensites", chapter in Martensite, a Tribute to Morris Cohen, G.B. Olson and W.S. Owen, eds., ASM International, Materials Park, 1992.
72. Barrett, C.S. Structure of Metals: Crystallographic Methods, Principles and Data, Pergamon, Oxford, 1980.
73. Honeyman, G.A. "The Ferritic 12% Cr Rotors for Supercritical Applications," Proceedings of the 12th International Forgemasters Meeting, Forging Industry Education and Research Foundation, Cleveland, Sep, 1994.
74. Schabtach, C., Fogleman, E.L., Rankin, A.W. and Winne, D.H. "Report of the Investigation of Two Generator Rotor Fractures," Transactions of the ASME, v78, 1956, pp. 1567-1584.
75. ASTM A 293, American Society of Testing and Materials, Philadelphia.
76. Schaeffer, A.O. "The Work of the Task Group on Brittle Failure of Steel Forgings," Transactions of the ASME, v78, Oct, 1956, pp. 1623-1626.
77. Lyle, Jr., F.F. and Burghard, Jr., H.C. "Cracking of Low Pressure Turbine Rotor Discs in US Nuclear Power Plants," Materials Performance, Nov, 1982, pp. 35-44.
78. Bandyopadhyay, N. and Briant, C.L. "Caustic Stress Corrosion Cracking of NiCrMoV Rotor Steels - The Effects of Impurity Segregation and Variation in Alloy Composition," Metallurgical Transactions A, v14A, Oct, 1983, pp. 2005-2019.
79. Bandyopadhyay, N., Briant, C.L. and Hall, E.L. "The Effect of Microstructural Changes on the Caustic Stress Corrosion Cracking

- Resistance of a NiCrMoV Rotor Steel," Metallurgical Transactions A, v16A, Jul, 1985, pp. 1333-1344.
80. Kawaguchi, S., Kanno, N., Iwadate, T. and Ohhashi, T. "Integrity of Full-Integral, Low-Pressure Nuclear Turbine Forgings," Steel Forgings, ASTM STP 903, E. G. Nisbett and A. S. Melilli, Eds., American Society for Testing and Materials, Philadelphia, 1986, pp. 203-214.
  81. Haverkamp, K.D., Fischer, K., Forch, K. and Piehl, K.H. "Production and Properties of a 200 T Generator Shaft Made From an Ingot of 435 Metric Tons", Proceedings of the 10th International Forgemaster's Meeting, Sheffield, England, 1985, p. 10.1.
  82. Tanaka, Y., Asuma, T., Ikeda, Y., Watanabe, O., Yamada, M., Kaplan, A., Schwant, R.C. "Production and Properties of a Superclean 2.5% Ni-CrMoV High Pressure/Low Pressure Rotor Shaft," Proceedings of the Robert I. Jaffee Memorial Symposium on Clean Materials Technology, ASM International, Materials Park, 1992, pp. 169-180.
  83. Newhouse, D.L. and Holtz, H.G. "Temper Embrittlement of Rotor Steels," Temper Embrittlement in Steel, ASTM STP 407, American Society for Testing and Materials, 1968.
  84. Watanabe, J. and Murakami, Y. American Petroleum Institute Preprint no. 28-81, 1981, pp. 216-224, cited in ref. 5, p. 2212.
  85. Wilson, A.D. "Ongoing Challenges for Clean Steel Technology," Proceedings of the Robert I. Jaffee Memorial Symposium on Clean Materials Technology, ASM International, Materials Park, 1992, pp. 135-143.
  86. Azuma, T., Tanaka, Y., Ikeda, Y. and Yoshida, H. "Production and Properties of Superclean 3.5% NiCrMoV Rotor Forging for Low Pressure Steam Turbine," Proceedings of the Robert I. Jaffee Memorial Symposium on Clean Materials Technology, ASM International, Materials Park, 1992, pp. 213-220.
  87. Sato, K., Kitagawa, I., Morinaka, K., Fujikawa, T. and Takeda, Y. "Manufacturing Experience of Superclean LP Rotor Forgings," Proceedings of the Robert I. Jaffee Memorial Symposium on Clean Materials Technology, ASM International, Materials Park, 1992, pp. 233-239.
  88. Fukui, Y., Shiga, M., Hidaka, K., Kaneko, R. and Tan, T. "Development of Superclean 0.2Mn-1.8Ni-Cr-Mo-V Steel Rotor for Hp-Lp Steam Turbine," Proceedings of the Robert I. Jaffee Memorial Symposium on Clean

- materials Technology, ASM International, Materials Park, 1992, pp. 249-257
89. Heesom, J.E. and Honeyman, G.A. "Superclean Steels for Pressure Vessel Technology," Proceedings of the Robert I. Jaffee Memorial Symposium on Clean Materials Technology, ASM International, Materials Park, 1992, pp. 117-126.
  90. Suzuki, K., Sato, I. and Tsukada, H. "Manufacturing and Material Properties of Ultra-Large Size Forgings for Advanced BWRPV," Proceedings of the 12th International Forgemasters Meeting, Forging Industry Education and Research Foundation, Cleveland, 1994.
  91. Bocquet, P., Cheviet, A. and Dumont, R. "Improved New Forgings for Upgraded Nuclear Power Plants," Proceedings of the 12th International Forgemasters Meeting, Forging Industry Education and Research Foundation, Cleveland, 1994.
  92. Luyckx, L. "Techniques for Controlling Sulfide Inclusions in Steels -- Primary Processing Aspects," Sulfide Inclusions in Steel, Proceedings of an International Symposium, J.J. deBarbadillo and E. Snape, eds., American Society for Metals, Metals Park, pp. 44-69.
  93. Kiessling, R. Non-Metallic Inclusions in Steel, Part V, The Institute of Metals, London, 1989.
  94. Jorgensen, C. Internal Report, Institute for Ferrous Metallurgy, Royal Institute of Technology, Stockholm, cited in ref. 46, p. 99.
  95. Turkdogan, E.T. "Theoretical Aspects of Sulfide Formation in Steel," Sulfide Inclusions in Steel, Proceedings of an International Symposium, J.J. deBarbadillo and E. Snape, eds., American Society for Metals, Metals Park, 1975, pp. 1-22.
  96. Guy, A.G. Elements of Materials Science, McGraw-Hill, New York, 1976.
  97. Chao, H.C., Van Vlack, L.H., Oberin, F. and Thomassen, L. "Hardness of Inclusion Sulfides", Transactions of the American Society for Metals, v57, 1964, pp. 885-891.
  98. Hassani, F. and Yue, S. "Detection of Low Hot Ductility Temperature Zones in Steels," 34th Mechanical Working and Steel Processing Conference Proceedings, Iron and Steel Society of the AIME, 1993, pp. 409-418.

99. Hanninen, H., Cullen, W. and Kemppainen, M. "Effects of MnS Inclusion Dissolution on Environmentally Assisted Cracking in Low-Alloy and Carbon Steels," Corrosion, v46, n7, Jul, 90, pp. 563-573.
100. Farrar, J.C.M., Charles, J.A. and Dolby, R.E. "Metallurgical Aspects of Lamellar Tearing," Effect of Second-Phase Particles on the Mechanical Properties of Steel, The Iron and Steel Institute, London, 1971, pp. 171-181.
101. Baker, T.J. and Charles, J.A. "Influence of Deformed Inclusions on the Short Transverse Ductility of Hot-Rolled Steel," Effect of Second-Phase Particles on the Mechanical Properties of Steel, The Iron and Steel Institute, London, 1971, pp. 28-36.
102. Middleton, C.J. "Control of Reheat and Creep Cavitation in Low Alloy Steels - The Roles of Residual Elements and Sulfur," Proceedings of the Robert I. Jaffee Memorial Symposium on Clean Materials Technology, ASM International, Materials Park, 1992, pp. 39-52.
103. Ito, Y., Masumitsu, N. and Matsubara, K. "Formation of Manganese Sulfide in Steel", Transactions of the Iron and Steel Institute of Japan, v21, 1981, pp. 477-484.
104. McMahon, Jr., C.J. "Diffusion-Controlled Brittle Fracture in Overheated Steels," Proceedings of the Robert I. Jaffee Memorial Symposium on Clean Materials Technology, ASM International, Materials Park, 1992, pp. 3-8.
105. Hipsley, C.A., Rauh, H. and Bullough, R. "Stress-Driven Solute Enrichment of Crack-Tips During Low-Ductility Intergranular Fracture of Low-Alloy Steel," Acta Metallurgica, v32, n9, 1984, pp. 1381-1394.
106. Rauh, H., Hipsley, C.A. and Bullough, R. "The Effect of Mixed-Mode Loading on Stress-Driven Solute Segregation During High-Temperature Brittle Intergranular Fracture," Acta Metallurgica, v37, n1, 1989, pp. 269-279.
107. Chen, I.-W. "Quasi-Static Intergranular Brittle Fracture at 0.5 T<sub>m</sub>: A Non-Equilibrium Segregation Mechanism of Sulphur Embrittlement in Stress-Relief Cracking of Low-Alloy Steels", Acta Metallurgica, v34, n37, 1986, pp. 1335-1349.
108. Porter, D.A. and Easterling, K.E. Phase Transformations in Metals and Alloys, Chapman and Hall, London, 1981.
109. Russell, K.C., Hall, M.G., Kinsman, K.R. and Aaronson, H.I. "The Nature of the Barrier to Growth at Partially Coherent FCC:BCC Boundaries", Metallurgical Transactions, v5, 1974, p. 1503-1505.

110. Takeuchi, S., Honma, T. and Ikeda, S. "Charts for Determination of Crystal Orientation by Surface Traces in Cubic Crystals", Sci. Rep. Res. Inst. Tohoku Univ. A11, 1959, pp. 81-93, cited in ref. 113, p. 275.
111. Drazin, M.P. and Otte, H.M. Tables for Determining Cubic Crystal Orientations from Surface Traces of Octahedral Planes, Harrod, Baltimore, 1964 cited in ref. 113, p. 275.
112. Drazin, M.P. and Otte, H.M. "The Systematic Determination of Crystallographic Orientations From Three Octahedral Traces on a Plane Surface," Phys. Statistics of Solids, 3, 1963, pp. 824-857 cited in ref. 113, p. 275.
113. Fong, H.S. "A New Method of {111} Trace Analysis", Metallography, v18, 1985, pp. 263-275.
114. Fullman, R.L. and Fisher, J.C. "Formation of Annealing Twins During Grain Growth," Journal of Applied Physics, v22, n11, Nov, 1951, pp. 1350-1355.
115. Agren, J., Scripta Metallurgica, v20, n11, 1986, pp. 1507-1510, cited in ref. 118, p. 243.
116. Nutting, J. Comments during discussion sessions at 12th International Forgemaster's Meeting, Sep, 1994.
117. Emmert, H.D. "Investigation of Large Steam-Turbine Spindle Failure," Transactions of the ASME, v78, 1956, pp. 1547-1565.
118. Diffusion and Defect Data, F. H. Wohlbier, ed., v51-52, Trans Tech Publications, 1987.



## **A Trace Analysis FORTRAN Programs and Output**

Detailed results of the computer trace analysis to determine sulfide rod orientation are summarized in this appendix. The FORTRAN codes for the TRACE and RODS programs are included as sections A.1 and A.3, respectively, while the outputs for each austenite grain analyzed are summarized in sections A.2 and A.4.

### A.1. TRACE Code for Determining Austenite Orientation

```
PROGRAM RODS
CHARACTER*64 RFL,TFL
REAL*8 PI,THETA,S1,C1,C2,IXIA,IXIB,XIA,XIB,RAMAG,RBMAG,DP
REAL*8 N1(3),N(3),N1CN(3),C(9),V(3)
REAL*8 RA(3),RB(3),TA(3),TB(3)
REAL*8 A(9,9),T(3,3)
C
C Define constants
C
PI = 3.141592654
THETA = 54.7356*(PI/180.)
S1 = DSIN(THETA)
C1 = DCOS(THETA)
C2 = 0.7071067814*C1
C
C Open files
C
WRITE (*,*) 'Traces file name?'
READ (*,*) TFL
OPEN (UNIT=3,FILE=TFL,STATUS='OLD')
C
WRITE (*,*) 'Solution file name?'
READ (*,*) RFL
OPEN (UNIT=4,FILE=RFL,STATUS='NEW')
C
C Read initial data
C
WRITE (*,*) 'IXIA,IXIB (in deg)?'
READ (*,*) IXIA,IXIB
WRITE (*,*) 'Print out checks? (y=1)'
ICHECK = 0
READ (*,*) ICHECK
XIA = PI*IXIA/180.
XIB = PI*IXIB/180.
READ (3,*) N1(1),N1(2),N1(3)
READ (3,*) NSOLS
C
TA(1) = -DCOS(XIA)
TA(2) = DSIN(XIA)
TA(3) = 0.0
TB(1) = DCOS(XIB)
TB(2) = 0.0
TB(3) = -DSIN(XIB)
C
```

```

WRITE (*,90) IXIA,IXIB
WRITE (4,90) IXIA,IXIB
90  FORMAT(/2X,'XIA = ',F7.2,' XIB = ',F7.2)
WRITE (*,100) N1(1),N1(2),N1(3)
WRITE (4,100) N1(1),N1(2),N1(3)
100  FORMAT(/2X,'Plane 1 normal = ',3F7.4)
WRITE (*,110) NSOLS
WRITE (4,110) NSOLS
110  FORMAT(/2X,'Number of solutions =',I4)
WRITE (*,120) TA(1),TA(2),TA(3)
WRITE (4,120) TA(1),TA(2),TA(3)
120  FORMAT(/2X,'Rod 1 trace = ',3F7.4)
WRITE (*,130) TB(1),TB(2),TB(3)
WRITE (4,130) TB(1),TB(2),TB(3)
130  FORMAT(/2X,'Rod 2 trace = ',3F7.4)
C
WRITE (*,150)
WRITE (4,150)
150  FORMAT(/2X,' Step  Rot Plane   Rod 1 Trace   Rod 2 Trace',/)
C
C   March through solutions
C
DO 900 I = 1,NSOLS
READ (3,*) IS,IR,IP,T1,T2,T3,DP,N(1),N(2),N(3)
CALL CROSSP3(N1,N,N1CN)
C
C   Build equation matrix
C
DO 180 J = 1,9
C(J) = 0.0
DO 180 K = 1,9
180  A(J,K) = 0.0
C
DO 200 J = 1,3
A(1,J) = N1(J)
A(2,J) = N(J)
A(3,J) = N1CN(J)
A(4,J+3) = N1(J)
A(5,J+3) = N(J)
A(6,J+3) = N1CN(J)
A(7,J+6) = N1(J)
A(8,J+6) = N(J)
200  A(9,J+6) = N1CN(J)
C
C   Build load vector
C

```

```

C(1) = 0.577350269
C(4) = 0.577350269
C(7) = 0.577350269
C(8) = 0.577350269
IF (IP.EQ.2) THEN
    C(2) = -0.577350269
    C(5) = 0.577350269
    C(3) = 0.0
    C(6) = -0.7071067814
    C(9) = 0.7071067814
ELSEIF (IP.EQ.3) THEN
    C(2) = -0.577350269
    C(5) = -0.577350269
    C(3) = 0.7071067814
    C(6) = -0.7071067814
    C(9) = 0.0
ELSEIF (IP.EQ.4) THEN
    C(2) = 0.577350269
    C(5) = -0.577350269
    C(3) = 0.7071067814
    C(6) = 0.0
    C(9) = -0.7071067814
ENDIF
C
C   Solve for transformation vector
C
C1
    IF (ICHECK.GT.0) THEN
    WRITE (4,*) 'A,C assembled:'
    DO 220 J = 1,9
220  WRITE (4,230) (A(J,K),K=1,9),C(J)
230  FORMAT(2X,10F7.4)
    ENDIF
C2
    CALL GAUSS(9,9,A,C)
C1
    IF (ICHECK.GT.0) THEN
    WRITE (4,*) 'Solved:'
    DO 250 J = 1,9
250  WRITE (4,260) (A(J,K),K=1,9),C(J)
260  FORMAT(2X,10F7.4)
    ENDIF
C2
C
C   Build transformation matrix
C

```

```

DO 300 J = 1,3
T(J,1) = C((J-1)*3+1)
T(J,2) = C((J-1)*3+2)
300 T(J,3) = C((J-1)*3+3)
C1
IF (ICHECK.GT.0) THEN
WRITE (4,*) 'T built:'
DO 320 J = 1,3
320 WRITE (4,330) (T(J,K),K=1,3)
330 FORMAT(2X,3F7.4)
C
C Check transformation matrix on input vectors
C
DO 350 J = 1,3
V(J) = 0.0
DO 350 K = 1,3
350 V(J) = V(J)+T(J,K)*N(K)
C
WRITE (4,*) 'V checked:'
370 WRITE (4,380) IP,(V(J),J=1,3)
380 FORMAT(2X,I6,3F7.4)
ENDIF
C2
C
C Transform rod traces to local unit vectors
C
DO 400 J = 1,3
RA(J) = 0.0
RB(J) = 0.0
DO 400 K = 1,3
RA(J) = RA(J)+T(J,K)*TA(K)
400 RB(J) = RB(J)+T(J,K)*TB(K)
CALL MAG(RA,RAMAG)
CALL MAG(RB,RBMAG)
DO 450 J = 1,3
RA(J) = RA(J)/RAMAG
450 RB(J) = RB(J)/RBMAG
C1
IF (ICHECK.GT.0) THEN
WRITE (*,500) IS,IR,IP,RA(1),RA(2),RA(3),RB(1),RB(2),RB(3)
WRITE (4,500) IS,IR,IP,RA(1),RA(2),RA(3),RB(1),RB(2),RB(3)
500 FORMAT(2X,3I5,6F7.4)
ENDIF
C2
C
C Printout results

```

```

C
WRITE (*,600) IS,IR,IP,RA(1),RA(2),RA(3),RB(1),RB(2),RB(3)
WRITE (4,600) IS,IR,IP,RA(1),RA(2),RA(3),RB(1),RB(2),RB(3)
600 FORMAT(2X,3I5,6F7.4)

```

```

C
900 CONTINUE
WRITE (*,*) 'Finished?'
READ (*,*) YN
CLOSE(3)
CLOSE(4)
END

```

```

C
C Unit cross product subroutine (3x3)
C

```

```

SUBROUTINE CROSSP3(U,V,W)
REAL*8 U(3),V(3),W(3)
W(1) = U(2)*V(3)-U(3)*V(2)
W(2) = U(3)*V(1)-U(1)*V(3)
W(3) = U(1)*V(2)-U(2)*V(1)
WMAG = DSQRT(W(1)**2+W(2)**2+W(3)**2)
W(1) = W(1)/WMAG
W(2) = W(2)/WMAG
W(3) = W(3)/WMAG
RETURN
END

```

```

C
C Gaussian reduction equation solver (inefficient)
C

```

```

SUBROUTINE GAUSS(NMAX,NEQ,A,B)
REAL*8 A(NMAX,NMAX),B(NMAX)
REAL*8 C,SUM
LIMIT=NEQ-1
DO 100 N=1,LIMIT
DO 50 I=N+1,NEQ
C=A(I,N)/A(N,N)
B(I)=B(I)-C*B(N)
DO 25 J=N,NEQ
25 A(I,J)=A(I,J)-C*A(N,J)
50 CONTINUE
100 CONTINUE
B(NEQ)=B(NEQ)/A(NEQ,NEQ)
DO 150 I=1,LIMIT
NI=NEQ-I
NI1=NI+1
SUM=0.0
DO 125 J=NI1,NEQ

```

```
125 SUM=SUM+A(NI,J)*B(J)
150 B(NI)=(B(NI)-SUM)/A(NI,NI)
RETURN
END
```

```
C
C Vector magnitude subroutine (3x3)
C
```

```
SUBROUTINE MAG(U,UMAG)
REAL*8 U(3),UMAG
UMAG = 0.0
DO 10 I = 1,3
10 UMAG = UMAG+U(I)*U(I)
UMAG = DSQRT(UMAG)
RETURN
END
```

## A.2. TRACE Output for Trace Analyses

### TRACE output for specimen 5-1-1:

PsiA1 = 49.00 PsiB1 = 82.00 PsiA2 =118.50

Rotation increments = .10 Tolerance = .00010

Trace of plane 1 on surface A: -.6561 .7547 .0000

Trace of plane 1 on surface B: .1392 .0000 -.9903

Unit normal to plane 1: -.7505 -.6524 -.1055

Trace of plane 2 on surface A: .4772 .8788 .0000

Step	Rot	Plane	Trace	Dotprod	Normal
78	8.	2	-.4857	-.8741	.0000 0.95D-04 -.6937 .3854 -.6085
79	8.	2	-.4855	-.8743	.0000 0.90D-04 -.6929 .3848 -.6098
80	8.	2	-.4852	-.8744	.0000 0.85D-04 -.6921 .3841 -.6111
81	8.	2	-.4850	-.8745	.0000 0.79D-04 -.6914 .3834 -.6124
82	8.	2	-.4847	-.8747	.0000 0.75D-04 -.6906 .3827 -.6137
83	8.	2	-.4845	-.8748	.0000 0.70D-04 -.6898 .3821 -.6149
84	8.	2	-.4842	-.8749	.0000 0.65D-04 -.6891 .3814 -.6162
85	8.	2	-.4840	-.8751	.0000 0.61D-04 -.6883 .3807 -.6175
86	9.	2	-.4837	-.8752	.0000 0.57D-04 -.6875 .3800 -.6188
87	9.	2	-.4835	-.8753	.0000 0.52D-04 -.6867 .3793 -.6201
88	9.	2	-.4832	-.8755	.0000 0.48D-04 -.6860 .3786 -.6214
89	9.	2	-.4830	-.8756	.0000 0.44D-04 -.6852 .3779 -.6226
90	9.	2	-.4827	-.8758	.0000 0.41D-04 -.6844 .3773 -.6239
91	9.	2	-.4825	-.8759	.0000 0.37D-04 -.6836 .3766 -.6252
92	9.	2	-.4822	-.8761	.0000 0.33D-04 -.6828 .3759 -.6264
93	9.	2	-.4820	-.8762	.0000 0.30D-04 -.6821 .3752 -.6277
94	9.	2	-.4817	-.8763	.0000 0.27D-04 -.6813 .3745 -.6290
95	9.	2	-.4814	-.8765	.0000 0.24D-04 -.6805 .3738 -.6303
96	10.	2	-.4812	-.8766	.0000 0.21D-04 -.6797 .3731 -.6315
97	10.	2	-.4809	-.8768	.0000 0.18D-04 -.6789 .3724 -.6328
98	10.	2	-.4806	-.8769	.0000 0.16D-04 -.6781 .3717 -.6340
99	10.	2	-.4804	-.8771	.0000 0.13D-04 -.6773 .3710 -.6353
100	10.	2	-.4801	-.8772	.0000 0.11D-04 -.6765 .3703 -.6366
101	10.	2	-.4798	-.8774	.0000 0.91D-05 -.6758 .3695 -.6378
102	10.	2	-.4795	-.8775	.0000 0.74D-05 -.6750 .3688 -.6391



103 10. 2 -.4792 -.8777 .0000 0.57D-05 -.6742 .3681 -.6403  
104 10. 2 -.4790 -.8778 .0000 0.43D-05 -.6734 .3674 -.6416  
105 10. 2 -.4787 -.8780 .0000 0.31D-05 -.6726 .3667 -.6428  
106 10. 2 -.4784 -.8781 .0000 0.20D-05 -.6718 .3660 -.6440  
107 11. 2 -.4781 -.8783 .0000 0.11D-05 -.6710 .3652 -.6453  
108 11. 2 -.4778 -.8785 .0000 0.60D-06 -.6702 .3645 -.6465  
109 11. 2 -.4775 -.8786 .0000 0.24D-06 -.6694 .3638 -.6478  
110 11. 2 -.4772 -.8788 .0000 0.00D+00 -.6686 .3631 -.6490  
111 11. 2 -.4769 -.8789 .0000 0.00D+00 -.6677 .3623 -.6502  
112 11. 2 -.4766 -.8791 .0000 0.48D-06 -.6669 .3616 -.6515  
113 11. 2 -.4763 -.8793 .0000 0.95D-06 -.6661 .3609 -.6527  
114 11. 2 -.4760 -.8794 .0000 0.17D-05 -.6653 .3602 -.6539  
115 11. 2 -.4757 -.8796 .0000 0.26D-05 -.6645 .3594 -.6552  
116 11. 2 -.4754 -.8797 .0000 0.39D-05 -.6637 .3587 -.6564  
117 12. 2 -.4751 -.8799 .0000 0.54D-05 -.6629 .3579 -.6576  
118 12. 2 -.4748 -.8801 .0000 0.69D-05 -.6621 .3572 -.6588  
119 12. 2 -.4745 -.8802 .0000 0.91D-05 -.6612 .3565 -.6601  
120 12. 2 -.4742 -.8804 .0000 0.11D-04 -.6604 .3557 -.6613  
121 12. 2 -.4739 -.8806 .0000 0.14D-04 -.6596 .3550 -.6625  
122 12. 2 -.4736 -.8808 .0000 0.17D-04 -.6588 .3542 -.6637  
123 12. 2 -.4733 -.8809 .0000 0.20D-04 -.6580 .3535 -.6649  
124 12. 2 -.4729 -.8811 .0000 0.23D-04 -.6571 .3527 -.6661  
125 12. 2 -.4726 -.8813 .0000 0.27D-04 -.6563 .3520 -.6674  
126 13. 2 -.4723 -.8814 .0000 0.31D-04 -.6555 .3512 -.6686  
127 13. 2 -.4720 -.8816 .0000 0.35D-04 -.6547 .3505 -.6698  
128 13. 2 -.4716 -.8818 .0000 0.40D-04 -.6538 .3497 -.6710  
129 13. 2 -.4713 -.8820 .0000 0.44D-04 -.6530 .3489 -.6722  
130 13. 2 -.4710 -.8822 .0000 0.50D-04 -.6522 .3482 -.6734  
131 13. 2 -.4706 -.8823 .0000 0.55D-04 -.6514 .3474 -.6746  
132 13. 2 -.4703 -.8825 .0000 0.61D-04 -.6505 .3467 -.6758  
133 13. 2 -.4699 -.8827 .0000 0.67D-04 -.6497 .3459 -.6770  
134 13. 2 -.4696 -.8829 .0000 0.74D-04 -.6489 .3451 -.6781  
135 13. 2 -.4693 -.8831 .0000 0.81D-04 -.6480 .3444 -.6793  
136 14. 2 -.4689 -.8832 .0000 0.88D-04 -.6472 .3436 -.6805  
137 14. 2 -.4686 -.8834 .0000 0.95D-04 -.6463 .3428 -.6817  
771 77. 3 .4685 .8835 -.0000 0.98D-04 .8697 -.4612 -.1757  
772 77. 3 .4687 .8833 -.0000 0.92D-04 .8698 -.4616 -.1741  
773 77. 3 .4690 .8832 -.0000 0.86D-04 .8700 -.4619 -.1725  
774 77. 3 .4692 .8831 -.0000 0.81D-04 .8701 -.4623 -.1710  
775 77. 3 .4695 .8829 -.0000 0.76D-04 .8702 -.4627 -.1694  
776 78. 3 .4698 .8828 -.0000 0.71D-04 .8703 -.4631 -.1678  
777 78. 3 .4700 .8827 -.0000 0.66D-04 .8704 -.4635 -.1662  
778 78. 3 .4703 .8825 -.0000 0.61D-04 .8705 -.4638 -.1646  
779 78. 3 .4705 .8824 -.0000 0.57D-04 .8706 -.4642 -.1630  
780 78. 3 .4708 .8823 -.0000 0.53D-04 .8707 -.4646 -.1614  
781 78. 3 .4710 .8821 -.0000 0.49D-04 .8708 -.4650 -.1598

782	78.	3	.4713	.8820	-.0000	0.45D-04	.8709	-.4653	-.1582
783	78.	3	.4715	.8819	-.0000	0.41D-04	.8710	-.4657	-.1566
784	78.	3	.4718	.8817	-.0000	0.37D-04	.8711	-.4661	-.1550
785	78.	3	.4720	.8816	-.0000	0.34D-04	.8712	-.4664	-.1534
786	78.	3	.4723	.8815	-.0000	0.31D-04	.8713	-.4668	-.1518
787	79.	3	.4725	.8813	-.0000	0.28D-04	.8713	-.4671	-.1502
788	79.	3	.4727	.8812	-.0000	0.25D-04	.8714	-.4675	-.1485
789	79.	3	.4730	.8811	-.0000	0.22D-04	.8715	-.4679	-.1469
790	79.	3	.4732	.8809	-.0000	0.20D-04	.8716	-.4682	-.1453
791	79.	3	.4735	.8808	-.0000	0.18D-04	.8717	-.4686	-.1437
792	79.	3	.4737	.8807	-.0000	0.15D-04	.8717	-.4689	-.1421
793	79.	3	.4740	.8805	-.0000	0.13D-04	.8718	-.4693	-.1405
794	79.	3	.4742	.8804	-.0000	0.11D-04	.8719	-.4696	-.1389
795	79.	3	.4744	.8803	-.0000	0.95D-05	.8720	-.4699	-.1373
796	79.	3	.4747	.8802	-.0000	0.80D-05	.8720	-.4703	-.1357
797	80.	3	.4749	.8800	-.0000	0.67D-05	.8721	-.4706	-.1341
798	80.	3	.4751	.8799	-.0000	0.52D-05	.8722	-.4709	-.1325
799	80.	3	.4754	.8798	-.0000	0.42D-05	.8722	-.4713	-.1309
800	80.	3	.4756	.8797	-.0000	0.31D-05	.8723	-.4716	-.1293
801	80.	3	.4758	.8795	-.0000	0.24D-05	.8723	-.4719	-.1276
802	80.	3	.4761	.8794	-.0000	0.15D-05	.8724	-.4723	-.1260
803	80.	3	.4763	.8793	-.0000	0.95D-06	.8725	-.4726	-.1244
804	80.	3	.4765	.8792	-.0000	0.60D-06	.8725	-.4729	-.1228
805	80.	3	.4768	.8790	-.0000	0.24D-06	.8726	-.4732	-.1212
806	81.	3	.4770	.8789	-.0000	0.00D+00	.8726	-.4736	-.1196
807	81.	3	.4772	.8788	-.0000	0.00D+00	.8727	-.4739	-.1180
808	81.	3	.4774	.8787	-.0000	0.12D-06	.8727	-.4742	-.1163
809	81.	3	.4777	.8785	-.0000	0.48D-06	.8727	-.4745	-.1147
810	81.	3	.4779	.8784	-.0000	0.72D-06	.8728	-.4748	-.1131
811	81.	3	.4781	.8783	-.0000	0.11D-05	.8728	-.4751	-.1115
812	81.	3	.4783	.8782	-.0000	0.18D-05	.8729	-.4754	-.1099
813	81.	3	.4785	.8781	-.0000	0.25D-05	.8729	-.4757	-.1083
814	81.	3	.4788	.8779	-.0000	0.33D-05	.8729	-.4760	-.1067
815	81.	3	.4790	.8778	-.0000	0.43D-05	.8730	-.4763	-.1050
816	81.	3	.4792	.8777	-.0000	0.52D-05	.8730	-.4766	-.1034
817	82.	3	.4794	.8776	-.0000	0.66D-05	.8730	-.4769	-.1018
818	82.	3	.4796	.8775	-.0000	0.79D-05	.8731	-.4772	-.1002
819	82.	3	.4798	.8774	-.0000	0.93D-05	.8731	-.4775	-.0986
820	82.	3	.4801	.8772	-.0000	0.11D-04	.8731	-.4778	-.0969
821	82.	3	.4803	.8771	-.0000	0.13D-04	.8731	-.4781	-.0953
822	82.	3	.4805	.8770	-.0000	0.14D-04	.8732	-.4784	-.0937
823	82.	3	.4807	.8769	-.0000	0.16D-04	.8732	-.4786	-.0921
824	82.	3	.4809	.8768	-.0000	0.18D-04	.8732	-.4789	-.0905
825	82.	3	.4811	.8767	-.0000	0.20D-04	.8732	-.4792	-.0888
826	83.	3	.4813	.8765	-.0000	0.23D-04	.8732	-.4795	-.0872
827	83.	3	.4815	.8764	-.0000	0.25D-04	.8732	-.4798	-.0856

828	83.	3	.4817	.8763	-.0000	0.27D-04	.8732	-.4800	-.0840
829	83.	3	.4819	.8762	-.0000	0.30D-04	.8732	-.4803	-.0823
830	83.	3	.4821	.8761	-.0000	0.32D-04	.8732	-.4806	-.0807
831	83.	3	.4823	.8760	-.0000	0.35D-04	.8732	-.4808	-.0791
832	83.	3	.4825	.8759	-.0000	0.38D-04	.8732	-.4811	-.0775
833	83.	3	.4827	.8758	-.0000	0.41D-04	.8732	-.4814	-.0758
834	83.	3	.4829	.8757	-.0000	0.44D-04	.8732	-.4816	-.0742
835	83.	3	.4831	.8755	-.0000	0.46D-04	.8732	-.4819	-.0726
836	84.	3	.4833	.8754	-.0000	0.50D-04	.8732	-.4821	-.0710
837	84.	3	.4835	.8753	-.0000	0.53D-04	.8732	-.4824	-.0693
838	84.	3	.4837	.8752	-.0000	0.56D-04	.8732	-.4826	-.0677
839	84.	3	.4839	.8751	-.0000	0.60D-04	.8732	-.4829	-.0661
840	84.	3	.4841	.8750	-.0000	0.63D-04	.8732	-.4831	-.0645
841	84.	3	.4843	.8749	-.0000	0.67D-04	.8732	-.4834	-.0628
842	84.	3	.4845	.8748	-.0000	0.70D-04	.8731	-.4836	-.0612
843	84.	3	.4847	.8747	-.0000	0.74D-04	.8731	-.4838	-.0596
844	84.	3	.4849	.8746	-.0000	0.78D-04	.8731	-.4841	-.0580
845	84.	3	.4851	.8745	-.0000	0.82D-04	.8731	-.4843	-.0563
846	84.	3	.4853	.8744	-.0000	0.86D-04	.8731	-.4846	-.0547
847	85.	3	.4855	.8743	-.0000	0.90D-04	.8730	-.4848	-.0531
848	85.	3	.4857	.8742	-.0000	0.94D-04	.8730	-.4850	-.0514
849	85.	3	.4858	.8740	-.0000	0.98D-04	.8730	-.4852	-.0498
1278	128.	3	.4857	.8741	-.0000	0.95D-04	.6937	-.3854	.6085
1279	128.	3	.4855	.8743	-.0000	0.90D-04	.6929	-.3848	.6098
1280	128.	3	.4852	.8744	-.0000	0.85D-04	.6921	-.3841	.6111
1281	128.	3	.4850	.8745	-.0000	0.80D-04	.6914	-.3834	.6124
1282	128.	3	.4847	.8747	-.0000	0.75D-04	.6906	-.3827	.6137
1283	128.	3	.4845	.8748	-.0000	0.70D-04	.6898	-.3821	.6149
1284	128.	3	.4842	.8749	-.0000	0.65D-04	.6891	-.3814	.6162
1285	128.	3	.4840	.8751	-.0000	0.61D-04	.6883	-.3807	.6175
1286	128.	3	.4838	.8752	-.0000	0.57D-04	.6875	-.3800	.6188
1287	129.	3	.4835	.8753	-.0000	0.52D-04	.6867	-.3793	.6201
1288	129.	3	.4832	.8755	-.0000	0.48D-04	.6860	-.3786	.6214
1289	129.	3	.4830	.8756	-.0000	0.44D-04	.6852	-.3780	.6226
1290	129.	3	.4827	.8758	-.0000	0.41D-04	.6844	-.3773	.6239
1291	129.	3	.4825	.8759	-.0000	0.37D-04	.6836	-.3766	.6252
1292	129.	3	.4822	.8760	-.0000	0.33D-04	.6829	-.3759	.6264
1293	129.	3	.4820	.8762	-.0000	0.30D-04	.6821	-.3752	.6277
1294	129.	3	.4817	.8763	-.0000	0.27D-04	.6813	-.3745	.6290
1295	129.	3	.4814	.8765	-.0000	0.24D-04	.6805	-.3738	.6302
1296	129.	3	.4812	.8766	-.0000	0.21D-04	.6797	-.3731	.6315
1297	130.	3	.4809	.8768	-.0000	0.18D-04	.6789	-.3724	.6328
1298	130.	3	.4806	.8769	-.0000	0.16D-04	.6781	-.3717	.6340
1299	130.	3	.4804	.8771	-.0000	0.13D-04	.6773	-.3710	.6353
1300	130.	3	.4801	.8772	-.0000	0.11D-04	.6765	-.3703	.6365
1301	130.	3	.4798	.8774	-.0000	0.91D-05	.6758	-.3695	.6378

1302	130.	3	.4795	.8775	-.0000	0.74D-05	.6750	-.3688	.6391
1303	130.	3	.4793	.8777	-.0000	0.57D-05	.6742	-.3681	.6403
1304	130.	3	.4790	.8778	-.0000	0.43D-05	.6734	-.3674	.6416
1305	130.	3	.4787	.8780	-.0000	0.31D-05	.6726	-.3667	.6428
1306	130.	3	.4784	.8781	-.0000	0.21D-05	.6718	-.3660	.6440
1307	131.	3	.4781	.8783	-.0000	0.13D-05	.6710	-.3653	.6453
1308	131.	3	.4778	.8785	-.0000	0.60D-06	.6702	-.3645	.6465
1309	131.	3	.4775	.8786	-.0000	0.24D-06	.6694	-.3638	.6478
1310	131.	3	.4772	.8788	-.0000	0.00D+00	.6686	-.3631	.6490
1311	131.	3	.4769	.8789	-.0000	0.00D+00	.6677	-.3624	.6502
1312	131.	3	.4767	.8791	-.0000	0.36D-06	.6669	-.3616	.6515
1313	131.	3	.4764	.8793	-.0000	0.95D-06	.6661	-.3609	.6527
1314	131.	3	.4761	.8794	-.0000	0.15D-05	.6653	-.3602	.6539
1315	131.	3	.4757	.8796	-.0000	0.26D-05	.6645	-.3594	.6552
1316	132.	3	.4754	.8797	-.0000	0.39D-05	.6637	-.3587	.6564
1317	132.	3	.4751	.8799	-.0000	0.52D-05	.6629	-.3579	.6576
1318	132.	3	.4748	.8801	-.0000	0.69D-05	.6621	-.3572	.6588
1319	132.	3	.4745	.8802	-.0000	0.91D-05	.6613	-.3565	.6601
1320	132.	3	.4742	.8804	-.0000	0.11D-04	.6604	-.3557	.6613
1321	132.	3	.4739	.8806	-.0000	0.14D-04	.6596	-.3550	.6625
1322	132.	3	.4736	.8808	-.0000	0.17D-04	.6588	-.3542	.6637
1323	132.	3	.4733	.8809	-.0000	0.20D-04	.6580	-.3535	.6649
1324	132.	3	.4729	.8811	-.0000	0.23D-04	.6572	-.3527	.6661
1325	132.	3	.4726	.8813	-.0000	0.27D-04	.6563	-.3520	.6673
1326	133.	3	.4723	.8814	-.0000	0.31D-04	.6555	-.3512	.6686
1327	133.	3	.4720	.8816	-.0000	0.35D-04	.6547	-.3505	.6698
1328	133.	3	.4716	.8818	-.0000	0.40D-04	.6538	-.3497	.6710
1329	133.	3	.4713	.8820	-.0000	0.44D-04	.6530	-.3489	.6722
1330	133.	3	.4710	.8822	-.0000	0.50D-04	.6522	-.3482	.6734
1331	133.	3	.4706	.8823	-.0000	0.55D-04	.6514	-.3474	.6746
1332	133.	3	.4703	.8825	-.0000	0.61D-04	.6505	-.3467	.6758
1333	133.	3	.4699	.8827	-.0000	0.67D-04	.6497	-.3459	.6769
1334	133.	3	.4696	.8829	-.0000	0.74D-04	.6489	-.3451	.6781
1335	133.	3	.4693	.8831	-.0000	0.80D-04	.6480	-.3444	.6793
1336	134.	3	.4689	.8832	-.0000	0.88D-04	.6472	-.3436	.6805
1337	134.	3	.4686	.8834	-.0000	0.95D-04	.6463	-.3428	.6817
1971	197.	4	-.4684	-.8835	.0000	0.98D-04	-.8697	.4611	.1758
1972	197.	4	-.4687	-.8834	.0000	0.92D-04	-.8698	.4615	.1742
1973	197.	4	-.4690	-.8832	.0000	0.86D-04	-.8700	.4619	.1726
1974	197.	4	-.4692	-.8831	.0000	0.81D-04	-.8701	.4623	.1710
1975	197.	4	-.4695	-.8829	.0000	0.76D-04	-.8702	.4627	.1694
1976	198.	4	-.4697	-.8828	.0000	0.71D-04	-.8703	.4631	.1678
1977	198.	4	-.4700	-.8827	.0000	0.66D-04	-.8704	.4635	.1662
1978	198.	4	-.4702	-.8825	.0000	0.62D-04	-.8705	.4638	.1646
1979	198.	4	-.4705	-.8824	.0000	0.57D-04	-.8706	.4642	.1630
1980	198.	4	-.4708	-.8823	.0000	0.53D-04	-.8707	.4646	.1614

1981	198.	4	-.4710	-.8821	.0000	0.49D-04	-.8708	.4649	.1598
1982	198.	4	-.4713	-.8820	.0000	0.45D-04	-.8709	.4653	.1582
1983	198.	4	-.4715	-.8819	.0000	0.41D-04	-.8710	.4657	.1566
1984	198.	4	-.4718	-.8817	.0000	0.38D-04	-.8711	.4660	.1550
1985	198.	4	-.4720	-.8816	.0000	0.34D-04	-.8712	.4664	.1534
1986	199.	4	-.4722	-.8815	.0000	0.31D-04	-.8712	.4668	.1518
1987	199.	4	-.4725	-.8813	.0000	0.28D-04	-.8713	.4671	.1502
1988	199.	4	-.4727	-.8812	.0000	0.25D-04	-.8714	.4675	.1486
1989	199.	4	-.4730	-.8811	.0000	0.23D-04	-.8715	.4678	.1470
1990	199.	4	-.4732	-.8809	.0000	0.20D-04	-.8716	.4682	.1454
1991	199.	4	-.4735	-.8808	.0000	0.18D-04	-.8717	.4685	.1438
1992	199.	4	-.4737	-.8807	.0000	0.15D-04	-.8717	.4689	.1422
1993	199.	4	-.4739	-.8806	.0000	0.13D-04	-.8718	.4692	.1406
1994	199.	4	-.4742	-.8804	.0000	0.11D-04	-.8719	.4696	.1390
1995	199.	4	-.4744	-.8803	.0000	0.98D-05	-.8720	.4699	.1374
1996	200.	4	-.4747	-.8802	.0000	0.81D-05	-.8720	.4703	.1358
1997	200.	4	-.4749	-.8800	.0000	0.67D-05	-.8721	.4706	.1342
1998	200.	4	-.4751	-.8799	.0000	0.54D-05	-.8722	.4709	.1326
1999	200.	4	-.4754	-.8798	.0000	0.42D-05	-.8722	.4713	.1309
2000	200.	4	-.4756	-.8797	.0000	0.32D-05	-.8723	.4716	.1293
2001	200.	4	-.4758	-.8795	.0000	0.21D-05	-.8723	.4719	.1277
2002	200.	4	-.4761	-.8794	.0000	0.17D-05	-.8724	.4723	.1261
2003	200.	4	-.4763	-.8793	.0000	0.95D-06	-.8725	.4726	.1245
2004	200.	4	-.4765	-.8792	.0000	0.60D-06	-.8725	.4729	.1229
2005	200.	4	-.4767	-.8790	.0000	0.24D-06	-.8726	.4732	.1213
2006	201.	4	-.4770	-.8789	.0000	0.00D+00	-.8726	.4735	.1197
2007	201.	4	-.4772	-.8788	.0000	0.00D+00	-.8727	.4739	.1180
2008	201.	4	-.4774	-.8787	.0000	0.12D-06	-.8727	.4742	.1164
2009	201.	4	-.4776	-.8786	.0000	0.24D-06	-.8727	.4745	.1148
2010	201.	4	-.4779	-.8784	.0000	0.72D-06	-.8728	.4748	.1132
2011	201.	4	-.4781	-.8783	.0000	0.95D-06	-.8728	.4751	.1116
2012	201.	4	-.4783	-.8782	.0000	0.17D-05	-.8729	.4754	.1100
2013	201.	4	-.4785	-.8781	.0000	0.24D-05	-.8729	.4757	.1083
2014	201.	4	-.4787	-.8780	.0000	0.31D-05	-.8729	.4760	.1067
2015	201.	4	-.4790	-.8778	.0000	0.42D-05	-.8730	.4763	.1051
2016	202.	4	-.4792	-.8777	.0000	0.52D-05	-.8730	.4766	.1035
2017	202.	4	-.4794	-.8776	.0000	0.64D-05	-.8730	.4769	.1019
2018	202.	4	-.4796	-.8775	.0000	0.77D-05	-.8731	.4772	.1003
2019	202.	4	-.4798	-.8774	.0000	0.93D-05	-.8731	.4775	.0986
2020	202.	4	-.4800	-.8772	.0000	0.11D-04	-.8731	.4778	.0970
2021	202.	4	-.4803	-.8771	.0000	0.13D-04	-.8731	.4781	.0954
2022	202.	4	-.4805	-.8770	.0000	0.14D-04	-.8731	.4783	.0938
2023	202.	4	-.4807	-.8769	.0000	0.16D-04	-.8732	.4786	.0922
2024	202.	4	-.4809	-.8768	.0000	0.18D-04	-.8732	.4789	.0905
2025	202.	4	-.4811	-.8767	.0000	0.20D-04	-.8732	.4792	.0889
2026	203.	4	-.4813	-.8766	.0000	0.22D-04	-.8732	.4795	.0873

2027	203.	4	-.4815	-.8764	.0000	0.25D-04	-.8732	.4797	.0857
2028	203.	4	-.4817	-.8763	.0000	0.27D-04	-.8732	.4800	.0840
2029	203.	4	-.4819	-.8762	.0000	0.29D-04	-.8732	.4803	.0824
2030	203.	4	-.4821	-.8761	.0000	0.32D-04	-.8732	.4805	.0808
2031	203.	4	-.4823	-.8760	.0000	0.35D-04	-.8732	.4808	.0792
2032	203.	4	-.4825	-.8759	.0000	0.37D-04	-.8732	.4811	.0776
2033	203.	4	-.4827	-.8758	.0000	0.40D-04	-.8732	.4813	.0759
2034	203.	4	-.4829	-.8757	.0000	0.43D-04	-.8732	.4816	.0743
2035	203.	4	-.4831	-.8755	.0000	0.46D-04	-.8732	.4819	.0727
2036	204.	4	-.4833	-.8754	.0000	0.49D-04	-.8732	.4821	.0711
2037	204.	4	-.4835	-.8753	.0000	0.53D-04	-.8732	.4824	.0694
2038	204.	4	-.4837	-.8752	.0000	0.56D-04	-.8732	.4826	.0678
2039	204.	4	-.4839	-.8751	.0000	0.59D-04	-.8732	.4829	.0662
2040	204.	4	-.4841	-.8750	.0000	0.63D-04	-.8732	.4831	.0645
2041	204.	4	-.4843	-.8749	.0000	0.67D-04	-.8732	.4834	.0629
2042	204.	4	-.4845	-.8748	.0000	0.70D-04	-.8731	.4836	.0613
2043	204.	4	-.4847	-.8747	.0000	0.74D-04	-.8731	.4838	.0597
2044	204.	4	-.4849	-.8746	.0000	0.78D-04	-.8731	.4841	.0580
2045	204.	4	-.4851	-.8745	.0000	0.82D-04	-.8731	.4843	.0564
2046	205.	4	-.4853	-.8744	.0000	0.86D-04	-.8731	.4845	.0548
2047	205.	4	-.4855	-.8743	.0000	0.90D-04	-.8730	.4848	.0532
2048	205.	4	-.4856	-.8742	.0000	0.94D-04	-.8730	.4850	.0515
2049	205.	4	-.4858	-.8741	.0000	0.98D-04	-.8730	.4852	.0499
2478	248.	4	-.4857	-.8741	.0000	0.95D-04	-.6937	.3855	-.6084
2479	248.	4	-.4855	-.8743	.0000	0.90D-04	-.6930	.3848	-.6097
2480	248.	4	-.4852	-.8744	.0000	0.85D-04	-.6922	.3841	-.6110
2481	248.	4	-.4850	-.8745	.0000	0.80D-04	-.6914	.3835	-.6123
2482	248.	4	-.4848	-.8747	.0000	0.75D-04	-.6907	.3828	-.6136
2483	248.	4	-.4845	-.8748	.0000	0.70D-04	-.6899	.3821	-.6149
2484	248.	4	-.4843	-.8749	.0000	0.66D-04	-.6891	.3814	-.6161
2485	248.	4	-.4840	-.8751	.0000	0.61D-04	-.6884	.3807	-.6174
2486	248.	4	-.4838	-.8752	.0000	0.57D-04	-.6876	.3801	-.6187
2487	249.	4	-.4835	-.8753	.0000	0.53D-04	-.6868	.3794	-.6200
2488	249.	4	-.4833	-.8755	.0000	0.49D-04	-.6860	.3787	-.6213
2489	249.	4	-.4830	-.8756	.0000	0.45D-04	-.6852	.3780	-.6225
2490	249.	4	-.4828	-.8758	.0000	0.41D-04	-.6845	.3773	-.6238
2491	249.	4	-.4825	-.8759	.0000	0.37D-04	-.6837	.3766	-.6251
2492	249.	4	-.4822	-.8760	.0000	0.33D-04	-.6829	.3759	-.6264
2493	249.	4	-.4820	-.8762	.0000	0.30D-04	-.6821	.3752	-.6276
2494	249.	4	-.4817	-.8763	.0000	0.27D-04	-.6813	.3745	-.6289
2495	249.	4	-.4815	-.8765	.0000	0.24D-04	-.6806	.3738	-.6302
2496	249.	4	-.4812	-.8766	.0000	0.21D-04	-.6798	.3731	-.6314
2497	250.	4	-.4809	-.8768	.0000	0.18D-04	-.6790	.3724	-.6327
2498	250.	4	-.4806	-.8769	.0000	0.16D-04	-.6782	.3717	-.6339
2499	250.	4	-.4804	-.8771	.0000	0.13D-04	-.6774	.3710	-.6352
2500	250.	4	-.4801	-.8772	.0000	0.11D-04	-.6766	.3703	-.6365

2501	250.	4	-.4798	-.8774	.0000	0.92D-05	-.6758	.3696	-.6377
2502	250.	4	-.4795	-.8775	.0000	0.74D-05	-.6750	.3689	-.6390
2503	250.	4	-.4793	-.8777	.0000	0.57D-05	-.6742	.3682	-.6402
2504	250.	4	-.4790	-.8778	.0000	0.43D-05	-.6734	.3675	-.6415
2505	250.	4	-.4787	-.8780	.0000	0.32D-05	-.6726	.3667	-.6427
2506	251.	4	-.4784	-.8781	.0000	0.21D-05	-.6718	.3660	-.6440
2507	251.	4	-.4781	-.8783	.0000	0.12D-05	-.6710	.3653	-.6452
2508	251.	4	-.4778	-.8784	.0000	0.60D-06	-.6702	.3646	-.6464
2509	251.	4	-.4776	-.8786	.0000	0.24D-06	-.6694	.3639	-.6477
2510	251.	4	-.4773	-.8788	.0000	0.00D+00	-.6686	.3631	-.6489
2511	251.	4	-.4770	-.8789	.0000	0.12D-06	-.6678	.3624	-.6502
2512	251.	4	-.4767	-.8791	.0000	0.24D-06	-.6670	.3617	-.6514
2513	251.	4	-.4764	-.8792	.0000	0.83D-06	-.6662	.3609	-.6526
2514	251.	4	-.4761	-.8794	.0000	0.15D-05	-.6654	.3602	-.6538
2515	251.	4	-.4758	-.8796	.0000	0.25D-05	-.6646	.3595	-.6551
2516	252.	4	-.4755	-.8797	.0000	0.37D-05	-.6638	.3587	-.6563
2517	252.	4	-.4752	-.8799	.0000	0.51D-05	-.6629	.3580	-.6575
2518	252.	4	-.4748	-.8801	.0000	0.69D-05	-.6621	.3573	-.6588
2519	252.	4	-.4745	-.8802	.0000	0.89D-05	-.6613	.3565	-.6600
2520	252.	4	-.4742	-.8804	.0000	0.11D-04	-.6605	.3558	-.6612
2521	252.	4	-.4739	-.8806	.0000	0.14D-04	-.6597	.3550	-.6624
2522	252.	4	-.4736	-.8807	.0000	0.16D-04	-.6589	.3543	-.6636
2523	252.	4	-.4733	-.8809	.0000	0.20D-04	-.6580	.3535	-.6648
2524	252.	4	-.4730	-.8811	.0000	0.23D-04	-.6572	.3528	-.6660
2525	252.	4	-.4726	-.8813	.0000	0.26D-04	-.6564	.3520	-.6673
2526	253.	4	-.4723	-.8814	.0000	0.30D-04	-.6556	.3513	-.6685
2527	253.	4	-.4720	-.8816	.0000	0.35D-04	-.6547	.3505	-.6697
2528	253.	4	-.4716	-.8818	.0000	0.39D-04	-.6539	.3498	-.6709
2529	253.	4	-.4713	-.8820	.0000	0.44D-04	-.6531	.3490	-.6721
2530	253.	4	-.4710	-.8821	.0000	0.49D-04	-.6522	.3482	-.6733
2531	253.	4	-.4706	-.8823	.0000	0.55D-04	-.6514	.3475	-.6745
2532	253.	4	-.4703	-.8825	.0000	0.61D-04	-.6506	.3467	-.6757
2533	253.	4	-.4700	-.8827	.0000	0.67D-04	-.6498	.3459	-.6769
2534	253.	4	-.4696	-.8829	.0000	0.73D-04	-.6489	.3452	-.6781
2535	253.	4	-.4693	-.8830	.0000	0.80D-04	-.6481	.3444	-.6792
2536	254.	4	-.4689	-.8832	.0000	0.87D-04	-.6472	.3436	-.6804
2537	254.	4	-.4686	-.8834	.0000	0.95D-04	-.6464	.3429	-.6816
3171	317.	2	-.4684	-.8835	.0000	0.98D-04	-.8697	.4611	.1759
3172	317.	2	-.4687	-.8834	.0000	0.93D-04	-.8698	.4615	.1743
3173	317.	2	-.4689	-.8832	.0000	0.87D-04	-.8699	.4619	.1727
3174	317.	2	-.4692	-.8831	.0000	0.81D-04	-.8701	.4623	.1711
3175	317.	2	-.4695	-.8830	.0000	0.76D-04	-.8702	.4627	.1695
3176	317.	2	-.4697	-.8828	.0000	0.71D-04	-.8703	.4630	.1679
3177	318.	2	-.4700	-.8827	.0000	0.67D-04	-.8704	.4634	.1664
3178	318.	2	-.4702	-.8825	.0000	0.62D-04	-.8705	.4638	.1648
3179	318.	2	-.4705	-.8824	.0000	0.57D-04	-.8706	.4642	.1632

3180	318.	2	-.4707	-.8823	.0000	0.53D-04	-.8707	.4646	.1616
3181	318.	2	-.4710	-.8821	.0000	0.49D-04	-.8708	.4649	.1600
3182	318.	2	-.4712	-.8820	.0000	0.45D-04	-.8709	.4653	.1584
3183	318.	2	-.4715	-.8819	.0000	0.41D-04	-.8710	.4657	.1568
3184	318.	2	-.4717	-.8817	.0000	0.38D-04	-.8711	.4660	.1552
3185	318.	2	-.4720	-.8816	.0000	0.35D-04	-.8712	.4664	.1535
3186	318.	2	-.4722	-.8815	.0000	0.31D-04	-.8712	.4667	.1519
3187	319.	2	-.4725	-.8813	.0000	0.28D-04	-.8713	.4671	.1503
3188	319.	2	-.4727	-.8812	.0000	0.25D-04	-.8714	.4675	.1487
3189	319.	2	-.4730	-.8811	.0000	0.23D-04	-.8715	.4678	.1471
3190	319.	2	-.4732	-.8810	.0000	0.20D-04	-.8716	.4682	.1455
3191	319.	2	-.4734	-.8808	.0000	0.18D-04	-.8717	.4685	.1439
3192	319.	2	-.4737	-.8807	.0000	0.15D-04	-.8717	.4689	.1423
3193	319.	2	-.4739	-.8806	.0000	0.14D-04	-.8718	.4692	.1407
3194	319.	2	-.4742	-.8804	.0000	0.12D-04	-.8719	.4696	.1391
3195	319.	2	-.4744	-.8803	.0000	0.99D-05	-.8719	.4699	.1375
3196	319.	2	-.4746	-.8802	.0000	0.82D-05	-.8720	.4702	.1359
3197	320.	2	-.4749	-.8801	.0000	0.67D-05	-.8721	.4706	.1343
3198	320.	2	-.4751	-.8799	.0000	0.55D-05	-.8721	.4709	.1327
3199	320.	2	-.4753	-.8798	.0000	0.44D-05	-.8722	.4712	.1311
3200	320.	2	-.4756	-.8797	.0000	0.33D-05	-.8723	.4716	.1294
3201	320.	2	-.4758	-.8796	.0000	0.24D-05	-.8723	.4719	.1278
3202	320.	2	-.4760	-.8794	.0000	0.17D-05	-.8724	.4722	.1262
3203	320.	2	-.4763	-.8793	.0000	0.12D-05	-.8724	.4726	.1246
3204	320.	2	-.4765	-.8792	.0000	0.72D-06	-.8725	.4729	.1230
3205	320.	2	-.4767	-.8791	.0000	0.24D-06	-.8726	.4732	.1214
3206	320.	2	-.4769	-.8789	.0000	0.00D+00	-.8726	.4735	.1198
3207	321.	2	-.4772	-.8788	.0000	0.00D+00	-.8727	.4738	.1182
3208	321.	2	-.4774	-.8787	.0000	0.12D-06	-.8727	.4741	.1165
3209	321.	2	-.4776	-.8786	.0000	0.24D-06	-.8727	.4745	.1149
3210	321.	2	-.4778	-.8784	.0000	0.72D-06	-.8728	.4748	.1133
3211	321.	2	-.4781	-.8783	.0000	0.12D-05	-.8728	.4751	.1117
3212	321.	2	-.4783	-.8782	.0000	0.17D-05	-.8729	.4754	.1101
3213	321.	2	-.4785	-.8781	.0000	0.24D-05	-.8729	.4757	.1085
3214	321.	2	-.4787	-.8780	.0000	0.32D-05	-.8729	.4760	.1068
3215	321.	2	-.4789	-.8778	.0000	0.43D-05	-.8730	.4763	.1052
3216	321.	2	-.4792	-.8777	.0000	0.52D-05	-.8730	.4766	.1036
3217	322.	2	-.4794	-.8776	.0000	0.64D-05	-.8730	.4769	.1020
3218	322.	2	-.4796	-.8775	.0000	0.77D-05	-.8731	.4772	.1004
3219	322.	2	-.4798	-.8774	.0000	0.92D-05	-.8731	.4775	.0988
3220	322.	2	-.4800	-.8773	.0000	0.11D-04	-.8731	.4778	.0971
3221	322.	2	-.4802	-.8771	.0000	0.12D-04	-.8731	.4780	.0955
3222	322.	2	-.4804	-.8770	.0000	0.14D-04	-.8731	.4783	.0939
3223	322.	2	-.4807	-.8769	.0000	0.16D-04	-.8732	.4786	.0923
3224	322.	2	-.4809	-.8768	.0000	0.18D-04	-.8732	.4789	.0907
3225	322.	2	-.4811	-.8767	.0000	0.20D-04	-.8732	.4792	.0890



```

3226 322. 2 -.4813 -.8766 .0000 0.22D-04 -.8732 .4794 .0874
3227 323. 2 -.4815 -.8765 .0000 0.24D-04 -.8732 .4797 .0858
3228 323. 2 -.4817 -.8763 .0000 0.27D-04 -.8732 .4800 .0842
3229 323. 2 -.4819 -.8762 .0000 0.29D-04 -.8732 .4803 .0825
3230 323. 2 -.4821 -.8761 .0000 0.32D-04 -.8732 .4805 .0809
3231 323. 2 -.4823 -.8760 .0000 0.35D-04 -.8732 .4808 .0793
3232 323. 2 -.4825 -.8759 .0000 0.37D-04 -.8732 .4811 .0777
3233 323. 2 -.4827 -.8758 .0000 0.40D-04 -.8732 .4813 .0760
3234 323. 2 -.4829 -.8757 .0000 0.43D-04 -.8732 .4816 .0744
3235 323. 2 -.4831 -.8756 .0000 0.46D-04 -.8732 .4818 .0728
3236 323. 2 -.4833 -.8754 .0000 0.49D-04 -.8732 .4821 .0712
3237 324. 2 -.4835 -.8753 .0000 0.52D-04 -.8732 .4823 .0695
3238 324. 2 -.4837 -.8752 .0000 0.56D-04 -.8732 .4826 .0679
3239 324. 2 -.4839 -.8751 .0000 0.59D-04 -.8732 .4828 .0663
3240 324. 2 -.4841 -.8750 .0000 0.63D-04 -.8732 .4831 .0647
3241 324. 2 -.4843 -.8749 .0000 0.66D-04 -.8732 .4833 .0630
3242 324. 2 -.4845 -.8748 .0000 0.70D-04 -.8731 .4836 .0614
3243 324. 2 -.4847 -.8747 .0000 0.74D-04 -.8731 .4838 .0598
3244 324. 2 -.4849 -.8746 .0000 0.77D-04 -.8731 .4841 .0582
3245 324. 2 -.4851 -.8745 .0000 0.81D-04 -.8731 .4843 .0565
3246 324. 2 -.4853 -.8744 .0000 0.85D-04 -.8731 .4845 .0549
3247 325. 2 -.4854 -.8743 .0000 0.89D-04 -.8730 .4848 .0533
3248 325. 2 -.4856 -.8742 .0000 0.93D-04 -.8730 .4850 .0516
3249 325. 2 -.4858 -.8741 .0000 0.98D-04 -.8730 .4852 .0500

```

**TRACE output for specimen 5-1-2:**

PsiA1 = 53.00 PsiB1 = 70.50 PsiA2 =169.50

Rotation increments = .10 Tolerance = .00010

Trace of plane 1 on surface A: -.6018 .7986 .0000

Trace of plane 1 on surface B: .3338 .0000 -.9426

Unit normal to plane 1: -.7685 -.5791 -.2721

Trace of plane 2 on surface A: .9833 .1822 .0000

Step	Rot	Plane	Trace	Dotprod	Normal
533	53.	4	.9815 .1916	-.0000 0.90D-04	.1846 -.9459 .2667
534	53.	4	.9816 .1909	-.0000 0.78D-04	.1839 -.9457 .2681

535 53. 4 .9817 .1902 -.0000 0.66D-04 .1832 -.9454 .2696  
536 53. 4 .9819 .1896 -.0000 0.56D-04 .1825 -.9451 .2710  
537 54. 4 .9820 .1889 -.0000 0.46D-04 .1817 -.9448 .2725  
538 54. 4 .9821 .1882 -.0000 0.37D-04 .1810 -.9446 .2739  
539 54. 4 .9823 .1875 -.0000 0.29D-04 .1803 -.9443 .2754  
540 54. 4 .9824 .1869 -.0000 0.22D-04 .1796 -.9440 .2768  
541 54. 4 .9825 .1862 -.0000 0.16D-04 .1788 -.9437 .2783  
542 54. 4 .9826 .1855 -.0000 0.11D-04 .1781 -.9434 .2797  
543 54. 4 .9828 .1848 -.0000 0.70D-05 .1774 -.9431 .2812  
544 54. 4 .9829 .1841 -.0000 0.38D-05 .1766 -.9428 .2826  
545 54. 4 .9830 .1835 -.0000 0.15D-05 .1759 -.9425 .2841  
546 54. 4 .9832 .1828 -.0000 0.36D-06 .1752 -.9422 .2855  
547 55. 4 .9833 .1821 -.0000 0.12D-06 .1744 -.9419 .2869  
548 55. 4 .9834 .1814 -.0000 0.83D-06 .1737 -.9416 .2884  
549 55. 4 .9835 .1807 -.0000 0.25D-05 .1730 -.9413 .2898  
550 55. 4 .9837 .1800 -.0000 0.51D-05 .1722 -.9410 .2913  
551 55. 4 .9838 .1793 -.0000 0.88D-05 .1715 -.9407 .2927  
552 55. 4 .9839 .1786 -.0000 0.13D-04 .1707 -.9404 .2941  
553 55. 4 .9840 .1779 -.0000 0.19D-04 .1700 -.9401 .2956  
554 55. 4 .9842 .1772 -.0000 0.26D-04 .1692 -.9398 .2970  
555 55. 4 .9843 .1765 -.0000 0.34D-04 .1685 -.9394 .2984  
556 56. 4 .9844 .1758 -.0000 0.42D-04 .1677 -.9391 .2999  
557 56. 4 .9845 .1751 -.0000 0.52D-04 .1670 -.9388 .3013  
558 56. 4 .9847 .1744 -.0000 0.63D-04 .1662 -.9385 .3027  
559 56. 4 .9848 .1737 -.0000 0.75D-04 .1655 -.9381 .3041  
560 56. 4 .9849 .1730 -.0000 0.88D-04 .1647 -.9378 .3056  
681 68. 2 .9846 .1747 -.0000 0.58D-04 .0257 -.1449 -.9891  
682 68. 2 .9838 .1793 -.0000 0.92D-05 .0266 -.1463 -.9889  
683 68. 2 .9830 .1837 -.0000 0.21D-05 .0276 -.1476 -.9887  
684 68. 2 .9822 .1880 -.0000 0.34D-04 .0285 -.1489 -.9884  
1733 173. 2 .9815 .1916 -.0000 0.91D-04 .1846 -.9459 .2666  
1734 173. 2 .9816 .1909 -.0000 0.78D-04 .1839 -.9457 .2681  
1735 173. 2 .9817 .1903 -.0000 0.67D-04 .1832 -.9454 .2695  
1736 174. 2 .9819 .1896 -.0000 0.56D-04 .1825 -.9451 .2710  
1737 174. 2 .9820 .1889 -.0000 0.46D-04 .1818 -.9448 .2725  
1738 174. 2 .9821 .1882 -.0000 0.37D-04 .1810 -.9446 .2739  
1739 174. 2 .9823 .1876 -.0000 0.29D-04 .1803 -.9443 .2754  
1740 174. 2 .9824 .1869 -.0000 0.22D-04 .1796 -.9440 .2768  
1741 174. 2 .9825 .1862 -.0000 0.16D-04 .1789 -.9437 .2782  
1742 174. 2 .9826 .1855 -.0000 0.11D-04 .1781 -.9434 .2797  
1743 174. 2 .9828 .1848 -.0000 0.70D-05 .1774 -.9431 .2811  
1744 174. 2 .9829 .1842 -.0000 0.39D-05 .1767 -.9428 .2826  
1745 174. 2 .9830 .1835 -.0000 0.15D-05 .1759 -.9425 .2840  
1746 175. 2 .9832 .1828 -.0000 0.24D-06 .1752 -.9422 .2855  
1747 175. 2 .9833 .1821 -.0000 0.12D-06 .1745 -.9419 .2869  
1748 175. 2 .9834 .1814 -.0000 0.83D-06 .1737 -.9416 .2883

1749 175. 2 .9835 .1807 -.0000 0.24D-05 .1730 -.9413 .2898  
1750 175. 2 .9837 .1800 -.0000 0.51D-05 .1722 -.9410 .2912  
1751 175. 2 .9838 .1793 -.0000 0.88D-05 .1715 -.9407 .2927  
1752 175. 2 .9839 .1787 -.0000 0.13D-04 .1708 -.9404 .2941  
1753 175. 2 .9840 .1780 -.0000 0.19D-04 .1700 -.9401 .2955  
1754 175. 2 .9842 .1773 -.0000 0.26D-04 .1693 -.9398 .2970  
1755 175. 2 .9843 .1766 -.0000 0.33D-04 .1685 -.9395 .2984  
1756 175. 2 .9844 .1759 -.0000 0.42D-04 .1678 -.9391 .2998  
1757 176. 2 .9845 .1752 -.0000 0.52D-04 .1670 -.9388 .3012  
1758 176. 2 .9847 .1744 -.0000 0.63D-04 .1663 -.9385 .3027  
1759 176. 2 .9848 .1737 -.0000 0.75D-04 .1655 -.9382 .3041  
1760 176. 2 .9849 .1730 -.0000 0.87D-04 .1648 -.9378 .3055  
1881 188. 3 -.9846 -.1746 .0000 0.61D-04 -.0257 .1449 .9891  
1882 188. 3 -.9838 -.1791 .0000 0.10D-04 -.0266 .1462 .9889  
1883 188. 3 -.9830 -.1835 .0000 0.18D-05 -.0275 .1475 .9887  
1884 188. 3 -.9822 -.1878 .0000 0.32D-04 -.0285 .1489 .9884  
2933 293. 3 -.9815 -.1916 .0000 0.92D-04 -.1847 .9460 -.2665  
2934 293. 3 -.9816 -.1910 .0000 0.79D-04 -.1840 .9457 -.2680  
2935 293. 3 -.9817 -.1903 .0000 0.67D-04 -.1833 .9454 -.2694  
2936 293. 3 -.9819 -.1896 .0000 0.57D-04 -.1825 .9451 -.2709  
2937 294. 3 -.9820 -.1890 .0000 0.47D-04 -.1818 .9449 -.2723  
2938 294. 3 -.9821 -.1883 .0000 0.38D-04 -.1811 .9446 -.2738  
2939 294. 3 -.9822 -.1876 .0000 0.30D-04 -.1804 .9443 -.2752  
2940 294. 3 -.9824 -.1869 .0000 0.23D-04 -.1796 .9440 -.2767  
2941 294. 3 -.9825 -.1863 .0000 0.17D-04 -.1789 .9437 -.2781  
2942 294. 3 -.9826 -.1856 .0000 0.12D-04 -.1782 .9434 -.2796  
2943 294. 3 -.9828 -.1849 .0000 0.74D-05 -.1774 .9432 -.2810  
2944 294. 3 -.9829 -.1842 .0000 0.42D-05 -.1767 .9429 -.2825  
2945 294. 3 -.9830 -.1835 .0000 0.18D-05 -.1760 .9426 -.2839  
2946 294. 3 -.9831 -.1828 .0000 0.48D-06 -.1752 .9423 -.2854  
2947 295. 3 -.9833 -.1822 .0000 0.00D+00 -.1745 .9420 -.2868  
2948 295. 3 -.9834 -.1815 .0000 0.60D-06 -.1738 .9417 -.2882  
2949 295. 3 -.9835 -.1808 .0000 0.21D-05 -.1730 .9414 -.2897  
2950 295. 3 -.9836 -.1801 .0000 0.48D-05 -.1723 .9410 -.2911  
2951 295. 3 -.9838 -.1794 .0000 0.83D-05 -.1716 .9407 -.2925  
2952 295. 3 -.9839 -.1787 .0000 0.13D-04 -.1708 .9404 -.2940  
2953 295. 3 -.9840 -.1780 .0000 0.18D-04 -.1701 .9401 -.2954  
2954 295. 3 -.9842 -.1773 .0000 0.25D-04 -.1693 .9398 -.2968  
2955 295. 3 -.9843 -.1766 .0000 0.33D-04 -.1686 .9395 -.2983  
2956 295. 3 -.9844 -.1759 .0000 0.41D-04 -.1678 .9392 -.2997  
2957 296. 3 -.9845 -.1752 .0000 0.51D-04 -.1671 .9388 -.3011  
2958 296. 3 -.9847 -.1745 .0000 0.62D-04 -.1663 .9385 -.3026  
2959 296. 3 -.9848 -.1738 .0000 0.74D-04 -.1656 .9382 -.3040  
2960 296. 3 -.9849 -.1731 .0000 0.87D-04 -.1648 .9378 -.3054  
3081 308. 4 .9847 .1742 -.0000 0.67D-04 .0256 -.1448 -.9891  
3082 308. 4 .9839 .1787 -.0000 0.13D-04 .0265 -.1461 -.9889

3083 308. 4 .9831 .1832 -.0000 0.95D-06 .0275 -.1474 -.9887  
 3084 308. 4 .9823 .1875 -.0000 0.29D-04 .0284 -.1488 -.9885  
 3085 308. 4 .9814 .1917 -.0000 0.94D-04 .0293 -.1501 -.9882

**TRACE output for specimen 5-1-S1:**

PsiA1 = 65.00 PsiB1 =119.00 PsiA2 =112.00

Rotation increments = .10 Tolerance = .00010

Trace of plane 1 on surface A: -.4226 .9063 .0000

Trace of plane 1 on surface B: -.4848 .0000 -.8746

Unit normal to plane 1: -.8099 -.3776 .4489

Trace of plane 2 on surface A: .3746 .9272 .0000

Step	Rot	Plane	Trace	Dotprod	Normal
159	16.	2	-.3835 -.9236	.0000 0.92D-04	-.8227 .3416 -.4543
160	16.	2	-.3822 -.9241	.0000 0.68D-04	-.8227 .3403 -.4554
161	16.	2	-.3810 -.9246	.0000 0.48D-04	-.8227 .3390 -.4564
162	16.	2	-.3798 -.9251	.0000 0.31D-04	-.8226 .3377 -.4574
163	16.	2	-.3786 -.9256	.0000 0.18D-04	-.8226 .3364 -.4584
164	16.	2	-.3773 -.9261	.0000 0.86D-05	-.8226 .3351 -.4594
165	16.	2	-.3761 -.9266	.0000 0.26D-05	-.8225 .3339 -.4605
166	16.	2	-.3749 -.9271	.0000 0.12D-06	-.8225 .3326 -.4615
167	17.	2	-.3736 -.9276	.0000 0.13D-05	-.8224 .3313 -.4625
168	17.	2	-.3724 -.9281	.0000 0.58D-05	-.8224 .3300 -.4635
169	17.	2	-.3711 -.9286	.0000 0.14D-04	-.8223 .3287 -.4645
170	17.	2	-.3699 -.9291	.0000 0.26D-04	-.8223 .3274 -.4655
171	17.	2	-.3686 -.9296	.0000 0.41D-04	-.8222 .3261 -.4665
172	17.	2	-.3674 -.9301	.0000 0.61D-04	-.8222 .3247 -.4675
173	17.	2	-.3661 -.9306	.0000 0.84D-04	-.8221 .3234 -.4685
1121	112.	4	.3788 .9255	-.0000 0.20D-04	.1653 -.0677 .9839
1122	112.	4	.3726 .9280	-.0000 0.48D-05	.1647 -.0661 .9841
1123	112.	4	.3663 .9305	-.0000 0.79D-04	.1642 -.0646 .9843
1359	136.	3	.3835 .9236	-.0000 0.92D-04	.8227 -.3416 .4543
1360	136.	3	.3822 .9241	-.0000 0.68D-04	.8227 -.3403 .4554
1361	136.	3	.3810 .9246	-.0000 0.48D-04	.8227 -.3390 .4564
1362	136.	3	.3798 .9251	-.0000 0.31D-04	.8226 -.3377 .4574
1363	136.	3	.3786 .9256	-.0000 0.18D-04	.8226 -.3364 .4584

1364	136.	3	.3773	.9261	-.0000	0.87D-05	.8226	-.3352	.4594
1365	136.	3	.3761	.9266	-.0000	0.26D-05	.8225	-.3339	.4605
1366	137.	3	.3749	.9271	-.0000	0.12D-06	.8225	-.3326	.4615
1367	137.	3	.3736	.9276	-.0000	0.12D-05	.8224	-.3313	.4625
1368	137.	3	.3724	.9281	-.0000	0.58D-05	.8224	-.3300	.4635
1369	137.	3	.3711	.9286	-.0000	0.14D-04	.8223	-.3287	.4645
1370	137.	3	.3699	.9291	-.0000	0.26D-04	.8223	-.3274	.4655
1371	137.	3	.3686	.9296	-.0000	0.41D-04	.8222	-.3261	.4665
1372	137.	3	.3674	.9301	-.0000	0.61D-04	.8222	-.3248	.4675
1373	137.	3	.3661	.9306	-.0000	0.83D-04	.8221	-.3235	.4685
2321	232.	2	.3792	.9253	-.0000	0.24D-04	.1654	-.0678	.9839
2322	232.	2	.3730	.9278	-.0000	0.30D-05	.1648	-.0663	.9841
2323	232.	2	.3668	.9303	-.0000	0.71D-04	.1642	-.0647	.9843
2559	256.	4	-.3836	-.9235	.0000	0.94D-04	-.8227	.3417	-.4543
2560	256.	4	-.3823	-.9240	.0000	0.70D-04	-.8227	.3404	-.4553
2561	256.	4	-.3811	-.9245	.0000	0.49D-04	-.8227	.3391	-.4563
2562	256.	4	-.3799	-.9250	.0000	0.33D-04	-.8226	.3378	-.4573
2563	256.	4	-.3787	-.9255	.0000	0.19D-04	-.8226	.3365	-.4583
2564	256.	4	-.3774	-.9260	.0000	0.93D-05	-.8226	.3352	-.4594
2565	256.	4	-.3762	-.9265	.0000	0.30D-05	-.8225	.3340	-.4604
2566	257.	4	-.3750	-.9270	.0000	0.24D-06	-.8225	.3327	-.4614
2567	257.	4	-.3737	-.9275	.0000	0.95D-06	-.8224	.3314	-.4624
2568	257.	4	-.3725	-.9280	.0000	0.54D-05	-.8224	.3301	-.4634
2569	257.	4	-.3712	-.9285	.0000	0.13D-04	-.8223	.3288	-.4644
2570	257.	4	-.3700	-.9290	.0000	0.25D-04	-.8223	.3275	-.4654
2571	257.	4	-.3687	-.9295	.0000	0.40D-04	-.8222	.3262	-.4664
2572	257.	4	-.3675	-.9300	.0000	0.59D-04	-.8222	.3249	-.4674
2573	257.	4	-.3662	-.9305	.0000	0.82D-04	-.8221	.3235	-.4684
3521	352.	3	-.3796	-.9251	.0000	0.29D-04	-.1654	.0679	-.9839
3522	352.	3	-.3735	-.9276	.0000	0.17D-05	-.1648	.0664	-.9841
3523	352.	3	-.3672	-.9301	.0000	0.63D-04	-.1642	.0648	-.9843

**TRACE output for specimen 5-1-S2:**

PsiA1 = 96.50 PsiB1 = 62.50 PsiA2 = 22.00

Rotation increments = .10 Tolerance = .00010

Trace of plane 1 on surface A: .1132 .9936 .0000

Trace of plane 1 on surface B: .4617 .0000 -.8870

Unit normal to plane 1: -.8825 .1005 -.4594

Trace of plane 2 on surface A: -.9272 .3746 .0000

Step	Rot	Plane	Trace	Dotprod	Normal
240	24.	4	.9308	-.3654	.0000 0.97D-04 -.3546 -.9031 -.2421
241	24.	4	.9306	-.3661	.0000 0.84D-04 -.3553 -.9032 -.2407
242	24.	4	.9303	-.3667	.0000 0.72D-04 -.3561 -.9033 -.2392
243	24.	4	.9301	-.3674	.0000 0.60D-04 -.3569 -.9034 -.2378
244	24.	4	.9298	-.3681	.0000 0.50D-04 -.3576 -.9035 -.2363
245	24.	4	.9295	-.3687	.0000 0.40D-04 -.3584 -.9035 -.2349
246	25.	4	.9293	-.3694	.0000 0.32D-04 -.3592 -.9036 -.2334
247	25.	4	.9290	-.3700	.0000 0.24D-04 -.3599 -.9037 -.2319
248	25.	4	.9288	-.3707	.0000 0.18D-04 -.3607 -.9038 -.2305
249	25.	4	.9285	-.3713	.0000 0.12D-04 -.3615 -.9038 -.2290
250	25.	4	.9282	-.3720	.0000 0.79D-05 -.3622 -.9039 -.2276
251	25.	4	.9280	-.3726	.0000 0.44D-05 -.3630 -.9039 -.2261
252	25.	4	.9277	-.3733	.0000 0.19D-05 -.3637 -.9040 -.2247
253	25.	4	.9274	-.3739	.0000 0.48D-06 -.3645 -.9040 -.2232
254	25.	4	.9272	-.3746	.0000 0.00D+00 -.3653 -.9041 -.2218
255	25.	4	.9269	-.3753	.0000 0.48D-06 -.3660 -.9041 -.2203
256	25.	4	.9267	-.3759	.0000 0.20D-05 -.3668 -.9042 -.2188
257	26.	4	.9264	-.3766	.0000 0.44D-05 -.3676 -.9042 -.2174
258	26.	4	.9261	-.3772	.0000 0.81D-05 -.3683 -.9043 -.2159
259	26.	4	.9259	-.3779	.0000 0.13D-04 -.3691 -.9043 -.2145
260	26.	4	.9256	-.3785	.0000 0.18D-04 -.3699 -.9043 -.2130
261	26.	4	.9253	-.3792	.0000 0.25D-04 -.3706 -.9044 -.2116
262	26.	4	.9250	-.3799	.0000 0.32D-04 -.3714 -.9044 -.2101
263	26.	4	.9248	-.3805	.0000 0.41D-04 -.3721 -.9044 -.2086
264	26.	4	.9245	-.3812	.0000 0.50D-04 -.3729 -.9044 -.2072
265	26.	4	.9242	-.3818	.0000 0.61D-04 -.3737 -.9045 -.2057
266	27.	4	.9240	-.3825	.0000 0.72D-04 -.3744 -.9045 -.2043
267	27.	4	.9237	-.3832	.0000 0.85D-04 -.3752 -.9045 -.2028
268	27.	4	.9234	-.3838	.0000 0.99D-04 -.3759 -.9045 -.2013
365	36.	2	-.9307	.3658	.0000 0.90D-04 .1429 .3636 -.9205
366	37.	2	-.9301	.3674	.0000 0.60D-04 .1430 .3621 -.9211
367	37.	2	-.9294	.3691	.0000 0.36D-04 .1432 .3605 -.9217
368	37.	2	-.9287	.3707	.0000 0.18D-04 .1433 .3590 -.9223
369	37.	2	-.9281	.3724	.0000 0.57D-05 .1434 .3575 -.9228
370	37.	2	-.9274	.3740	.0000 0.24D-06 .1435 .3559 -.9234
371	37.	2	-.9267	.3757	.0000 0.13D-05 .1437 .3544 -.9240
372	37.	2	-.9261	.3774	.0000 0.88D-05 .1438 .3529 -.9246
373	37.	2	-.9254	.3791	.0000 0.23D-04 .1439 .3513 -.9251
374	37.	2	-.9247	.3808	.0000 0.44D-04 .1440 .3498 -.9257
375	37.	2	-.9240	.3825	.0000 0.72D-04 .1441 .3482 -.9263
1440	144.	2	.9308	-.3654	.0000 0.98D-04 -.3546 -.9031 -.2421

1441 144. 2 .9306 -.3661 .0000 0.84D-04 -.3553 -.9032 -.2407  
1442 144. 2 .9303 -.3667 .0000 0.72D-04 -.3561 -.9033 -.2392  
1443 144. 2 .9301 -.3674 .0000 0.60D-04 -.3569 -.9034 -.2378  
1444 144. 2 .9298 -.3680 .0000 0.50D-04 -.3576 -.9035 -.2363  
1445 144. 2 .9295 -.3687 .0000 0.40D-04 -.3584 -.9035 -.2349  
1446 145. 2 .9293 -.3694 .0000 0.32D-04 -.3592 -.9036 -.2334  
1447 145. 2 .9290 -.3700 .0000 0.25D-04 -.3599 -.9037 -.2320  
1448 145. 2 .9288 -.3707 .0000 0.18D-04 -.3607 -.9038 -.2305  
1449 145. 2 .9285 -.3713 .0000 0.13D-04 -.3614 -.9038 -.2291  
1450 145. 2 .9282 -.3720 .0000 0.81D-05 -.3622 -.9039 -.2276  
1451 145. 2 .9280 -.3726 .0000 0.45D-05 -.3630 -.9039 -.2261  
1452 145. 2 .9277 -.3733 .0000 0.20D-05 -.3637 -.9040 -.2247  
1453 145. 2 .9275 -.3739 .0000 0.48D-06 -.3645 -.9040 -.2232  
1454 145. 2 .9272 -.3746 .0000 0.00D+00 -.3653 -.9041 -.2218  
1455 145. 2 .9269 -.3753 .0000 0.48D-06 -.3660 -.9041 -.2203  
1456 146. 2 .9267 -.3759 .0000 0.20D-05 -.3668 -.9042 -.2189  
1457 146. 2 .9264 -.3766 .0000 0.44D-05 -.3676 -.9042 -.2174  
1458 146. 2 .9261 -.3772 .0000 0.80D-05 -.3683 -.9043 -.2159  
1459 146. 2 .9259 -.3779 .0000 0.12D-04 -.3691 -.9043 -.2145  
1460 146. 2 .9256 -.3785 .0000 0.18D-04 -.3698 -.9043 -.2130  
1461 146. 2 .9253 -.3792 .0000 0.25D-04 -.3706 -.9044 -.2116  
1462 146. 2 .9250 -.3799 .0000 0.32D-04 -.3714 -.9044 -.2101  
1463 146. 2 .9248 -.3805 .0000 0.41D-04 -.3721 -.9044 -.2087  
1464 146. 2 .9245 -.3812 .0000 0.50D-04 -.3729 -.9044 -.2072  
1465 146. 2 .9242 -.3818 .0000 0.61D-04 -.3737 -.9045 -.2057  
1466 147. 2 .9240 -.3825 .0000 0.72D-04 -.3744 -.9045 -.2043  
1467 147. 2 .9237 -.3831 .0000 0.85D-04 -.3752 -.9045 -.2028  
1468 147. 2 .9234 -.3838 .0000 0.99D-04 -.3759 -.9045 -.2014  
1565 156. 3 .9307 -.3658 .0000 0.90D-04 -.1429 -.3636 .9205  
1566 157. 3 .9301 -.3674 .0000 0.60D-04 -.1430 -.3621 .9211  
1567 157. 3 .9294 -.3690 .0000 0.36D-04 -.1432 -.3606 .9217  
1568 157. 3 .9288 -.3707 .0000 0.18D-04 -.1433 -.3590 .9223  
1569 157. 3 .9281 -.3723 .0000 0.61D-05 -.1434 -.3575 .9228  
1570 157. 3 .9274 -.3740 .0000 0.24D-06 -.1435 -.3560 .9234  
1571 157. 3 .9268 -.3757 .0000 0.12D-05 -.1437 -.3544 .9240  
1572 157. 3 .9261 -.3773 .0000 0.87D-05 -.1438 -.3529 .9245  
1573 157. 3 .9254 -.3790 .0000 0.23D-04 -.1439 -.3514 .9251  
1574 157. 3 .9247 -.3807 .0000 0.44D-04 -.1440 -.3498 .9257  
1575 157. 3 .9240 -.3824 .0000 0.71D-04 -.1441 -.3483 .9262  
2640 264. 3 -.9309 .3654 .0000 0.98D-04 .3545 .9031 .2422  
2641 264. 3 -.9306 .3660 .0000 0.85D-04 .3553 .9032 .2408  
2642 264. 3 -.9303 .3667 .0000 0.73D-04 .3560 .9033 .2393  
2643 264. 3 -.9301 .3673 .0000 0.61D-04 .3568 .9034 .2379  
2644 264. 3 -.9298 .3680 .0000 0.51D-04 .3576 .9035 .2364  
2645 264. 3 -.9296 .3687 .0000 0.41D-04 .3583 .9035 .2350  
2646 264. 3 -.9293 .3693 .0000 0.33D-04 .3591 .9036 .2335

2647	265.	3	-.9290	.3700	.0000	0.25D-04	.3599	.9037	.2321
2648	265.	3	-.9288	.3706	.0000	0.19D-04	.3606	.9038	.2306
2649	265.	3	-.9285	.3713	.0000	0.13D-04	.3614	.9038	.2292
2650	265.	3	-.9283	.3719	.0000	0.83D-05	.3622	.9039	.2277
2651	265.	3	-.9280	.3726	.0000	0.48D-05	.3629	.9039	.2262
2652	265.	3	-.9277	.3732	.0000	0.21D-05	.3637	.9040	.2248
2653	265.	3	-.9275	.3739	.0000	0.48D-06	.3644	.9040	.2233
2654	265.	3	-.9272	.3745	.0000	0.00D+00	.3652	.9041	.2219
2655	265.	3	-.9269	.3752	.0000	0.36D-06	.3660	.9041	.2204
2656	265.	3	-.9267	.3759	.0000	0.18D-05	.3667	.9042	.2190
2657	266.	3	-.9264	.3765	.0000	0.42D-05	.3675	.9042	.2175
2658	266.	3	-.9261	.3772	.0000	0.76D-05	.3683	.9043	.2161
2659	266.	3	-.9259	.3778	.0000	0.12D-04	.3690	.9043	.2146
2660	266.	3	-.9256	.3785	.0000	0.18D-04	.3698	.9043	.2131
2661	266.	3	-.9253	.3791	.0000	0.24D-04	.3706	.9044	.2117
2662	266.	3	-.9251	.3798	.0000	0.31D-04	.3713	.9044	.2102
2663	266.	3	-.9248	.3805	.0000	0.40D-04	.3721	.9044	.2088
2664	266.	3	-.9245	.3811	.0000	0.49D-04	.3728	.9044	.2073
2665	266.	3	-.9243	.3818	.0000	0.60D-04	.3736	.9045	.2058
2666	266.	3	-.9240	.3824	.0000	0.72D-04	.3744	.9045	.2044
2667	267.	3	-.9237	.3831	.0000	0.84D-04	.3751	.9045	.2029
2668	267.	3	-.9234	.3838	.0000	0.98D-04	.3759	.9045	.2015
2765	276.	4	-.9308	.3656	.0000	0.93D-04	.1429	.3638	-.9205
2766	277.	4	-.9301	.3673	.0000	0.62D-04	.1430	.3622	-.9211
2767	277.	4	-.9295	.3689	.0000	0.38D-04	.1432	.3607	-.9216
2768	277.	4	-.9288	.3706	.0000	0.19D-04	.1433	.3592	-.9222
2769	277.	4	-.9281	.3722	.0000	0.66D-05	.1434	.3576	-.9228
2770	277.	4	-.9275	.3739	.0000	0.48D-06	.1435	.3561	-.9234
2771	277.	4	-.9268	.3755	.0000	0.95D-06	.1437	.3545	-.9239
2772	277.	4	-.9261	.3772	.0000	0.79D-05	.1438	.3530	-.9245
2773	277.	4	-.9254	.3789	.0000	0.21D-04	.1439	.3515	-.9251
2774	277.	4	-.9247	.3806	.0000	0.42D-04	.1440	.3499	-.9256
2775	277.	4	-.9240	.3823	.0000	0.69D-04	.1441	.3484	-.9262



### A.3. RODS Code for Determining Rod Crystallographic Orientation

```
PROGRAM RODS
CHARACTER*64 RFL,TFL
REAL*8 PI,THETA,S1,C1,C2,IXIA,IXIB,XIA,XIB,AMAG,RBMAG,DP
REAL*8 N1(3),N(3),N1CN(3),C(9),V(3)
REAL*8 RA(3),RB(3),TA(3),TB(3)
REAL*8 A(9,9),T(3,3)

C
C Define constants
C
PI = 3.141592654
THETA = 54.7356*(PI/180.)
S1 = DSIN(THETA)
C1 = DCOS(THETA)
C2 = 0.7071067814*C1

C
C Open files
C
WRITE (*,*) 'Traces file name?'
READ (*,*) TFL
OPEN (UNIT=3,FILE=TFL,STATUS='OLD')

C
WRITE (*,*) 'Solution file name?'
READ (*,*) RFL
OPEN (UNIT=4,FILE=RFL,STATUS='NEW')

C
C Read initial data
C
WRITE (*,*) 'IXIA,IXIB (in deg)?'
READ (*,*) IXIA,IXIB
WRITE (*,*) 'Print out checks? (y=1)'
ICHECK = 0
READ (*,*) ICHECK
XIA = PI*IXIA/180.
XIB = PI*IXIB/180.
READ (3,*) N1(1),N1(2),N1(3)
READ (3,*) NSOLS

C
TA(1) = -DCOS(XIA)
TA(2) = DSIN(XIA)
TA(3) = 0.0
TB(1) = DCOS(XIB)
TB(2) = 0.0
TB(3) = -DSIN(XIB)

C
```

```

WRITE (*,90) IXIA,IXIB
WRITE (4,90) IXIA,IXIB
90  FORMAT(/2X,'XIA = ',F7.2,' XIB = ',F7.2)
    WRITE (*,100) N1(1),N1(2),N1(3)
    WRITE (4,100) N1(1),N1(2),N1(3)
100  FORMAT(/2X,'Plane 1 normal = ',3F7.4)
    WRITE (*,110) NSOLS
    WRITE (4,110) NSOLS
110  FORMAT(/2X,'Number of solutions =',I4)
    WRITE (*,120) TA(1),TA(2),TA(3)
    WRITE (4,120) TA(1),TA(2),TA(3)
120  FORMAT(/2X,'Rod 1 trace = ',3F7.4)
    WRITE (*,130) TB(1),TB(2),TB(3)
    WRITE (4,130) TB(1),TB(2),TB(3)
130  FORMAT(/2X,'Rod 2 trace = ',3F7.4)
C
    WRITE (*,150)
    WRITE (4,150)
150  FORMAT(/2X,' Step  Rot Plane   Rod 1 Trace   Rod 2 Trace',/)
C
C   March through solutions
C
    DO 900 I = 1,NSOLS
    READ (3,*) IS,IR,IP,T1,T2,T3,DP,N(1),N(2),N(3)
    CALL CROSSP3(N1,N,N1CN)
C
C   Build equation matrix
C
    DO 180 J = 1,9
    C(J) = 0.0
    DO 180 K = 1,9
180  A(J,K) = 0.0
C
    DO 200 J = 1,3
    A(1,J) = N1(J)
    A(2,J) = N(J)
    A(3,J) = N1CN(J)
    A(4,J+3) = N1(J)
    A(5,J+3) = N(J)
    A(6,J+3) = N1CN(J)
    A(7,J+6) = N1(J)
    A(8,J+6) = N(J)
200  A(9,J+6) = N1CN(J)
C
C   Build load vector
C

```

```

C(1) = 0.577350269
C(4) = 0.577350269
C(7) = 0.577350269
C(8) = 0.577350269
IF (IP.EQ.2) THEN
    C(2) = -0.577350269
    C(5) = 0.577350269
    C(3) = 0.0
    C(6) = -0.7071067814
    C(9) = 0.7071067814
ELSEIF (IP.EQ.3) THEN
    C(2) = -0.577350269
    C(5) = -0.577350269
    C(3) = 0.7071067814
    C(6) = -0.7071067814
    C(9) = 0.0
ELSEIF (IP.EQ.4) THEN
    C(2) = 0.577350269
    C(5) = -0.577350269
    C(3) = 0.7071067814
    C(6) = 0.0
    C(9) = -0.7071067814
ENDIF

C
C   Solve for transformation vector
C
C1
    IF (ICHECK.GT.0) THEN
    WRITE (4,*) 'A,C assembled:'
    DO 220 J = 1,9
220  WRITE (4,230) (A(J,K),K=1,9),C(J)
230  FORMAT(2X,10F7.4)
    ENDIF

C2
    CALL GAUSS(9,9,A,C)

C1
    IF (ICHECK.GT.0) THEN
    WRITE (4,*) 'Solved:'
    DO 250 J = 1,9
250  WRITE (4,260) (A(J,K),K=1,9),C(J)
260  FORMAT(2X,10F7.4)
    ENDIF

C2
C
C   Build transformation matrix
C

```

```

DO 300 J = 1,3
T(J,1) = C((J-1)*3+1)
T(J,2) = C((J-1)*3+2)
300 T(J,3) = C((J-1)*3+3)
C1
IF (ICHECK.GT.0) THEN
WRITE (4,*) 'T built:'
DO 320 J = 1,3
320 WRITE (4,330) (T(J,K),K=1,3)
330 FORMAT(2X,3F7.4)
C
C Check transformation matrix on input vectors
C
DO 350 J = 1,3
V(J) = 0.0
DO 350 K = 1,3
350 V(J) = V(J)+T(J,K)*N(K)
C
WRITE (4,*) 'V checked:'
370 WRITE (4,380) IP,(V(J),J=1,3)
380 FORMAT(2X,I6,3F7.4)
ENDIF
C2
C
C Transform rod traces to local unit vectors
C
DO 400 J = 1,3
RA(J) = 0.0
RB(J) = 0.0
DO 400 K = 1,3
RA(J) = RA(J)+T(J,K)*TA(K)
400 RB(J) = RB(J)+T(J,K)*TB(K)
CALL MAG(RA,RAMAG)
CALL MAG(RB,RBMAG)
DO 450 J = 1,3
RA(J) = RA(J)/RAMAG
450 RB(J) = RB(J)/RBMAG
C1
IF (ICHECK.GT.0) THEN
WRITE (*,500) IS,IR,IP,RA(1),RA(2),RA(3),RB(1),RB(2),RB(3)
WRITE (4,500) IS,IR,IP,RA(1),RA(2),RA(3),RB(1),RB(2),RB(3)
500 FORMAT(2X,3I5,6F7.4)
ENDIF
C2
C
C Printout results

```

```

C
WRITE (*,600) IS,IR,IP,RA(1),RA(2),RA(3),RB(1),RB(2),RB(3)
WRITE (4,600) IS,IR,IP,RA(1),RA(2),RA(3),RB(1),RB(2),RB(3)
600 FORMAT(2X,3I5,6F7.4)

```

```

C
900 CONTINUE
WRITE (*,*) 'Finished?'
READ (*,*) YN
CLOSE(3)
CLOSE(4)
END

```

```

C
C Unit cross product subroutine (3x3)
C

```

```

SUBROUTINE CROSSP3(U,V,W)
REAL*8 U(3),V(3),W(3)
W(1) = U(2)*V(3)-U(3)*V(2)
W(2) = U(3)*V(1)-U(1)*V(3)
W(3) = U(1)*V(2)-U(2)*V(1)
WMAG = DSQRT(W(1)**2+W(2)**2+W(3)**2)
W(1) = W(1)/WMAG
W(2) = W(2)/WMAG
W(3) = W(3)/WMAG
RETURN
END

```

```

C
C Gaussian reduction equation solver (inefficient)
C

```

```

SUBROUTINE GAUSS(NMAX,NEQ,A,B)
REAL*8 A(NMAX,NMAX),B(NMAX)
REAL*8 C,SUM
LIMIT=NEQ-1
DO 100 N=1,LIMIT
DO 50 I=N+1,NEQ
C=A(I,N)/A(N,N)
B(I)=B(I)-C*B(N)
DO 25 J=N,NEQ
25 A(I,J)=A(I,J)-C*A(N,J)
50 CONTINUE
100 CONTINUE
B(NEQ)=B(NEQ)/A(NEQ,NEQ)
DO 150 I=1,LIMIT
NI=NEQ-I
NI1=NI+1
SUM=0.0
DO 125 J=NI1,NEQ

```

```
125 SUM=SUM+A(NI,J)*B(J)
150 B(NI)=(B(NI)-SUM)/A(NI,NI)
RETURN
END
```

C

C Vector magnitude subroutine (3x3)

C

```
SUBROUTINE MAG(U,UMAG)
REAL*8 U(3),UMAG
UMAG = 0.0
DO 10 I = 1,3
10 UMAG = UMAG+U(I)*U(I)
UMAG = DSQRT(UMAG)
RETURN
END
```

#### A.4. RODS Output for Trace Analyses

##### RODS output for specimen 5-1-1:

XIA = 30.00 XIB = 138.00

Plane 1 normal = -.7505 -.6524 -.1055

Number of solutions = 6

Rod 1 trace = -.8660 .5000 .0000

Rod 2 trace = -.7431 .0000 -.6691

Step	Rot	Plane	Rod 1 Trace	Rod 2 Trace
110	11	2	-.3783 .9256 .0134	-.2622 .5769 .7736
807	81	3	.4848 .6553 -.5793	.0395 .9979 .0509
1310	131	3	.9256 .0134 -.3783	.5769 .7736 -.2622
2007	201	4	.6553 -.5793 .4848	.9979 .0509 .0395
2510	251	4	.0135 -.3783 .9256	.7736 -.2622 .5769
3207	321	2	-.5793 .4846 .6554	.0510 .0393 .9979

##### RODS output for specimen 5-1-2:

XIA = 21.00 XIB = 30.00

Plane 1 normal = -.7685 -.5791 -.2721

Number of solutions = 6

Rod 1 trace = -.9336 .3584 .0000

Rod 2 trace = .8660 .0000 -.5000

Step	Rot	Plane	Rod 1 Trace	Rod 2 Trace
547	55	4	.3464 .8750 -.3382	-.8097 -.4652 .3578
683	68	2	.5097 .7658 -.3922	-.9073 -.3022 .2924
1747	175	2	.8750 -.3382 .3464	-.4652 .3578 -.8097
1882	188	3	.7667 -.3920 .5085	-.3034 .2930 -.9067
2947	295	3	-.3381 .3463 .8751	.3578 -.8096 -.4653

3083 308 4 -.3922 .5095 .7659 .2925 -.9072 -.3023

**RODS output for specimen 5-1-S1:**

XIA = -1.00 XIB = 58.00

Plane 1 normal = -.8099 -.3776 .4489

Number of solutions = 6

Rod 1 trace = -.9998 -.0175 .0000

Rod 2 trace = .5299 .0000 -.8480

Step Rot Plane Rod 1 Trace Rod 2 Trace

166	16	2	-.0001	.7160	.6981	-.6629	-.7487	.0088
1122	112	4	.5277	.8486	.0377	-.8838	-.0542	-.4648
1366	137	3	.7160	.6981	-.0001	-.7487	.0088	-.6629
2322	232	2	.8487	.0377	.5276	-.0542	-.4647	-.8838
2566	257	4	.6981	-.0001	.7160	.0088	-.6628	-.7488
3522	352	3	.0377	.5275	.8487	-.4646	-.8839	-.0542

**RODS output for specimen 5-1-S2:**

XIA = 19.50 XIB = 67.50

Plane 1 normal = -.8825 .1005 -.4594

Number of solutions = 6

Rod 1 trace = -.9426 .3338 .0000

Rod 2 trace = .3827 .0000 -.9239

Step Rot Plane Rod 1 Trace Rod 2 Trace

254	25	4	.6956	.7127	.0907	-.6382	.0187	.7697
370	37	2	.7638	.6381	.0971	-.7113	.1828	.6787
1454	145	2	.7127	.0907	.6956	.0187	.7697	-.6382
1570	157	3	.6382	.0971	.7638	.1827	.6787	-.7113
2654	265	3	.0907	.6955	.7128	.7697	-.6381	.0186



2770 277 4 .0971 .7637 .6382 .6788 -.7113 .1826

## B Remarks on Heat Treatment of Specimens in Air

As mentioned previously, decarburization due to heat treating in air was not considered to be a serious problem. In order to ensure this blank designs and treatment times were chosen which were virtually identical to those employed by Hale, Preston and Nutting in their work for the EPRI superclean rotor program. To further verify it, small samples were cut from the remains of the fracture specimens and tested for carbon content by a professional testing laboratory (Luvack, Inc., Boylston, MA) using the high-temperature combustion method. Table B.1 summarizes the results. As seen there, the most significant level of decarburization occurred for specimen 4-3-2, a drop of about 20% from a nominal level of 0.27-0.28%. Decarburization in the remaining specimens was almost undetectable.

Table B.1 Decarburization Levels Determined by Chemical Check

Specimen	Preheat T (°C)	Preheat Time (hrs)	Carbon (%)
3-1-2	1300	1	0.270
3-1-3	1300	1	0.277
4-3-2	1350	1	0.220
4-3-4	1350	1	0.279
4-5-2	n/a	n/a	0.281
4-5-3	n/a	n/a	0.285

Agren provides an expression for the diffusivity of carbon in austenite [B-1]:

$$D = a[1 + y(1 - y)\left(\frac{b}{T}\right)]\exp\left[-\left(\frac{1}{T} - c\right)(d - ey)\right]$$

where  $a = 4.53 \times 10^{-7}$ ,  $b = 8339.9$ ,  $c = 2.221 \times 10^{-4}$ ,  $d = 17767$ ,  $e = 26436$ ,  $y = x/(1-x)$ , and  $x$  is the mole fraction of carbon. The one-hour diffusion length at 1350°C calculated using this expression is 2.7 mm. Reference B-3 provides example micrographs of air-heat treated steels, etched to reveal the extent of

decarburation. Decarburation layers there are typically 1/10 of the diffusion lengths predicted by the above equation. It is hypothesized that decarburation levels in steels heat treated in air may be less than those expected analytically due to an inhibiting effect of the oxide layer developed on the specimen surface. It is believed that this is especially true for cold samples inserted directly into a hot furnace, rather than heated gradually to temperature. In any case, it was concluded that decarburation does not significantly affect the results of this thesis, in particular with respect to the central question of precipitation behavior of the manganese sulfide.

### **Appendix B References**

- B-1. Agren, J. Scripta Metallurgica, v20, n11, 1986, pp. 1507-1510, cited in B-2, p. 243.
- B-2. Diffusion and Defect Data, Wöhlbier, F. H., ed., v51-52, 1987, p. 243.
- B-3. "Carbon and Alloy Steels," in Metallographic Techniques and Microstructures volume, Metals Handbook, 9th Edition.